DEVELOPMENT OF A MULTI-FREQUENCY SYSTEM FOR MEDICAL APPLICATION OF FOCUSED IMPEDANCE METHOD (FIM)

A dissertation submitted

by

Muhammad Abdul Kadir

in partial fulfillment of the requirements

for the Degree of

Doctor of Philosophy

in Biomedical Physics & Technology

Registration no: 157 (Session: 2013-14)
Old registration no: 04 (Session: 2009-10)

Department of Biomedical Physics & Technology
University of Dhaka
Dhaka 1000, Bangladesh

October 01, 2017

Declaration

I hereby declare that this thesis entitled *"DEVELOPMENT OF A MULTI-FREQUENCY SYSTEM FOR MEDICAL APPLICATION OF FOCUSED IMPEDANCE METHOD (FIM)"* and the work in it was carried out by me for the degree of *Doctor of Philosophy* in Biomedical Physics and Technology under the guidance and supervision of *Professor Khondkar Siddique-e Rabbani*, Department of Biomedical Physics and Technology, University of Dhaka, Bangladesh and *Professor Adrian J. Wilson*, Department of Physics, University of Warwick, United Kingdom. This thesis is a presentation of my original research work. Wherever contributions of others are involved, every effort is made to indicate this clearly, with due reference to the literature, and acknowledgement of collaborative research and discussions. This thesis or any part of it has not been submitted elsewhere for the award of any degree or diploma
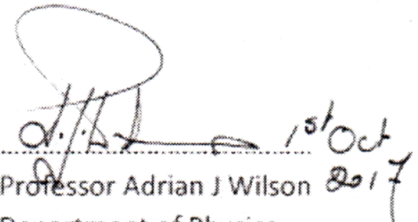
…………………………..

Muhammad Abdul Kadir
Registration no: 157
Session: 2013-14
Department of Biomedical Physics and Technology
University of Dhaka

Certificate

This is to certify that the work incorporated in the thesis *"DEVELOPMENT OF A MULTI-FREQUENCY SYSTEM FOR MEDICAL APPLICATION OF FOCUSED IMPEDANCE METHOD (FIM)"* submitted by *Muhammad Abdul Kadir* was carried out by the candidate under my guidance and supervision. It meets acceptable standards and can be submitted for evaluation in partial fulfillment of the requirements for the degree of Doctor of Philosophy in Biomedical Physics and Technology. To the best of my knowledge, this dissertation has not been submitted elsewhere for any other degree or diploma.

Professor Khondkar Siddique-e Rabbani
Department of Biomedical Physics and Technology
University of Dhaka
Dhaka 1000

Professor Adrian J Wilson
Department of Physics
University of Warwick
United Kingdom

Acknowledgements

I am grateful to Almighty ALLAH who has given me the strength, patience, ability and opportunity for successful completion of this research work.

I wish to sincerely thank all those who have contributed in one way or another to this research. Words can only inadequately express my deep gratitude to my supervisors, *Professor Khondkar Siddique-e Rabbani* and *Professor Adrian J Wilson*, for their meticulous care, kindness and generosity. Their fruitful comments and insightful suggestions have been a crucial formative influence on the present research. They have supported me in every possible way since the beginning of my research. Without their guidance and encouragement, my research would have never come out in the present form.

I would like to thank *Tung Yu* (Nixon) of University of Wariwck for his kind help during PCB manufacturing of the prototype circuits. Special thanks to my beloved student *Rufaida Mahmud*, University of Dhaka who performed the impedance measurements in clinical settings. I also wish to extend my appreciation to all the human subjects who volunteered in the experiments.

Finally, I am very thankful to my parents who have been a towering pillar of support, guidance, inspiration, and sacrifice and even more importantly a great source of prayers throughout my upbringing.

…….

Muhammad Abdul Kadir
Department of Biomedical Physics and Technology
University of Dhaka
Dhaka 1000, Bangladesh

List of Publications

Full papers

1. **M Abdul Kadir**, K Siddique-e Rabbani and Adrian J Wilson, 2012. Development of a multi-frequency system for medical applications of focused electrical impedance method (FIM) appropriate for developing countries, *Proceedings: The 7th International Conference on Appropriate Healthcare Technologies for Developing Countries - AHT2012, London, UK,* **2012**(608CP):1-6 (IET Publications).

2. Abdullah Al Amin, Shahnaj Parvin, **M A Kadir**, Tasmia Tahmid, S Alam and K S Rabbani, 2014. Classification of breast tumour using electrical impedance and machine learning techniques**,** *Physiological Measurement* **35**(6):965, 2014 (IOP Publishing).

3. **M Abdul Kadir**, Humyra Ferdous, Tanvir Noor Baig and K Siddique-e Rabbani, 2010. Ventilation mapping of chest using Focused Impedance Method (FIM), *J. Phys.: Conf. Ser. 224*(1):012031 (IOP Publishing)

4. **M Abdul Kadir**, Tanvir Noor Baig, K Siddique-e Rabbani, 2015. Focused Impedance Method (FIM) to detect localized lung ventilation disorders in combination with conventional spirometry, Biomed. Eng. Appl. Basis Commun. **27**(3):1550029. doi:10.4015/S1016237215500295 (World Scientific Publishing)

5. K Siddique-e Rabbani and **M Abdul Kadir**, 2011. Possible applications of Focused Impedance Method (FIM) in biomedical and other areas of study, *Bangladesh Journal of Medical Physics*, **4**(1):67-74

6. **M Abdul Kadir**, S P Ahmed, G D Al Quaderi, R Rahman, K S Rabbani, Application of the Focused Impedance Method (FIM) to determine the volume of an object within a volume conductor, *Proceedings (on-line) COMSOL Conference, Bangalore, India*, 17-18 September 2013, Available: http://www.comsol.com/ paper/download/182751/ kadir_paper.pdf

Abstract

Monitoring of anatomical structures and physiological processes by electrical impedance techniques has attracted scientists as it is noninvasive, nonionizing and the instrumentation is relatively simple. Focused Impedance Method (FIM) is attractive in this context as it has enhanced sensitivity at the central region beneath the electrode configuration and can localize a region of interest minimizing contribution from neighboring regions. The present work is divided into 3 components. Firstly, a multi-frequency FIM (MFFIM) system capable of measuring all three versions of FIM (FIM-4, FIM-6 and FIM-8 with 4, 6 and 8 electrodes respectively) in the frequency range 10kHz – 1MHz was developed using IC chips readily available in Bangladesh. Secondly, FEM simulations were used to investigate the 3D sensitivity profiles of all versions of FIM in order to be able to use this system appropriately in a given situation. Thirdly, the feasibility of using MFFIM in the study of localized lung ventilation disorders and breast tumour classification was explored – using both simulation and human subject measurements.

For the MFFIM instrumentation, a microcontroller based multi-frequency signal generator and a balanced Howland current source with high output impedance ($476k\Omega$ at $10kHz$ and $58.3k\Omega$ at $1MHz$) were implemented for driving currents of constant amplitude into biological tissues with error <1%. The peak values of voltage signals were measured using two different approaches: analogue synchronous peak detection and digital demodulation. The overall accuracy of the measurement (error< 2%, except 1MHz), resolution better than 0.2Ω and frame rate ($> 1.35sec^{-1}$) of the designed MFFIM system was deemed adequate for noninvasive impedance measurements on the human body.

The effects of the *drive/receive electrode separation, electrode diameter*, volume conductor *inhomogeneity* and *proximity of electrode to the boundary* on the sensitivity profiles were investigated using FEM simulations and compared for the 3 FIM and standard tetra-polar impedance measurement (TPIM) electrode configurations. Two new parameters, *Percentage Depth Sensitivity (PDS)* and *Degree of localization (dol)* were introduced in the present work which suggested that FIM-4 offers superior depth penetration and localization ability when compared to other FIM and TPIM

configurations. An experiment was also designed and performed to investigate 3D sensitivity distributions, which gave good agreement with the simulated results.

An FEM based model of the human thorax was created in the Comsol Multiphysics software and *focused impedance* measurements were simulated with an FIM-4 electrode probe placed on the surface of the thorax. The changes in impedance between maximum inspiration and expiration on different vertical levels of thorax were in the range 5-24% for the FEM model whereas the changes were in the range 5-17% for a human subject. The impedance changes at different vertical levels on the thorax model matched well with experimental findings on the human subject. A simulation study showed that the impedance change between maximum inspiration and expiration, measured using an FIM-4 probe with appropriate electrode separation, was substantially lower in the region of thorax where the underlying lung is filled with fluid (5.1%) compared to that without fluid (16.8%) for a fluid volume of $663cm^3$. Based on this simulation study, a new technique is proposed to detect fluid accumulation in lungs using FIM measurements.

An experimental study was performed on 16 female subjects for classification of palpable breast tumours (whether the tumour is benign or malignant) using the developed MFFIM device. Applying k-nearest neighbors (k-NN) algorithms the *sensitivity*, *specificity* and prediction *accuracy* of breast tumour classification was found to be 75%, 87.5% and 81.25% respectively for k=3. Tissue anisotropy was found to be an important feature for classification of breast tumours. The area under *ROC* curve for the feature representing tissue anisotropy was 0.82.

Overall, the present work has produced a reliable and accurate multi-frequency universal FIM system for noninvasive impedance measurements on the human body, suitable for a resource constrained setting with limited availability of electronic components. The work has expanded knowledge of the spatial sensitivity characteristics of FIM and demonstrated how this new knowledge can help the application of this technique in physiological measurements. In this thesis this knowledge is applied in the detection of lung disease and to the characterization of breast tumours, through modeling and preliminary measurements on human subjects.

Table of Contents

List of Figures

List of Tables

Abbreviations

Bioimpedance Spectroscopy	*BIS*
Degree of Localization	*dol*
Electrical Impedance Tomography	*EIT*
Finite Element Method	*FEM*
Focused Impedance	*FZ*
Focused Impedance Method	*FIM*
Focused Impedance Method: 4 electrode configuration	*FIM-4*
Focused Impedance Method: 6 electrode configuration	*FIM-6*
Focused Impedance Method: 8 electrode configuration	*FIM-8*
Multi-frequency Focused Impedance Method	*MFFIM*
Percentage Depth Sensitivity	*PDS*
Tetra Polar Impedance Measurement	*TPIM*
Tetra-polar Impedance Measurement: Linear electrode configuration	*TPIM_Linear*
Tetra-polar Impedance Measurement: Square electrode configuration	*TPIM_Square*
Separation between two current drive electrodes	*ESD*
Separation between two potential measuring electrodes	*ESR*

Chapter 1 Introduction

1.1 Background and Motivation

Electrical bioimpedance is the opposition to a flow of current by biological tissues(Grimnes and Martinsen, 2008). Monitoring of anatomical structures and physiological events by electrical impedance techniques have attracted scientists as it is noninvasive, nonionizing and the instrumentation is relatively simple. In bioimpedance measurements, usually an alternating current of constant amplitude is applied to a biological tissue through a pair of electrodes and the resulting voltage is measured across another pair of electrodes; commonly known as tetra-polar impedance measurement technique (TPIM). The ratio of the measured voltage to the applied current is the transfer impedance (Brown et al., 2000a, Martinsen and Grimnes, 2009). The extent to which a change in resistivity of a point within a volume conductor contributes to the measured transfer impedance is defined as the sensitivity. In TPIM electrode configuration, if $\mathbf{J}_1$ and $\mathbf{J}_2$ are the current density vectors at a point within the volume conductor due to injection of current I through the exciting and sensing electrode pairs respectively, then the sensitivity of the point can be defined as below (Geselowitz, 1971, Grimnes and Martinsen, 2008),

$$S = \frac{J_1 \cdot J_2}{I^2} \qquad \text{1-1}$$

The sensitivity distribution of the tetra-polar configuration extends to a large distance within the volume conductor and may not be suitable for identifying localized changes in impedivity. Moreover, the presence of negative sensitivity zones may lead to errors when measuring impedance in non-homogeneous medium (Grimnes and Martinsen, 2006). Electrical Impedance Tomography (EIT, initially termed Applied Potential Tomography - APT) was developed which uses a number of electrodes, typically 8, 16 or 32 fixed circumferentially around a cylindrical volume in a particular plane, to image the 2 dimensional conductivity distribution in the said plane (Barber et al., 1984, Holder, 2010). However, since current flows in 3D, there is significant and complex contribution to the image from points in the 3rd dimension (Rabbani and Kabir, 1991, Rabbani et al., 1996). Thus the individual pixel values of the reconstructed image do not give the resistivity distribution expected. Work has been undertaken to obtain a 3D image by having more of the above set of electrodes in several planes along the length of the

cylinder(Metherall et al., 1996, Cherepenin et al., 2001). 2D EIT itself is complex, and a 3D EIT is far more complex, and therefore it would be quite some time before practically usable 3D EIT systems are developed for regular use.

For localized impedance information in a volume conductor, a new measurement technique termed *Focused Impedance Method (FIM)* has been proposed (Rabbani et al., 1999, Rabbani and Karal, 2008). In FIM, transfer impedance is measured by injecting current and measuring voltage values in two orthogonal directions. FIM has enhanced sensitivity at the central region underneath the electrode configuration and can localize a region of interest minimizing contribution from neighboring regions. There are three electrode configurations for FIM measurements: (i) 8-electrode FIM, (ii) 6-electrode FIM and (iii) 4-electrode FIM (Rabbani et al., 1999, Rabbani and Karal, 2008). FIM has been successful in the study of gastric emptying (Rabbani et al., 1999), lung ventilation (Kadir et al., 2009) and abdominal fat thickness (Surovy et al., 2012). There is the potential of using multi-frequency FIM in similar studies and also in tissue characterization. Commercial devices are available for both TPIM and EIT but not for FIM. Devices meant for TPIM can be used for FIM measurements by manually changing the drive and receive electrode pairs (Bioscan-II, Sciospec), but this is not desirable in a practical measurement scenario where the whole measurement should be automatic, giving the possibility of obtaining dynamic measurements with time. But, as shown in section 3.8.6, not all commercial devices are accurate enough throughout the whole range of frequencies (Sciospec ISX-5) or some has limited frequency choice (Bioscan-II).

1.1.1 Instrumentation and Modelling

To investigate the potential application of FIM an integrated multi-frequency FIM (MFFIM) system was required. Considering the socio-economic status of developing countries like Bangladesh, a low cost, portable and reliable system is required that can be maintained and repaired in the field by the researchers in order to investigate the potential applications of the FIM technique in that environment. However, the limited local availability of even quite basic electronic components is a challenge. Therefore, design and fabrication of a multi-frequency FIM system using low cost IC chips commonly available in Bangladesh or other low resource countries is a great necessity, which is one of the challenges addressed in this thesis.

The other challenge addressed by this thesis is in the application of multi-frequency FIM in biological measurements in the human body, particularly for diagnosis and detection of liquids (lung edema) and solids (breast tumour) in human body. Multi-frequency bioimpedance measurements using TPIM have been attempted in a variety of research applications including lung ventilation (Frerichs, 2000), breast tumour screening (da Silva et al., 2000, Zou and Guo, 2003), abdominal fat thickness (Scharfetter et al., 2001) and cervical cancer detection (Abdul et al., 2006). The present work was taken up to investigate the use of *multi-frequency FIM* in the study of localized lung ventilation disorders and breast tumour classification; because localized impedance information could give better results. However an appropriate FIM configuration and optimum electrode separation is needed for appropriate localization. The spatial sensitivity distribution is different for different impedance measurement techniques. Again, for a particular measurement method, the sensitivity distribution is different for different electrode separations. 3D sensitivity distributions of bioimpedance measurement methods could give an idea about which portion of the volume conductor can be sensed using surface electrodes and may be helpful in choosing an appropriate electrode configuration to suit a particular application. For example, for measurement of skin impedance is useful if the most sensitive region is just below the electrode plane. On the other hand, for measurement of impedance changes of lung due to breathing, it is desirable to have significant sensitivity deep below the electrode plane. For a semi-infinite homogeneous medium and point current sources, sensitivity of TPIM and FIM configurations have been investigated analytically using vector lead fields by determining the vector paths from the electrode to the point where the sensitivity is to be determined (Brown et al., 2000a, Islam et al., 2010). But in practice, the volume conductor (human body) is finite and inhomogeneous. Moreover, the electrodes are not point sources as assumed by (Brown et al., 2000a) but of finite size. Pettersen et al. showed that Comsol Multiphysics® software (Multiphysics, 2012) is a very useful finite element method (FEM) tool to investigate volume impedance measurement problems (Pettersen and Høgetveit, 2011) and they analyzed and compared sensitivity fields of FIM electrode configurations graphically and numerically considering a spheres beneath the center of the electrode array (Pettersen et al., 2014). However, sensitivity distributions throughout the volume conductor could give a better visualization. Importantly, the *depth penetration*, *localization ability* and the effect of various factors like *electrode separation*, *electrode diameter*, *volume conductor inhomogeneity* and *proximity of*

boundary to electrodes array on the sensitivity profiles needed to be explored. More importantly, accuracy of the simulation results needed to be investigated experimentally. To address these issues, the current work aims to analyze 3D sensitivity profiles throughout a volume conductor at different planes for various impedance measurement techniques using FEM simulations. Within this thesis the 3D sensitivity distributions of FIM were investigated experimentally.

1.1.2   Application of FIM

In diseases like pulmonary edema, abscess, TB or pneumonia, localized regions within the lungs are filled with fluids or masses restricting air to flow to the alveoli (Robin et al., 1973, Nelson et al., 1995). Chest radiography is the widely used method of assessing and quantifying lung edema (Milne et al., 1985). However, radiographic methods involve ionizing radiations and these are not suitable for long term monitoring. Besides, in the rural areas of the low resource countries, even X-ray facilities are not readily available. Accumulation of fluid in the air spaces of the lung changes the dielectric properties of lung tissue and researchers have applied bioimpedance techniques to investigate fluid accumulation in lungs. In earlier studies, transthoracic impedance measurements were measured for the diagnosis of pulmonary edema but with limited success (Fein et al., 1979a, Pomerantz et al., 1969). Electrical Impedance Tomography (EIT) was also used for the estimation of liquid volumes in the lung in dogs where liquid volumes were accurate to within 10 ml (Adler et al., 1997, Newell et al., 1996). (Campbell et al., 1994) reported some preliminary results that EIT can be used in human subjects in the clinical environment to detect small changes in intra-thoracic fluid. FIM has particular advantages in studies of lung function and preliminary studies on lung ventilation have demonstrated success of FIM in measuring the impedance changes of the thorax due to breathing (Kadir et al., 2009, Kadir et al., 2010). In this thesis an FEM model of the human thorax is developed and a technique to detect localized ventilation disorder is proposed based on a simulation study.

One of the features of FIM is the improved sensitivity beneath the centre of the electrode array suggesting its use in the detection of solid tumours in otherwise near homogeneous surroundings, in particular breast tumours. Breast cancer is the second leading cause of cancer death in women (Stewart and Wild, 2014). Many females come to the physician after they feel a lump when it is already quite large (Laver et al., 1999). At this stage, the only way to know for sure whether a breast tumour is cancerous or non-cancerous is

biopsy. In biopsy samples of tissue from the suspicious area are taken invasively and the tissue is examined under microscope. This can be done surgically by making an incision in the skin and removing a part of the suspicious area. However, nowadays, nonsurgical needle biopsy (i) Fine Needle Aspiration Cytology (FNAC) (Wu and Burstein, 2004) or (ii) Core Needle Biopsy (CNB) (Florentine et al., 1997) are commonly used for breast tumour examination (Moschetta et al., 2014). Core biopsy gives a better result but needs a considerable amount of tissue to be taken out at several locations under local anesthesia. A biopsy is not hazard-free. In a few per cent of cases where the tumour is cancerous, tissue adhering to the tip of the needle introduces cancer at the upper cutaneous layers (Chao et al., 2001). Biochemical and morphological properties of healthy, benign and cancerous tissue are different (Castro et al., 2008, Baba and Catoi, 2007, Liotta, 1983). Therefore the dielectric properties (conductivity and relative permittivity) of cancerous tissue is expected to be different from healthy tissue. Based on measurements on excised human breast tissue, Surowiec et al reported that the frequency spectrum of dielectric properties (conductivity and permittivity) in the range 20kHz-100MHz for healthy and cancerous breast tissues are different (Surowiec et al., 1988). This means that the electrical resistance of intra and extra-cellular fluids and cell membrane capacitance of cancerous tissue and that of healthy tissue are different as reported from in vivo impedance measurements on human subjects by (Morimoto et al., 1990). This is the basis of using bioimpedance techniques in the study of breast tumour. Significant differences between cancerous and normal tissue have been reported by in vitro measurements on freshly excised breast tissue by (Jossinet, 1998, Jossinet, 1996, Jossinet and Schmitt, 1999, da Silva et al., 2000). Difference between electrical conductivity and permittivity values of normal and abnormal tissue based on multi-frequency EIT measurements on breast have also been reported by (Hartov et al., 2005, Soni et al., 2004). Using EIT measurements, the detection of breast malignancy has been investigated (Cherepenin et al., 2001, Kerner et al., 2002, Halter et al., 2015). However, these works have showed that EIT requires complex measurement instrumentation and accurate electrode placement. FIM requires much simpler instrumentation, allows electrode placement based on palpation and having the feature of better spatial localization, there is a potential of multi-frequency FIM in the characterization of breast tumour whether a tumour is benign or malignant. This thesis describes a preliminary study on human subjects for breast tumour classification using multi-frequency FIM applying machine learning algorithms and statistical analysis.

1.2   Aims and Objectives

The overall aim of the current research work was to develop a low cost and reliable multi-frequency FIM system for use and maintenance in resource constrained environments; and to study the feasibility of using multi-frequency FIM in the study of localized lung ventilation disorders and breast tumour classification.

Specific Aims and objectives of the PhD research work:

i) To design and develop a microcontroller based multifrequency FIM instrument capable of measuring all the three electrode configurations of FIM satisfy safety standards so that it can be used in clinical settings. This involves the following:

   a. Design and development of a microcontroller based sinusoidal signal generator and a constant current source circuit capable of driving variable loads at multiple frequencies.

   b. Design and development of circuitry for amplification of voltage signal from human subjects minimizing noise.

   c. Development of hardware and software algorithms for demodulation of absolute impedance and phase.

ii) To analyze the performance of the implemented FIM system and to compare its performance with that of commercially available system.

iii) To investigate the three dimensional sensitivity profiles of different bioimpedance measurement techniques using FEM simulations in Comsol Multiphysics and their comparison to visualize which electrode configuration is most suitable for the study of human lung ventilation disorder and breast tumour using bioimpedance.

iv) To design and implement an experiment to study 3D sensitivity profiles of FIM.

v) To develop an FEM model of the human thorax to compute transfer impedance values and to visualize contributions of specific domains within the model.

vi) To study localized lung ventilation using on FEM simulations.

vii) To study the feasibility of using multi-frequency FIM measurements on human subjects for classification of breast tumour whether it is benign or malignant applying machine learning algorithms and statistical analysis.

1.3 Thesis Outline

This thesis is divided into five chapters. The literature related to electrical bioimpedance, bioimpedance measurement techniques and its application in the study of lung ventilation and breast tumour characterization has been reviewed in Chapter 2. The design and development of the multi-frequency FIM system has been described and its performance has been analysed in Chapter 3. The Chapter 4 is divided into three parts. In the first part, 3D sensitivity distributions of various impedance measurement techniques have been analysed and compared using FEM simulations and validated experimentally. An FEM model of the human thorax and a simulation study for detection of localized lung ventilation disorder is described in the second part. The third part of Chapter 4 describes a preliminary experimental study for classification of breast tumour whether it is benign or malignant using multi-frequency FIM measurements. Finally, the overall findings of this research and some future research directions has been concluded in Chapter 5. References have been arranged alphabetically and cited in the text according to Harvard referencing style.

Chapter 2   Literature Review

2.1   Electrical Properties of biological tissues

2.1.1   Bioimpedance

The human body is a complex volume conductor where various tissues differ in specific electrical properties such as conductivity and relative permittivity. Bioimpedance is the opposition to a flow of electric current through biological tissue. In bioimpedance measurements, usually an alternating current is applied to a tissue through a pair of electrodes and the resulting voltage across another pair of electrode is measured. The ratio of the measured voltage to the applied current gives the transfer impedance (Martinsen and Grimnes, 2009), quantified as ohms. Dielectric properties are different for different tissues of the body (Gabriel et al., 1996b, Foster and Schwan, 1995, Geddes and Baker, 1967); and for a particular tissue it is different in health and disease. For example, electrical impedance of cancerous tissue is significantly lower than that of normal tissue (Brown et al., 2000b, Smith et al., 1986). Bioimpedance can reflect different physiological conditions and events; eg. transthorasic impedance changes during breathing because the electrical impedance of lung tissue changes as a function of air content (Nopp et al., 1993). Therefore monitoring of anatomical structures and physiological processes and characterization of tissues by electrical bioimpedance techniques have attracted scientists as it is noninvasive, nonionizing and the instrumentation is relatively simple.

2.1.2   Biological tissue in electric field

Cells are the structural and functional units of biological tissues which are bounded by semipermeable membranes. Cell membranes are made of a phospholipid bilayer and behave as electrical insulators whereas the intra and extracellular fluids contain ions and therefore are conducting. Effectively, biological tissues contain free ions as well as electric dipoles. In an applied electric filed, the ions move, but in a restricted manner. In contrast, the dipoles tend to polarize and produce a field inside the tissue that opposes the applied field. The ratio of the applied electric filed to the resultant field inside the tissue is defined as relative permittivity(ε_r). Therefore, biological tissues can be described as materials having both conductivity (σ) and permittivity (ε). The complex quantities conductivity and permittivity can be expressed as follows (Miklavčič et al., 2006, Pethig and Kell, 1987):

$$\sigma^* = \sigma + i\omega\varepsilon \qquad\qquad \text{......... } 2\text{-}1$$

$$\varepsilon^* = \varepsilon_r - \frac{i\sigma}{\omega\varepsilon_0} = \varepsilon_r' + i\varepsilon_r'' \qquad \text{.........}2\text{-}2$$

and

$$\sigma^* = i\omega\varepsilon^* = i\omega\varepsilon_0\varepsilon_r^* \qquad\qquad \text{........}2\text{-}3$$

where ω is the frequency of the applied electric field; ε_0 is the permittivity of free space and $\varepsilon_r' = \varepsilon_r$ and $\varepsilon_r'' = \frac{\sigma}{\omega\varepsilon_0}$.

The dielectric properties (conductivity and permittivity) of biological materials are frequency dependent. The permittivity (ε_r') and conductivity (σ') of biological material exhibit various frequency dispersions (Schwan, 1957) as shown in Figure 2-1.
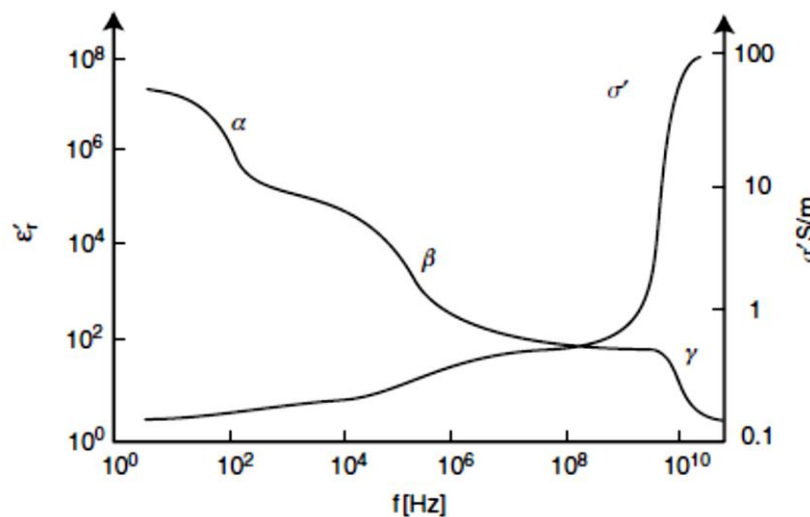
Figure 2-1 Frequency dependence of conductivity and permittivity of biological material Source: (Grimnes and Martinsen, 2008)p-90.

The α dispersion is considered to be associated with the diffusion processes of the ionic species, cell membrane permeability and gated channels; the β dispersion is associated with the dielectric properties of cell membrane and their interactions with intra- and extra-cellular fluids. The γ dispersion is associated with dipolar mechanism in polar media such as water, salt and proteins (Foster and Schwan, 1995, Ivorra, 2003, Martinsen et al., 2002).

2.1.3 Frequency response of bioimpedance

Electronically, the cell membrane can be modelled as capacitors whereas intra and extracellular regions can be modeled as resistors. The widely known electrical equivalent model of biological tissue is the Cole model (Cole and Cole, 1941) as shown in Figure 2-2

9

where R_e and R_i are the resistances of extra and intracellular spaces respectively; C_m is the membrane capacitance.

Figure 2-2 Electrical equivalent model of biological tissues: Cole model

At low frequencies, the current cannot penetrate the cell membrane because of its capacitive behavior and therefore most of the current flows through the extra cellular spaces. But at higher frequencies, the cell membrane is permeable for currents and therefore current flows through both intra and extra cellular spaces as shown in Figure 2-3.
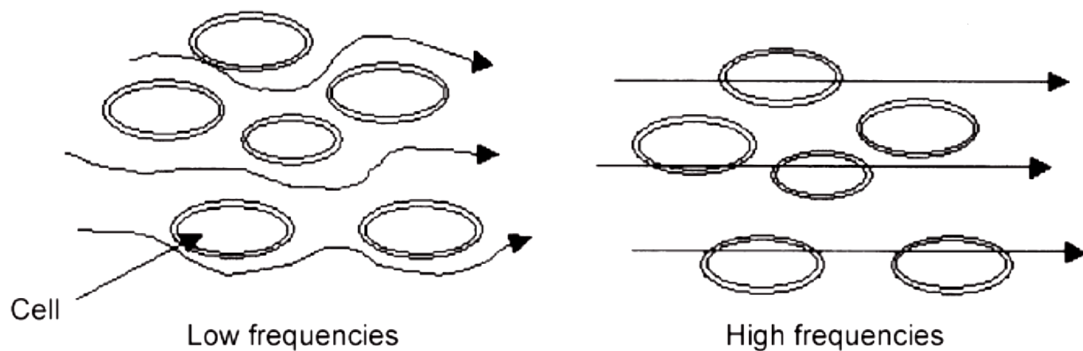
Figure 2-3 Current paths through biological tissues both at low and high frequencies of the applied electric field. Source: (Holder, 2004) p-416

In order to fit modeled impedance values to actual measured bioimpedance values, the capacitor in the *Cole model* needed to be replaced by a *Constant Phase Element* (*CPE*) (Grimnes and Martinsen, 2008)p-296 as shown in Figure 2-4.

The impedance of the equivalent model of Figure 2-4 can be expressed as Cole equation given below (Cole, 1940)

Figure 2-4 Equivalent electrical circuit of biological tissue with three elements: a low-frequency resistor R_0, a high- frequency resistor R_∞ and a constant phase element (CPE)

$$Z = R_\infty + \frac{\Delta R}{1+(j2\pi f\tau)^\alpha} \qquad \text{-- } 2\text{-}4$$

where $\Delta R = R_0 - R_\infty$; R_0 and R_∞ represent the resistances at zero and infinite frequency respectively, f is the frequency of the applied current and τ is the time constant (ΔRC). The parameter α is related to constant phase element (CPE) which represents frequency dependent capacitance and its value is between 0.5 and 1 (Grimnes and Martinsen, 2008, Ivorra, 2003).

10

2.2 Measurement of bioimpedance

2.2.1 Lead Vector and Lead Field

Lead vector determines how much a dipole source located at a point inside a volume conductor contributes to the potential difference between two points (a lead) on the surface of the volume conductor (Geselowitz, 1971, Schmitt, 1957). Let us consider a dipole source ($\boldsymbol{p}_k$) at point Q within a finite homogeneous volume conductor as shown in Figure 2-5. The potential difference due to this dipole is to be measured across two point A and B located on the surface of the volume conductor. If c_x, c_y and c_z are the potential measured across the bipolar lead (A,B)

Figure 2-5 A dipole source placed at a point Q inside a volume conductor. The points A and B defines a lead to measure the potential difference.

for placing a *unit dipole source* along x, y and z axis respectively, the lead voltage φ_k due to the dipole source ($\boldsymbol{p}_k$) can be given by

$$\varphi_k = c_x p_x + c_y p_y + c_z p_z \qquad \text{------ 2-5}$$

assuming the volume conductor as a linear medium; where p_x, p_y and p_z are the components of $\boldsymbol{p}_k$ along x, y and z axis respectively.

$$\varphi_k = c_x p_x + c_y p_y + c_z p_z \qquad \text{------ } \textit{2-5} \text{ can be written as}$$

$$\varphi_k = c_k \cdot p_k \quad \text{----- } \textit{2-6}$$

The vector $\boldsymbol{c} = c_x \boldsymbol{i} + c_y \boldsymbol{j} + c_z \boldsymbol{k}$ is called the lead vector (Malmivuo and Plonsey, 1995). The lead vector depends on the position of the dipole source, the position of the measurement lead, the conductivity of the volume conductor and of course on the shape of the volume conductor (Malmivuo and Plonsey, 1995). The lead vector has different value at different source location. The field of lead vectors ($\boldsymbol{c}$) within the volume conductor is called the *Vector Lead Field* denoted as $\boldsymbol{L}$ (Geselowitz, 1971). The lead field concept implies that the contribution of a source located at a point on the volume conductor to the measured potential across a lead depend on the magnitude of the source dipole as well as on the angle between the lead vector and the dipole.

11

For distributed sources within the volume conductor the total voltage across the lead (A,B) is given by

$$\varphi_{AB} = \sum_k c_k \cdot p_k \quad \text{----- 2-7}$$

2.2.2 Reciprocity theorem and Transfer Impedance

In case of electrical impedance measurements in a volume conductor, the source (dipole) mentioned above is not endogenic (i.e., not from an internal source within the volume conductor) but an electric field is applied externally through a lead. It is convenient to describe lead field theorem regarding electrical impedance measurement using the theorem of reciprocity introduced by Hermann von Helmholtz in 1853 (Helmholtz, 1853).
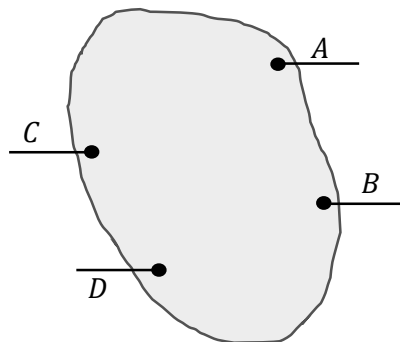
Figure 2-6 Volume conductor with two leads

Suppose a current I_{AB} is introduced to the lead (A,B) and the resulting voltage across the lead (C,D) is φ_{CD} (Figure 2-6). Conversely, voltage across the lead (A,B) is φ_{AB} for current I_{CD} on the lead (C,D). Reciprocity theorem says that if the current and the potential electrode pairs are interchanged in the above system, the measured values remain the same. Therefore the transfer impedance can be given as (Geselowitz, 1971) :

$$Z = \frac{\varphi_{AB}}{I_{AB}} = \frac{\varphi_{CD}}{I_{CD}} \quad \text{------- 2-8}$$

2.2.3 Sensitivity

The extent to which a change in conductivity of a point within the volume conductor contributes to the measured transfer impedance is defined as the sensitivity of that point. Therefore the sensitivity to the transfer impedance may be determined considering only current driven through both the pairs of electrodes. Suppose, $\boldsymbol{J_{AB}}$ and $\boldsymbol{J_{CD}}$ are the current density vectors at a point (P) within the volume conductor v (Figure 2-7) due to injection of current I_{AB}

Figure 2-7 Current density vectors for two leads at a point within a volume conductor

and I_{CD} through the exciting and sensing electrode pairs respectively.

For an infinitesimal change in conductivity, $\Delta\sigma$ of volume v, within the medium the change in transfer impedance can be given as (Geselowitz, 1971):

$$\Delta Z = -\Delta\sigma \int \mathbf{L}_{AB} \cdot \mathbf{L}_{CD} dv \text{ ------2-9}$$

where $\mathbf{L}_{AB}$ and $\mathbf{L}_{CD}$ are vector lead fields given by $\mathbf{L}_{AB} = -\frac{\nabla\varphi_{AB}}{I_{AB}}$ and $\mathbf{L}_{CD} = -\frac{\nabla\varphi_{CD}}{I_{CD}}$ respectively. Now, the gradient of the scalar potential φ can be written as $\nabla\varphi = -\frac{\mathbf{J}}{\sigma}$ where $\mathbf{J}$ is the current density and σ is the electrical conductivity of the medium. Substituting these values in equation *2-9* for ΔZ we have,

$$\Delta Z = -\frac{\Delta\sigma}{\sigma^2} \int \frac{\mathbf{J}_{AB} \cdot \mathbf{J}_{CD}}{I_{AB} I_{CD}} dv \text{ ------- 2-10}$$

with the units of ohms. If the current through both the leads are same (I) then

$$\Delta Z = -\frac{\Delta\sigma}{\sigma^2} \int \frac{\mathbf{J}_{AB} \cdot \mathbf{J}_{CD}}{I^2} dv \text{ -------- 2-11}$$

This gives a value for S, the sensitivity of a point within the volume conductor as:

$$S = \frac{\mathbf{J}_{AB} \cdot \mathbf{J}_{CD}}{I^2} \text{ ------ 2-12}$$

with the units m^{-4}. The term $\frac{\mathbf{J}_{AB} \cdot \mathbf{J}_{CD}}{I^2}$ gives the shape of the sensitivity distribution and $\frac{\Delta\sigma}{\sigma^2}$ scales the values.

Let us assume that σ_m is the conductivity of the medium and σ_c is the conductivity of the region where $\sigma c \neq \sigma m$, then equation 2-11 can be rewritten as

$$\Delta Z = -\frac{\Delta\sigma}{\sigma_m^2} \int \frac{\mathbf{J}_{AB} \cdot \mathbf{J}_{CD}}{I^2} dv = -\frac{\sigma_m - \sigma_c}{\sigma_m^2} \int \frac{\mathbf{J}_{AB} \cdot \mathbf{J}_{CD}}{I^2} dv \text{ ------2-13}$$

Substituting $\Delta Z = Z_m - Z_c$; where Z_m is the measured transfer impedance without the change in conductivity and Z_c is the measured transfer impedance with the change in conductivity we get:

$$Z_m - Z_c = -\frac{\sigma_m}{\sigma_m^2} \int \frac{\mathbf{J}_{AB} \cdot \mathbf{J}_{CD}}{I^2} dv + \frac{\sigma_c}{\sigma_m^2} \int \frac{\mathbf{J}_{AB} \cdot \mathbf{J}_{CD}}{I^2} dv \text{ ------- 2-14}$$

A physical interpretation of this equation is that the change in the measured transfer impedance is due to the volume, v, of conductivity, σ_m, being replaced by a volume, v, of conductivity σ_c. Since $\Delta\sigma$ is infinitesimally small whilst $\sigma_m \neq \sigma_c$; it can be approximated that $\sigma_m \approx \sigma_c$. Substituting this value into equation *2-14* and setting sign of the terms so that when $\sigma_m < \sigma_c$ then $Z_m > Z_c$ we have:

13

$$Z_m - Z_c = \frac{1}{\sigma_m} \int \frac{J_{AB} \cdot J_{CD}}{I^2} \, dv - \frac{1}{\sigma_c} \int \frac{J_{AB} \cdot J_{CD}}{I^2} \, dv \text{ ------ } 2\text{-}15$$

The first and second terms on the right hand side of equation *2-15* corresponds to Z_m and Z_c respectively. If the medium is made up of N regions of changed conductivity, σ_i, where i = 1----N then we can write

$$Z_m - \sum_{i=1}^{N} Z_i = \frac{1}{\sigma_m} \int \frac{J_{AB} \cdot J_{CD}}{I^2} \, dv - \sum_{i=1}^{N} \frac{1}{\sigma_i} \int \frac{J_{AB} \cdot J_{CD}}{I^2} \, dv \text{ ------ } 2\text{-}16$$

In the limit Z_m becomes one of the N regions then equation *2-16* can be rewritten as:

$$Z_T = \sum_{i=1}^{N} Z_i = \sum_{i=1}^{N} \frac{1}{\sigma_i} \int \frac{J_{AB} \cdot J_{CD}}{I^2} \, dv \text{ -------- } 2\text{-}17$$

where Z_T is the total (measured) transfer impedance of the volume conductor.

2.2.4 Bipolar Impedance Measurement

In bipolar impedance measurements, a constant current is injected to a volume conductor through two electrodes and the resulting voltage drop is measured across the same electrode pair. According to Ohm's law, the ratio of the measured voltage to the injected current gives the electrical impedance of the volume conductor under investigation $Z = \frac{V}{I}$. The technique is simple, however, if the volume conductor is a liquid (an electrolyte), contact potentials, polarization (Schwan, 1968) and contact impedances (resistance and capacitance) arise at the electrode-liquid interface which may completely mask the impedance of the bulk material (Hwang et al., 1997). Use of alternating currents (ac) in the measurement can eliminate the contact potentials to a large extent since they are basically dc and almost constant with time.
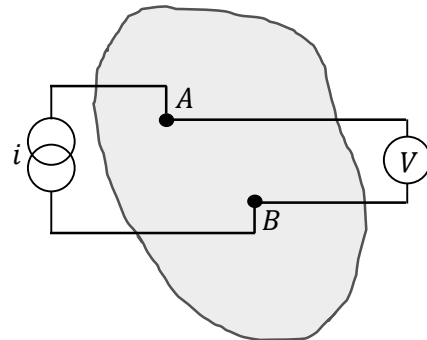
Figure 2-8 Bipolar Impedance measurement technique, current injected and voltage measured using two electrodes.

Polarization problems may also be eliminated through the use of ac. However, contact impedances cannot be eliminated using the simple two electrode configuration.

2.2.5 Tetra-polar Impedance Measurements (TPIM)

A slightly different technique known as Tetrapolar Impedance Measurement (TPIM) has been in use for a long time. Here four electrodes are used as shown in Figure 2-10 in a 2 dimensional representation of the method. Current I is passed through two outer electrodes, while potential V developed across the other two are measured. Since potential measuring devices have very high input impedances, current drawn through the two central potential electrodes is almost zero, rendering the potential difference across the contact impedances
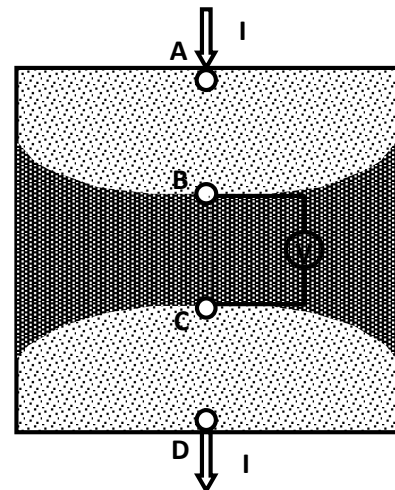
Figure 2-10 TPIM scheme and the wide sensitive zone between the equipotential lines of interest.

negligible. Thus the potential measured is the true potential dropped across the bulk region between the two potential electrodes. The potential dropped across the contact impedances of the two current electrodes do not contribute to the potential measurement. In this method, the measured voltage (V) is the potential difference between the marked iso-potential lines passing through the two potential electrodes (B,C), as shown by the central shaded region in Figure 2-10. The ratio of the potential developed across the potential measurement electrodes to the injected current is defined as transfer impedance $Z_t = \frac{V}{I}$ (Martinsen and Grimnes, 2009). The advantage of tetra-polar technique over bipolar technique is that it can minimize the effect of electrode artifact (Ragheb et al., 1992) and significantly reduce the effect of tissue-electrode contact impedance.
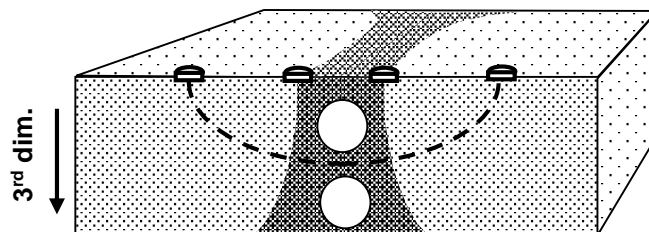
Figure 2-9 Extension of sensitive zone into the 3rd dimension.

Although the discussions with respect to Figure 2-10 relate more to a 2 dimensional situation, this can be extended to target objects in the 3rd dimension using surface electrodes as shown in Figure 2-9. The current gets distributed in the 3rd dimension with equi-current lines spreading out; and current density decreasing with depth. The

15

equipotential surfaces through the potential electrodes bend outwards with depth, encompassing more volume with increasing depth. Therefore within the sensitive zone, an object of a fixed size and shape placed near the surface will have more contribution to the measured impedance than when it is taken to increasing depths, which is akin to saying that the sensitivity decreases with depth. An undesirable feature of a tetrapolar system is the presence of a region with negative sensitivity which exists between the drive and receive electrodes and occurs because of the angle between the current density vectors in equation 2-12 due to the relative positions of the drive and receive electrodes. An object of different conductivity to the surrounding medium placed within negative sensitive region will perturb the equipotential surfaces in the opposite direction to an object placed in the positive sensitive region. Therefore the effective impedance of the negative sensitive region will contribute to a reduction of the impedance desired to be measured. This is also demonstrated in the results obtained by Brown et al. (Brown et al., 2000a). Therefore while measuring the impedance of a large object extending to negative sensitive regions; one needs to interpret the results carefully. The sensitivity distribution of tetra-polar configuration extends to a large distance within the volume conductor and may not be suitable for identifying localized changes in impedivity. Moreover, the presence of negative sensitive zones may lead to large errors when measuring impedance in a non-homogeneous medium (Grimnes and Martinsen, 2006).

2.2.6   Electrical Impedance Tomography (EIT)

Observing Figure 2-10, one point is clear that the sensitive zone is rather broad and if one wants to have localized information this is not the right system to work with. To overcome this difficulty, Electrical Impedance Tomography (EIT, initially termed Applied Potential Tomography - APT) was developed which uses a number of electrodes, typically 8, 16 or 32 fixed transversely around a cylindrical volume in a particular plane, to image the 2 dimensional conductivity distribution in the said plane (Barber et al., 1984, Holder, 2010). A known alternating current (I) is applied to a volume conductor through a pair of electrodes and the resulting potential differences (V) is measured across the remaining pair of electrodes as shown in Figure 2-11A. The adjacent electrode pair is used for the next current application and potential differences is measured across the remaining pair of electrodes (Figure 2-11B). Location of the current injecting and measuring electrode pairs successively rotates around the whole geometry. For 16-electrode EIT, one complete rotation creates 208 impedance values. The collected data are then used on

reconstruction algorithms to get image of the plane of the volume conductor. However, since current flows in 3D, there is significant and complex contribution to the image from points in the 3rd dimension (Rabbani and Kabir, 1991, Rabbani et al., 1996). Thus the individual pixel values of the reconstructed image do not give the right point sensitivity as expected. Work has been undertaken to obtain a 3D image by having more of the above set of electrodes in several planes along the length of the cylinder(Metherall et al., 1996, Cherepenin et al., 2001). 2D EIT itself is complex, and a 3D EIT is far more complex, and therefore it would be quite some time before practically usable 3D EIT systems are developed for regular use.
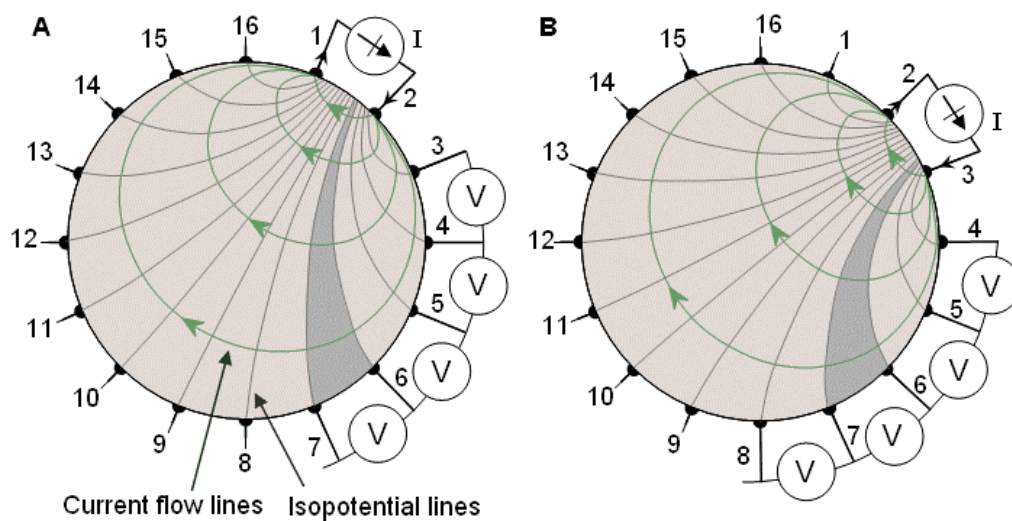
Figure 2-11 Measurement principles of a 16 electrode EIT system showing the iso-current and iso-potential lines, source: (Malmivuo and Plonsey, 1995)p-521.

2.2.7 Focused Impedance Method (FIM)

If one is to measure the impedance of a localized object at a known location, which is embedded in a volume conductor of uniform but different conductivity, then a practical method would be to ensure that the object lies within the central sensitive zone by proper placement of electrodes. Focused Impedance Method (FIM), is a simple technique of impedance measurement that can localize a zone of interest in a volume conductor minimizing the effects of neighboring regions (Rabbani et al., 1999). The basis of the FIM technique is that the transfer impedance is measured by injecting current and measuring voltage values in two orthogonal directions giving a higher sensitivity in the central region compared to its surroundings. This technique is particularly useful if the

impedance of the target object changes between two sets of measurements while the background remains unchanged, even if it has regions with different conductivity. The above impedance change could be due to time dependent activity, when measurement at two different times could indicate the change. Alternatively, if the impedance of the target object changes with frequency while the background remains constant, it is also possible to use such measurements. There are 3 possible electrode configurations for FIM measurements and that these are discussed in the following sections.

2.2.7.1   8-electrode FIM (FIM-8)

The basic concept of FIM involves two orthogonal and concentric TPIM measurements and summing the two measured impedance. With reference to Figure 2-12, ABCD are the electrodes in a conventional four electrode measurement while EFGH form another similar set perpendicular to the former with the zone bounded by B,F,C & G forming the common zone of interest. Potential measuring electrodes B and C work for the current drive pair AD while G and H
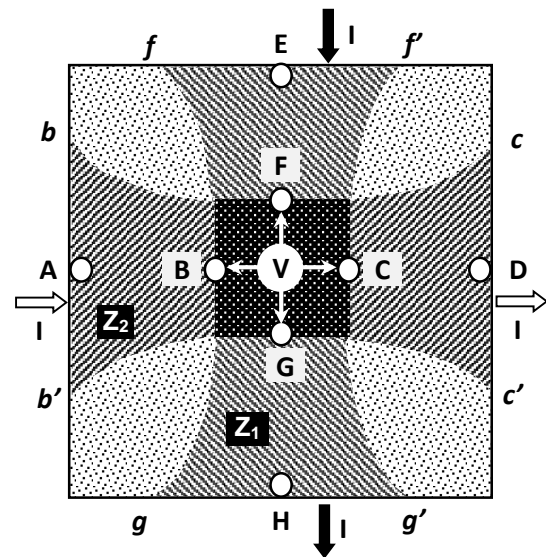
Figure 2-12 Basic concept of 8 electrode Focused Impedance Method (FIM). Central square zone has a dominant sensitivity, and is therefore, focused.

similarly work for the pair EF. A conventional four electrode measurement through ABCD gives the effective impedance of the zone bounded by equipotentials fg and $f'g'$ (shown shaded, $Z_1 = \frac{V}{I}$) with sensitivity falling away from the centre. Similarly, measurement through electrodes EFGH gives the effective impedance between the equipotential lines bc and $b'c'$ (shown shaded, Z_2) with sensitivity varying in a similar way. The central square zone contributes to the sum (Z_1+Z_2) more than double than the neighboring regions (Rabbani et al., 1999). Thus the central region has a dominant contribution to the total summed value, i.e., in effect, the measurement focuses onto the central square region; hence the name, '***Focused Impedance***'. Practically, the equipotentials would change shape and location if there are objects of various conductivities in the active region. However, assuming that the condcutivities do not differ much from a case of uniform conductivity throughout, this model would provide a simple approach. This basic FIM requires 8 electrodes. The two orthogonal

measurements can be done in two different sequence by switching the drive and receive electrodes and then summing the two impedance values. Alternatively, the FIM value can be measured simultaneously by using two isolated current sources (Rabbani et al., 1999).

2.2.7.2   6-electrode FIM (FIM-6)

As mentioned above, the focused system basically involves two independent four electrode measurements which need eight electrodes in all. However, the equipotential
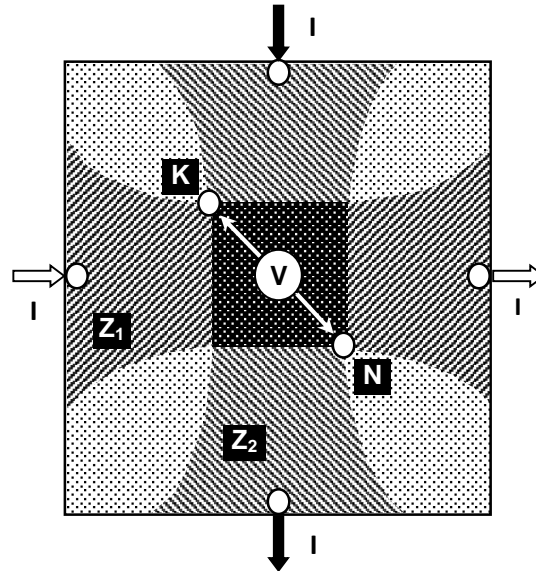
Figure 2-13 Basic concept of 6 electrode Focused Impedance Method.

lines *b-c* and *f*-g (Figure 2-12) intersect at point *K*. Similarly the equipotential lines *b'-c'* and *f'*-g' intersect at point *N* as shown in Figure 2-13. (Rabbani et al., 1999) suggested that potential measuring electrodes *B,F* can be replaced by electrode *K*; similarly potential measuring electrodes *C,G* can be replaced by electrode *N*. In this case, two potential measuring electrodes (K,N) are placed at diagonal positions of the central focused region as shown in Figure 2-13. Since each of these falls on the intersection of two equipotential lines, these two can replace the role of the four potential electrodes in Figure 2-12 (Rabbani et al., 1999). This version is called a 6 electrode FIM. The square region produced by the diagonal between the two common potential electrodes K & N is the approximate focused region. The measurements of the two orthogonal TPIM systems can be made sequentially, with the measured potentials kept in memory and summed later to get FIM. Alternatively, if the two orthogonal driving currents are electrically isolated (allowing simultaneous current drives without cross-interference) but synchronized in appropriate phase relationship, a single measurement of potential across K & L will give the summed

19

impedance value, or, the FIM. The orthogonal current drives can be isolated using two isolation transformers as described by (Rabbani et al., 1999).

2.2.7.3 4-electrode FIM (FIM-4)
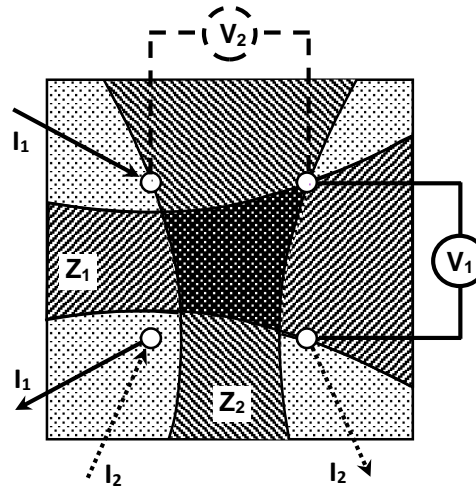
Figure 2-14 Basic concept of 4 electrode Focused Impedance Method

This technique needs 4 electrodes for focused impedance measurements (Rabbani and Karal, 2008). Current is passed through two adjacent electrodes and potential is measured across the opposite pair from which an impedance value is obtained. Then measurement is taken with the arrangement rotated through 90°. These have been indicated by I_1 , Z_1 and I_2, Z_2 respectively. The sum of the two orthogonal impedance measurements, $Z_1 + Z_2$ again gives a dominant sensitivity in the central region which has been shown through regions bounded by appropriate equipotential lines in Figure 2-14.

2.2.8 Sensitivity distribution in bioimpedance measurements

The spatial sensitivity distribution of Bipolar and Tetra-polar Impedance Measurement (TPIM) techniques was investigated with numerical vector analysis by Brown et al considering a semi-infinite homogeneous volume conductor (Brown et al., 2000a). For bipolar measurement, there were no negative sensitive region and the mean sensitivity over a plane parallel to the electrode plane was shown to fall rapidly with depth. For TPIM, the mean sensitivity over a plane was maximum at a depth equal to approximately one third of the spacing between two current injecting electrodes as shown in Figure 2-15. The mean sensitivity over a plane at depth zero, i.e. in the electrode plane, was maximum for bipolar case but zero for the TPIM case because the sum of the positive and negative sensitivities in that plane sum to zero. The spatial sensitivity for different FIM

configuration was investigated using numerical vector analysis by Islam et al (Islam et al., 2010) and compared with the TPIM. It was shown that FIM can localize a region of interest beneath the electrode configuration minimizing contribution from neighbouring regions. The above analysis was done for point electrodes and semi-infinite homogeneous volume conductor using Geselowitz's theorem (Geselowitz, 1971). But the human body is a finite volume conductor consists of tissues which are nonlinear, inhomogeneous and arranged in a complex geometry. Therefore, these predictions should be verified either by a finite element method (FEM) analysis using the specific application geometry or by measurement on phantoms approximating the application geometry and tissues as indicated by (Islam et al., 2010). (Pettersen et al., 2014) showed that Comsol Multiphysics is a very useful FEM tool to investigate sensitivity distributions and also compared sensitivity distributions of FIM electrode configurations.
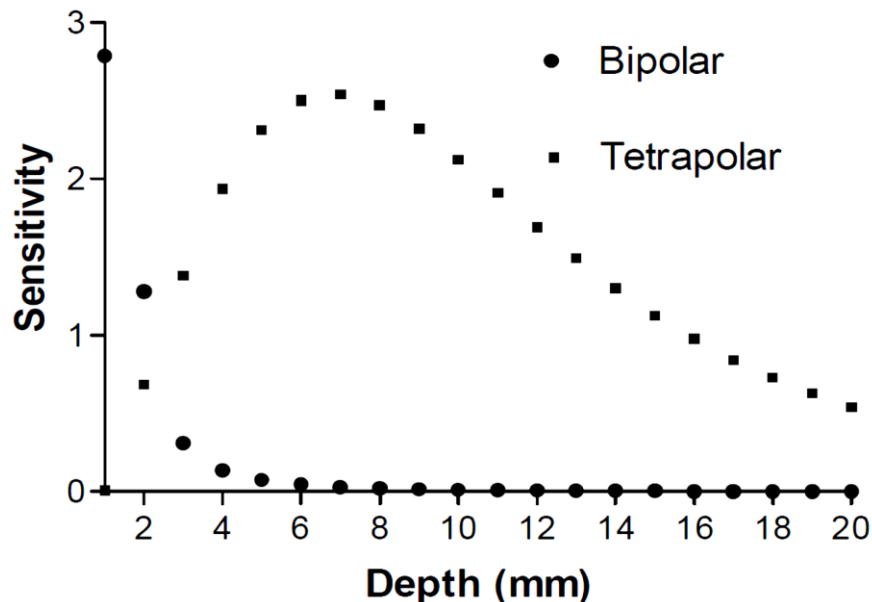
Figure 2-15 Mean sensitivity over a plane as a function of depth for both tetra-polar and bipolar placement of electrodes. The sensitivities are x10^{-3} and the tetrapolar sensitivities x10^{-6} of the scale shown on the left. Source: (Brown et al., 2000a)

2.3 Instrumentation for multi-frequency bioimpedance measurements

In multi-frequency measurements, bioimpedance is measured at multiple frequencies of the excitation signal. The excitation signal, typically sinusoidal, is generated from a waveform generator. The output of the waveform generator is then converted to a constant current signal to drive the current electrodes. A voltage measurement circuit is used to measure the potential dropped across the pair of potential electrodes and its phase with respect to the input current signal.

2.3.1   Current drive circuit

The functional purpose of a current drive circuit is to generate an electric current signal with a specific magnitude. In multi-frequency measurements, the frequency of the current is varied. Analog oscillators, such as Wien-bridge oscillators are used to generate sinusoidal waveforms (Franco, 2001, Horowitz et al., 1989). However, analog oscillators
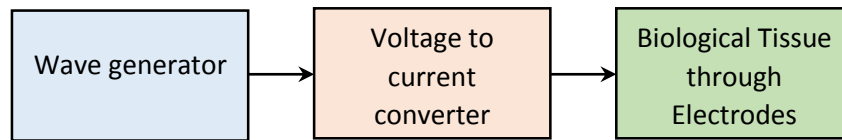
Figure 2-16 Block diagram of the current drive circuitry for bioimpedance measurements.

need hardware changes to change the signal frequency and are not suitable for high frequency signals i.e. in the MHz range. Triangular or square waves generated from integrated ICs or microcontrollers can be converted into sine wave by using filters. Direct Digital Synthesis (DDS) techniques are also in use for the generation of sine waves (Ping et al., 2008, Zexi et al., 2009, JISONG, 2007).

Usually, the amplitude of the injected current is kept constant so that the transfer impedance is proportional to the measured voltage difference. Therefore the signal from the wave generator is passed through a voltage to current converter i.e. a constant current source as shown in Figure 2-16. For accurate measurements of multi-frequency bioimpedance, it is necessary to assure that the injecting current has a
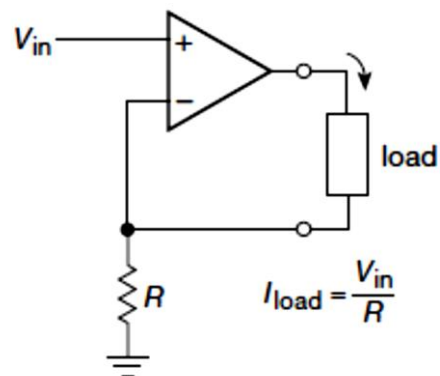
Figure 2-17 Operational amplifier based floating load voltage to current converter, source: (Horowitz et al., 1989)p-228.

constant amplitude over a wide range of load impedances, which may be obtained by using a current source with high output impedance (Annus et al., 2008). Operational amplifier based floating load Voltage to current converters are in use where the load is in the feedback loop as shown in Figure 2-17 (Horowitz et al., 1989, Smith, 1990). Negative feedback results in V_{in} at the inverting input, producing a current $I_{load} = \frac{V_{in}}{R}$ through the load. This current source works at lower frequencies, but its performance is degraded at higher frequencies.
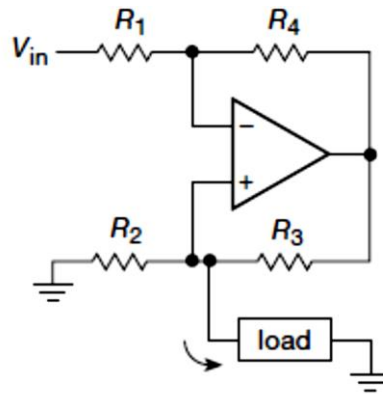
Figure 2-19 Circuit diagram of the basic Howland current pump, source: (Horowitz et al., 1989) p-230.

Howland current source (Figure 2-19) offers an improvement as a voltage controlled current source working over wide frequency ranges. In this case, the resistor ratios must be matched exactly; otherwise it does not work as a constant current source(Horowitz et al., 1989, Smith, 1990). Another weaknesses of the Basic Howland Current Pump is its output capability. Its output node does not normally swing very close to the rail. Some modified improved versions of the Howland current source have been reported by several authors (Ross et al., 2003, Tucker et al., 2013, Bera and Jampana, 2010). The output swing of the modified *Howland* circuit is close to the rail voltage allowing it higher output capability. Importantly, the output impedance of modified *Howland* source is higher (about 1.5 times) compared to that of basic *Howland* source in the frequency range 10kHz-500kHz (Chen et al., 2010).
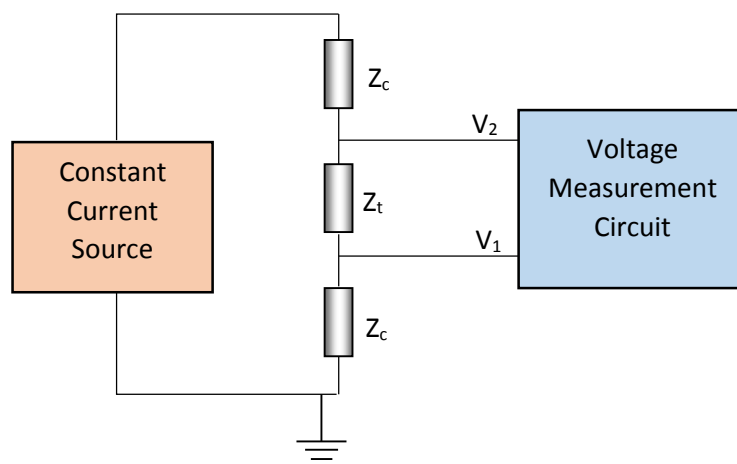
Figure 2-18 Illustration of the common mode errors because of the grounded load constant current sources.

Both the basic Howland and the modified Howland current sources contain grounded load. This creates a high common mode voltage to the input of the voltage measurement amplifier because of the presence of contact impedance (Hinton et al., 1998).

In Figure 2-18, Z_t is the transfer impedance of a biological tissue sample to be measured using four electrode system. Here Z_c on both side of Z_t are the electrode contact impedances and in practice, $Z_c >> Z_t$. Therefore the common voltage (arising from Z_c) on the input terminals V_1 and V_2 of the voltage measurement circuit is much higher compared to the voltage difference (arising from Z_t) to be measured. This may give common mode errors. In addition, the relatively high voltage on the input terminals of the *voltage measurement circuit* may cause some current which can pass through the sample impedance to leak to earth via the input cable capacitance, especially at high frequency signals. The use of a balanced current generator (Figure 2-20) can reduce errors due to common mode voltages and leakage through the 0V connection allowing more precise measurements of the sample impedance (Bertemes-Filho et al., 2012, Bertemes-Filho et al., 2013). Moreover, an idealised balanced current source produces a net zero dc common mode voltage and therefore minimises polarisation of the tissue.
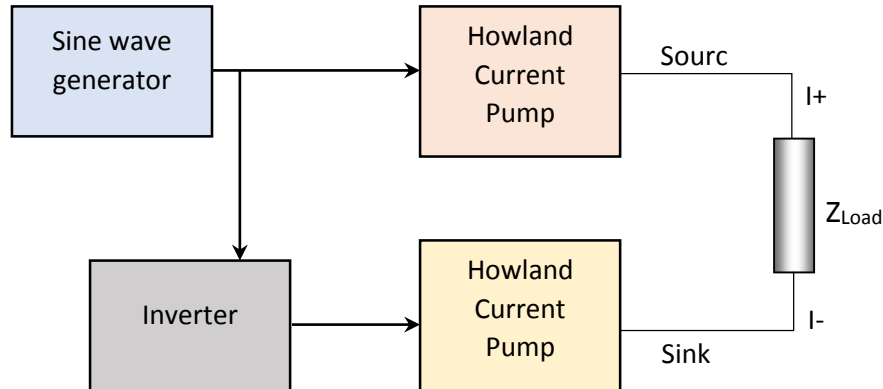
Figure 2-20 Bock diagram of a balanced current source.

2.3.2 Voltage measurement circuit

The voltage difference between the measurement electrodes is amplified minimizing noise and then the amplitude and phase of the voltage signal is measured. The amplifiers mostly used for measuring the voltage difference across tissue have differential inputs. A third input is used as the reference potential for the amplifier. The reference is usually the 0V connection of the amplifier and is connected to a third electrode placed on the target body. The mean of the voltage on the two differential inputs measured with respect to the reference electrode is called the common-mode voltage. It is very important that the differential amplifier rejects common-mode voltage. Simple differential amplifiers are not suitable for amplifying bio signals because there is a possibility of

Figure 2-21 Schematic of an instrumentation amplifier

mismatch of electrode contact impedance (Legatt, 1995). Mismatch in contact impedance reduces the Common Mode Rejection Ratio (CMRR) of the differential amplifiers (Pallás-Areny and Webster, 1991). Therefore, Instrumentation amplifiers with high CMRR are used for amplification of the voltage signal (Boone and Holder, 1996, Pallas-Areny and Webster, 1993a).

In analogue circuitry, peak detector and zero crossing detector circuits are used in frequency domain measurements for demodulating the amplitude and phase of the voltage signal (Schröder et al., 2004). Analog synchronous demodulation has been preferred in portable and wearable devices. Nowadays, digital signal processing (DSP) is used in multi-frequency bioimpedance measurements because of the advancement of microelectronics (Hamidi et al., 2010, Wilson et al., 2001, Pallas-Areny and Webster, 1993b, Min et al., 2007a). However, time domain measurements using broadband excitation signal can significantly reduce measurement time and suitable for applications where high frame rate is needed (Pliquet et al., 2000).

2.4   Application of Bioimpedance in lung ventilation study

2.4.1   Human Respiratory system

The respiratory system provides oxygen to the body's cells while removing carbon dioxide. There are 3 major parts of the respiratory system: the airway, the lungs, and the muscles of respiration (diaphragm and intercostal) shown in Figure 2-22. The upper airway system comprises trachea and bronchi. The lower airway system consists of bronchioles, small airways and alveolar spaces within the lungs. The muscles of

Figure 2-22 Parts of human respiratory system, it should be noted that the intercostal muscles which have their point of insertion on the ribs, are not shown in this diagram. Source: (Siebens et al., 2017)

respiration, including the diaphragm and intercostal muscles, work together to act as a pump pulling air into and pushing air out of the lungs during breathing (Pernkopf, 1964).

2.4.2   Lung anatomy
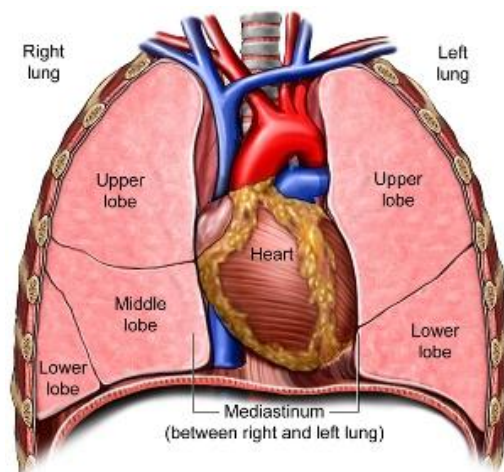
Figure 2-23 Human lungs in the thorax in the presence of heart, Source: http://images .lifescript.com/images/ebsco/images/BQ0004 2.jpg

Human beings have two lung organs, a right and a left, which are located in the chest cavity. Each lung is enclosed within a thin membranous sac called the pleura, and each is connected with the trachea by its main bronchus and with the heart by the pulmonary arteries. Most of the intrathoracic space is occupied by the lungs. The space between two lungs is occupied by airways, heart, major blood vessels, esophagus, and the thymus gland. The right lung contains three lobes: a superior, middle, and inferior lobe, separated

from each other by a horizontal and an oblique fissure as shown in Figure 2-23. The left lung contains only two lobes separated by an oblique fissure. The left lung is slightly smaller in volume than the right lung because of the asymmetrical position of the heart.

The right lung represents approximately 56 percent of the total lung volume (Siebens et al., 2017). In the thorax, the two lungs rest with their bases on the diaphragm, while their apexes extend above the first rib (Rogers, 2011).

2.4.3 Respiratory physiology

The lungs act as the functional units of the respiratory system by passing oxygen into the body and carbon dioxide out of the body. Gas exchange of oxygen and carbon dioxide takes place in the alveoli (Figure 2-24). Oxygen from the inhaled air diffuses through the walls of the alveoli and adjacent capillaries into the red blood cells. The oxygen is then carried by the blood to the body tissues. Carbon dioxide produced by the body's metabolism returns to the lung via the pulmonary circulation. It then diffuses across the capillary and alveolar walls into the air to be removed from the body with expiration.
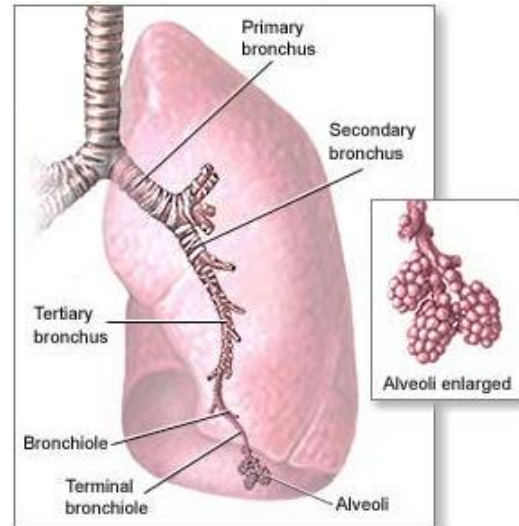
Figure 2-24 Pulmonary alveoli are the terminal ends of the respiratory tree where gas exchange occurs. Source: https://www.verywell.com/what-are-alveoli-2249043

2.4.4 Lung ventilation

In respiratory physiology, ventilation is the exchange of air between the lungs and the environment. Lung ventilation is done by expansion and compression of lung by following two steps (Hall, 2015) as illustrated in Figure 2-25:

a) By movement of the diaphragm downward and upward to lengthen or shorten the chest cavity,

b) By elevation and depression of the ribs to increase and decrease the anteroposterior diameter of the chest cavity.

The amount of air that enters or leaves the lung during normal breathing at resting is defined as the tidal volume (~8ml/Kg body weight). Again, the volume of air that enters or leaves the lungs between enforced maximum inspiration and maximum expiration is defined as vital capacity.
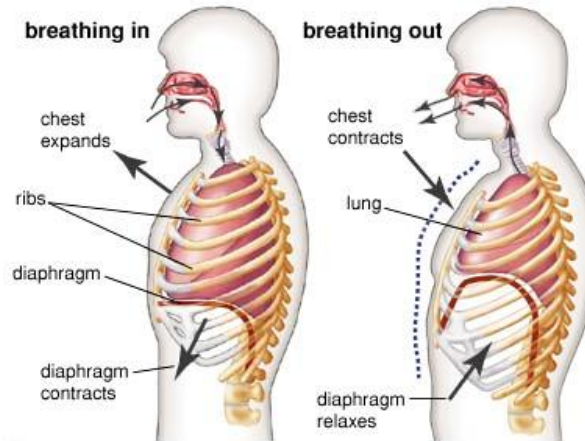
Figure 2-25 Graphical representation of the mechanism of respiration, Source: http://simplebiologyy.blogspot.com/ 2015/01/mechanism-and-events-occurring-during-breathing.html

According to (Johansen et al., 1993) the vital capacities of left and right lung are different; 2.17 L and 2.41 L respectively. If for any reason (eg. lung disorder), if air cannot reach a particular region of lung tissue then that region of lung is said to be *not ventilated*.

2.4.5 Lung disorders: Fluid accumulation in lungs

Lung ventilation is essential for proper gas exchange (Haldane and Priestley, 1905). In diseases like pulmonary edema, abscess, TB or pneumonia, localized regions within the lungs are filled with fluids or masses restricting the air to flow into the alveoli resulting poor ventilation (Puligandla and Laberge, 2008). Fluid accumulation in the air spaces of lung tissue is known as pulmonary edema as shown in Figure 2-26 (Staub, 1974). The most common cause of pulmonary edema is congestive heart failure. When the heart is not able to pump efficiently, blood can back up into the veins that take blood through the lungs. As the pressure in these blood vessels increases, fluid is pushed into the air spaces and alveolar membranes in the lungs. The fluid in the alveolar space prevents the passage of inhaled gas to the alveolar surface; the fluid in the alveolar membrane prevents the passage of oxygen from the inhaled gas to the blood and CO2 from the blood to the alveolar gas compartment through the lungs. Pneumonia is the inflammation in the lung tissue. It can be caused by a bacterial or viral infection (Tumer et al., 1987, Virkki et al., 2002). In pneumonia, the alveoli within the lungs become inflamed and fill up with fluids. Lung abscess is a type of liquefactive necrosis of the lung tissue and formation of cavities

(more than 2 cm) containing necrotic debris or fluid caused by microbial infection (Kuhajda et al., 2015).

2.4.6 Existing techniques for the diagnosis of fluids in lungs

Traditional physical examinations such as respiration rate, heart rate, body temperature, chest sound etc. may be useful in the diagnosis of pneumonia. But the physical examination is not sufficiently accurate on its own to confirm or exclude the diagnosis of pneumonia (Wipf et al., 1999). Chest X-rays/CT imaging are helpful to diagnose pneumonia and determine the extent and location of the infection. However, it cannot provide the information about what kind of germ is causing the pneumonia. Blood tests and plural fluid culture examinations are used to confirm an infection and to identify the type of organism causing the infection. Presence of abnormal fluid in lungs can prevent lungs from exchanging enough oxygen into the bloodstream resulting in a low oxygen saturation in the blood. Therefore pulse oximetry may indicate the presence of abnormal fluid/mass in lungs. The chest radiograph is the widely used method of assessing and quantifying lung edema (Milne et al., 1985).
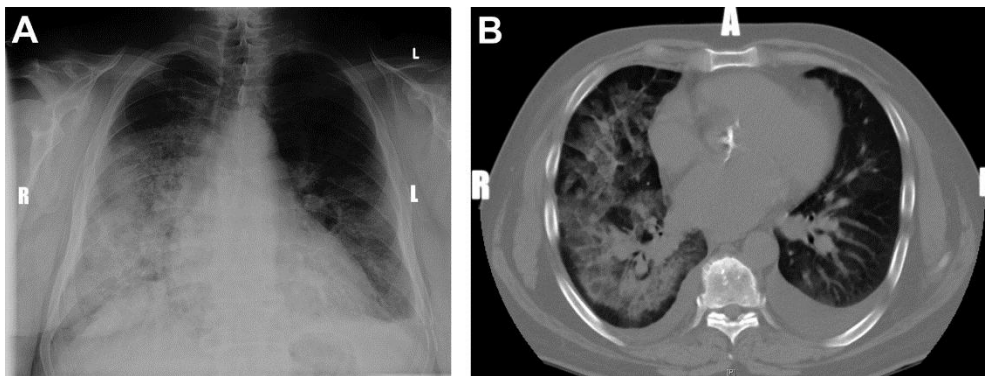
Figure 2-26 Chest X-ray (A) and CT image (B) demonstrate right sided pulmonary edema.
Source: (Warraich et al., 2011)

2.4.7 Electrical properties of lung tissue

The dielectric property of biological tissue is a basic biophysical parameter. Gabriel et al. studied the dielectric properties i.e. conductivity and relative permittivity of animal and human tissues at multiple frequencies (Gabriel et al., 1996a, Gabriel et al., 1996b). They established the corresponding parametric models for the dielectric spectrum of tissues (Gabriel et al., 1996c). The models were used to estimate the dielectric properties of 55 kinds of human tissues in the range of 10 Hz to 100 GHz by the Italian Institute for Applied Physics (Andreuccetti D, 1997). According to their results, inflated and deflated lung tissues have different dielectric properties. For example, at 10 kHz, the conductivity and relative permittivity of deflated lung tissue is 0.2429 S/m and 34044 respectively whereas for inflated lung tissue it is 0.093172 S/m and 17174 respectively. This indicates that the dielectric properties of lung tissue changes as a function air content as observed by (Nopp et al., 1993). (Wang et al., 2014) measured the dielectric properties of human lung tissue (both normal and cancerous) in vitro at multiple frequencies as shown in Figure 2-27. According to the measurement of Wang et al the conductivity of normal human lung tissue at 10 kHz is around 0.2 S/m which corresponds to the results obtained by Gabriel et al.
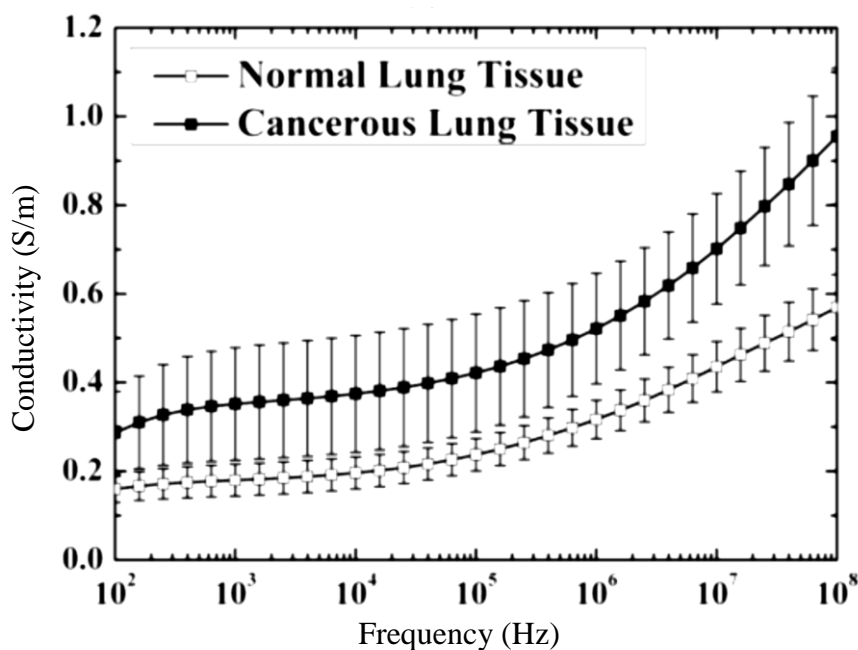
Figure 2-27 Electrical conductivity of normal and cancerous human lung tissue measured in vitro. Impedance spectroscopy of the specimen were completed within 30 minutes after the   issue removal from body. Source: (Wang et al., 2014)

2.4.8 Potential of multi-frequency FIM in the study of fluid/mass in lungs

Accumulation of fluid in the air spaces of the lung changes the dielectric properties of lung tissue. Researchers applied bioimpedance techniques to investigate fluid accumulation in lungs. In earlier studies, transthoracic impedance measurements were measured for the diagnosis of pulmonary edema but with limited success (Fein et al., 1979a, Pomerantz et al., 1969). Mayer et al. used 3D finite element model to study the feasibility of using focused impedance spectroscopy for monitoring lung edema (Mayer et al., 2005) but this needed to be evaluated experimentally on human subjects. Schlebusch et al. developed a textile integrated bioimpedance early warning system for lung edema (Schlebusch et al., 2010). This system has been evaluated using several Bioimpedance Spectroscopy (BIS) dummies and showed promising results but these have not been verified in clinical study in practice. Electrical Impedance Tomography (EIT) was also used for the estimation of liquid volumes in the lung in dogs where liquid volumes measured using EIT were accurate to within 10 ml (Adler et al., 1997, Newell et al., 1996). Campbell et al reported some preliminary results that EIT can be used in human subjects in the clinical environment to detect small changes in intra-thoracic fluid (Campbell et al., 1994). Kimura et al. showed that electrical impedance analysis can be used in the diagnosis of pulmonary masses i.e. cancerous tissue, organizing pneumonia (Kimura et al., 1994). However, in this study the impedance measurements were invasive using needle electrodes. Peacock et al suggested that bioimpedance measurement may detect pulmonary fluid not apparent on routine chest radiography (Peacock et al., 2000).

Preliminary work done by the author of this thesis demonstrated success of FIM in the study of lung ventilation by measuring the impedance changes during breathing (Kadir et al., 2009, Kadir et al., 2015). In these studies, normal healthy subjects took a deep breath and then expired a little air at a time in steps and held the breath for a
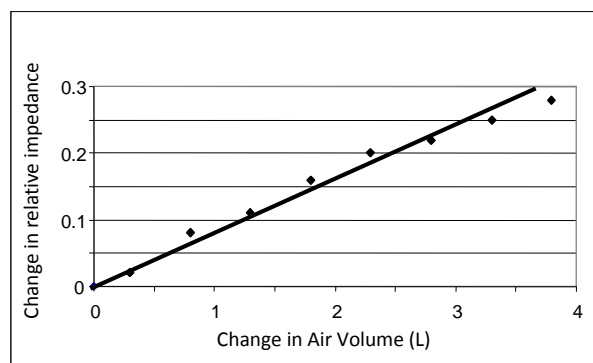
Figure 2-28 Lung ventilation study using FIM showing linear relationship to change in air volume.

short while each time. During the breath holding period FIM data from the lower frontal right lobe of the lungs was taken. The volume of air expired was also measured simultaneously using a standard bellows type spirometer. Figure 2-28 shows a typical data

from one of the subjects which shows very good correlation between the relative FIM values and the volume of air expired. This shows the potential of FIM for measuring lung ventilation in localized regions, and from any direction, to identify zones with ventilation disorders. Moving the FIM electrodes over the thorax using a portable spring loaded electrode holder is being carried out to map the regional ventilation of the lungs (Kadir et al., 2010, Ferdous et al., 2013). Therefore, there is a great potential of using multi-frequency FIM in the study of fluid accumulation in lungs.

2.5   Application of bioimpedance in breast tumour classification

2.5.1   Breast tumour: benign and malignant

The female breast is made up from glandular and connective tissues surrounded by adipose tissue (Birkenfeld and Kase, 1994). Each breast contains 15-20 glands called lobes. Ducts are surrounded with dense connective tissue that support the glands. A tumor is a mass of abnormal tissue. There are two types of breast tumors: *benign (non-cancerous)* and *malignant (cancerous)*. Breast cancer is the result of an accumulation of a large number of individual genetic mutations that collectively alter elements of the complex internal signaling system of a cell. These abnormal genetic alterations, when assembled in a single breast cell, disrupt the control system to the extent that the cell functions autonomously in an erratic and irregular manner (Wren, 2007). Most breast tumours begin in the ducts, some start in the glands. Breast cancer is the second leading cause of cancer death in women (Stewart and Wild, 2014). Reductions in mortality have been observed where screening has been introduced (Shapiro et al., 1998). The benign tumour cells grow locally and do not spread, invade or metastasise. But malignant tumour cells can invade neighbouring tissues, enter blood cells and metastasize to the other tissues (Baba and Catoi, 2007). The growth rate of benign cells are slow whereas the growth rate is rapid in malignant cells. The boundary of the benign tumour is regular but that for a malignant tumour is irregular (Kim et al., 2002). Blood flow is also very different in malignant and benign conditions, being much higher in malignancy (Sohn et al., 1992).

2.5.2   Diagnosis of breast cancer

Mammography is a type of breast imaging that uses low-energy x-rays to detect cancer in the early stage (Logan, 1983, Zuley, 2010). The x-ray images make it possible to detect tumors that cannot be felt. The principal mammographic signs of breast carcinoma are

densities and calcifications (Sickles, 1984). Mammography is a screening tool to detect small, non-palpable, asymptomatic breast tumours. However, it results in a significant number of false positives; positive predictive value (true positive out of all detected as positives) was reported to be as low as 35.8% (Kolb et al., 2002). Besides, x-ray techniques expose the subject to ionizing radiation which has its own associated hazards including induction of cancer. Moreover, it cannot be used on pregnant women.

Magnetic Resonance Imaging (MRI) can be used along with mammograms for screening women who have a high risk of developing breast cancer, or it can be used to better examine suspicious areas found by a mammogram (Morrow et al., 2011). Compared with mammography, MRI has a higher sensitivity for the detection of breast cancer and is not affected by breast density (Sardanelli et al., 2004). But breast MRI is expensive and requires highly specialized equipment and highly trained experts. Relatively few breast MRI centers exist, especially outside of major cities.

Ultrasound examination of the breast is an important adjunct to mammography and clinical examination in the further assessment of both palpable and impalpable breast lumps (Gordon, 2002), especially in women younger than 30 years of age. However, the use of ultrasound in population screening in asymptomatic women is associated with high rates of both false positive and false negative outcomes (Teh and Wilson, 1998).

Ultrasound elastography is a new technique that maps the elastic properties of soft tissues. The basis of elastography imaging depends on the deformation of the target lesion compared to the background tissue (Sarvazyan et al., 2011, Goddi et al., 2012). Cancerous tumours are often harder than the surrounding and therefore elastography can characterize breast lesions (Itoh et al., 2006). The predictive values (accuracy, sensitivity, specificity etc) for elastography is higher than mammography in differentiating benign and malignant lesions in the breast (Zhi et al., 2007). However, classification outcome depends on the skills of the operator (Ophir et al., 1999).

The only way to know for sure whether a breast tumour is cancerous or non-cancerous is biopsy. In biopsy samples of tissue from the suspicious area is taken invasively and the tissue is examined under microscope. This can be done surgically by making an incision in the skin and removing a part of the suspicious area. However, nowadays, nonsurgical needle biopsy (i) Fine Needle Aspiration Cytology (FNAC) (Wu and Burstein, 2004) or (ii) Core Needle Biopsy (CNB) (Florentine et al., 1997) are commonly used for breast

tumour examination (Moschetta et al., 2014). Core biopsy gives a better result but needs a considerable amount of tissue to be taken out at several locations under local anesthesia. A biopsy is not hazard-free. In a few per cent of cases where the tumour is cancerous, tissue adhering to the tip of the needle sometimes introduces cancer at the upper cutaneous layers (Chao et al., 2001).

2.5.3 Bioimpedance in the study of breast tumour

It was reported from in-vivo measurements on human subjects that the electrical resistance of intra and extra-cellular fluids and cell membrane capacitance of cancerous tissue and that of healthy tissue is different (Morimoto et al., 1990, Ohmine et al., 2000). Moreover, significant differences in impedivity between cancerous and normal breast tissue have been reported by in vitro measurements on freshly excised breast tissue by (Jossinet, 1998, Jossinet, 1996, Jossinet and Schmitt, 1999, da Silva et al., 2000). Significant difference between electrical conductivity and permittivity values of normal and abnormal tissue based on multi-frequency EIT measurements on breast has also been reported by (Hartov et al., 2005, Soni et al., 2004). This implies that the dielectric properties (conductivity and relative permittivity) of cancerous tissue is different from healthy tissue; and this is the basis of using bioimpedance techniques in the study of breast tumour. Trans-spectral impedance (*T-scan)* is a non-tomographic imaging device used as an adjunct tool to mammography in the detection of breast cancer and was reported to improve sensitivity and specificity (Assenheimer et al., 2001, Kerner et al., 2002). Using electrical impedance tomography (EIT), some attempts have been made at detection of breast cancer (Cherepenin et al., 2001, Kerner et al., 2002, Halter et al., 2015). However, these works have showed that EIT requires complex measurement instrumentation and accurate electrode placement. FIM requires much simpler instrumentation, allows electrode placement based on palpation and having the feature of better spatial localization, there is a potential of multi-frequency FIM in determining whether palpable breast tumours are benign or malignant.

Chapter 3 Design and Development of a Multi-frequency FIM system

3.1   Introduction

This chapter describes the design and development of a multi-frequency FIM system (MFFIM) suitable for use in resource constraint settings. Considering the socio-economic status of developing countries like Bangladesh, a low cost and reliable system was required that can be maintained and repaired in the field by the researchers in order to investigate the potential applications of the FIM technique. However, the limited local availability of even quite basic electronic components is a challenge. Therefore, in the present work, a system based on widely available electronic components is described. This chapter describes the instrumentation of a multi-frequency FIM system capable of measuring bioimpedance using suitable electrode configurations and excitation frequencies of choice under software control from microcontroller and PC. As discussed in Chapter 2, these measurements are essentially based on four-electrode or Tetrapolar Impedance Measurements (TPIM). There are two major parts in a TPIM device: current drive circuitry and voltage measurement circuitry. A microcontroller based current generator capable of driving excitation signal to biological tissue constructed using readily available low cost IC chips is explained in this chapter. In bioimpedance measurements, impedance value appears as a modulation of the signal frequency that needs to be demodulated. Two different demodulation approaches based on *analogue synchronous peak detection* and *digital demodulation* are explained and their performances are analyzed in the present work. For multi-frequency measurements, similar measurements are to be carried out at chosen frequencies, which could be in a switched mode. The design aspects of the instrumentation of the MFFIM system are presented in the next section.

3.2   Design Requirements

3.2.1   Excitation Frequency

Biological tissues contain ions and therefore application of dc current to human body can cause electrolysis and if the current is large, may cause tissue burn (Leeming et al., 1970). Besides, the dc contact potentials created at the electrode-tissue interface makes measurement of the bulk impedance difficult. Therefore, dc is not normally used for bioimpedance measurements. The current threshold required to stimulate nerves is a

minimum at low frequencies (0.1Hz-500Hz) and rises linearly with log frequency up to about 10 kHz. Beyond this the current required to stimulate neural tissue rises rapidly (Brown, 1981). Therefore, this range of frequency (0.1Hz-500Hz) is also avoided. Stray capacitance becomes a substantial problem at frequencies beyond 1MHz contributing to error in measurements. Instrumentation with excitation current in the GHz frequency range is very difficult because the effect of the stray capacitance becomes more significant (McEwan et al., 2007, Bolton et al., 1998), therefore such frequencies are also not used in typical bioimpedance measurements. Fortunately, the body tissues have significant dependence on the intermediate range of frequencies that provide the opportunity to devise reasonably simple instrumentation. Electrical properties of body tissues change significantly in the frequency range kHz to MHz. For example, the conductivity of inflated and deflated lung tissues increase by 46% and 38% respectively over the frequency range 10 kHz – 1 MHz (Gabriel et al., 1996b). The impedance values of normal and cancerous cervical tissues decrease by about 100% and 38% respectively over the frequency range 10 kHz – 1MHz (Brown et al., 2000b). The variation of impedance over a particular frequency range is different for normal and diseased tissue which allows tissue characterization using bioimpedance measurements. Therefore, the frequency range 10 kHz – 1 MHz was chosen for the excitation signal of the implemented multi-frequency FIM system in the present work. To measure the impedance response over the entire frequency range 10 kHz – 1 MHz, the system was designed for 8 octave related frequencies which are 10 kHz, 20 kHz, 40 kHz, 80 kHz, 160 kHz, 320 kHz, 640 kHz and 1024 kHz; a complete frame would consist of measurements at all these frequencies. However, the highest measurement frequency implemented (1024 kHz) is not an octave multiple of its previous frequency; it was a practical maximum that could be achieved using available IC chips. The octave progression of measurement frequency was chosen to get equi-distant points in the frequency range in a logarithmic scale. More importantly, considering the time required for data acquisition by the ADC of the microcontroller used (discussed in section 3.4.1.7), these 8 measurement frequencies were chosen to achieve high enough frame rate in order to allow dynamic lung and cardiac studies.

3.2.2   Requirements for current source

The MFFIM system aims to inject sinusoidal signals of constant current amplitude into the body through an electrode pair so that the measured voltage across another electrode pair is proportional to the transfer impedance of the volume conductor under investigation. However, the output impedance of the constant current source should be much higher compared to the electrode-tissue contact impedance at all measurement frequencies so that the amplitude of the signal remains constant with changing load impedance. The load impedance to be driven by the constant current source in the frequency range 10 kHz – 1 MHz was estimated experimentally using two stainless steel electrodes of diameter 1cm. The electrodes were placed on the human chest using
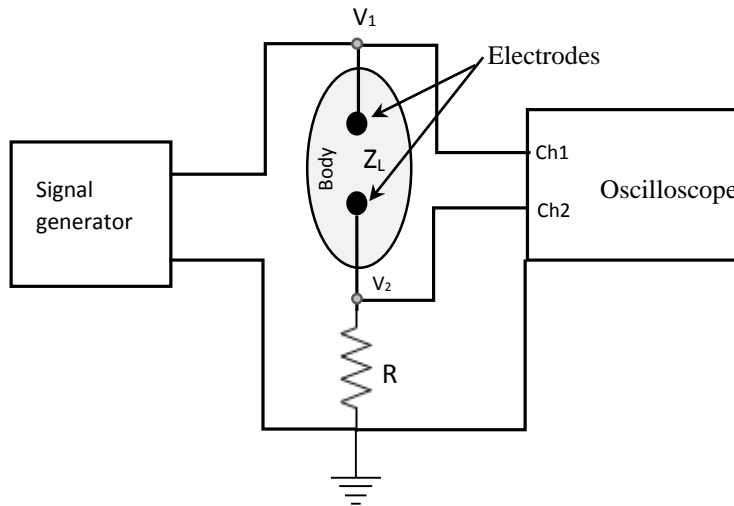
Figure 3-1 Circuit diagram used to measure the load impedance
(total electrode-tissue contact impedance) given by $Z_L = \frac{R(V_1 - V_2)}{V_2}$.

electrolytic jelly in the electrode-tissue interface. This arrangement was chosen as it is likely to be the one that will be used for impedance measurements on human subject as part of this thesis. The electrodes were then connected to a known small resistor (R) and sinusoidal signals were applied from a signal generator as shown in Figure 3-1. The value of the resistance R was chosen so that the voltage V_2 across R is approximately one-half of the voltage V_1 at 10 kHz. The value of R chosen on this basis was 1kΩ.

The load impedance (Z_L) at a particular frequency was then calculated using the equation below.

$$Z_L = \frac{R(V_1 - V_2)}{V_2} \qquad (3\text{-}1)$$

The variation of load impedance with frequency, as obtained, is shown in Figure 3-2. The load impedance decreased with increased frequency. At 10 kHz and 1 MHz the load impedance values are around 2 kΩ and 500 Ω respectively which are similar to the data reported by (McEwan et al., 2007). (Brown et al., 1994) reported that for Ag/AgCl electrodes load impedance is <500Ω even at 9.6 kHz.

The output impedance of the constant current source was specified to be at least 100 times greater than the maximum load impedance i.e. $Z_C > 200k\Omega$ at 10 kHz and $Z_C > 50k\Omega$ at 1MHz.
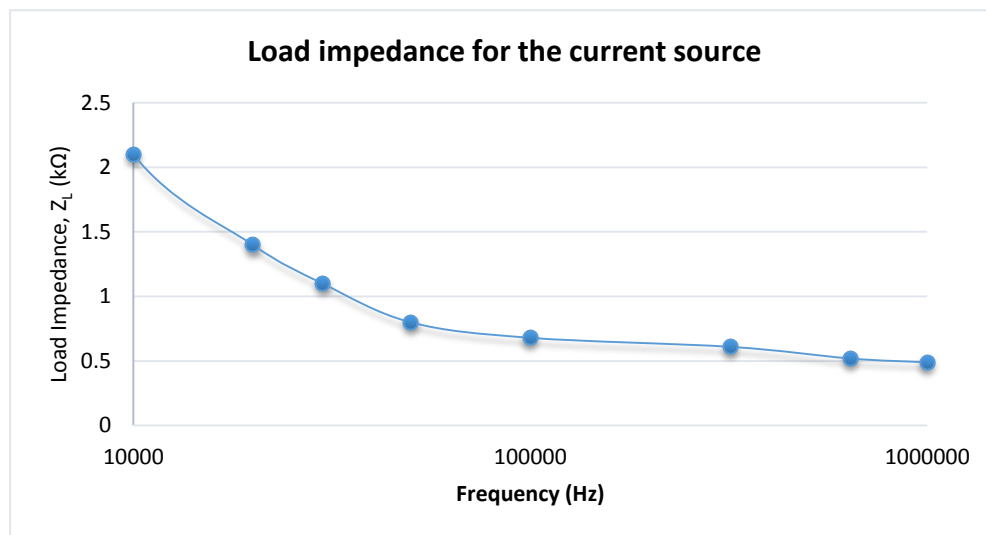
Figure 3-2 Load impedance to be driven by the current source at different frequencies.

International Electrotechnical Commission (IEC) defined the safe auxiliary current limit for medical equipment to be 100μA(rms)/kHz (IEC, 2004). According to the *American National Standard*, safe auxiliary current limits for electromedical apparatus is 5mA at 10 kHz; higher currents (maximum limit 10mA) are safe at higher frequencies (AAMI, 1985). At higher frequencies, tissue heating (Joule heating) is the limiting factor. Tissue heating depends on different factors, such as: current density, time of exposure, blood flow in the tissue etc. For surface electrodes current densities of less than 1mA/mm^2 are unlikely to cause damage (Brown, 1981). Therefore the maximum current of the MFFIM was specified to be 1mA (p-p).

3.2.3 Transfer impedance range

As mentioned before, the ratio of the measured voltage across a receive electrode pair to the current injected through another pair of electrode is called transfer impedance. Because of this, the measured voltage in TPIM are much lower compared to that in bipolar or 3-electrode measurements (Grimnes and Martinsen, 2006). However, the measured voltage depends not only on electrical properties of the tissue sample under investigation, but also on the excitation current amplitude and the electrode configuration. Based on measurements from 12 normal human subjects, (Brown et al., 1994) reported that typical transfer impedance values of the human thorax are (24.56±4.09)Ω and (15.70±2.80)Ω at frequencies of 9.6 kHz and 614.4 kHz respectively. On the other hand, the transfer impedance in the breast tissue varies from 10Ω to 60Ω in the frequency range 5 kHz to 200 kHz (Al Amin et al., 2014). Therefore the transfer impedance range was specified as 5Ω -100Ω in the present work for the multi-frequency FIM system implemented, keeping a large margin for accuracy.

3.2.4 Sampling requirements

Electrical properties of some tissues/organs like lung, heart etc. change with time with different periodicities. Therefore, investigation of slow changes of the lung by impedance measurements placing electrodes on chest surface may be affected by cardiac movement having a faster periodicity. A complete set of multi-frequency measurement i.e. one frame (measurements at all 8 frequencies with FIM switching) should be performed fast enough to allow dynamic lung or cardiac studies. Typical range of respiration rate is 12-18 bpm and that of cardiac rate is 60-72 bpm which may increase in diseased condition. Therefore the frame rate should be much higher than 150 fpm (frame per minute) or 2.5 fps (frame per second) i.e., much greater than 2 times cardiac period if one wants to study both respiratory and cardiac related changes. Considering the worst scenario, the frame rate was specified to be greater than 10 fps in the present work.

3.2.5 Specifications

The design requirements for the multi-frequency FIM system, which are based on the published variation of tissue impedance with frequency as discussed above are summarized in Table 3-1.

Table 3-1 Specification of the multi-frequency FIM system

Feature	*Specification*
Excitation frequency	10 kHz - 1024 MHz
Drive current	1 mA (p-p)
Current drive output impedance	>50KΩ at 1MHz >200KΩ at 10kHz
Transfer impedance range	5Ω - 100Ω
Frame rate	>10 fps

3.3   Current drive circuit design

3.3.1   Signal generation

For multi-frequency bioimpedance applications, the current drive circuitry needs to set the excitation signal at different frequencies. In the current drive circuitry of the designed MFFIM system, a microcontroller was used to generate the excitation signal which was chosen to be sinusoidal. A microcontroller (ATmega8) as shown in Figure 3-3 was used to generate sinusoidal waves through programming.

Digital (8bit) amplitude values of samples from a full cycle of a sine wave were calculated and corresponding binary values were stored in the programme memory of the microcontroller. The 360 degrees of a complete sinusoidal wave was divided into *n* equal intervals and then corresponding amplitude values were calculated using the following formula:

$$interval, \Delta\theta = \frac{360°}{n} \qquad\qquad \text{------------ (3-2)}$$

where n is the no of intervals.

$$sample\ points, \theta_n = 0, \Delta\theta, 2 \times \Delta\theta, 3 \times \Delta\theta, \ldots \ldots \ldots, (n-1) \times \Delta\theta \quad \text{-----(3-3)}$$

$$amplitude\ values, Sn = 128 + 127sin(\theta n) \qquad\qquad \text{------------(3-4)}$$

These 8 bit amplitude values (binary) were then cyclically clocked through 8 I/O ports of the microcontroller to a digital to analogue converter (DAC0808) where the clocking rate determines the frequency of the output signal.
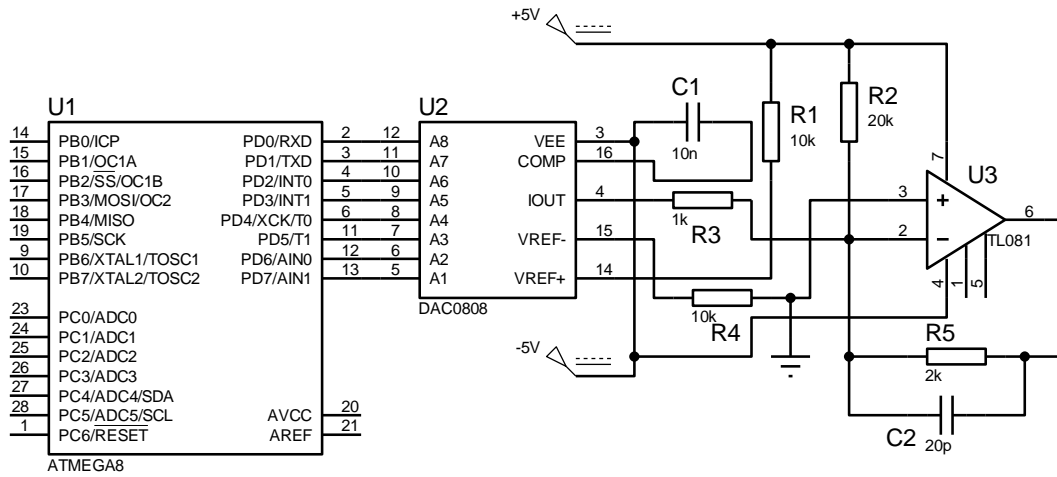
Figure 3-3 Circuit diagram for the microcontroller based sinusoidal signal generator with current to voltage converter.

The number of sample points is limited by the maximum clocking rate of the microcontroller used (Atmega8) which is 16MHz. Therefore 25 sample values per cycle with intervals of $14.4°$ as listed in Table 3-2, can be used for generation of a sinusoidal signals of maximum 640 kHz.

Clocking these values from the microcontroller (μC) to the DAC at 16 MHz resulted in a sinusoidal signal of 640 kHz. Signals of other lower frequencies were generated by slowing down the clocking frequency. However, a lower number of sample points per cycle (i.e. 15 samples per cycle) as shown in Table 3-3 was used for generation of signal of 1MHz.

A schematic of the signal generation circuitry is shown in Figure 3-3. The output of the DAC0808 is a current signal given by the equation below:

$$I_{out} = I_{ref}\left(\frac{B_7}{2} + \frac{B_6}{4} + \frac{B_5}{8} + \frac{B_4}{16} + \frac{B_3}{32} + \frac{B_2}{64} + \frac{B_1}{128} + \frac{B_0}{256}\right) \quad \text{-------- } 3\text{-}5$$

where B_7 and B_0 are MSB and LSB of a sample value respectively and I_{ref} is the reference current produced at pin 14 of the DAC through the resistor R_1.

Table 3-2 Sample values used to generate sinusoidal signals of (10-640) kHz with varying clocking frequency

Sample points, θ_n (degree)	Amplitude value (Sn) (rounded)	Binary value (B)
0	128	10000000
14.4	160	10011111
28.8	189	10111101
43.2	215	11010110
57.6	235	11101011
72	249	11111000
86.4	255	11111110
100.8	253	11111100
115.2	243	11110010
129.6	226	11100001
144	203	11001010
158.4	175	10101110
172.8	144	10001111
187.2	112	01110000
201.6	81	01010001
216	53	00110101
230.4	30	00011110
244.8	13	00001101
259.2	3	00000011
273.6	1	00000001
288	7	00000111
302.4	21	00010100
316.8	41	00101001
331.2	67	01000010
345.6	96	01100000

Table 3-3 Sample values used to generate sinusoidal signals of 1 MHz with 16 MHz clocking frequency

Sample points, θ_n (degree)	Amplitude value (Sn) (rounded)	Binary value (B)
0	128	10000000
24	180	10110011
48	222	11011110
72	249	11111000
96	254	11111110
120	238	11101101
144	203	11001010
168	154	10011010
192	102	01100101
216	53	00110101
240	18	00010010
264	2	00000001
288	7	00000111
312	34	00100001
336	76	01001100

The resistor R1 was chosen to be 10kΩ so that the maximum reference current is 0.5mA for a supply voltage of 5V. The current signal was then converted to a voltage signal using a voltage to current converter as shown in Figure 3-3. The value of the feedback resistor *R5* was chosen as 2kΩ so that the maximum output voltage is 1V (p-p). The output of the DAC is unidirectional. Resistor *R2* was used to provide an offset of 0.5V so that the signal output voltage signal is bidirectional. The clocking rate of the digital values from the μC to the DAC was then changed to generate signal of frequencies 10 kHz, 20 kHz, 40 kHz, 80 kHz, 160 kHz, 320 kHz, 640 kHz and 1 MHz.

3.3.2 Constant current source

As mentioned before, a current source with high output impedance is needed for bioimpedance measurements so that the amplitude of the applied current remains constant with changing load impedance over a wide frequency range. Howland current pump as discussed in section 2.3.1 is widely used for application of constant currents. But limited output voltage swing capability is one of the weaknesses of the basic Howland Current

Pump (HCP). The voltage swing at the output node of HCP is less than half of the op amp output voltage swing. Therefore HCP can drive only a small load impedance beyond which its opamp output saturates. Therefore conventional HCP is not suitable for bioimpedance measurements which needs to drive a higher output impedance with a constant ac current. Moreover, its output is less accurate, with more offset and noise.

Therefore a *bipolar modified Howland current source* reported by *Bertemes Filho, 2002* was used in the implemented MFFIM as shown in Figure 3-4 (Bertemes Filho, 2002). It is
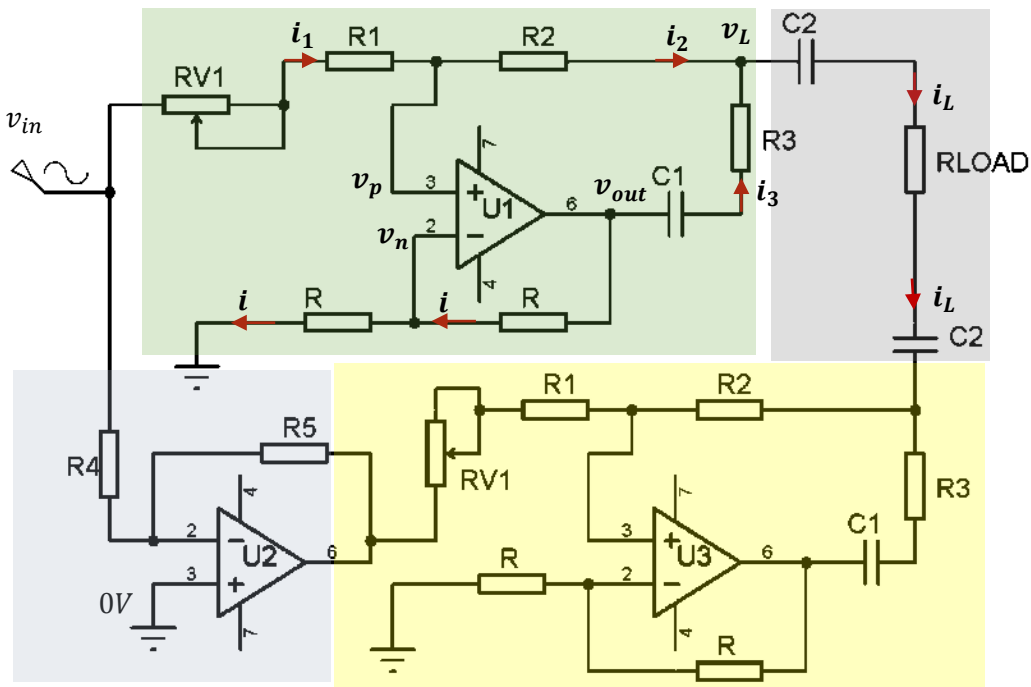
Figure 3-4 Circuit diagram of the implemented bipolar modified Howland current source with DC coupling capacitors.

a combination of two identical *modified Howland current pumps*. The input of the 2nd *modified HCP* is inverted so that the current sourced from the 1st *modified HCP* is totally sinked at the 2nd *IHCP*. A unity gain inverting amplifier was used to feed the 2nd *modified HCP* ($R_4 = R_5 = 10$ kΩ).

The output current through the load resistor R_{Load} is given by

or, $i_L = \dfrac{v_{in}}{z_C}$ -------- (3-6)

where v_{in} is the input voltage to the current source and $z_C = \sqrt{R_3{}^2 + X_{C1}{}^2}$. Here $X_{C1} = \dfrac{1}{2\pi f C_1}$ is the reactance of the capacitor C_1 and f is the frequency of the current signal.

This means the current through the load resistor is independent of the value of load resistance and depends only on Z_C. However, for better output impedance of the current source the ratio of resistors must be equal i.e. $\frac{R_2+Z_C}{R_1+RV_1} = \frac{R}{R}$. Choosing appropriate electronic components (resistors, capacitors and opamps) are very important for an accurate current source. Therefore, resistors of tolerance 1% (minimum tolerance available locally) were used in the implemented circuit. Moreover, multi-turn variable resistors RV1's were used to trim the resistor ratios. The output current accuracy depends on the magnitude of resistors $R, R_1 \ and \ R_2$. Larger values of these resistors improves the current accuracy. It was shown that to achieve 0.5% current accuracy, $R, R_1 \ and \ R_2$ should be at least 40 kΩ (Guo, 2013). Therefore, the values of resistors and capacitors chosen for the implemented IHCP circuit were $R = R_1 = R_2 = 100 \ k\Omega, RV_1 = 2k\Omega$ (multi-turn variable), $R_3 = 1 \ k\Omega$ and $C_1 = C_2 = 470 \ nF$. At the lower end of measurement frequency (10 kHz) the value of Z_C is 1000.573Ω; and at the higher end of measurement frequency (1MHz) the value of Z_C is around 1000Ω. Therefore the effect of the capacitors on the output current amplitude is negligible in the measurement frequency range. For an input signal of $v_{in} = 1V$ (p-p), the load current is be approximately equal to 1 mA. For accurate current output in the frequency range 10 kHz -1 MHZ, fast and low power op amps with high Common Mode Rejection Ratio (CMRR) and high gain bandwidth (GBW) were required. For this purpose, a high speed opamps AD8055 with *CMRR*, *GBW* and *slew rate* of 82dB, 300 MHz and 1400 $V/\mu S$ respectively was chosen for the implemented circuitry.

Capacitors C_1 and C_2 were used to minimize op amp offset voltages and to prevent any dc signal to flow into the human body which may cause harm. The capacitive reactance (X_c) decreases with increased frequency, thereby decreasing the value of Z_c which in turn results in a slight higher current. Therefore capacitor C1 was also intended to compensate the loss of current amplitude due to stray capacitance with increasing signal frequency.

3.4   Voltage Measurement circuit design

In bioimpedance measurements, a sinusoidal signal of constant amplitude is applied to a volume conductor through a pair of drive electrodes and the transferred voltage to another pair of receive electrodes is measured. The Changes in impedance within the volume conductor amplitude modulate the measured voltage and the transfer impedance is calculated from the peak value of the measured voltage as shown in Figure 3-5. The ratio
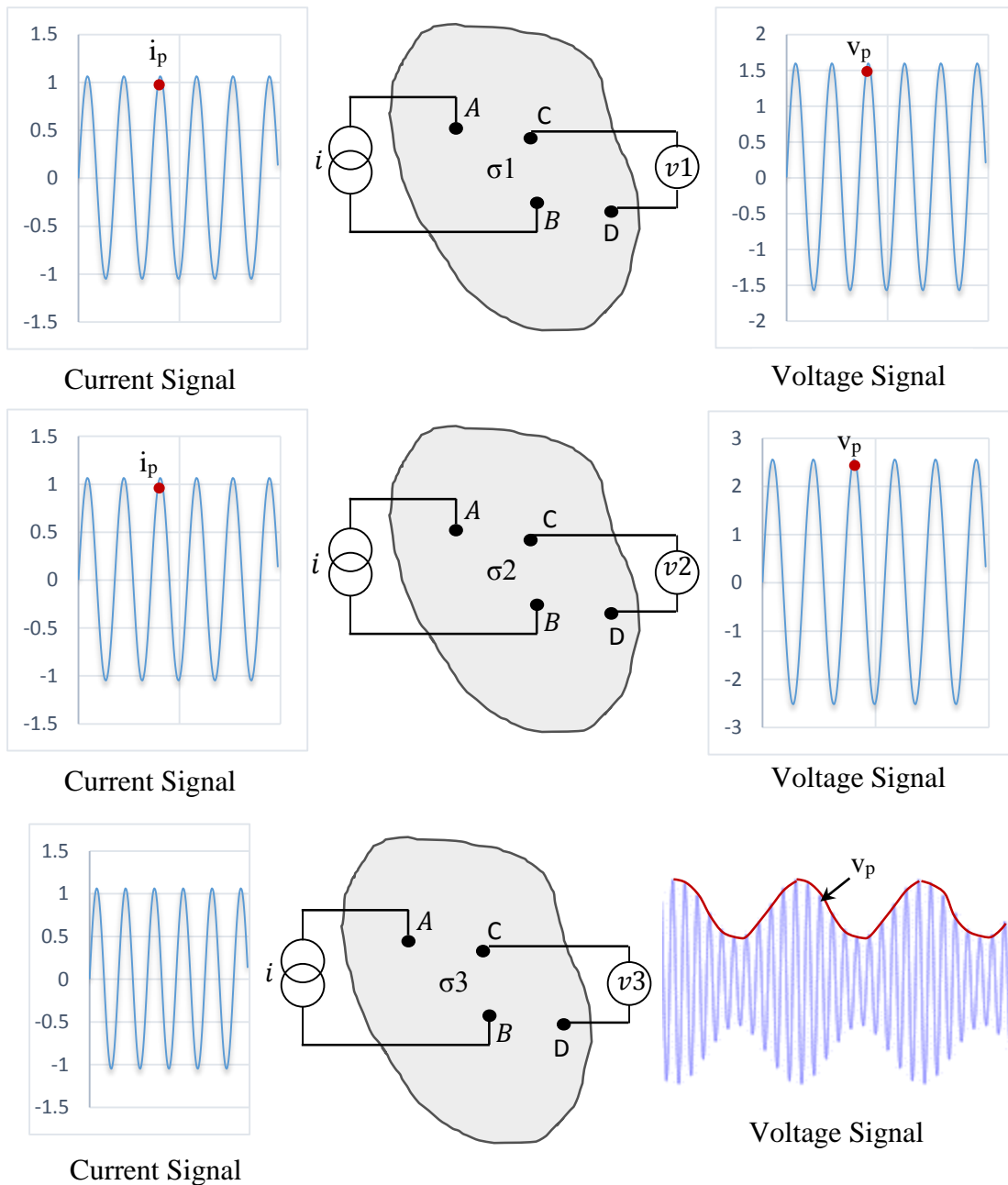
Figure 3-5 Amplitude modulation of the impedance value on the applied signal. Here conductivity of the volume conductor σ1> σ2 and therefore amplitude of the voltage signal v2>v1. In the lower figure, the conductivity of the volume conductor, σ3 is changing periodically with time and hence the amplitude of the voltage signal v_p is also changing with time; the red curve represents the impedance variations.

of peak voltage to the peak current at a particular signal frequency gives the magnitude of the transfer impedance. If the conductivity of the volume conductor decreases ($\sigma_1 > \sigma_2$), the amplitude of the voltage signal increases ($v_2 > v_1$); although the signal frequency remains constant as illustrated in Figure 3-5. Similarly, for time varying conductivity of the volume conductor, the amplitude of the voltage signal varies accordingly while signal frequency remains constant. Therefore, the transfer impedance value is amplitude modulated within the voltage signal which needs to be demodulated. Two different approaches based on analogue synchronous demodulation and digital demodulation were taken in the current work which are described below.

3.4.1 Analogue Synchronous peak detection

3.4.1.1 Block diagram

Figure 3-6 shows the block diagram of the multi-frequency FIM system where two microcontrollers were used. Microcontroller-1, together with a DAC circuit giving a current output and a current to voltage converter, was used to generate the sinusoidal voltages at the desired frequencies as described in section 3.3.1; the signal was then converted to a constant current source using a balanced Howland current circuit. The constant current signal was then applied to biological tissue through multiplexers (FIM
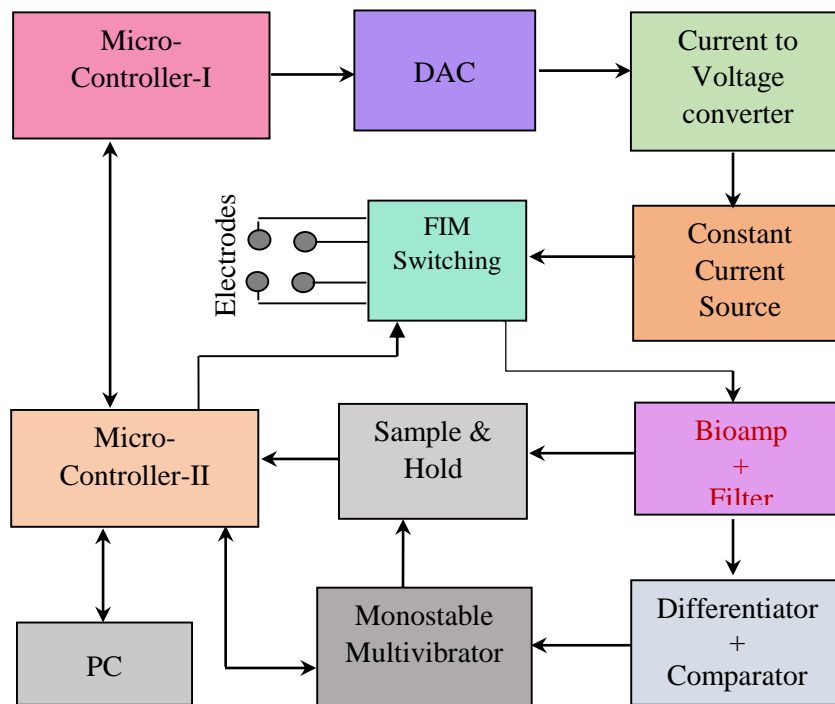
Figure 3-6 Block diagram of the multi-frequency FIM system based on analogue synchronous demodulation.

switches). The received voltage signal is then amplified using a bioelectric amplifier and passed through filters to reduce noise and unwanted signal components.
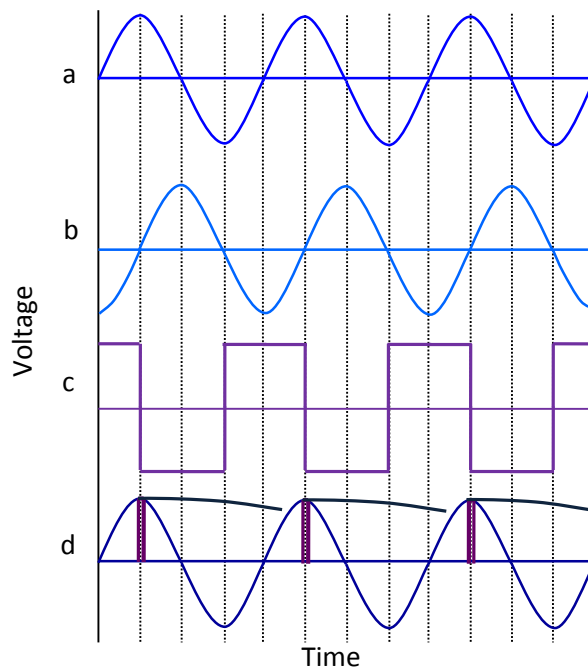
Figure 3-7 Peak detection method used in the voltage measurement circuit, (a) Output signal of the Bioelectric amplifier, (b) Output of the Differentiator circuit, (c) Output of voltage comparator, (d) Sampling pulse generated at the peak of the bioamp signal that activates a S&H circuit to hold the peak voltage.

The next requirement was to determine the peak voltage of the output sinusoidal signal for which the rest of the circuit blocks in Figure 3-6 was used. The scheme of this peak detection method at a particular frequency by the analogue synchronous demodulation method is explained with the help of Figure 3-7. The signal from the bioelectric amplifier is first differentiated by passing it through an analogue differentiator (block shown in Figure 3-6), so there is a phase difference of 90 degree between the bioelectric amplifier output (Figure 3-7a) and the differentiator output (Figure 3-7b). The differentiated signal is then passed through a voltage comparator (Figure 3-6) to produce a square wave (Figure 3-7c) where the falling edges correspond to the positive peak values of the input signal (bioamp output). The falling edges of the square wave were used as triggers for a monostable multivibrator (block shown in Figure 3-6) to generate pulses of 70nS. The choice of this 70ns duration was rather arbitrary. One requirement was that it should be long enough so that the sampling capacitor in the S&H circuit can be fully charged to the peak value (described later in section 3.4.1.5). The other requirement is that it should come back to the resting state (0V) before the next signal peak arrives, which for the

48

highest signal frequency of about 1MHz is due about 1000ns later. What is needed is that the rising edge of the pulse originating from monostable multivibrator should correspond to the peak of the bioamp signal which has been obtained in this arrangement. These pulses in turn trigger a *Sample & Hold* (S&H) circuit (Figure 3-6) to take samples of bioamp output signal (Figure 3-7d) at the peak and to hold them for a certain period so that the peak voltage values can be read by subsequent analogue to digital converter (ADC) circuit of Microcontroller-II. The rising edges of the monostable pulses also trigger the external interrupt of Microcontroller-II (Figure 3-6) to start the analogue to digital conversion.

3.4.1.2 Bioelectric amplifier with filters

The voltage signal developed across the sensing electrode pair needs to be amplified minimizing interference and noise. The main source of common mode noise is due to the 50 Hz mains power supply interference. Because of electrical capacitance between human body and nearby mains supply and also with the earth, 50Hz interference can be up to 1000 times larger than the voltages produced by the injected current (Brown, 1981)p-267. Common mode noise due to 50Hz mains can be minimized using high-pass filters since the lowest measurement frequency (10 kHz) is much higher than the noise
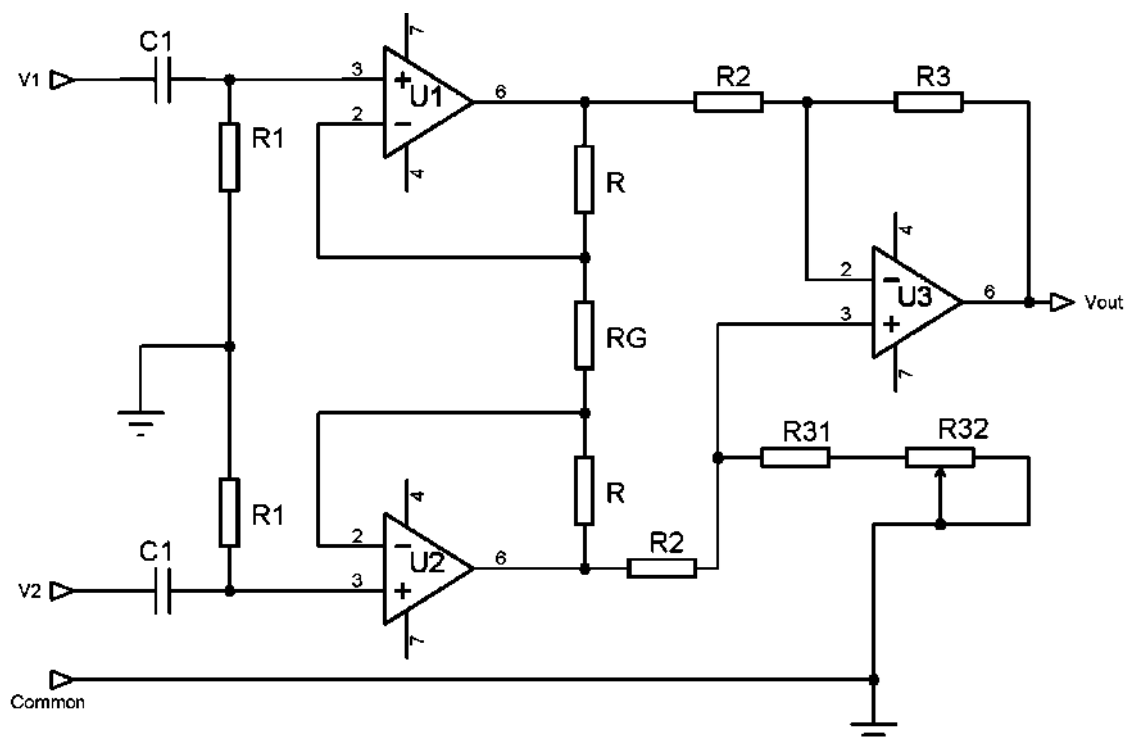
Figure 3-8 Bioelectric amplifier with high pass filter for amplification of the voltage signal across recording electrodes minimizing noise.

frequency. The voltage difference across the receive electrodes at measurement frequency can be amplified using a differential amplifier of high CMRR. However, any mismatch in the electrode-tissue contact impedance due to movement artefact or due to changes in electrode geometry may drastically decrease the CMRR of a differential amplifier. Therefore, a standard three-op-amp bioelectric amplifier (Pallas-Areny and Webster, 1993a) having two input buffer amplifiers (U1, U2) were used in the implemented in the MFFIM system as shown in Figure 3-8.

The main purpose of the high pass filters at the inputs of the bioelectric amplifier is to block any dc (contact potential) originating from electrical activity and to minimize 50 Hz noise as well as to prevent any dc bias current of the opamps to flow into the body. In addition to the voltage signal due to the injected current to the body, the recording electrodes may pick signal originating from endogenic electric activities within the body such as ECG or EMG. The dominant frequency range of ECG and EMG signals are 0.01 Hz-100 Hz and 2 Hz-1 kHz respectively. The values of R1 and C1 in the highpass filter were chosen as 100 kΩ and 1 nF respectively so that the cutoff frequency of the highpass filter is 1592 Hz to minimize any noise due to ECG, EMG etc. The cutoff frequency was set to at least 5 times lower than the lowest frequency of the measurement signal so that the filters only block noise but not the signal.

For better CMRR, the resistors of tolerance 1% were chosen so that $\frac{R_3}{R_2} = \frac{R_{31}+R_{32}}{R2} = 1$ nominally (R_2=R_3=10kΩ, R_{31}=4.7kΩ and R_{32}=10kΩ). A multi-turn variable resistor R_{32} was used to trim the resistor ratios so that the common mode gain can be adjusted to a minimum. The gain of the differential amplifier section is unity and the values of resistors R and R_G were chosen to be 47 kΩ and 2kΩ respectively so that the gain in the buffer amplifier stage is around 48. The main challenge was getting opamps with sufficient bandwidth available locally. Since the highest frequency of signal to be amplified is 1MHz, fast amplifiers with high gain bandwidth (AD8055, unity gain bandwidth: 300 MHz, Slew rate:$1400V/\mu S$) were used in the implemented circuitry. The overall gain of the bioelectric amplifier was set to 48 so that the amplified signal voltage do not exceed the maximum opamp output swing (6.2V, p-p) with a power supply voltage of $\pm 5V$. If the transfer impedance to be measured is 100Ω (maximum as specified) with applied current 1mA(p-p), the voltage developed across the *receive* electrode pair equals 100mV. With a gain of 48, amplified signal voltage is 4.8V (p-p) which is well below the maximum output swing of AD 8055.

3.4.1.3 Differentiation of the voltage signal

We need to differentiate the output signal from the bioelectric amplifier to be able to measure the peak values of the signal. Ideal differentiator circuits enhances the high frequency noise in the signal and produces low level drift due to signal baseline changes. In practice, differentiator circuit as shown in Figure 3-9 is normally used for signal differentiation (Bakshi and Godse, 2008)p 5-58. Here R_i and C_f are called the compensating components. The resistance R_{comp} is used for bias compensation. If $f_a = \frac{1}{2\pi R_f C_i}$ is the highest frequency of the input signal to be differentiated, then for proper differentiation $f_b = \frac{1}{2\pi R_i C_i}$ needs to be at least 10 times higher than f_a. The output signal of the differentiator is a negative cosine wave if its input is a sine wave i.e there is a phase difference of 90° between the input and output signal. Therefore, the differentiator output crosses zero from negative to positive at the positive peak of the bioamp output signal. Similarly the differentiator output crosses zero from positive to negative at the negative peak of the bioamp output signal.
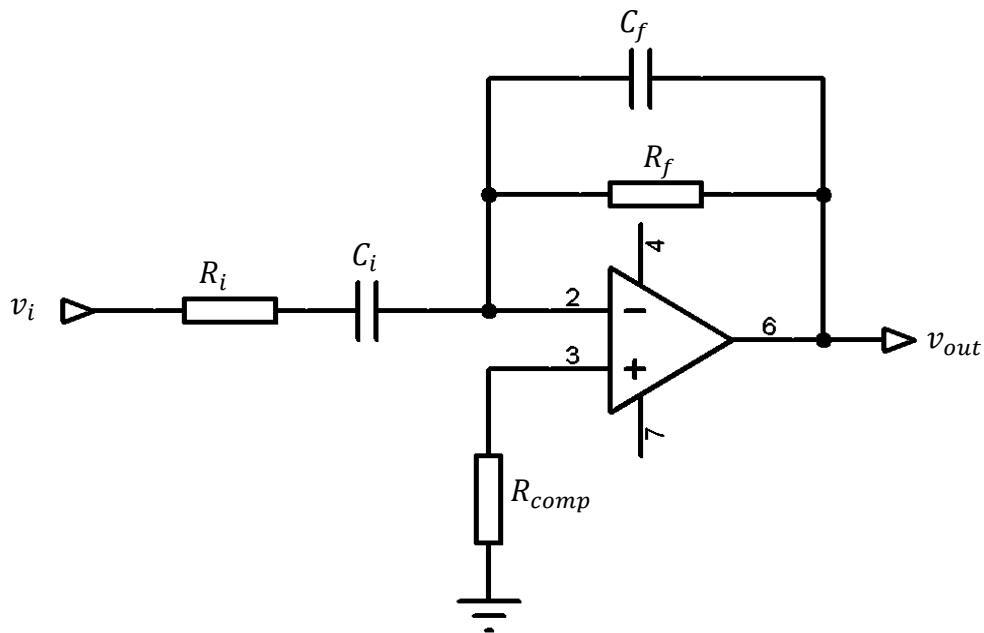
*Figure 3-9 Circuit used to differentiate the bioamp signal to give a **90°** phase shift.*

The output of the differentiator must be within the maximum output swing (±3.2V) of the opamp (OPA656) used in the circuit. Since the maximum specified output of the bioamp is ±2.5V, the maximum gain of the differentiator circuit can be 1.28. However, the output from the differentiator is proportional to the signal frequency. The signal frequency range

is 10kHz - 1MHz and therefore we have a 100:1 dynamic range. Again, the *transfer impedance* range specified is 5-100Ω, a 20:1 dynamic range. So the differentiator needs to work over a 2000:1 dynamic range (i.e. >60dB).

Table 3-4 Circuit parameters of four different differentiator circuits designed for various measurement frequencies.

Differentiator	R_i (Ω)	C_i (nF)	R_f (kΩ)	C_f (pF)	Measurement frequency (kHz)	Gain
I	100	1	10	10	10	0.628
					20	1.256
II	100	1	2.2	10	40	0.553
					80	1.104
III	20	1	0.56	10	160	0.563
					320	1.125
IV	20	1	0.20	10	640	0.802
					1024	1.276

This ignores the need to achieve this in the presence of low frequency and high frequency noise that will effectively increase the dynamic range still further. Hence a single circuit of the type shown in Figure 3-9 to cover the required frequency range was not practically achievable.
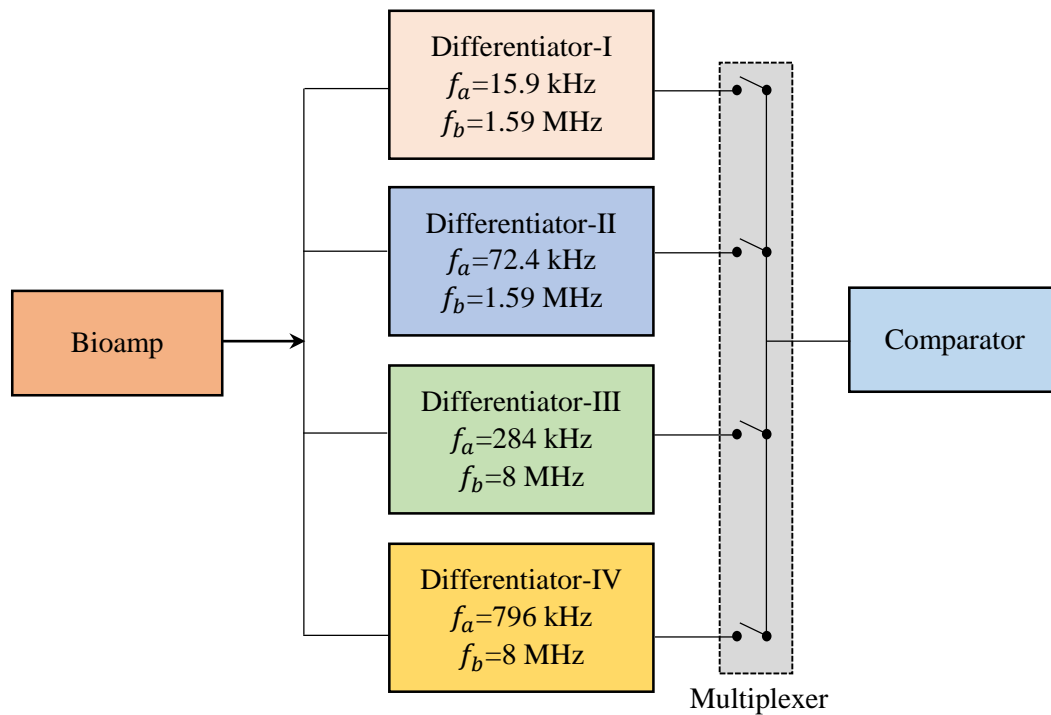
Figure 3-10 Four differentiators used for differentiating the signals of frequency range 10lHz-1MHz. Appropriate differentiator circuit for a particular input frequency was chosen by the multiplexer.

Therefore 4 circuits with the characteristics shown in Table 3-4 were used where the output was selected on the basis of the input frequency. The four differentiator circuits were switched according to the measurement frequency using a multiplexer as shown in Figure 3-10. An analogue multiplexer (74HC4052), controlled by microcontroller-II, was used to select appropriate differentiator for a particular signal frequency.

For proper differentiation the unity gain band width (*GBW*) of the opamps used in the circuits should be higher than the cutoff frequency (f_b). Therefore high speed opamps *OPA656* having GBW of 500MHz which is much higher than f_b was chosen for this circuits.

3.4.1.4 Zero crossing detection

A voltage comparator is designed to detect zero crossing of the differentiator output. An inverting comparator is implemented (Figure 3-11) so that the falling edge of the comparator output correspond to the positive peak of the bioamp signal as explained in Figure 3-7.

Superimposed noise in the signal, although small in amplitude, may switch a comparator output which is not desired. Therefore, in order to stop output transition because of the presence of noise a hysteresis is applied by feeding back a small fraction of the output voltage to the positive input (a Schmidt Triggere circuit). The reference voltage of the comparator designed is 0V and hence its hysteresis can be expressed as:

$V_{hysteresis} = \frac{R_1(V_{OH}-V_{OL})}{R_1+R_2}$ where, V_{OH} and V_{OL} are the maximum and minimum output voltages (saturation voltages of the op amp) respectively.
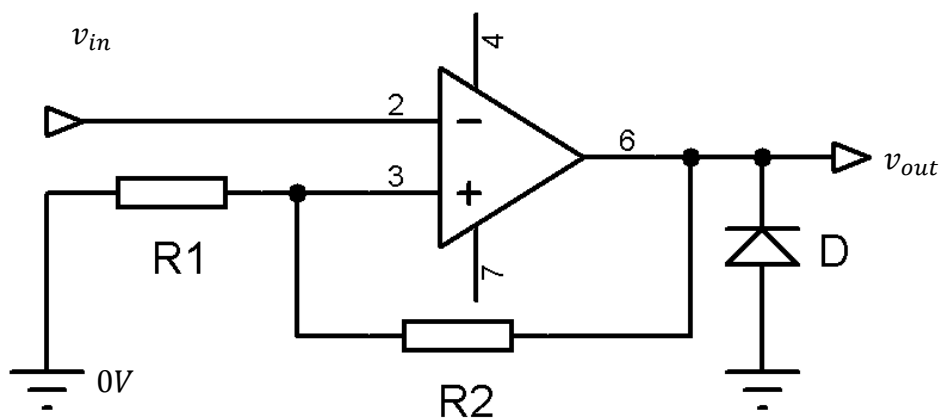
Figure 3-11 Voltage comparator circuit designed for zero crossing detection
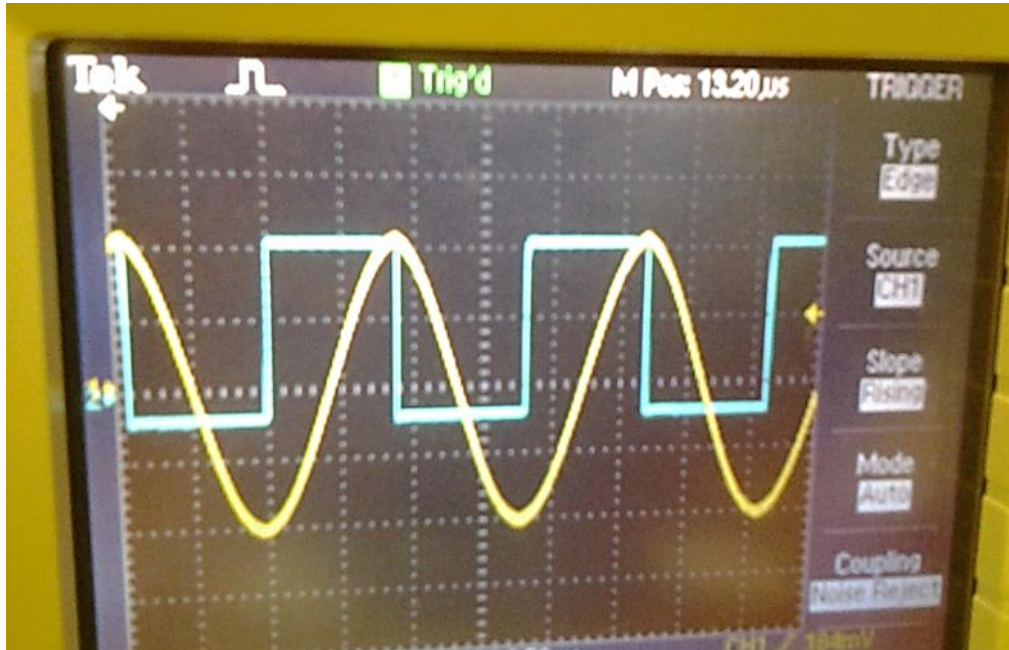
Figure 3-12 Bioamp output (yellow) and corresponding comparator output (green) as achieved in the implemented multi-frequency FIM system. This shows that the falling and rising edges of the comparator output correspond to the peaks of the voltage signal.

The values of resistors R_1 and R_2 were chosen as 5Ω and $10k\Omega$ respectively. For power supply voltages of $\pm 5V$, the thresholds of output transitions are $V_{th} = \pm 2.5mV$.

Figure 3-12 shows both the bioamp output signal and the corresponding comparator output signal of the implemented multi-frequency FIM system. The falling and rising edges of the square wave generated by the comparator correspond to the positive and negative peaks of the voltage signal respectively.
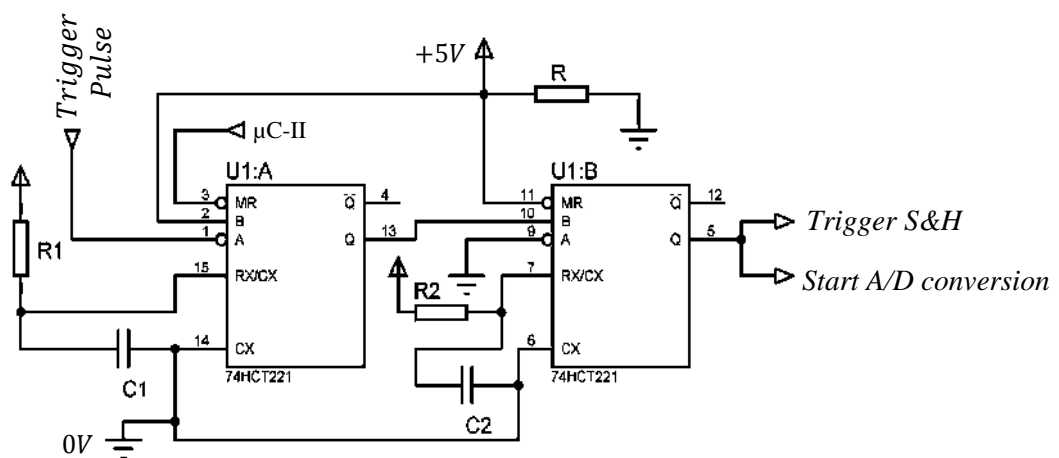
Figure 3-13 Schematic of the sampling pulse generator circuit.

3.4.1.5   Sampling pulse generation

From the falling edge of the generated square wave, pulses were generated to trigger a Sample & Hold Circuit (S&H) circuit in order to sample the peak value of the voltage signal. The output of the voltage comparator is a square wave where the falling edges correspond to the positive peak of the bioamp signal. So the falling edges of the square wave can be used to trigger a monostable multivibrator to generate sampling pulses. But multiple transitions at zero crossing detector because of the presence of superimposed noise may generate multiple sampling pulses. Therefore, sampling pulses were generated from a dual non-retriggerable monostable multivibrator *(CD74HCT221)* circuit as shown in Figure 3-13.
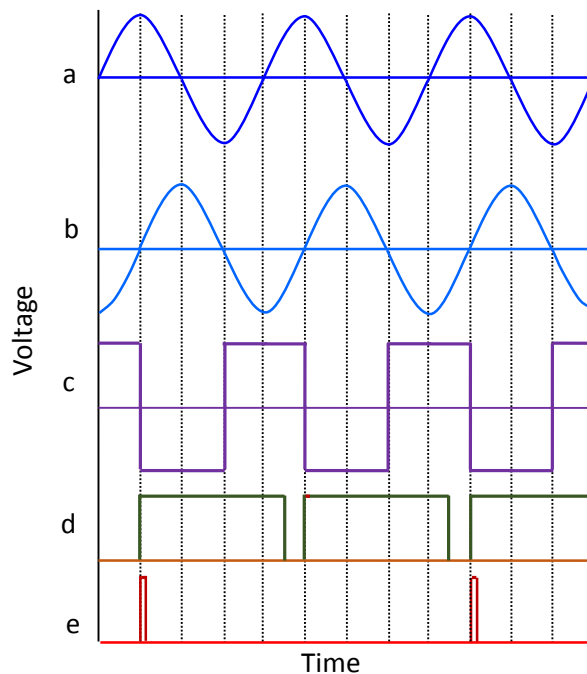
Figure 3-14 Sampling pulse generation (a) Output signal of the bioelectric amplifier, (b) Differentiated signal, (c) Square wave from the zero crossing detector, (d) Pulses from the first monostable multivibrator, (e) pulses from the second multivibrator with smaller duration (red) are sampling pulses.

The falling edges of the square wave (output of the zero crossing detector) triggers the first monostable and generates a pulse of relatively larger duration as shown in Figure 3-14(d). Since the monostable is non-retriggerable, it will not be retriggered until the pulse already generated is finished and again, there will be no change in the active pulse duration.

Table 3-5 Function table for the sampling pulse generator.

Inputs			Outputs	
A	B	MR	Q	$\bar{Q}$
X	X	L	L	H
↓	H	H	⊓	⊐⌐
L	↑	H	⊓	⊐⌐
H	X	H	L	H
X	L	H	L	H

H = High Voltage Level, L= Low Voltage Level, X = Irrelevant, ↑ = Transition from Low to High Level, ↓ = Transition from High to Low Level, ⊓ = One High Level Pulse, ⊐⌐ = One Low Level Pulse

The rising edges of the first monostable pulse is then used to trigger the 2nd monostable to generate a sampling pule of shorter width (Figure 3-14e). This is to prevent generation of multiple sampling pulses at the peak of the voltage signal if there is any multiple transition in the square wave originating from the zero crossing detector. The function table for the sampling pulse generator shown in Table 3-5.
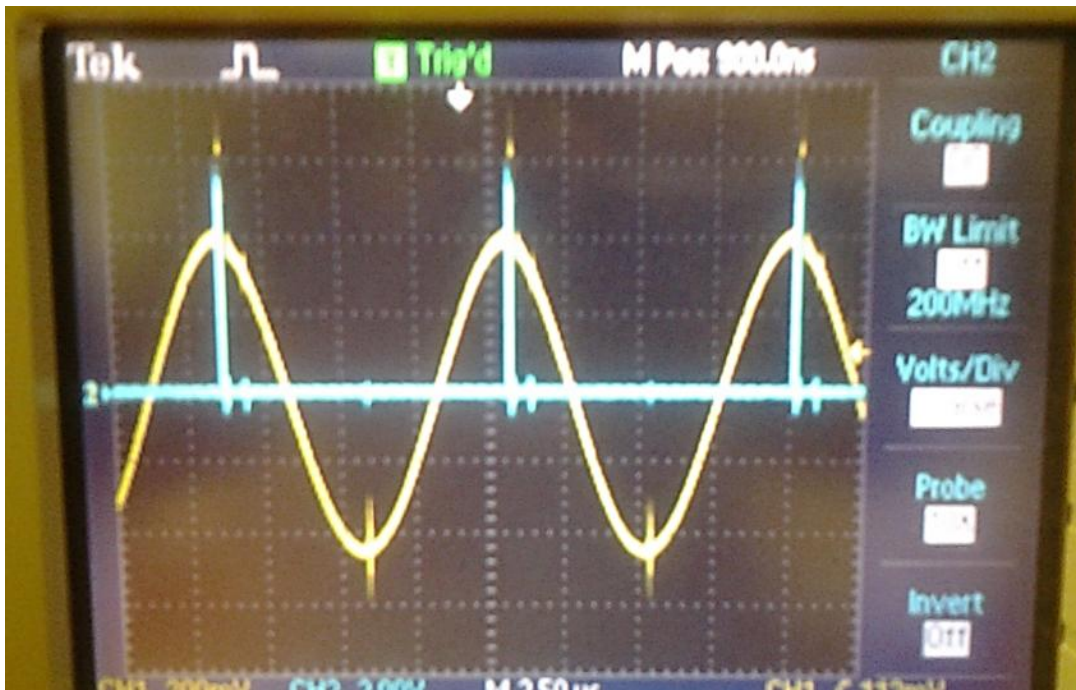
Figure 3-15 Sampling pulses generated at the positive peaks of the voltage signal as achieved in the implemented MFFIM system. This shows that sampling pulses corresponds to the positive peaks of the voltage signal.

The pulse width of the monostable multivibrator *(CD74HCT221)* is determined by the external resistor and capacitor, and can be given as:

$$Pulse\ Width = 0.7 \times R_x \times C_x$$

The time length between two successive peaks of the voltage signal at the highest measurement frequency (1MHz) is $1000\ nS$. So the pulse width of the first monostable was set to $700\ nS$ by choosing $R_1=1k\Omega$ and $C_1=1nF$. The sampling pulse needs to be short enough so that it enables the S&H circuit only to sample the peak value; but long enough to fully charge the sampling capacitor. The width of the sampling pulse was set to $70\ nS$ by choosing $R_1=1k\Omega$ and $C_1=100pF$. Figure 3-15 shows the sampling pulses generated at the positive peaks of the voltage signal as achieved in the implemented MFFIM system. The rising edge of the sampling pulse simultaneously activates the *S&H* circuit as well as initiate the *A/D module* of the microcontroller-II (Atmega8).

3.4.1.6   Sample and Hold circuit

The purpose of the sample and hold circuit is to sample the peak value of the voltage signal amplified by the bioelectric amplifier and then to hold it until the A/D module of the microcontroller-II stores the value. Figure 3-16 shows the schematic of the S& H circuit implemented in the MFFIM system.
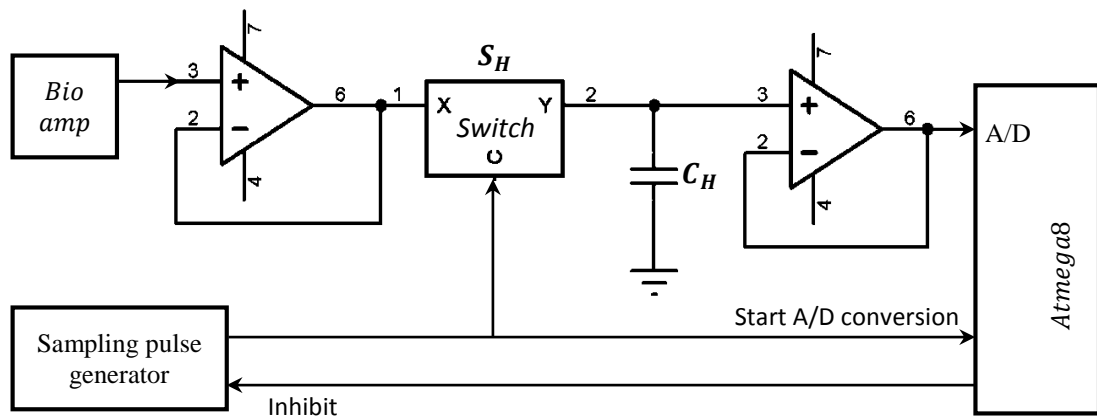
Figure 3-16 Schematic of the Sample and Hold circuit designed for measurement of the peak value of the voltage signal.

The sampling pulse turns the switch (S_H) ON for a short period and allows the capacitor, C_H to sample the peak value of the bioamp signal. The input buffer amplifier charges or discharges the capacitor so that the capacitor voltage is equal to the bioamp voltage as long as the switch is ON. In the hold state, the switch is OFF and the output buffer offers a high impedance to the capacitor so that it can hold the sampled voltage.

A fast CMOS multiplexer *CD4051* was used as the sampling switch. Time constant for charging the capacitor depends on the *ON resistance* (R_{ON}) of the switch and on the capacitance (C_H). The typical value of R_{ON} for *CD4051* is 80 Ω and the value of the hold capacitor was chosen to be $100\ pF$ so that the charging time constant is $8\ nS$. The time duration of the sampling pulse ($70\ nS$, as described in the previous section) is about 9 times longer than the charging time constant. Therefore the sampling pulse width is long enough to charge the capacitor at bioamp voltage level.

In the hold state, the switch is open; the capacitor C_H needs to hold the voltage value until the A/D conversion is complete. But in practice, the capacitor is discharged through the input resistance (R_{in}) of the buffer amplifier as well as due to capacitive leakage current. The input resistance of the opamp (AD8055) used in the buffer amplifier is $10M\Omega$. So the discharge time constant $(R_{in}C_H)$ is $1mS$. Typically, the A/D conversion of the microcontroller (Atmega8) needs $13.5uS$; and during this period the hold capacitor discharges only 1.34% of its initial value which is practically acceptable. Figure 3-17 shows the sampled value (pink line) that equals the peak value of the voltage signal as achieved in the implemented multi-frequency FIM system.
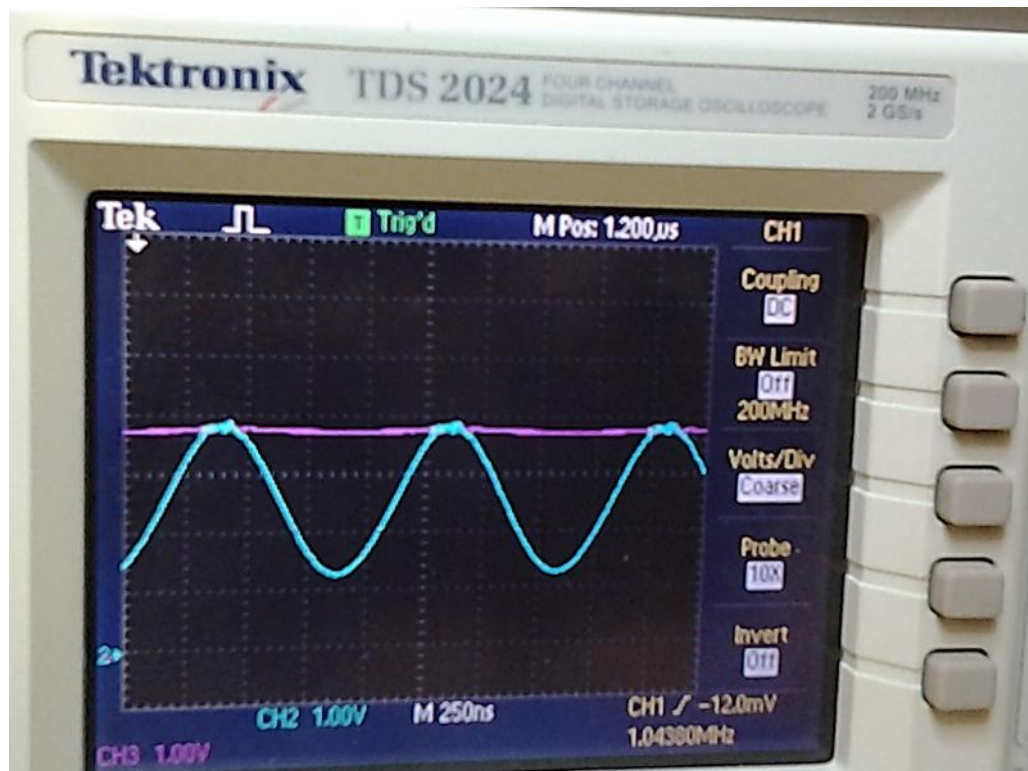
Figure 3-17 Sampled the hold the peak value (pink) of the voltage signal (green) as implemented in the multi-frequency FIM system.

3.4.1.7 A/D conversion

The rising edge of the sampling pulse of the S&H circuit was also used as interrupt pulse which initiates the A/D conversion of the microcontroller-II. There is a 2 clock pulse delay between triggering of the interrupt and initiation of the conversion process during which the ADC was initialized (Atmel). Therefore no extra delay is necessary between the sampling pulse of the S&H circuit and that to trigger the ADC circuit enabling the same pulse to trigger both. The ADC of the Atmega8 microcontroller requires 13.5μS for each conversion. For measurement frequencies greater than 80 KHz, time duration between two successive peak is $< 13.5 \mu S$, therefore, subsequent trigger pulses could be generated from the sampling pulse generator (Monostable multivibrator) before the ADC conversion of the previous sample is complete. To prevent this, the monostable multivibrator output was gated (inhibited) by programming the microcontroller-II so that it cannot initiate further sampling pulses before completion of the current ADC conversion. The overall gain of the voltage measurement circuit based on analogue synchronous peak detection was set to 48. Therefore for a drive current of 1mA (p-p) and transfer impedance of 100Ω, the voltage across the receive electrode pair is 100mV before amplification. After 48 times amplification the voltage should be 4.8V (p-p). Just before sampling the peak value, the signal was given a positive dc shift of 2.5V so that the whole signal is positive. Therefore, the detectable peak ranges from 2.5 (corresponding to zero output signal) to 5V (corresponding to the maximum output signal, sampling IC was driven from ±7V). The resolution of the *ADC* of the voltage measurement microcontroller is 10 bit with reference voltage 5V. So the detected peak voltage range is 2.5-5V corresponding to transfer impedance range **0-100Ω** and the measurement resolution for the synchronous peak detection method is about **0.1Ω**.

3.4.1.8 Data acquisition

The Universal Synchronous and Asynchronous serial Receiver and Transmitter (USART) peripheral of the ATmega8 microcontroller was used to communicate with the personal computer that employed to acquire and process measured data. Microcontroller-II collected 10 consecutive peak values of the bioamp output through ADC conversion for each measurement frequency and then averaged them before sending the value to the PC via a serial link. A serial to USB adaptor (TTL232-5V) was used to connect the FIM system to the commonly available USB port of a PC. The average of 10 peak values at

each frequency is sent to PC for further analysis. The sequence was repeated for other measurement frequencies.

3.4.2 Digital Demodulation

The voltage measurement circuit based on analogue synchronous peak detection was initially fabricated and tested by manually wiring and soldering on prototype Vero-boards which worked correctly. However, the differentiator circuit became unstable when the whole circuit was fabricated on printed circuit boards (PCB). This is because the board layout is very critical for circuits involving high speed op-amps. Moreover, the circuit based on analogue synchronous peak detection is capable of measuring the magnitude of the impedance, but not its phase. Body tissues contain both resistive and capacitive components. So the voltage signal across the pickup electrodes are not in the same phase with the injected current signal i.e. there is a phase difference. However, the ratio of peak voltage to the peak current can give the modulus of the transfer impedance at a particular frequency. In many applications the phase difference between the drive and receive signal is also important. The fastest microcontroller available locally when this research work was started could be clocked at 16 MHz maximum. Therefore digital demodulation at 1MHz was not possible. However, while working with the thesis, high speed microcontrollers (e.g. the Kinetis K2x family) were becoming available that could be overclocked to >100MHz which made digital demodulation viable at 1MHz. Therefore, the performance of a digital demodulator was investigated using a *Picoscope(PicoTech)* which uses this technology. Digital demodulation algorithms were written in Matlab. A multi-frequency FIM system based on digital demodulation and capable of measuring both magnitude of impedance and phase was designed and developed as described in this section.

3.4.2.1   Block diagram of Digital Demodulation circuit

Figure 3-18 shows the block diagram of the multi-frequency FIM system based on digital demodulation which uses a portable oscilloscope for data acquisition. As before the excitation signal was generated from a microcontroller (section 3.3.1). The signal was then converted to a current of constant amplitude using a modified Howland current pump (section: 3.3.2). The purpose of the multiplexer is to choose appropriate drive and receive electrode pairs for a particular FIM configuration (described later in section 3.5). The voltage across receive electrodes is amplified using a bioelectric amplifier and filtered using a bandpass filter as described in section 3.4.1.2. The amplified voltage signal as well as the drive current signal was acquired by a PC using the portable oscilloscope (Picosope 2208A) mentioned before and then the data is analyzed in a PC.
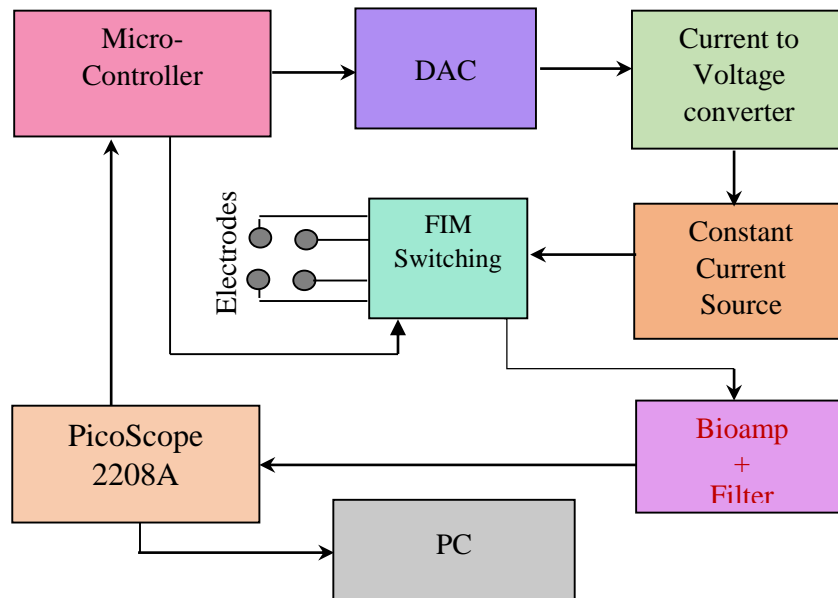
Figure 3-18 Block diagram of the multi-frequency FIM system based on digital demodulation.

61

Picoscope 2208A (PicoTech) is a low cost portable oscilloscope with bandwidth 200MHz and sampling rate up to 1GS/s. It contains two input channels and also an arbitrary wave form generator as shown in Figure 3-20. The Picoscope is interfaced with PC through USB. A software based on Matlab (2014b) was developed to control the Picoscope and hence the FIM measurements. The two input channels were used to acquire both the *current* and *voltage* signals. For a particular frequency of measurement, the signals were acquired to PC as a block of data points and each block contains 8192 samples. However, the sampling rate is different for signals of different frequencies. Figure 3-19 shows the acquired current and voltage signals of 10 kHz where the sampling rate is 10MS/s. On the other hand, for signals of 1MHz

Input   Output

Figure 3-20 Portable oscilloscope (Picoscope) used for data acquisition.
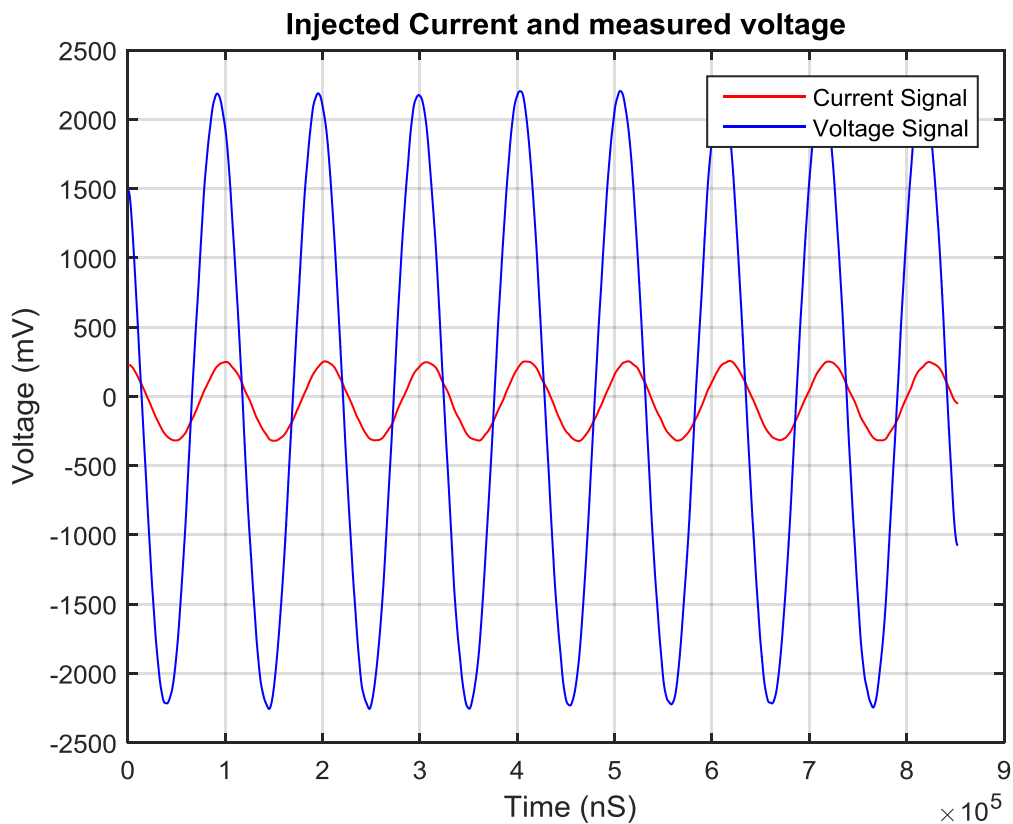
Figure 3-19 Voltage and current signals of 10 kHz acquired simultaneously to PC using the Picoscope. This window contains 8192 samples where the sampling rate is 10MS/s.

62

the sampling rate is 500MS/s to achieve adequate amplitude resolution. For a particular measurement frequency, the appropriate sampling rate is chosen under Matlab control.

3.4.2.3   Decoding the impedance value

The voltage and current signals acquired by Picoscope are stored in a PC as *arrays* in Matlab sortware and then the impedance values are calculated. As described earlier, the impedance at a particular frequency is the ratio of the p-p (peak to peak) value of the voltage signal to that of the current signal. The p-p value of the current signal is known (1mA) as it is driven from a constant current source. Therefore, only the p-p value of the voltage signal is to be determined. For this purpose, the positive and negative peaks of the sinusoidal voltage signal is determined using *peakfinder* algorithm in Matlab as shown in Figure 3-21. The average of the negative peak values were subtracted from the average of positive peak values which is the p-p value of the voltage signal. The p-p value of the voltage signal was then divided by p-p value of the current signal (1mA) and also divided by the overall circuit gain which gives the magnitude of the impedance. The overall gain of the voltage measurement section based on digital demodulation was 100.
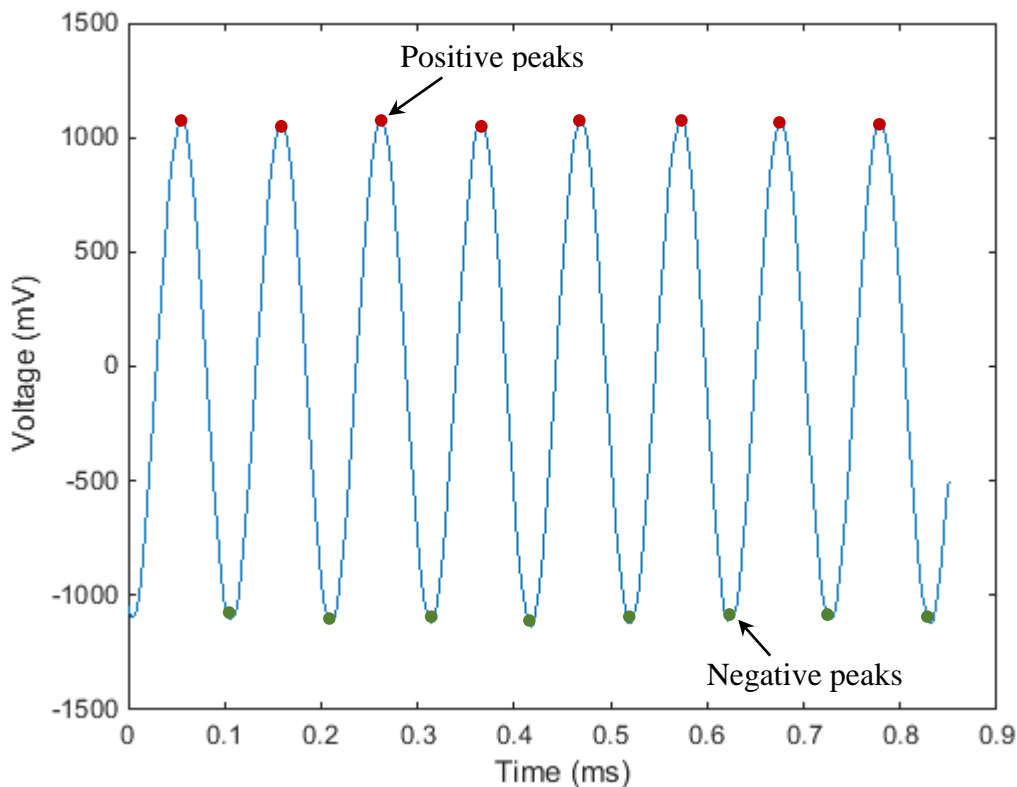
Figure 3-21 Positive and negative peaks of a voltage signal (10kHz) is identified using peakfinder algorithm in Matlab.

The maximum output swing of the amplifiers used were ±3.2V (6.4V p-p) with supply voltage ±5V. For a transfer impedance of 60Ω with a drive current of 1mA (p-p), the amplified (gain 100) signal will be 6V (p-p) which is close to the output voltage swing of the opamps used and therefore maximum measurable transfer impedance is **60Ω**. The amplitude resolution of the portable oscilloscope (Picoscope 2208A) is 8 bit. So for a voltage range of 5V, the measurement resolution is around **0.2Ω**. Again, for a voltage range of 2V, the measurement resolution is around **0.078Ω**.

3.4.2.4 *Measurement of the phase difference*

The biological tissue contains capacitive components and therefore the voltage signal lags behind the current signal. The phase difference is an important parameter in diagnosis or tissue characterization. In FIM, only the magnitude of impedance is measured using two orthogonal TPIM configurations and summed to get more localized information from the region beneath the electrode array minimizing contribution from surrounding regions; the phase is not usually considered since its physical significance is not well understood. However, two separate orthogonal TPIM measurements of *phase* could give useful information in tissue characterization, for example, frequency response of *phase*, level of tissue anisotropy etc. Therefore the MFFIM system with digital demodulation records the phase values at all measurement frequencies for two orthogonal TPIM configurations.

An algorithm (*phdiffmeasure*) was written in Matlab to measure the phase difference between the drive and receive signals. The algorithm performs *FFT* on both the drive and receive signals and the magnitudes of the transformed signals are computed. For a particular signal, the angle is obtained at maximum magnitude component of the FFT signal. The difference of these angles between drive and receive signals gives the phase difference in radians which is then converted to degree. The drive and receive signals pass through multiple electrical pathways within the electronic circuitry, so there is a phase difference between the signals without any phase difference in the load impedance to be measured. Therefore, the phase difference values at all measurement frequencies were measured using a purely resistive load and recorded. The algorithm subtracts these phase values during calculation from any load under measurement.

3.5 FIM Switching

As described earlier, there are 3 versions of the FIM electrode configurations i.e. FIM-8, FIM-6 and FIM-4. Again, Focused Impedance Method needed two measurements at each frequency where the direction of current drive and voltage measuring electrode pairs were altered

Table 3-6 Position of drive and receive electrodes pairs for different FIM configurations

FIM Electrode Configuration	Measurement 1 (Z_1)	Measurement 2 (Z_2)
FIM-8	Drive: A,D Receive: B,C	Drive: E,H Receive: F,G
FIM-6	Drive: A,D Receive: K, N	Drive: E,H Receive: K,N
FIM-4	Drive: K,L Receive: M,N	Drive: K,M Receive: L,N

orthogonally (Rabbani et al., 1999, Rabbani and Karal, 2008) summarized in Table 3-6 and Figure 3-22c. This section describes the FIM switching mechanism implemented. There are four signal terminals; two for current ($i+$ and $i-$) and two for voltage ($v+$ and $v-$) originating from the FIM device hardware (Figure 3-22a). FIM measurements were achieved by switching the current and voltage signals to appropriate electrodes (Figure 3-22c) for a particular FIM configuration. For this purpose, eight *BNC* ports (denoted:1-8) were used on the device panel as shown schematically in Figure 3-22b. These BNC ports were used for the electrical connections to the electrodes. An analog multiplexer (CD4052) were used to establish electrical conduction path among *signal*
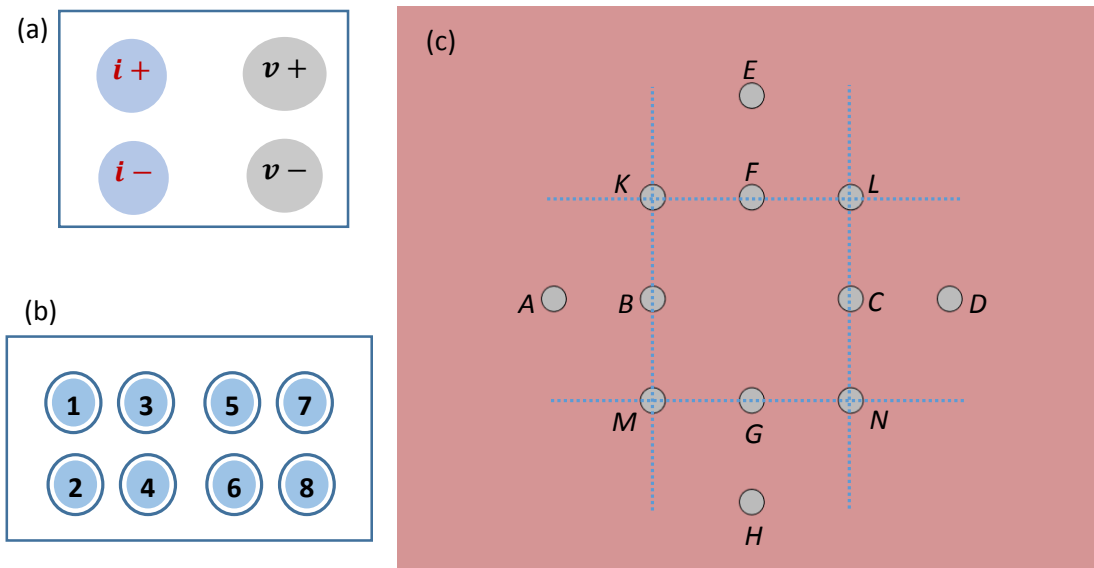
Figure 3-22 Electrical conduction path was established between signal terminals and body electrodes via BNC ports. (a) Signal terminals (b) BNC ports on device panel (c) Electrodes on body surface
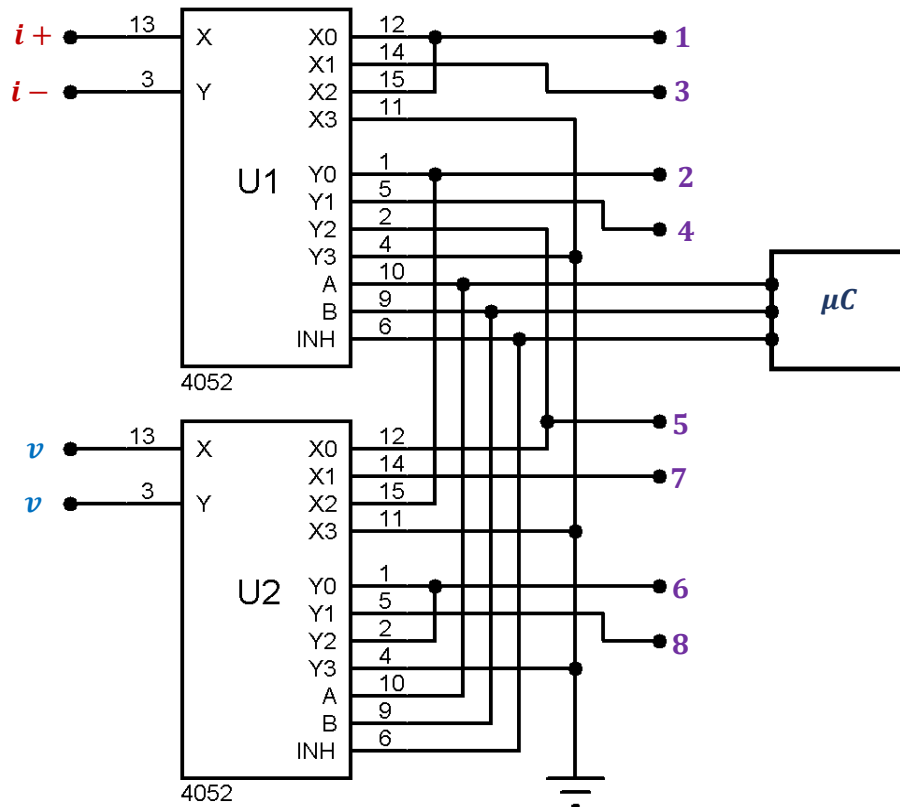
Figure 3-23 Circuit implemented for multiplexing signal terminals among body electrodes through BNC ports to achieve FIM measurements. The numbers (1-8) on right hand side of the figure represented the BNC ports shown in figure 3-22b.

terminals and *BNC* ports (Figure 3-23) appropriate for a particular FIM configuration as listed in Table 3-7. The multiplexers are controlled from the microcontroller using I/O terminals.

For FIM-8 configuration, all the eight BNC ports (1-8) need to be used and two orthogonal measurements are performed by switching *signal terminals* among body electrodes sequentially according to Table 3-7. The measurement-I is performed by connecting *signals terminals* to the *BNC* ports *1,2,5,6* and then the measurement-II is performed by connecting *signal terminals* to the *BNC* ports *3,4,7,8*; which in turn connect *signal terminals* to the electrodes *A,B,C,D* and *E,F,G,H* respectively. The microcontroller is programmed so that it records voltage signal from horizontal electrodes; and then changes the multiplexer control inputs to record the signal for vertical electrodes of Figure 3-22c at each measurement frequency.

In FIM-6 configuration, the BNC ports 7 and 8 are not in use; only the *current* terminals are switched while voltage signal is recorded from the same electrode pair (K, N). In FIM-4 configuration, only four BNC ports ($1,2,5$ *and* 6) need to be used. In this case,

66

only the signal terminals $i-$ and $v+$ are switched between the electrodes L and M (BNC ports 2 and 5) to achieve the FIM measurements. Impedance measurements for all of the three FIM configurations can be performed using the designed multi-frequency FIM system as explained in Table 3-7.

Table 3-7 Switching sequences for different FIM measurements. Multiplexers are controlled by a microcontroller to established electrical conducting path between signal terminals and body electrodes for FIM measurements.

Electrode Configuration	Measurement Sequence	Multiplexer Control Input			Multiplexer ON channel	Electrical Connection Pathway		
		Multi-plexer	B	A		Circuit Terminal	BNC Port	Body Electrode
FIM-8	I	U1	0	0	X-X_0 Y-Y_0	$i+$	1	A
						$i-$	2	D
		U2	0	0	X-X_0 Y-Y_0	$v+$	5	B
						$v-$	6	C
	II	U1	0	1	X-X_1 Y-Y_1	$i+$	3	E
						$i-$	4	H
		U2	0	1	X-X_1 Y-Y_1	$v+$	7	F
						$v-$	8	G
FIM-6	I	U1	0	0	X-X_0 Y-Y_0	$i+$	1	A
						$i-$	2	D
		U2	0	0	X-X_0 Y-Y_0	$v+$	5	K
						$v-$	6	N
	II	U1	0	1	X-X_1 Y-Y_1	$i+$	3	E
						$i-$	4	H
		U2	0	0	X-X_0 Y-Y_0	$v+$	5	K
						$v-$	6	N
FIM-4	I	U1	0	0	X-X_0 Y-Y_0	$i+$	1	K
						$i-$	2	L
		U2	0	0	X-X_0 Y-Y_0	$v+$	5	M
						$v-$	6	N
	II	U1	1	0	X-X_2 Y-Y_2	$i+$	1	K
						$v+$	2	L
		U2	1	0	X-X_2 Y-Y_2	$i-$	5	M
						$v-$	6	N

3.6 Multi-frequency FIM control algorithm

In the developed multi-frequency FIM there are 8 measurement frequencies, and at each frequency two measurements are needed for FIM. Effectively the developed FIM based on digital demodulation measures 16 magnitude and 16 phase values in one frame. The microcontroller and the PC used for data acquisition effectively control the whole measurement sequences. Initially, the PC send a pulse to the current generating microcontroller to set multiplexer connections for a particular electrode configuration, say first sequence of FIM measurement (FIM-1). After setting the switching multiplexers, the microcontroller starts generating signals of 10 kHz. The PC records both the current and voltage signal. Once the data acquisition for FIM-1 configuration at 10kHz is complete, the PC sends another pulse to the microcontroller to change the multiplexer switches to establish electrical connections for the second measurement of FIM (FIM-2) but do not change the signal frequency. After completing the both FIM measurements at 10 kHz, the PC sends another pulse to the microcontroller to change the signal frequency to 20 kHz but not changing multiplexer switching. In this case the PC acquires data for FIM-2 configuration at 20 kHz. The control algorithm continues in this way for all measurement frequencies and the PC records data for 16 measurements at 8 frequencies. The data is analyzed further to calculate absolute impedance and phase difference after acquiring all data. As mentioned before, the data acquisition aims at achieving the maximum frame rate.

3.7 Isolation and safety

To ensure patient safety all patient connections on electro-medical equipment should be electrically isolated from the mains supply. The multi-frequency FIM system described in this thesis required a total current of approximately ±100mA from a ±5V supply. The need for electrode switching under microprocessor control means that the voltage measurement and current source sections cannot be easily isolated from the other parts of the system. Therefore the whole measurement system is powered from a medical grade isolated power supply (*THB 3-1222* manufactured by *TRACO® POWER*) which satisfy the *IEC/EN 60601-1* safety standards (IEC, 2004) for patient connected electro-medical equipment. The output of the power supply is ±7V which was converted to ±5V using regulators. The power supply can isolate up to 5kV.

For storage and analysis of data, the device is also connected to a PC which may be connected to mains supply. In the voltage measurement circuitry based on analogue synchronous peak detection, isolation between the measurement system and the PC that is used to collect data was achieved by using high speed *opto-couplers* (HCPL 2531) on the serial data lines *(Rx, Tx)* which connect the two. The isolation measures taken for patient safety is illustrated in Figure 3-24.
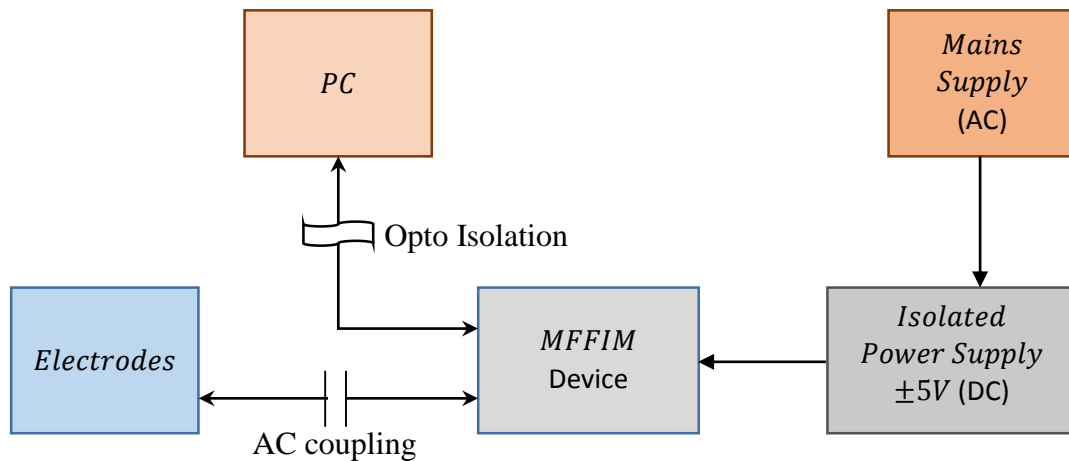
Figure 3-24 Isolation of the measurement device from mains supply to ensure patient safety. The power is taken from a medical grade isolated dc power supply while the communication with PC is optically coupled for the device based on analogue synchronous peak detection.

For the case of data acquisition using portable oscilloscope, the *Picoscope 2208A* satisfies the *BS EN 61010-1:2001 IEC 61010-1:2001* safety standards for laboratory electro-medical equipment (PicoTech). In addition, all electrode connections to the patient were ac coupled using capacitors to prevent any dc currents passing to the patient. However, the inputs of the Picoscope are not electrically isolated. Therefore, a laptop PC powered on battery (not connected to mains supply) was used for data collection from human subjects.

3.8   Performance analysis

The performances of various sections of the designed multi-frequency FIM system have been analysed and the results are described in this section. However, the results and observations will be discussed later in section 3.9.

3.8.1   Signal frequency

The microcontroller based signal generator of the MFFIM was designed to generate sinusoidal signals of frequencies: 10 kHz, 20 kHz, 40 kHz, 80 kHz, 160 kHz, 320 kHz,

640 kHz and 1024 kHz. However, the actual frequencies of the signals generated by the implemented circuit were 10 kHz, 20 kHz, 40 kHz, 80 kHz, 160 kHz, 296 kHz, 633 kHz and 1033 kHz respectively (rounded). The generated signal frequencies are close to the frequencies specified except signals at 296 kHz which is 24 kHz lower than that specified. The number of sample points for generation of the signal was determined by the clock frequency and this produced the difference between designed frequencies and those obtained in practice. However, the differences are small and the resultant values are acceptable since it is the variation of transfer impedance with frequency that will be analysed in the studies on human subjects (Chapter 4).

3.8.2   Current source output impedance

The current source can be modelled as a constant current generator in parallel with a resistance (output impedance). To measure the output impedance (z_o) of the current drive circuit, two different load resistances (R_L) were driven by the current at each frequency (Figure 3-25).

If V_1 and V_2 were the voltage developed across $R_L=R_1$ and $R_L=R_2$ respectively, then:

$$V_1 = i \left(\frac{1}{z_0} + \frac{1}{R_1} \right)^{-1}$$

$$or, \frac{i}{V_1} = \left(\frac{1}{z_0} + \frac{1}{R_1} \right) \qquad 3\text{-}7$$

Similarly,

$$\frac{i}{V_2} = \left(\frac{1}{z_0} + \frac{1}{R_2} \right) \qquad 3\text{-}8$$
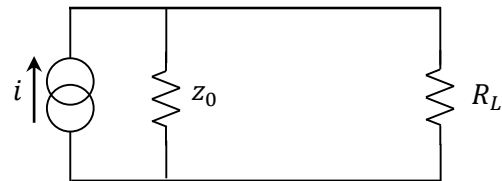
Figure 3-25 Equivalent circuit used to model the output impedance of the current source

Combining above two equations and solving for z_o, it can be shown that

$$z_0 = \frac{(V_2 - V_1)R_1 R_2}{(V_1 R_2 - V_2 R_1)} \qquad 3\text{-}9$$

Therefore, the output impedance (z_o) was calculated using the equation (3-9) by measuring voltage across two different load resistors 97.8Ω and 991Ω (these are measured resistance values using a multi-meter for standard resistors 100 Ω and 1000 Ω respectively). The output impedance of the current source was measured to be 476 kΩ at 10 kHz signal and 58.3 kΩ at 1033 kHz signal respectively. The current source was

designed to deliver 1 mA (p-p) to load resistance of up to 4kΩ. Figure 3-26 shows the drive current against load resistances at different frequencies.

The drive current is almost constant up to a load of 3kΩ for signals below up to 80 kHz but drops significantly above this. For 296 kHz signal, the current drops above a load of 2kΩ. However, for 1033 kHz signals, the drive current remains almost constant up to a load of 1.5 kΩ but drops gradually above loads 2kΩ.
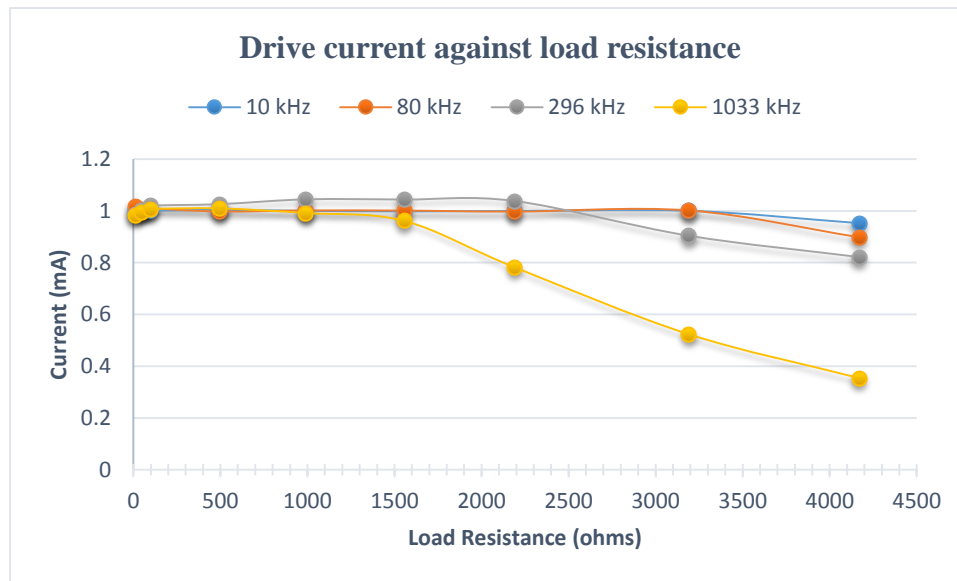
Figure 3-26 Drive current plotted against load resistances at four representative frequencies.

3.8.3 Common Mode Rejection Ratio (CMRR)

The Common Mode Rejection Ratio (CMRR) of the differential amplifiers used to design the bioelectric amplifier (AD8055) is 82dB. However, in practical design, the presence of series impedance and stray capacitance attenuate the CMRR. The CMRR of the voltage measurement circuit of the designed MFFIM was obtained experimentally at all the eight measurement frequencies. The differential mode gain (A_d) and the common mode gain A_{cm} was measured as illustrated in Figure 3-28. CMRR is then calculated using the equation:

$$CMRR = 20\ log(\frac{A_d}{A_{cm}})\quad \text{---- 3-10}$$

71
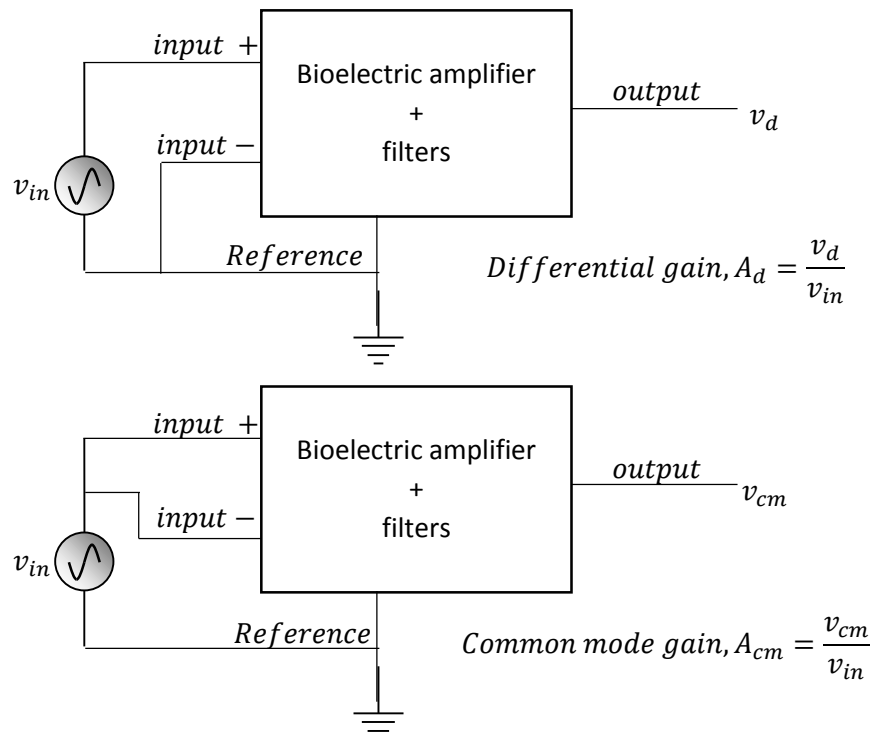
Figure 3-28 Schematic diagram used for measuring the common mode rejection ration (CMRR); here A_d and A_{cm} are differential and common mode gain respectively.

Experimental values of CMRR were plotted against frequency in Figure 3-27. It can be observed that the value of CMRR was 63dB at 10 kHz and remains above 60 dB up to 100 kHz beyond which it decreases and reduced to 37 dB at 1024 kHz.
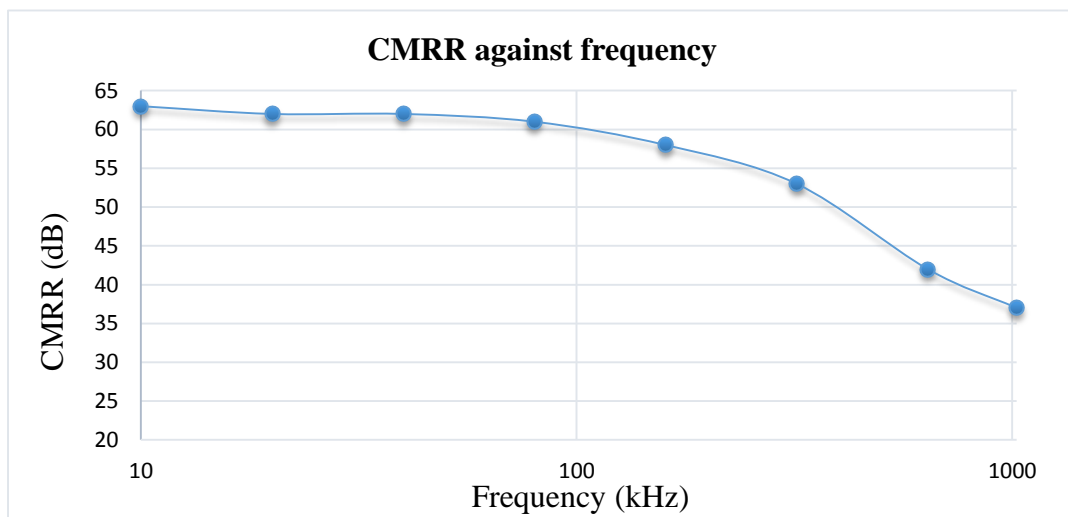
Figure 3-27 Frequency response of CMRR of the voltage measurement circuit of the designed MFFIM system.

3.8.4   Linearity and measurement accuracy in resistive phantom

To study the linearity of voltage measurements, transfer impedance values were measured on different known resistors (R_t) from a resistive phantom shown in Figure 3-29 at all the eight measurement frequencies, where R_t represents the tissue impedance. The values of R_t were measured initially using a precision digital multi-meter and then using both analogue and digital demodulation technique of the designed multi-frequency FIM system. The values of R_t was variable in the measurable transfer impedance range.
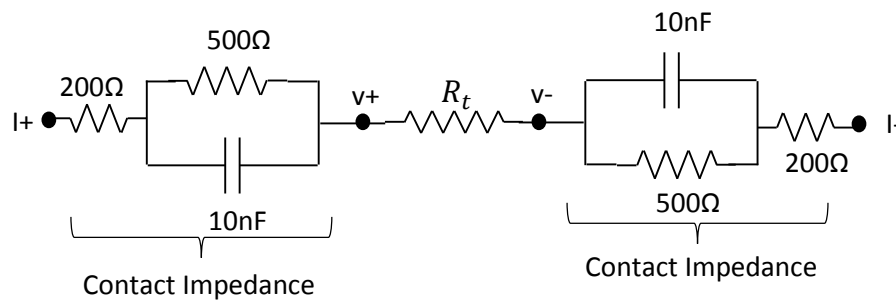
Figure 3-29 Resistor phantom used to study the linearity of the designed MFFIM system.

The electrode-tissue equivalent circuit (200Ω resistor in series with parallel combination 10nF capacitor and 500Ω resistor) on both side of R_t were used to simulate the electrode-tissue contact impedance. The values of the components on the electrode-tissue equivalent circuits above *(total contact impedance 1.4 kΩ at 10kHz, 700Ω at 100 kHz and 430 Ω at 1MHz)* was chosen to approximately represent the *load impedance* values measured in section 3.2.2.
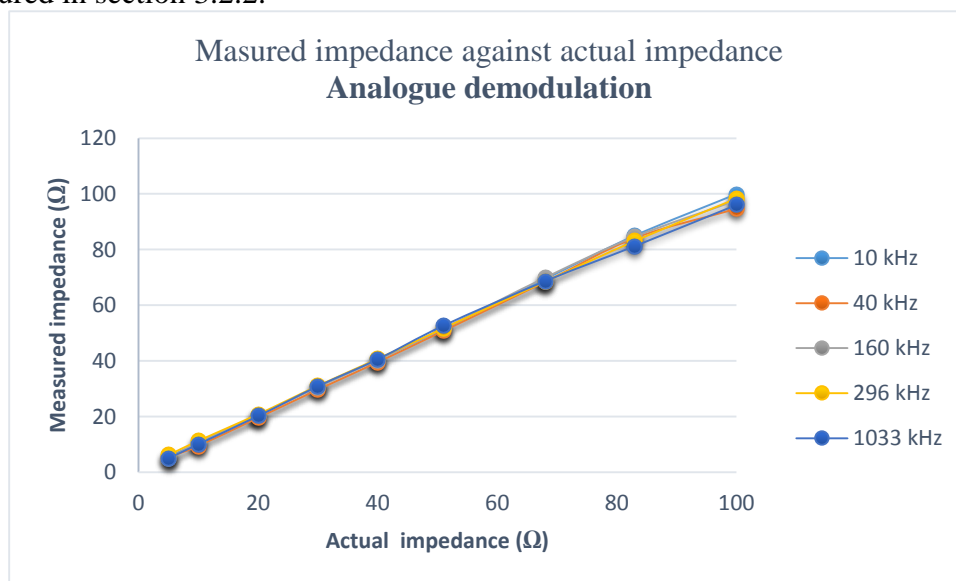
Figure 3-30 Comparison of measured impedance with actual impedance values. Measurements were performed on the resistive phantom shown in Figure 3-29 using analogue synchronous peak detection method.
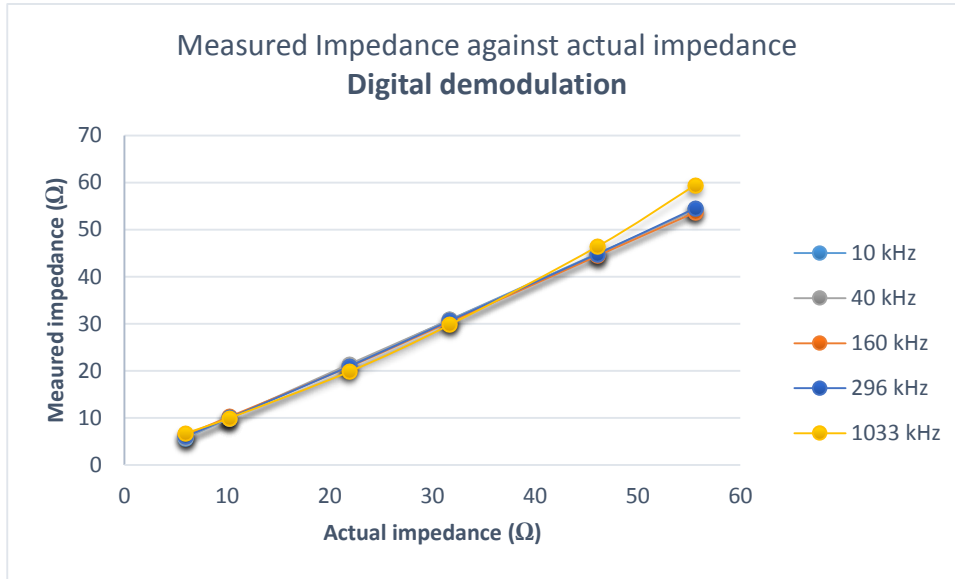
Figure 3-31 Comparison of measured impedance with actual impedance values. Measurements were performed on the resistive phantom shown in Figure 3-29 based on digital demodulation technique.

In Figure 3-30, the impedance values measured using analogue synchronous peak detection method were plotted against actual impedance values. Figure 3-31 shows the similar plots for the impedances measured based on digital demodulation technique. It can be observed that there is some nonlinearity for amplification of signals at 1033 kHz.

For the above measurements on resistive phantoms, the accuracy of measurements were calculated. If the applied known resistance was R_{known} and the resistance measured by the multi-frequency FIM system was $R_{measured}$, then the percentage of error (absolute value) was calculated using equation 3-11.

$$Error = \frac{|R_{known} - R_{measured}|}{R_{known}} \times 100\% \qquad \text{-------- (3-11)}$$

Figure 3-32 and Figure 3-33 shows the percentage of measurement error against actual resistance values at five representative frequencies. Figure 3-32 shows the percentage error for measurements based on analogue demodulation method and the Figure 3-33 shows that for measurements based on digital demodulation method. If the results at low resistances (≤10Ω) are ignored, the measurement error was below 5%.

74
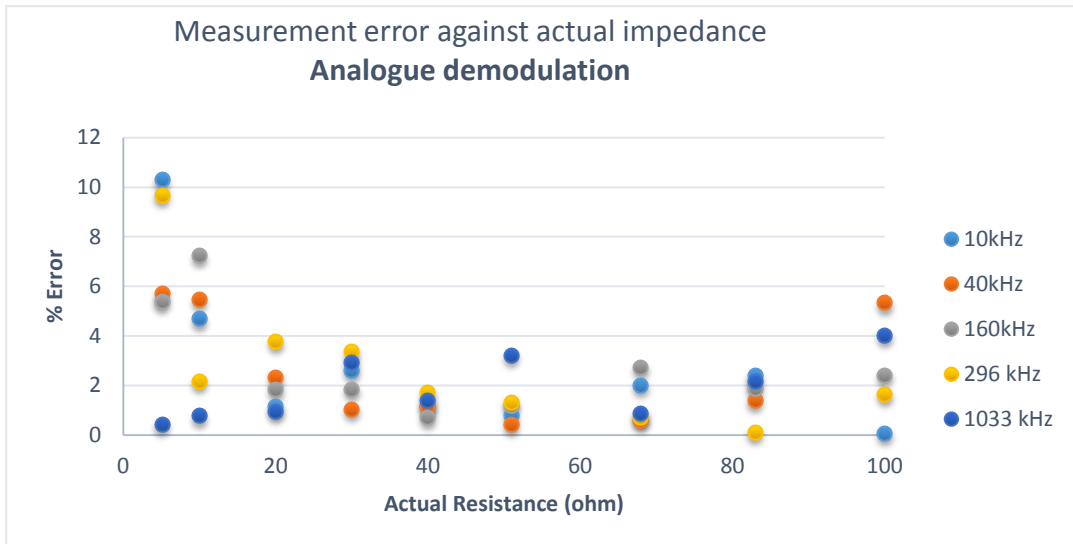
Figure 3-32 Percentage of error for different known resistances at 5 representative frequencies. The measurements were performed using analogue demodulation method (synchronous peak detection).
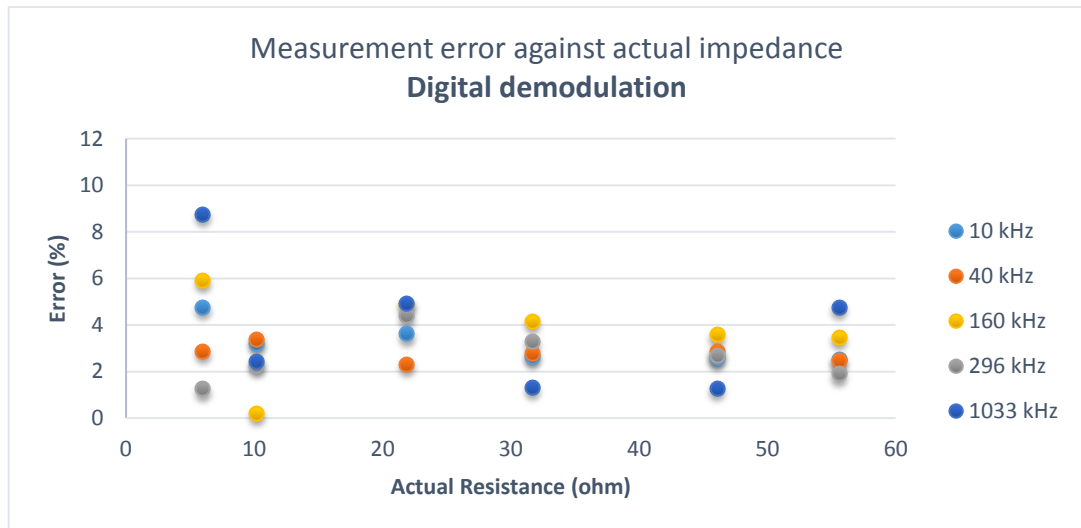
Figure 3-33 Percentage of error for different known resistances at 5 representative frequencies. The measurements were performed using circuitry based on digital demodulation method. (Note the highest load resistance used, which is 60Ω, less than that in Figure 3-32).

3.8.5 Measurement accuracy in capacitive phantom (Cole-Cole model)

The designed multi-frequency FIM system was also tested for capacitive loads by replacing the load resistor R_t with a Cole-Cole model phantom as shown in Figure 3-34 where C represents membrane capacitance, R represents extra cellular resistance and S represents intra cellular resistance. The resistor-capacitor model on both side of the Cole-Cole model is to simulate contact impedances.

The impedance values measured using the analogue synchronous peak detection technique from the Cole-Cole model (R=77.8Ω, S=20.1Ω and C=10nF) is plotted against calculated impedance values in Figure 3-35. In preliminary studies, it was observed by the author of this thesis that impedance values measured on human chest and breast vary from 10 to 60 ohms in the frequency range 10kHz to 1MHz (Kadir et al., 2010, Kadir et al., 2015, Al Amin et al., 2014). So the values of the Cole-Cole model components were chosen to represent similar transfer impedance values in the measurement frequency range. Analysing the errors between the measured and calculated impedance values for this phantom showed that the maximum error was around 6.7% at signal frequencies 160kHz and 296 kHz whereas the error at other frequencies was below 4% as shown in Figure 3-36.
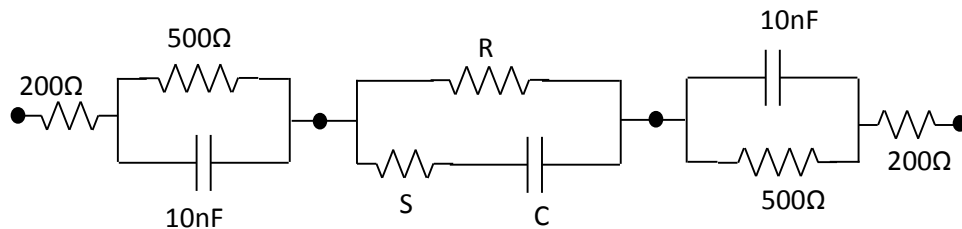
Figure 3-34 Cole-Cole phantom with modeled contact impedance used to study the accuracy of the designed multi-frequency FIM system.
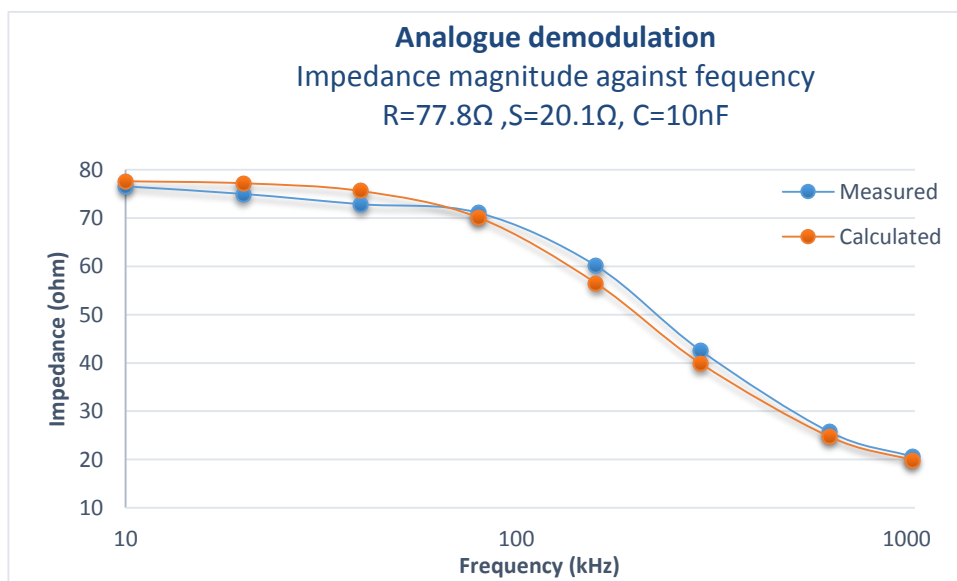
Figure 3-35 Comparison of measured impedance magnitude with calculated impedance on a Cole-Cole phantom for the MFFIM system based on analogue synchronous peak detection.
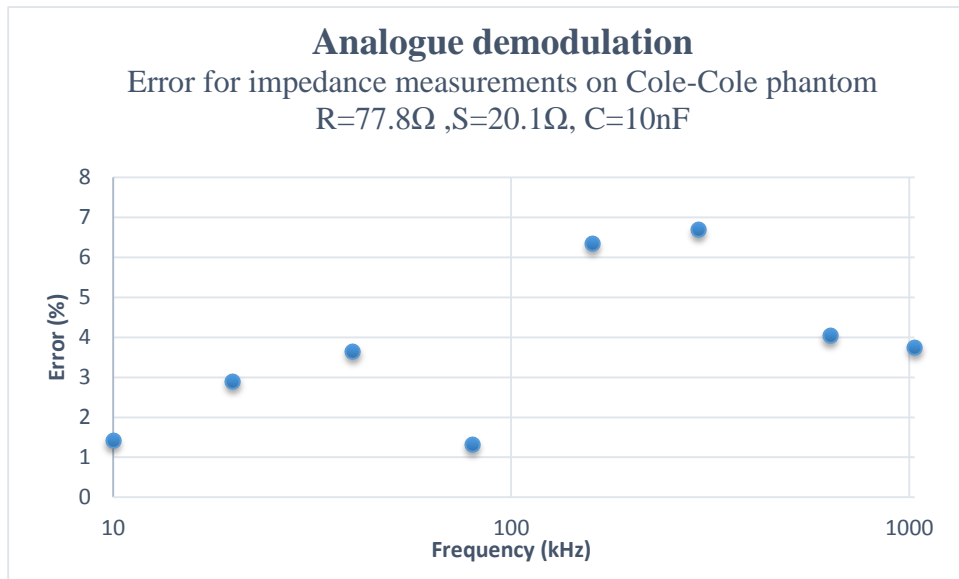
Figure 3-36 Percentage of error at different frequencies for impedance measurements on a Cole-Cole phantom using analogue demodulation technique.

The impedance values measured using the MFFIM system based on digital demodulation is plotted against calculated impedance values in Figure 3-37. The measurement error is less than 2% at all frequencies except at 1033kHz where is 7.34% as shown in Figure 3-38. So digital demodulation gives a better result compared to the analogue demodulation technique for such impedances.
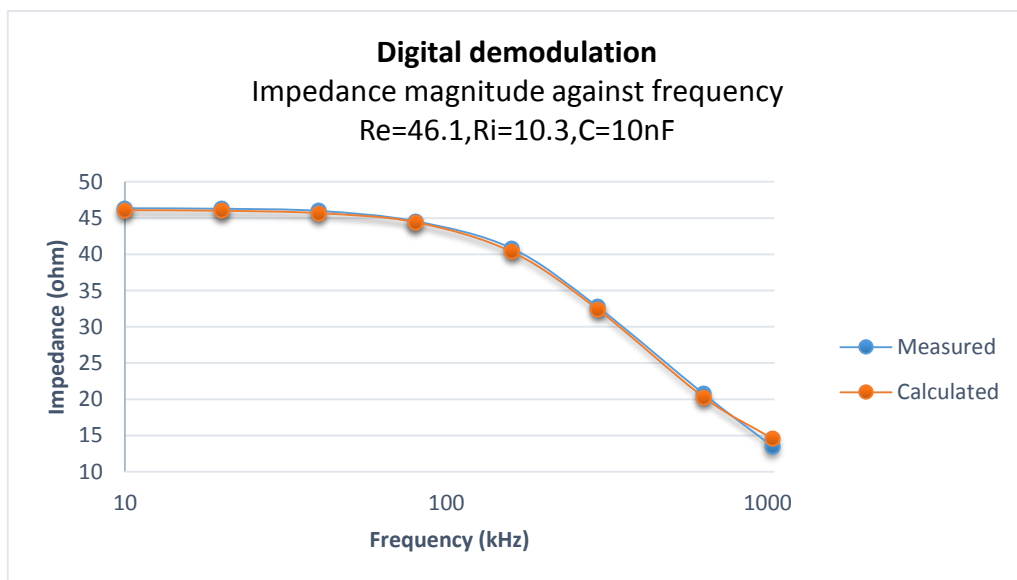
Figure 3-37 Comparison of measured impedance magnitude with calculated impedance on a Cole-Cole phantom for the MFFIM system based on portable oscilloscope.
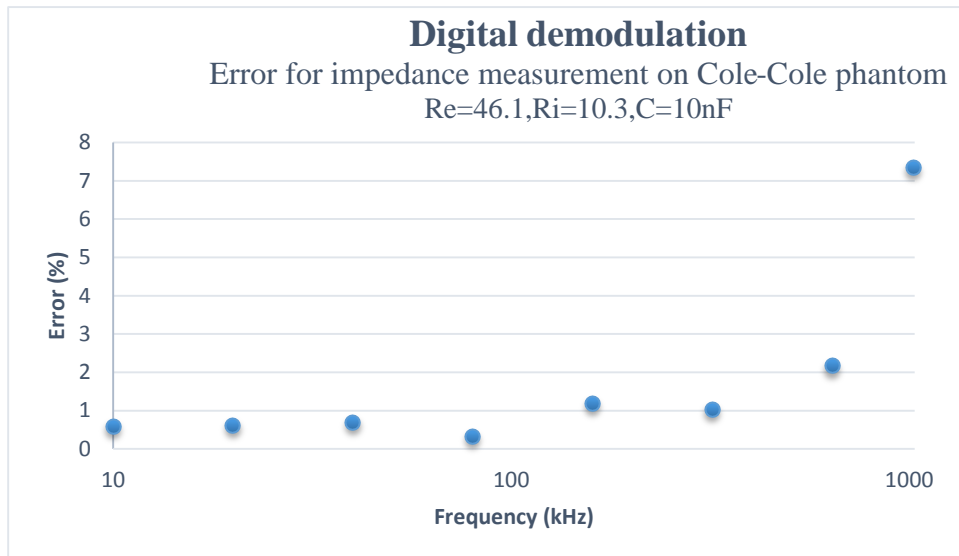
Figure 3-38 Percentage of error at different frequencies for impedance measurements on a Cole-Cole phantom for both digital and analogue demodulation techniques.

3.8.6   Accuracy in phase measurements

As mentioned earlier, the multi-frequency FIM system based on digital demodulation technique is capable of measuring magnitude of impedance as well as the phase difference between the drive and receive signal. The measurement accuracy was tested in a Cole-Cole phantom as shown in Figure 3-39. The resistor $R_c=200\Omega$ on both side of the Cole-Cole model was used to simulate contact impedance. The phase values of the model was measured using the designed multi-frequency FIM. The measured values were then compared with calculated values.
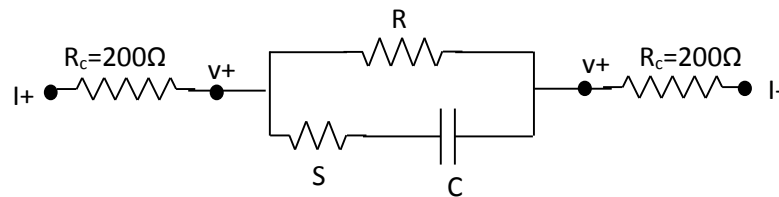
Figure 3-39 Cole-Cole phantom used for phase measurements

Figure 3-40 shows comparison of measured phase with calculated phase values for Cole-Cole phantom (R=46.1Ω, S=10.3Ω and C=10nF). It can be observed that the measured phase values are very close to the actual values for signal frequencies up to 296 kHz but deviated above this frequency. The maximum error was 7.58% occurring at signal frequency 1033 kHz as shown in Figure 3-41.

78
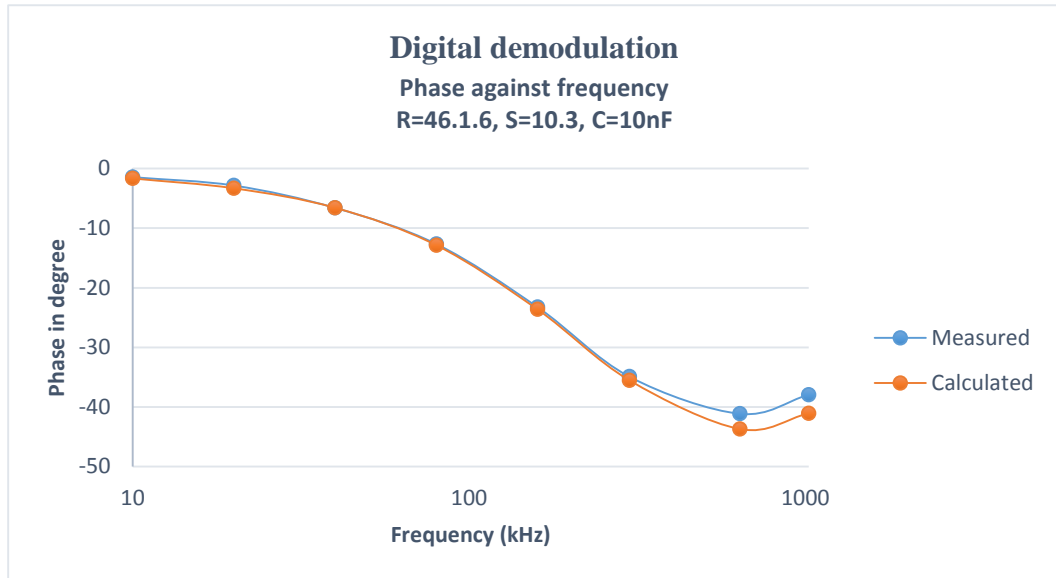
Figure 3-40 Comparison of measured phase values with actual phase values for measurements on a Cole-Cole phantom using the multi-frequency FIM system based on digital demodulation
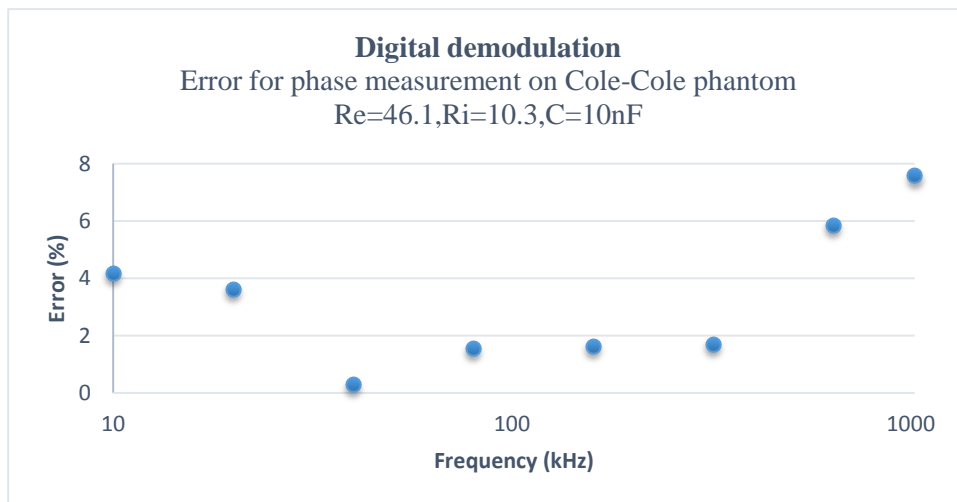
Figure 3-41 Percentage error at different frequencies for phase measurements on Cole-Cole phantom

3.8.7 Comparison with commercially available device

The performance of developed multi-frequency FIM system based on digital demodulation method was compared with a commercially available impedance analyzer named *Sciospec ISX-5* manufactured by *Sciospec Scientific Instruments GmbH, Germany* (Sciospec). For this purpose, impedance values were measured from a Cole-Cole phantom shown before in Figure 3-39. The value of contact impedance R_c was changed and its effect on measurement accuracy was analyzed. The variations of impedance with frequency measured from a Cole-Cole phantom (R=55.6Ω, S=10.2Ω and C=10nF) using the developed multi-frequency FIM system and that using the *Sciospec* are shown in
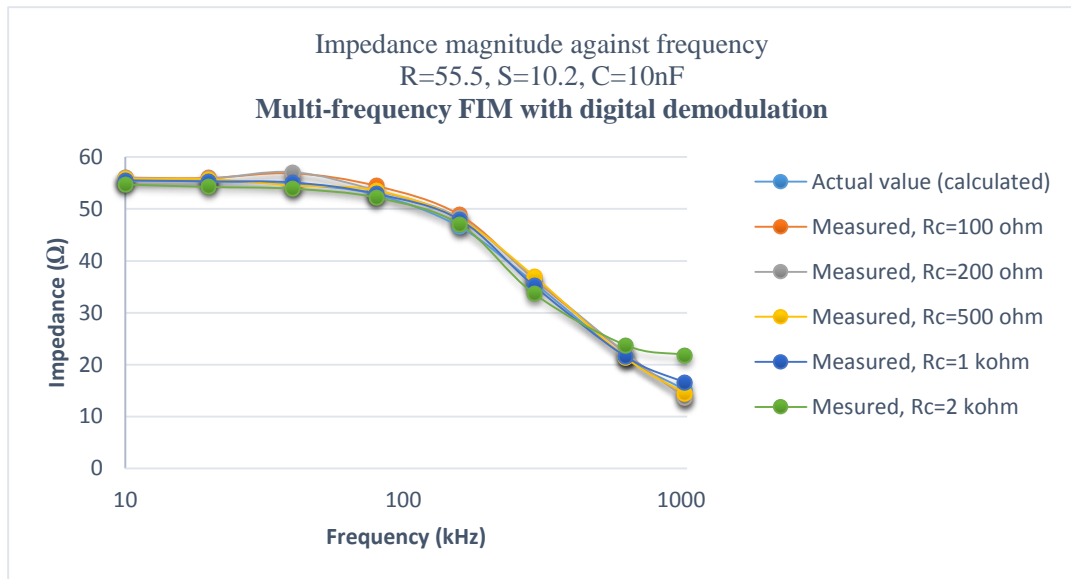
Figure 3-42 Variation of impedance with frequency for a Cole-Cole plot for different contact impedance measured using the developed multi-frequency FIM system based on digital demodulation.

Figure 3-42 and Figure 3-43 respectively. Different curves, together with the curve for actual calculated values, shows measured impedances at different contact impedances (R_c). It can be observed that for contact impedance up to 2kΩ (Rc=1kΩ means that contact impedance is 1kΩ+1kΩ=2kΩ) the measured values are close to the actual calculated values (percentage error less than 4.9%) for the developed multi-frequency FIM system with digital demodulation technique, except at 1033 kHz. However, for 1033 kHz signal, the percentage error is maximum and is 10.01% for contact impedance up to 2 kΩ but the error increases further with increasing contact impedance values.
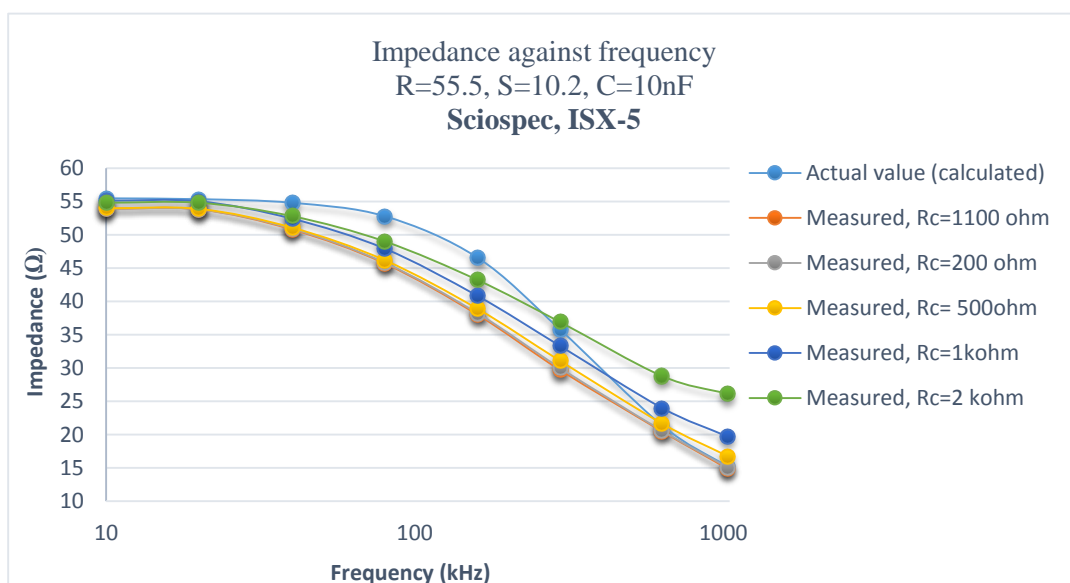
Figure 3-43 Variation of impedance with frequency for a Cole-Cole plot for different contact impedance measured using the commercially available Sciospec device.

In contrast, for measurements using Sciospec system (commercial device), the maximum percentage error is 18% even at contact impedance 200Ω for signal frequency 60 kHz. At signal frequency 1033 kHz and contact impedance 2000Ω, the measurement error is 29.6%. None of these are practically acceptable (section 3.2) and the error is even more at higher contact impedance values.

Similar measurements were performed using both MFFIM and Sciospec devices from a resistive phantom of known value (31.9Ω) for different values of R_C. For this, the Cole-Cole model in Figure 3-39 was replaced by a pure resistor. Figure 3-44 shows the percentage of measurement errors at three frequencies (10kHz, 633kHz and 1033kHz) for different contact impedance (R_C) values. It should be noted that the total contact impedance of both the electrodes is $2R_C$. It can be observed that the measurement error for both MFFIM and Sciospec at 10 kHz is relatively low (less than 2.5% for MFFIM and less than 3.4% for Sciospec). However, for the MFFIM system at 1033 kHz, the measurement error is less
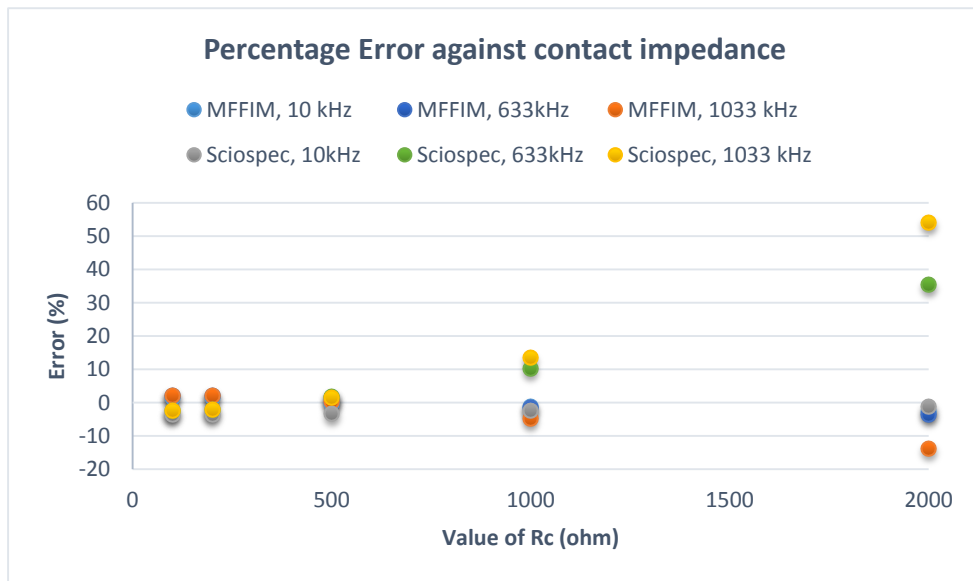
Figure 3-44 Percentage of measurement error for both MFFIM based on digital demodulation and Sciospec device at different contact impedance values.

than 4.8% up to an R_C of 1kΩ, but around 13% for an R_C of 2kΩ . On the other hand, for Sciospec, at 1033 kHz the measurement error is 13% for an R_C of 1kΩ and around 54.2% for an R_C of 2kΩ. It may be noted that in actual situation, the maximum individual contact impedance (R_C) at 1033 kHz will be below 1kΩ. Therefore the measurement using MFFIM will give practically acceptable results but Sciospec ISX-5 may give substantial errors.

3.8.8　FIM Switching test

One of the major purposes of the multi-frequency FIM system was to perform two orthogonal TPIM measurements at each frequency by switching the drive and receive electrode pairs automatically (as described in section 3.5). To test this switching performance, measurements were taken by the developed
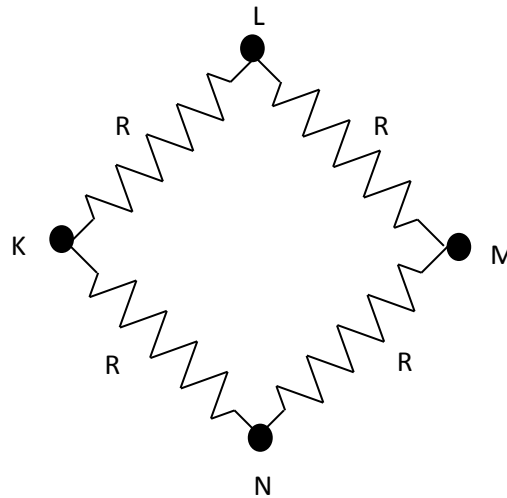
Figure 3-45 Resistive phantom used to test FIM switching

multi-frequency FIM on a resistive phantom shown in Figure 3-45. For one set of FIM measurement (FIM-1) the current drive terminals of MFFIM instrument $i+$ and $i-$ (*BNC-1* and *BNC-2*) were connected to phantom terminals K and L respectively and the potential measuring (receive) terminals of the MFFIM instrument $v+$ and v- (*BNC-5* and *BNC-6*) were connected to the phantom terminals M and N respectively. For an orthogonal test (FIM-2) the current drive points were K and N while the potential measuring points were M and L respectively; the switching between points was
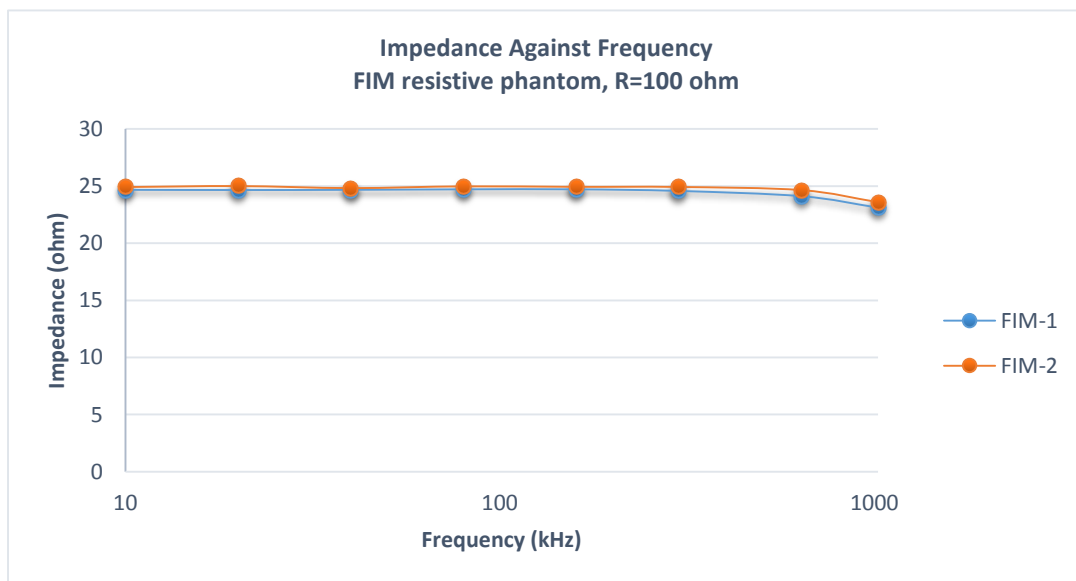
Figure 3-46 FIM measurements using digital demodulation by changing drive and receive electrode pairs on a resistive phantom.

performed by the MFFIM device automatically. Figure 3-46 shows the results of these two orthogonal TPIM measurements for R=100Ω which we call FIM-1 and FIM-2 respectively. All the four resistors were chosen from a lot with 1% tolerance.

The current I applied (1mA) between terminal *K* and *L* will flow through two paths: *K-L* and *K-N-M-L*. Since the values of all the resistors are same (R=100Ω), the current through path *K-N-M-L* will be one fourth of the applied current. Therefore, Therefore, the voltage V across *M-L* would be *25*I (=100*I/4)* and theoretically the expected transfer impedance, *V/I* would give a value of **25Ω**. It can be seen that the measured values follow the theoretical values closely at all frequencies except the highest.

The differences in measured impedance values for two switched FIM measurements $[FIM(2) - FIM(1)]$ are plotted Figure 3-47. The switched values are very close to each other and the maximum difference is 0.53 Ω (for a base measurement value of 25 Ω, giving an error of about 2%). The values of *FIM-2* was higher than that of *FIM-1* at all measurement frequencies. This may attributed to mismatch in the resistor values because of tolerance (resistor tolerance was 1%).
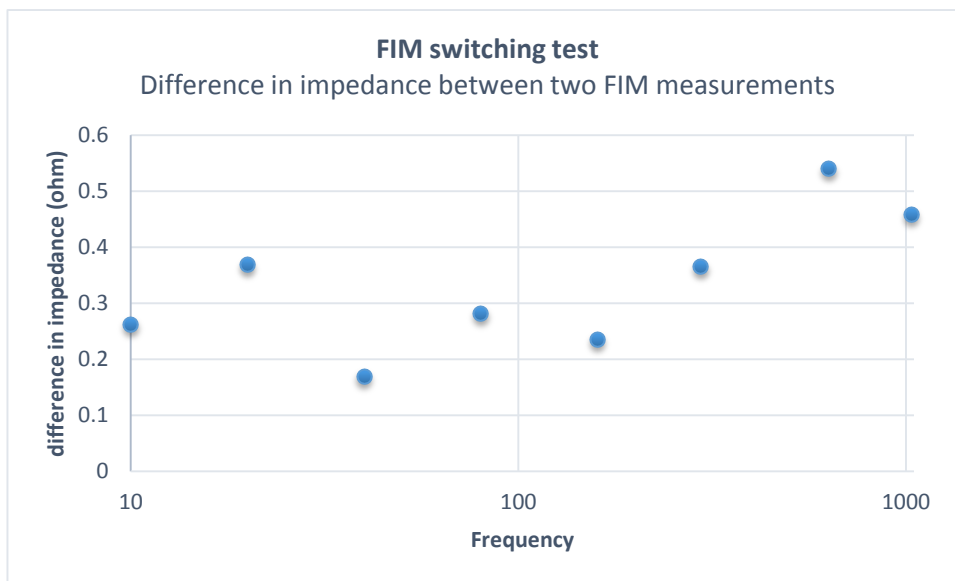
Figure 3-47 Difference in impedance between two FIM measurements for 4-electrode FIM configuration.

3.9　Discussion

A multi-frequency FIM system capable of selecting all three version of FIM electrode configuration in the frequency range *10kHz-1MHz* was developed aimed at potential applications in the diagnosis of lung disorders, breast malignancy or other bioimpedance applications (Figure 3-48). The prototype FIM system developed allows bioimpedance measurements selecting a particular electrode configuration at multiple frequencies under software control from microcontroller and PC.

Figure 3-48 Prototype of the designed multi-frequency FIM system.

The output impedance of the current generator fell from 476 kΩ at 10 kHz to 58.3 kΩ at 1MHz just above the 50kΩ specified (section 3.8.2). However, these values were higher than necessary in practice. Brown et al reported that for Ag/AgCl electrodes contact impedance is <500Ω at 9.6 kHz (Brown et al., 1994). At 1MHz the contact impedance will be very much smaller than that at 10 kHz and therefore the achieved output impedances should be adequate for the FIM measurement on human subjects. With an output impedance of 58.3kΩ at 1MHz, the current source can drive a load impedance of 500Ω with error less than 1%. However, a further improvement in the output impedance of the current generator at the higher frequencies, if required, can be achieved by using higher frequency op-amps and resistors and capacitors with lower tolerance values.

For epithelial tissue measurements inside body orifices and cavities the electrodes will be smaller and closer together (e.g. (Abdul et al., 2006)) and the drive current will need to be reduced to microampere range to prevent local tissue heating due to a high current density. For such applications the analogue circuitry has to be redesigned and evaluated but the switching circuitry can be used as it is.

The common mode rejection ratio (CMRR) of the bioelectric amplifier used to amplify the voltage signal was 63dB and 37dB at 10 kHz and 1024 kHz respectively (Figure 3-27).

However, the common mode noise mostly occurs from main line 50 Hz, so the value of 60dB would be relevant to the measurements. For the voltage measurement circuit based on analogue synchronous peak detection (analogue demodulation), the overall gain of the bioelectric amplifier was set to 48. The output voltage of the bioamp could not be greater than 5V in order to avoid exceeding the input voltage range of the ADC of the microcontroller. On the other hand, if the bioamp output was less than 250mV, then the output of the differentiator at 10 kHz woule be too small to be detected by the voltage comparator. Taking the gain to be approximately 50, the measurable input voltage range for the measurement section was 5mV to 100mV. Therefore, with the excitation current of 1mA the measurable range for transfer impedance range is 5Ω to 100Ω, a dynamic range of 1:20. On the other hand, voltage measurement circuit based on digital demodulation method, the measurable transfer impedance range is 5Ω to 60Ω. Brown et. al. reported that transfer impedance in the thorax region for signal frequencies 9.6 kHz to 614.4 kHz lies between 14Ω to 25Ω (Brown et al., 1994). In another study the impedance associated with alveolar edema was found to be 35% below an initial impedance value of 21Ω (Fein et al., 1979b). According to Al Amin et. al. the transfer impedance in the breast tissue varies from 10Ω to 60Ω in the frequency range 5 kHz to 200 kHz (Al Amin et al., 2014). Therefor the transfer impedance range of the designed multi-frequency FIM system is adequate for impedance measurements in thorax or breast tissues. However, the gain of the voltage measurement circuit could be adjusted to investigate tissues having other impedance ranges. Although not currently implemented, a switched gain with the gain controlled from microcontroller could be implemented. As the switching would be under microprocessor control and the amplifier output was digitized/acquired by the same microprocessor, it would be possible to implement an automatic gain control.

The percentage of measurement error of the prototype multi-frequency FIM was below 5% in the frequency range 10 kHz to 633 kHz for resistive phantoms greater than 10Ω. But for measurements at 1033 kHz and impedance below 10Ω, the error is around 10% which is a limitation. However, for the circuitry based on digital data demodulation, even for capacitive loads, the measurement error is less than 2% except at 1033 kHz where it is around 7% which is practically acceptable (Figure 3-38). It can be noted that the percentage errors for measurements on capacitive phantom using analogue demodulation are higher than those for digital demodulation (Figure 3-36 and Figure 3-38). This may be due to noise originated by the opamps while driving a capacitive load making the peak

detection inaccurate. The measurement accuracy problems at 1MHz was the result of the limited range of electronic devices, particularly the non-availability of high speed and low noise op-amps. The lack of suitable op-amps and passive electronic components with lower tolerance was a considerable challenge in achieving the final design. It should be noted that all multi-frequency impedance measurement systems have used some form of digital demodulation (e.g. (Wilson et al., 2001)) and the use of analogue demodulation was a considerable challenge.

The percentage errors on measured phase values were below 4% for frequencies below 640 kHz whereas the maximum error was 7.8% at 1MHz. The excitation signal is discrete in time and is only known at multiples of 14.4^0. The discrete signal from the *DAC* passes through the V/I converter and into the tissue. This circuitry & the tissue will have RC time constants and these will apply an averaging to the steps producing a smoothed signal. However, the value of the signal between the known 14.4^0 points is dependent on the values *R* and *C* which the signal passes through. Moreover, the amplitude resolution of the Picoscope is 8 bits giving steps in the acquired signals. These stepping may lead to inaccuracy in the phase measurements depending on the values *R* and *C* through which the signal passes and also on the signal amplification by the voltage measurement circuit.

The measurement resolution of the designed multi-frequency FIM system based on analogue synchronous demodulation technique is **0.1Ω** as explained in section 3.4.1.7. For digital demodulation technique, the measurement resolution is **0.2Ω** and **0.078Ω** for the voltage range 5V and 2V respectively (section: 3.4.2.3). According to Brown et. el. respiratory and cardiac related impedance change in the thorax region is around **1.5Ω** and **0.08Ω** respectively (Brown et al., 1994). The resolution of the designed multi-frequency FIM system is therefore adequate for monitoring respiratory related changes, but the not suitable for monitoring cardiac related impedance changes. However, although not implemented in the MFFIM system based on digital demodulation, other model of picoscope with amplitude resolution 10 bits or higher may be useful for monitoring cardiac related changes. Furthermore, the advantage of the system based on digital demodulation is that it can measure phase difference in addition to absolute impedance.

The comparison between the prototype *MFFIM* system and commercially available device *Sciospec ISX-5* showed that the measurement error at frequencies less than ≤633

kHz for the developed *MFFIM* system (total contact impedance $2R_C$ =2kΩ) was below 2.4% which is practically acceptable. But for *Sciospec ISX-5* the error for same measurement set-up was up to 10.3% which does not suitable for applications where the impedance change is less than 10% e.g. respiratory related impedance changes of human thorax. Furthermore, for total contact impedance 4kΩ, the error was even higher, 35% for *Sciospec ISX-5*. On the other hand, it was only 3.5% for the developed *MFFIM* system at frequencies up to 633 kHz (Figure 3-44). It is evident that Sciospec ISX-5 impedance analyzer is not suitable for transfer impedance measurements in situations having total contact impedance higher than 1kΩ ($2R_C$). This device may require use of Ag/AgCl electrodes with low contact impedance (not widely available in Bangladesh) with good skin preparation. However, the designed MFFIM system is capable of measuring impedance even if the total contact impedance is 4kΩ ($2R_C$) up to 633kHz. For the highest frequency, 1033 kHz, at this contact impedance, the results would be less accurate as indicated above.

```
getBlockData: Assigning Analogue data to array and converting to milliVolts.
getBlockData: Data succesfully retrieved.
1033 kHz FIM-2 Data collection complete.
runBlock:- Collecting block of data:
        Timebase: 1
        Pre-trigger samples: 0
        Post-trigger samples: 8192
runBlock: Waiting for device to become ready...
runBlock: Device ready.

getBlockData: Setting up data buffers...
getBlockData: Retrieving data...
getBlockData: Assigning Analogue data to array and converting to milliVolts.
getBlockData: Data succesfully retrieved.
1033 kHz FIM-1 Data collection complete.
Elapsed time is 0.743113 seconds.
Connection to PicoScope 2208A with serial number CO823/086 closed successfully.
Libraries unloaded successfully.
Processing data.....
Plotting data...
Measurement completed successfully
```

Figure 3-49 A representative snapshot of the Matlab command window showing the tame taken for whole measurements.

The frame rate of the impedance measurement system based on analogue synchronous peak detector was determined from the clock speed of the microcontroller and was found to be greater than **45 *fps***. This is above the specified frame rate which allows impedance measurements on the thorax region avoiding dynamic changes due to respiration. On the

other hand, total time taken to measure 16 impedance and 16 phase values at 8 frequencies (one frame) by the developed *MFFIM* system based on digital demodulation technique requires approximately 0.743 seconds (Figure 3-49). So the frame rate is around 1.35fps which is much below the specified frame rate. This frame rate may be just enough to avoid dynamic changes of thorax due to respiration considering respiration rate up to 20 per minutes. The time required by Matlab for data acquisition and processing may be a major reason for low frame rate because it runs off an interpreter, uses an attributed grammar and only uses 1 core of a multi-core processor. However, the frame rate can be improved using a high speed data acquisition system and a PC with faster processing speed or by reducing the number of measurement frequencies. Currently 8192 sample values are acquired at each measurement frequency; reduction of sample values could also improve the frame rate. Broadband signal can be used for excitation for faster bioimpedance measurements as reported by Min et al. (Min et al., 2007b, Min et al., 2008).

The multi-frequency FIM system has been developed with the aim of assessing the utility of FIM in diagnosing lung diseases, breast tumour and measuring abdominal fat thickness in low resource countries. Pneumonia, TB, edema are common lungs diseases in developing countries, especially amongst children. So a small, low cost, non-invasive system has the potential to benefit a large number of people, particularly those living in the rural areas where modern healthcare facilities are not available. Therefore, the performance and safety standards of the measurement device described in this chapter is adequate to undertake field trials in the areas of lung disorders, abdominal fat thickness and breast cancer studies.

Chapter 4   Medical Applications of FIM

4.1 Introduction

The single frequency FIM has been applied successfully in the study of gastric emptying (Rabbani et al., 1999), lung ventilation (Kadir et al., 2009, Kadir et al., 2015) and abdominal fat thickness (Surovy et al., 2012). These results encouraged us to investigate the use of multi-frequency FIM in the study of lung fluid and breast tumour characterization which are described in this chapter. This chapter is divided into three parts. In the first part (sections 4.2, 4.3 and 4.4), three dimensional sensitivity distribution of different bioimpedance measurements techniques are analyzed and compared using finite element method (FEM). Effect of various factors including electrode configuration, electrode separation, inhomogeneity and volume conductor boundary on 3D sensitivity distribution were investigated. This part also explains an experimental study to validate the 3D sensitivity distribution obtained using FEM simulations. The second part (section 4.5) of this chapter describes an FEM model of human thorax. A simulation study to detect localized lung ventilation disorder (fluid accumulation in lung) using FIM is described. Finally, an experimental study for the classification of breast tumour (benign or malignant) using multi-frequency FIM measurements is described in the third part (section 4.6).

Part: 1

4.2 Three dimensional sensitivity distributions of impedance measurements: FEM analysis

The extent to which a change in conductivity of a point within a volume conductor contributes to the measured transfer impedance is defined as the sensitivity (section 2.2.3). In TPIM arrangement, if $\mathbf{J}_1$ and $\mathbf{J}_2$ are the current density vectors at a point within the volume conductor due to injection of current I through the exciting and sensing electrode pairs respectively, then the sensitivity of the point can be defined as (Geselowitz, 1971, Grimnes and Martinsen, 2008),

$$S = \frac{\mathbf{J}_1 \cdot \mathbf{J}_2}{I^2} \qquad 4\text{-}1$$

The spatial sensitivity distribution is different for different impedance measurement techniques. Again, for a particular measurement method, the sensitivity distribution is different for different electrode separations. 3D sensitivity distributions of bioimpedance measurement methods could give an idea about which portion of the volume conductor can be sensed using surface electrodes and may be helpful in choosing appropriate electrode configuration to suit a particular application. For example, for measurements of skin impedance it is useful if the most sensitive region is just below the electrode plane. On the other hand, for measurement of impedance changes of lung due to breathing, it is desirable to have significant sensitivity deep below the electrode plane. For a semi-infinite homogeneous medium, sensitivity distributions of TPIM and FIM configurations have been investigated analytically using vector lead fields by determining the vector paths from the electrode (point electrode) to the point where the sensitivity is to be determined (Brown et al., 2000a, Islam et al., 2010). But in practice, the volume conductor (human body) is finite and inhomogeneous. Moreover, the electrodes are not point sources but of finite size.

To address these issues, 3D sensitivity distributions of different bioimpedance measurement techniques were obtained using Finite Element Method (FEM) considering finite volume conductor and electrodes with finite dimensions. Finite element based simulation software COMSOL Multiphysics® (version: 4.3a) was used to calculate the sensitivity values. The effect on the 3D sensitivity distribution because of the following factors were studied.

90

i.   Variation of *drive/receive electrode separation*

ii.   Variation of the *electrode dimension*

iii.   Variation of *boundary* conditions and *inhomogeneity* of conductivity

3D sensitivity distribution for different FIM electrode configurations was also obtained experimentally to validate the FEM results.
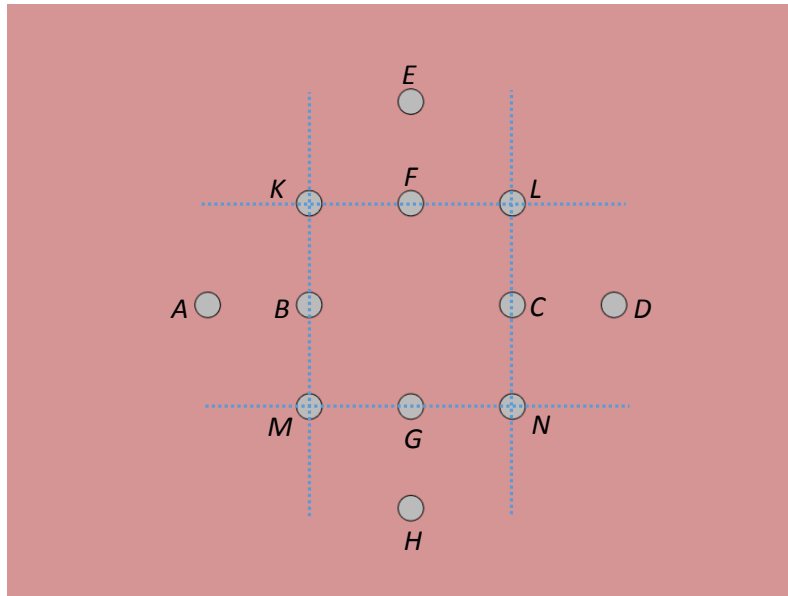
Measurement Method	Measurement 1 (Z_1)	Measurement 2 (Z_2)	Sensitivity
Tetra-polar (Linear)	Drive: A,D Receive: B,C	N/A	$S = \dfrac{J_{AD} \cdot J_{BC}}{I^2}$
Tetra-polar (Square)	Drive: K,L Receive: M,N	N/A	$S = \dfrac{J_{KL} \cdot J_{MN}}{I^2}$
FIM-8	Drive: A,D Receive: B,C	Drive: E,H Receive: F,G	$S = \dfrac{J_{AD} \cdot J_{BC} + J_{EH} \cdot J_{FG}}{I^2}$
FIM-6	Drive: A,D Receive: K, N	Drive: E,H Receive: K,N	$S = \dfrac{J_{AD} \cdot J_{KN} + J_{EH} \cdot J_{KN}}{I^2}$
FIM-4	Drive: K,L Receive: M,N	Drive: K,M Receive: L,N	$S = \dfrac{J_{KL} \cdot J_{MN} + J_{KM} \cdot J_{LN}}{I^2}$

Figure 4-1 Position of drive and receive electrodes for various bioimpedance measurement techniques with corresponding expressions of sensitivity

4.2.1   Electrode configurations

Electrode configurations for various electrical bioimpedance measurement techniques were discussed in detail in chapter 2. Figure 4-1 summarizes the position of *drive* and *receive* electrode pairs for measurement of electrical transfer impedance on a volume

conductor for five different impedance measurement techniques studied in the present work. For tetra-polar (linear and square) methods, only one measurement is required is required to determine the transfer impedance. For the FIM technique, two measurements are summed to obtain the Focused transfer impedance (FZ). The equations for calculating the sensitivity for different measurements methods, obtained by applying the reciprocity theorem, are given in the right most column. Here $\mathbf{J}_{ij}$ is the current density at the measurement point within the volume conductor due to current I applied through surface electrodes i and j. The square region bounded by the *receive* electrodes (dotted square KLMN in blue) beneath the electrode plane is defined as the *Focused Zone* for FIM measurements.

4.2.2 The FEM model for sensitivity study

A cubic tank of side 60 cm was modeled as a volume conductor. Cylindrical electrodes of radius 0.5cm and thickness 0.2cm where placed on a surface (xy plane) centrally on the volume conductor as shown in Figure 4-2. The circular areas of the cylinders are in contact with the volume conductor. Electrical conductivity (σ) and relative permittivity (ε_r) of the volume conductor was assigned as 1.5 S/m and 98.919 respectively to simulate body fluid (Andreuccetti D, 1997). Similarly
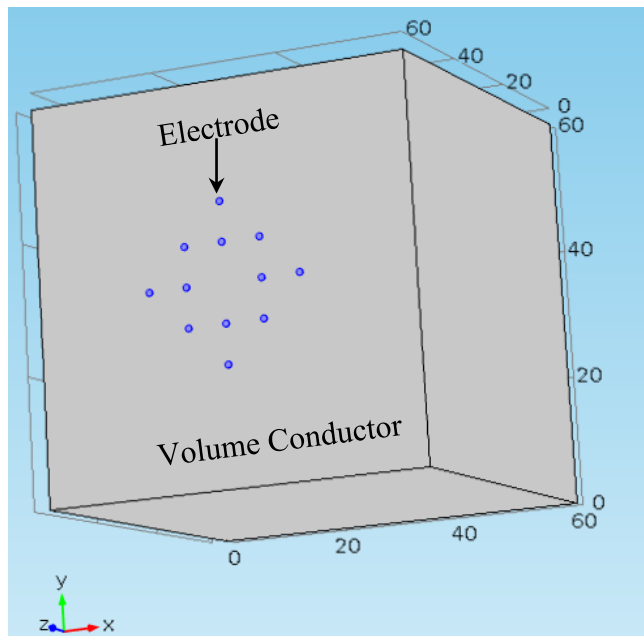
Figure 4-2 3D FEM model used to calculate the sensitivity distribution. A solid cubic tank of edge 60cm was modeled as volume conductor. Electrodes were placed on a surface of the volume conductor.

electrical properties of steel (σ = 4.032e6 S/m, ε_r=1) were used for the electrodes to represent practical impedance measurement arrangements.

4.2.3 Calculation of sensitivity

Current of unit amplitude (1A) was introduced to the corresponding electrode pair for a particular measurement technique (Figure 4-1) using the *electric current (ec)* interface in the *frequency domain* of *AC/DC* module in Comsol Multiphysics-4.3a. *Terminal* and *Ground* peripherals of *ec* interface were used to inject current through a pair of electrodes.

For an electrode pair with current interface *ec*, the *x*, *y* and *z* components of current density vectors can be expressed as *ec.Jx, ec.Jy* and *ec.Jz* respectively (Multiphysics, 2007, Pettersen and Høgetveit, 2011). Similarly for another electrode pair with current interface *ec1*, the corresponding components of current density vectors can be expressed as *ec1.Jx, ec1.Jy* and *ec1.Jz* respectively. Mathematical expressions for calculations of point sensitivities within the volume conductor using Comsol Multiphysics simulations for 5 different electrode configurations under investigation are summarized in Table 4-1.

The governing equations for the FEM computations are,

$$\nabla . J = Q_j \qquad\qquad 4\text{-}2$$

$$J = (\sigma + j\omega\varepsilon_0\varepsilon_r)E + J_e \qquad 4\text{-}3$$

$$E = -\nabla V \qquad\qquad 4\text{-}4$$

Table 4-1 *Electric current interfaces and corresponding expressions for calculation of sensitivity in Comsol Multiphysics*

Measurement Method	Electrode pair	*ec* interface	Expression for Sensitivity in COMSOL Multiphysics
Tetra-polar (Linear)	(A,D)	*ec*	((ec.Jx*ec2.Jx+ec.Jy*ec2.Jy+ec.Jz*ec2.Jz))/((1 [A])^2)
	(B,C)	*ec1*	
Tetra-polar (Square)	(K,L)	*ec*	
	(M,N)	*ec1*	
FIM-8	(A,D)	*ec*	((ec.Jx*ec2.Jx+ec.Jy*ec2.Jy+ec.Jz*ec2.Jz) +(ec3.Jx*ec4.Jx+ec3.Jy*ec4.Jy+ec3.Jz*ec4.Jz))/((1[A])^2)
	(B,C)	*ec1*	
	(E,H)	*ec2*	
	(F,G)	*ec3*	
FIM-6	(A,D)	*ec*	
	(K,N)	*ec1*	
	(E,H)	*ec2*	
	(K,N)	*ec3*	
FIM-4	(K,L)	*ec*	
	(M,N)	*ec1*	
	(K,M)	*ec2*	
	(L,N)	*ec3*	

where, J, Q_j, σ, ω, ε_0 , ε_r , E and V are the current density, current source, electrical conductivity, frequency, permittivity in free space and relative permittivity of the material, electric field and electric potential respectively. J_e is the external source current density (there is none in our model).

Boundary condition for the model is

$$n.J = 0 \qquad\qquad 4\text{-}5$$

The meshing tool in Comsol Multiphysics was used to generate 3D mesh grid in the geometric model. For better accuracy, Physics controlled *finer* mesh was used for computation of sensitivity values. Figure 4-3 shows the mesh representation of a model with FIM-4 configuration and the corresponding mesh statistics. Sensitivity values within 3D mesh grid was computed in steps of 1mm using equations summarized in Table 4-1. 3D sensitivity profiles were then plotted to show the spatial sensitivity distributions.

Statistics

Complete mesh

Element type: All elements

Tetrahedral elements: 111022
Triangular elements: 6378
Edge elements: 360
Vertex elements: 40

Domain element statistics

Number of elements: 111022
Minimum element quality: 0.1087
Average element quality: 0.7609
Element volume ratio: 1.964E-5
Mesh volume: 216000.0 cm^3
Maximum growth rate: 3.329
Average growth rate: 1.642
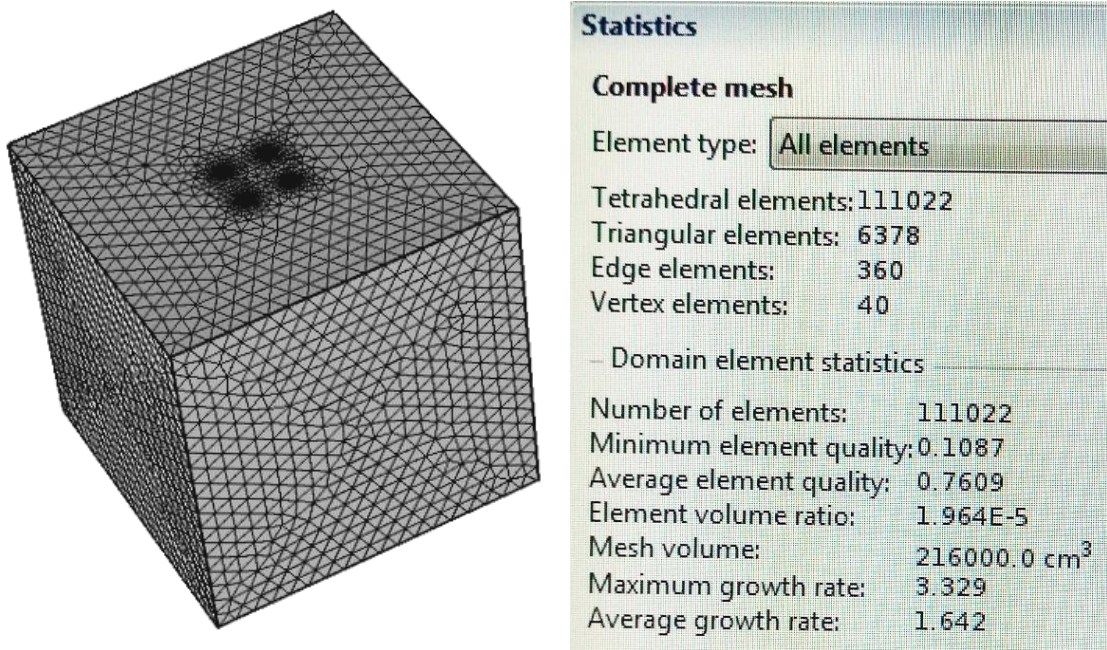
Figure 4-3 Mesh representation of a model with FIM-4 configuration (left) and corresponding mesh statistics (right).

4.2.4 Depth Sensitivity

Electrical Impedance techniques provide an opportunity for impedance measurement down to reasonable depths within the body using surface electrodes. Depth sensitivity could give an idea how deep into the volume conductor regions if changed impedance can be sensed using surface electrodes. The perpendicular distance from the electrode plane to the point of calculation within the volume conductor is defined as *depth* (*d*) as shown in Figure 4-4. Sensitivity values over a plane parallel to the electrode plane were calculated in steps of 1mm within the volume conductor, so there were 360000 values in each plane. Positive, negative and average sensitivity over planes parallel to the electrode plane were calculated to study depth sensitivity. The average sensitivities over planes were then plotted against depth from the electrode plane.
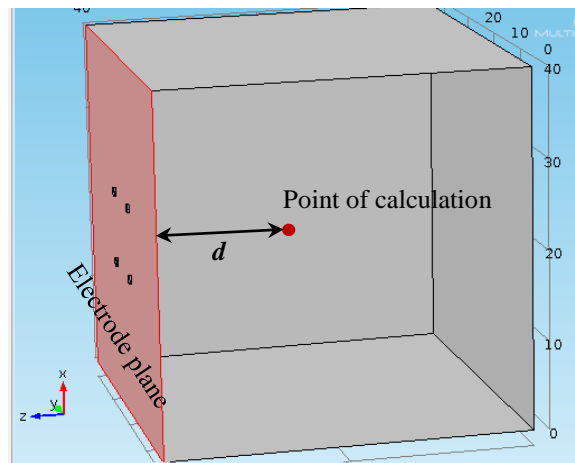
Figure 4-4 Point of calculation is at depth d from the electrode plane.

4.2.5 Study of the effect of electrode separation

The sensitivity profiles are different for different impedance measurement techniques. Again, for a particular electrode configuration, the sensitivity profiles depend on *drive* and *receive* electrode separations. The effect of electrode separation was studied by obtaining the sensitivity profiles for all measurement technique with different electrode separations. For *TPIM_Square* and *FIM-8* configurations, the separation between two *drive* electrodes (A-D or E-H) was denoted as *ESD (electrode separation- drive)* and the separation between the corresponding *receive* electrodes (B-C or F-G) were denoted as *ESR (electrode separation- receive)* as shown in Figure 4-5. The region below the area bounded by the square *KLNM* is defined as the *focused zone*. For FIM-6 configuration, the electrode pair *K-N* is used as receive electrodes for both orthogonal measurements. In

this case, the distance *KL* (or *KM*) was considered as *ESR* in order to keep the *focused zone* the same for all measurement methods. However, it should be noted that the actual separation between the receive electrodes in FIM-6 configuration is the distance *KN*. For TPIM_Linear, FIM-6 and FIM-8 methods, the sensitivity distribution was obtained by changing ESR while ESD was also changed proportionately. In other words, the ratio of *drive* to *receive* electrode pairs ($ES_{\_ratio} = \frac{ESD}{ESR}$) was kept constant=2 and the sensitivity distributions were calculated for changing electrode separations (i.e. *ESR* and *ESD*). Again, sensitivity profiles were obtained for varying *ESD* keeping *ESR* constant i.e. for various *ES_ratio* the sensitivity profiles were obtained keeping *ESR* constant. For TPIM_Square and FIM-4 methods, the *drive* (K-L) and *receive* (M-N) electrode separations are always equal. Therefore, $ES_{\_ratio}$ for TPIM_Square and FIM-4 techniques were unity.

4.2.6 Study of localization ability

To obtain localized information from a tissue/organ within the body using electrical impedance techniques it is desirable that the maximum contribution to the measured impedance come from that tissue/organ and the contributions from the neighbouring
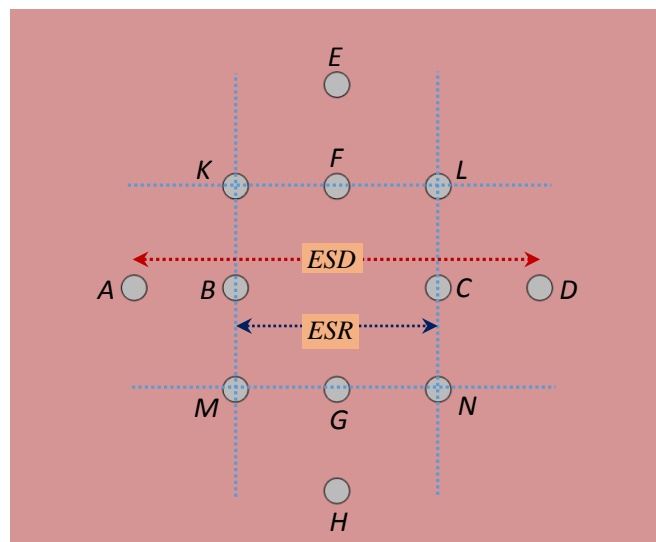
Figure 4-5 Separation between receive electrodes was denoted as ESR and that between corresponding drive electrodes was denoted as ESD. For TPIM_Square and FIM-4, ESR and ESD are equal.

regions are as low as possible. By admittance analysis it was shown that FIM electrode configurations have enhanced sensitivity beneath the area bounded by the *receive electrodes* which may provide more localized information (Rabbani et al., 1999). To study the localization ability quantitatively, the square region under the *receive* electrode

was defined as the *focused zone* (area bounded by KLMN in Figure 4-5). In the present work, a parameter named *degree of localization (dol)* was introduced as defined below for a plane parallel to the electrode plane at a certain depth:

$$dol = \frac{sum\ of\ sensitivities\ of\ the\ focused\ zone\ over\ a\ plane}{sum\ of\ absolute\ sensitivities\ of\ the\ whole\ region\ over\ a\ plane} \times 100\% \qquad \text{4-6}$$

If the sum of sensitivities within the *focused zone* is zero, then *dol* is 0% which signifies that there is no contribution from the *focused zone* of the volume conductor to the measured transfer impedance. On the other hand, if the sum of the sensitivities within the focused region equals the sum of absolute sensitivities over the whole volume conductor, then *dol* is 100% which signifies that all the contribution to the measured impedance is from the *focused zone*. Since the aim is to get the maximum contribution from the *focused zone* and minimum contribution from outside, higher *dol* indicates higher localization ability. It is obvious that *dol* will vary with the depth of the individual plane.

4.2.7   Study of the effect of electrode size

In practice, to measure electrical impedance from biological tissue one must use electrodes which have finite dimensions. Any variation on the size of electrodes (electrode-tissue contact area) may affect the sensitivity distribution. The effect of electrode size on the sensitivity distribution within the volume conductor was studied using cylindrical electrodes (circular areas are in contact with the volume conductor) of varying diameter. It was observed that the FIM-4 configuration has more depth penetration ability as well as higher degree of localization compared to other methods which will be illustrated in the sections 4.3.2 and 4.3.5. Therefore, the effect of electrode diameter was studied for FIM-4 configuration only. The distance between the centers of *drive* and *receive* electrodes were kept constant and edge-to-edge distance between the electrodes were changed (the diameter of the electrodes were changed) to investigate any effect on the sensitivity distribution.

4.2.8 Study of the effect of inhomogeneity

In the previous sections, the sensitivity distribution for homogeneous volume conductor was studied. However, real life applications involve inhomogeneous volume conductors, e.g human body. To understand how the sensitivity distribution changes due to the presence of an inhomogeneity within the volume conductor, two types of inhomogeneity were simulated: a *cylinder* of small finite dimension and a *sheet* covering the whole cross section in a plane parallel to the electrode plane as shown in Figure 4-6. The inhomogeneity in the form of a *sheet* was chosen to understand the effect of tissue layers in the body (e.g. fat layer). There was no specific reason of choosing a *cylindrical* inhomogeneity. However, the main objective was to observe sensitivity changes because of a small isolated region of changed tissue conductivity (e.g. a tumour) within the human body. The effect of both more conducting ($\sigma = 3\ S/m$, twice of the conductivity of background) and less conducting ($\sigma = 0.75\ S/m$, half of the conductivity of background) inhomogeneities compared to the background volume conductor (($\sigma = 1.5\ S/m$)) were studied.
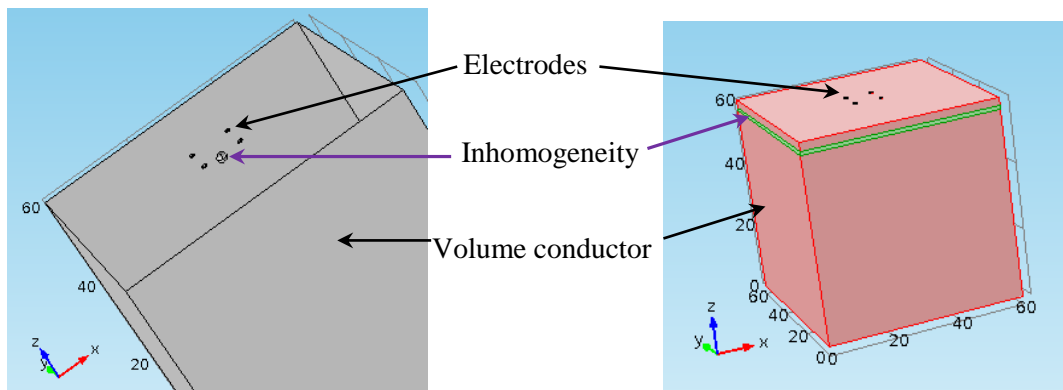
Figure 4-6 Cylinder of different conductivity embedded within the volume conductor to simulate inhomogeneity (left). A thick sheet of different conductivity embedded within the volume conductor to simulate inhomogeneity (Right). Electrodes for FIM-4 configuration are shown on the top surface with drive-receive separation of 8cm.

The *cylinder* having radius $1 cm$ and length $1 cm$ was placed at the center of the electrode configuration, with the center of the cylinder at a depth 3 cm from the electrode plane. The sensitivity distributions were obtained with the presence of the cylinder which was then compared with the sensitivity distributions obtained without the cylinder, only with the homogeneous volume conductor. Similar simulations were performed by placing the *cylinder* just below the drive-receive electrode pair at variable depths. Sensitivity distributions were also obtained with a *sheet* of variable thickness having length and breadth same as the volume conductor placed at depth 3 cm from the electrode plane.

4.2.9 Study of the effect of conductor boundary proximity to electrode position in sensitivity distribution

Practical applications of bioelectrical impedance measurements involve volume conductors of different size and shape. For example, investigation of lung placing electrodes on chest surface and investigation of cervical tissue placing electrodes on cervix will involve volume conductors of different shape and size. So far the sensitivity distributions were obtained using a cubic volume conductor of edge length 60 cm placing
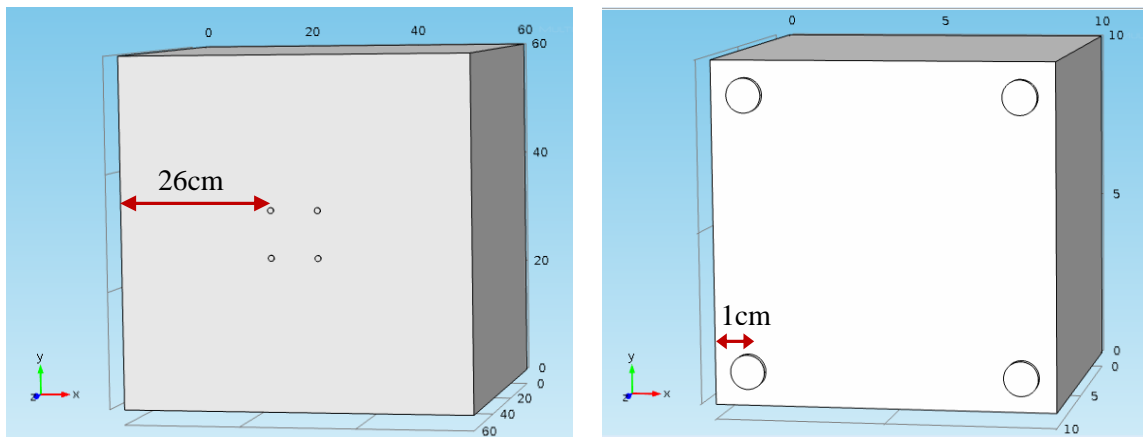
Figure 4-7 Edge length of the cubic tank was changed keeping the electrode separation constant (8cm) to study the effect of bounday in the medium on sensitivity distribution. Left: edge length 60 cm, Right: edge length 10 cm.

electrodes at the center. To study the effect of boundary in the medium on sensitivity distribution, electrodes for FIM-4 configuration was placed on a surface of the volume conductor. The edge length of the cubic volume conductor was reduced keeping the electrode separation constant (*ESR*=8cm); this effectively decreased the distance between the boundary and electrodes. Initially the length of an edge of the cube was 60 cm; shortest distance of boundary from centre of any electrode was 26cm (Figure 4-7). The edge length of the cube was then decreased in steps to 10 cm (shortest distance of boundary from center of any electrode was 1cm) to see effect of boundary on sensitivity distribution, if any.

4.2.10 Experimental validation

An experiment was designed to understand if Comsol Multiphysics can simulate 3D sensitivity distributions (in other words, transfer impedance measurements) accurately. To validate the sensitivity distribution experimentally, measurements were performed on
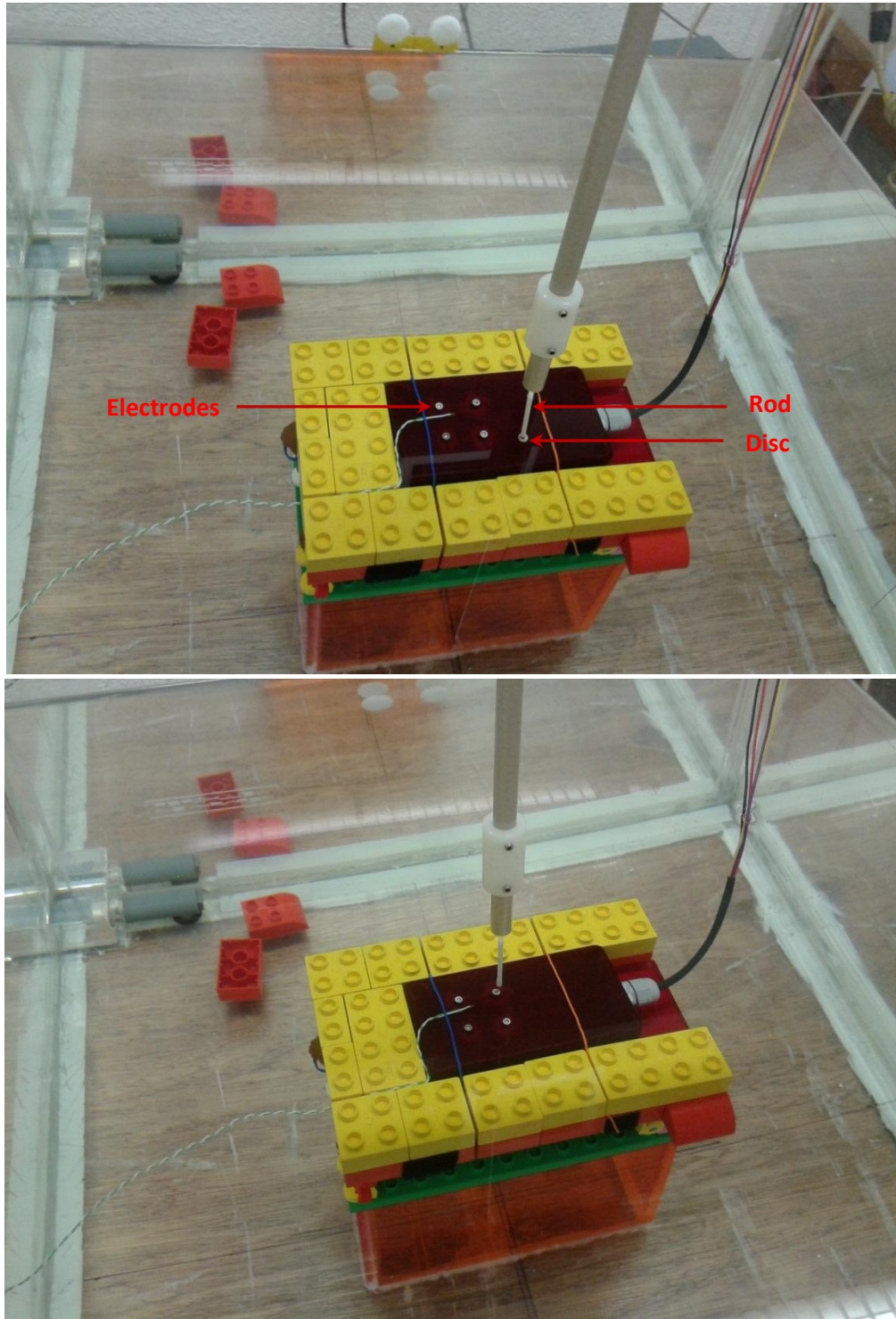
Figure 4-8 Set-up for measument of the 3D sensitivity profiles experimentally. Electrodes were mounted on a waterproof plastic box placed on a platform at the bottom of a tank filled with saline. A disc supported by a rod was moved using motors (top). Only the supporting rod without the disc moved over the same points (bottom).

a cubic tank of edge length 60cm. Electrodes of FIM-4 were mounted on the surface of a waterproof rectangular plastic box as shown in Figure 4-8. The diameter of each electrode was 2.5mm and the separation between two neighboring electrodes was 20 mm. The electrode material was chosen as stainless steel to keep it similar to that of the FEM simulations. The rectangular box was attached to a platform mounted on the bottom of the tank so that the electrodes face upwards. The tank was then filled with saline (conductivity=1.003mS/cm) so that the depth of saline above the electrode plane is 60 mm. In the FEM simulations, sensitivities at points (nodes) on a 3D grid were calculated to obtain the sensitivity distribution. But experimental measurement of point sensitivity is difficult. To address this issue, a plastic disc of diameter $5\ mm$ and height $1\ mm$ supported by a plastic rod of diameter $3\ mm$ and length $60\ mm$ was introduced in the saline at a certain depth from the electrode plane. An alternating current of amplitude 10mA at 16 kHz was injected into the volume conductor through two adjacent electrodes from a differential current source similar to the one shown in *Figure 4-3*. The resulting potential difference across two other electrodes were amplified using a differential amplifier and the true RMS values of the ac voltages were measured using an ac voltmeter *(Keithley 177 Microvolt DMM)*. Since the applied current amplitude is constant, the measured voltage is proportional to the transfer impedance. The disc attached with the supporting rod was moved in a plane parallel to the electrode plane in steps of 2.5mm. The measurement process was automated and the movements of the rod-disc arrangement was controlled by a Matlab algorithm. The algorithm also captured the voltage measurements from the *Keithley 177* through an *IEEE 488* interface. Similar measurements were performed with the supporting rod only (no disc). For experimental purpose, the sensitivity of a point within the volume conductor (tank) was defined as below:

Sensitivity = (Measured voltage with the rod and disc –Measured voltage with the rod) --- 4-7

The measurements were repeated at others depths from the electrode plane to obtain 3D sensitivity profiles.

The experiment explained above was then modeled exactly in Comsol Multiphysics as shown in Figure 4-9. A plastic disc (conductivity= $10^{-14} S/m$ and relative permittivity=1) attached with a rod of same geometrical dimension (as in the experiment) was moved in steps of 2.5 mm on a plane parallel to the electrode plane. Alternating

current of same amplitude and frequency was introduced to the *drive* electrodes using electric current interface of AC/DC module.
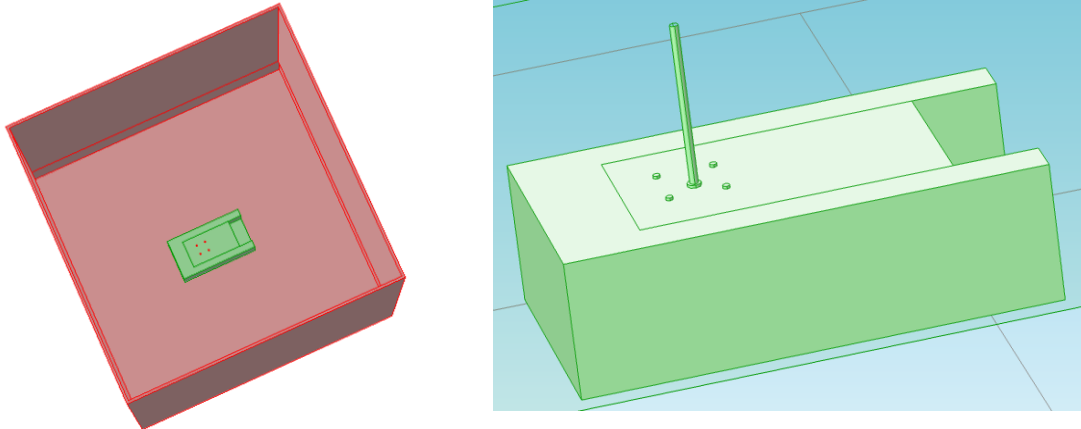
Figure 4-9 Comsol model identical to the experimental set-up for validation of sensitivity profile; Volume conductor with electrodes on the bottom (left), Electrodes facing upwards supported by a waterproof plastic box and the disc with supporting rod (right).

The resulting potential difference was calculated considering the *receive* electrodes as boundary probes. Similar computations were performed with only the rod (no disc) and 3D sensitivity distribution was then obtained using equation 3.7.

4.3 Results

4.3.1 3D sensitivity distribution

As previously (section 4.2.4), sensitivity values over a planes parallel to the electrode plane were calculated in steps of 1mm within the volume conductor, so there were 600×600 values in each plane. Figure 4-10 shows the sensitivity profiles of different impedance measurement techniques at a depth of 1cm from the electrode plane. The sensitivity matrix was exported to Matlab software and then plotted (surface plot) to show the sensitivity in the vertical axis; only the central portion around the electrode array is shown for enhanced visibility. For TPIM_Linear, FIM-6 and FIM-8 techniques, the *receive* and *drive* electrode separations were 8 cm and 16 cm respectively i.e. *ES_ratio* was 2. For TPIM_Square and *FIM-4* the both *drive* and *receive* electrode separations were 8cm i.e. *ES_ratio* was 1. For all methods the central *focused zone* was same.
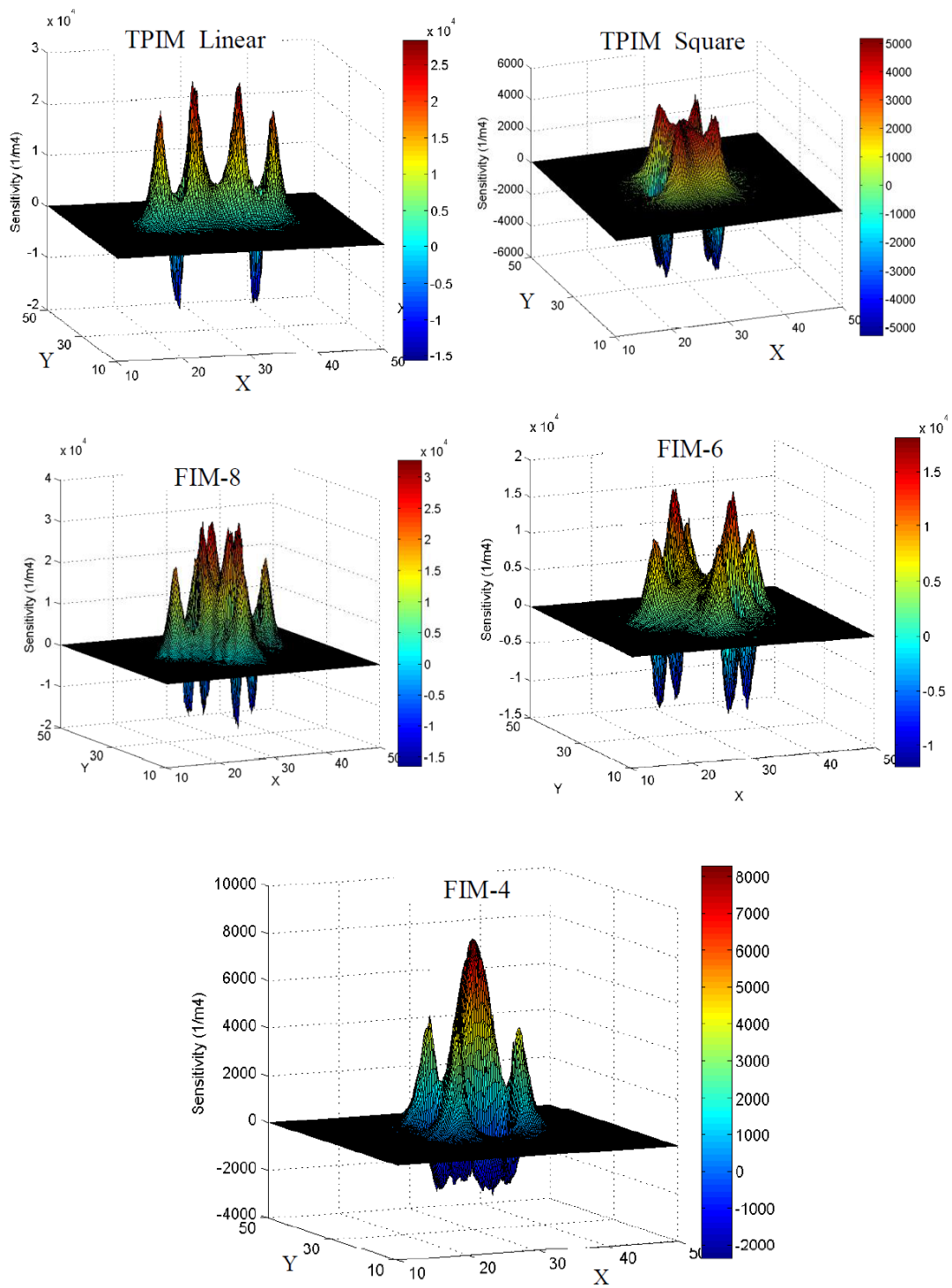
Figure 4-10 Sensitivity profiles obtained by Comsol simulations for different impedance measurement methods at depth 1 cm from the electrode plane with receive and drive electrode separation of 8 cm and 16 cm respectively. X and Y axes indicates the position on xy plane in cm where (30,30) is the center of electrode configurations for all methods. The central (8×8) cm² around the point (30,30) is the focused zone. The simulation was performed on a tank of edge length 60 cm; only the central portions around the electrode array are shown for enhanced visibility. The unit of sensitivity shown in the vertical axis is 1/m⁴ and the unit of position along X and Y axes is cm.
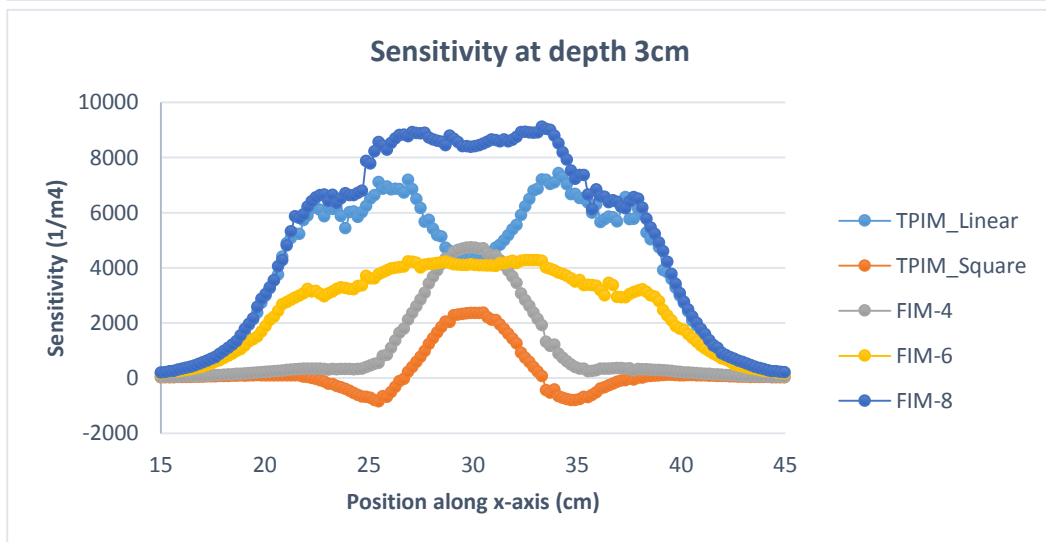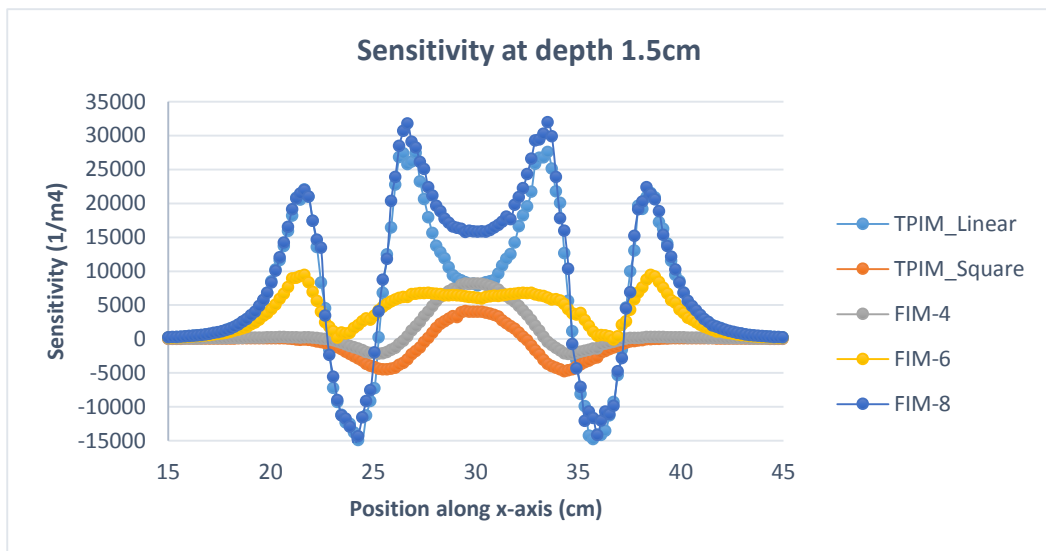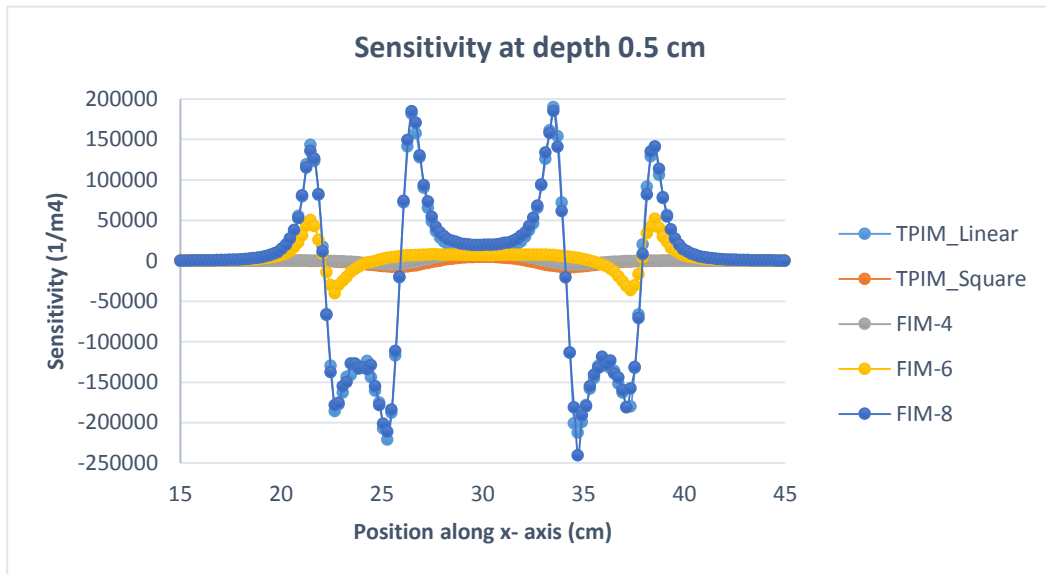
Figure 4-11 Sensitivity profiles along x-axis passing through the center of the electrode configuration at depths 0.5cm (top), 1.5cm (middle) and 3cm (bottom) for different impedance measurement techniques. The receive and drive electrode separation was 8cm and 16cm respectively, for TPIM_Square and FIM-4 both drive and receive electrode separation was 8cm. The length 26cm to 34cm is within the focused zone.

104

There are positive sensitive regions as well as negative sensitive regions. It can be observed that negative sensitivity regions lie between the drive-receive electrode pairs. An increase in the impedivity (specific impedance, like resistivity) in the positive sensitive region will increase the transfer impedance while a decrease in the impedivity in the positive sensitive region will decrease the transfer impedance. On the other hand, an increase in the impedivity in the negative sensitive region will decrease the transfer impedance while a decrease in the impedivity in the negative sensitive region will increase the transfer impedance.

The sensitivities at different depths along x-axis passing through the center of the electrode array are plotted in Figure 4-11. The spatial distribution of sensitivity is different for different electrode configurations. At the center of the electrode array, the sensitivity values for FIM-8 and FIM-4 configurations are twice that for TPIM_Linear and TPIM_Square respectively which is expected as FIM essentially is the sum of two TPIM measurements. It can be observed that in the TPIM_Linear, FIM-8 and FIM-6 configurations the amplitude of sensitivity values (both positive and negative) are much higher compared to that of TPIM_Square and FIM-4 techniques; particularly at lower depths. But, significant higher sensitive regions lies well outside the central *focused zone* for TPIM_Linear, FIM-8 and FIM-6 configurations. For TPIM_Square and FIM-8 significant positive sensitive region lies within the focused zone. Negative sensitivity decreases with depth for all measurement techniques. It can be noted that negative sensitivity is much lower relative to positive sensitivity for FIM-4 configuration compared to TPIM_Square configurations. For example, at depth of 3cm, there is no negative sensitive region for FIM-4 configuration although TPIM_Square configuration contains negative sensitive regions (Figure 4-11, bottom). This is because positive and negative sensitivities from the two TPIM measurements were summed to obtain the FIM sensitivity values. The depth sensitivity is investigated further in details in the next section.

4.3.2   Depth Sensitivity

Depth Sensitivity predicts how deep within the body regions of changed impedance can be detected. In Figure 4-12a the summed values of positive sensitivities over planes parallel to the electrode plane were plotted against depth for different measurement methods (the points with negative sensitivities were left out of the calculation). Similarly, the summed values of negative sensitivities over planes parallel to the electrode plane

was plotted against depth in Figure 4-12b (the points with positive sensitivities were left out of the calculation). At shallow depths both positive and negative sensitivity values are relatively higher for FIM-8 configuration which decreases with depth. The sensitivity values are relatively much lower for TPIM_Square and FIM-4 configurations. There are
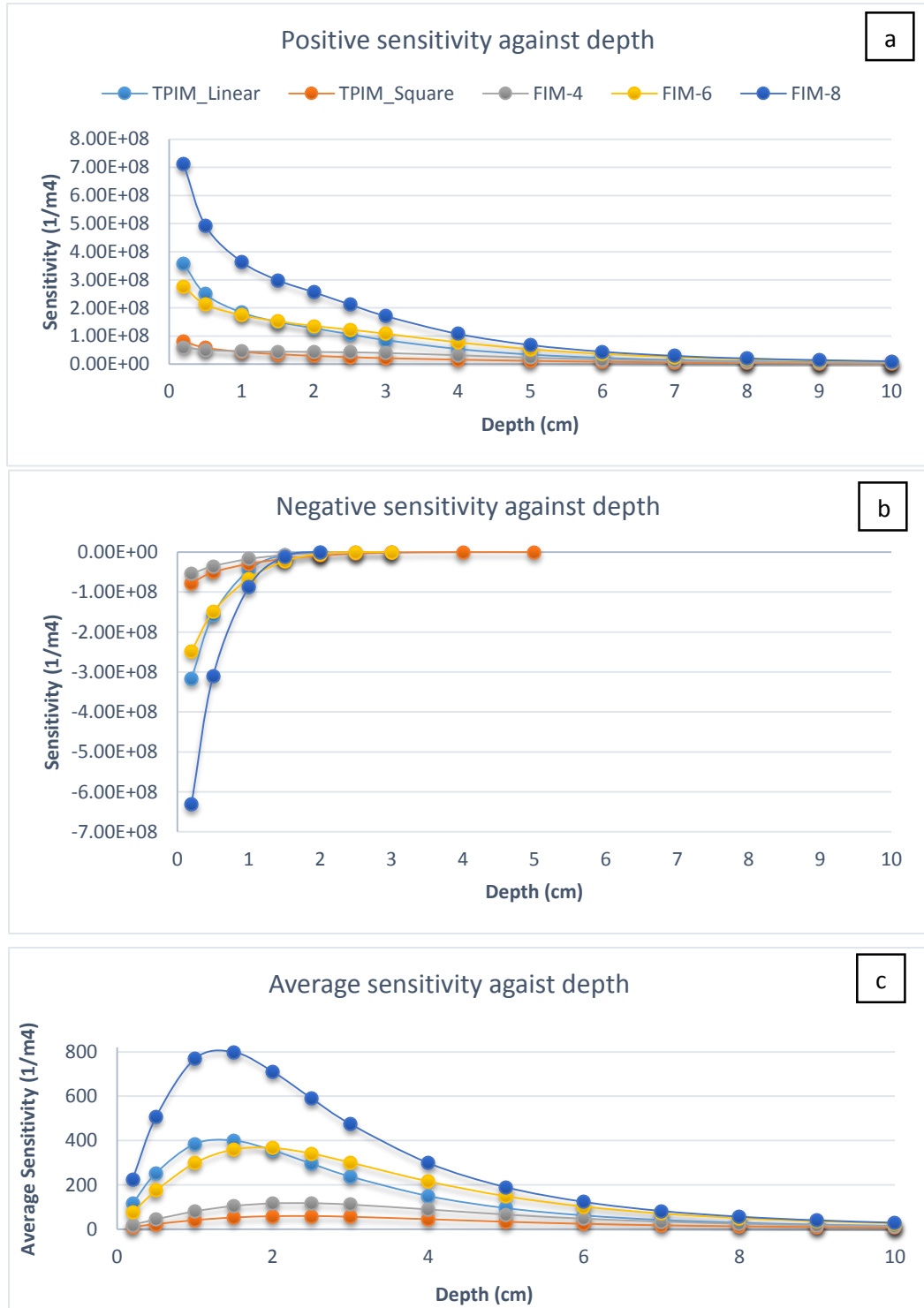
Figure 4-12 Total positive sensitivity (a), negative sensitivity (b) and average sensitivity (c) over planes parallel to the electrode plane against depth. Receive and drive electrode separations are 8cm and 16 cm respectively (ESR=8cm, ESD=16cm).

negative sensitivities at shallow depths for all electrode configurations but these diminish within a short increase in depth depth (in these examples beyond 1cm depth). It should be noted that effective sensitivity is the sum of positive and negative sensitivities over
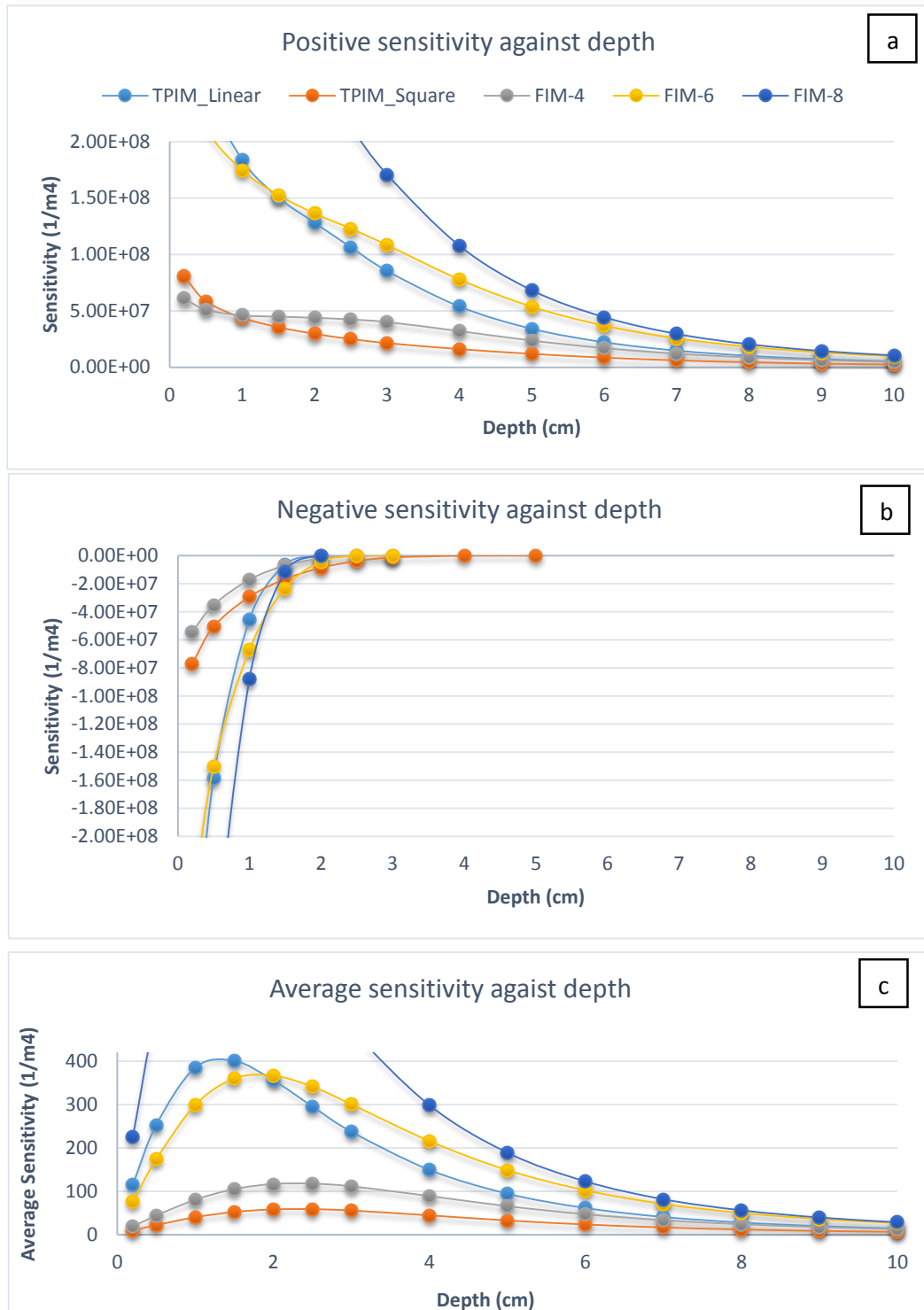
Figure 4-13 Total positive sensitivity (top, a), negative sensitivity (middle, b) and average sensitivity (bottom, c) over planes parallel to the electrode plane against depth as in Fig 4-12 but with expanded vertical scale. It reveals the sensitivities of TPIM-Square and FIM4 better. (ESR=8cm, ESD=16cm)

the whole volume conductor. The average sensitivity over planes parallel to the electrode array are plotted in Figure 4-12c. It can be observed that average sensitivity is very low close to the electrode plane. However, average sensitivity increases rapidly with depth, reaches a peak and then falls again gradually. The dependence of average sensitivity with depth agrees with that calculated analytically (Brown et al., 2000a, Islam et al., 2010). It is clear from the plots that the low value of average sensitivity at small depths is due to almost equal values of positive and negative sensitivity values for both TPIM and FIM. Again, the sensitivity of FIM8 is just the double of that of TPIM_Linear which is reasonable. Sensitivity of FIM6 appears to be lower than TPIM_Linear.

The same graphs are drawn with an expanded vertical scale in Figure 4-13 to show clearly the sensitivities of TPIM_Square and FIM4, which are comparatively lower. The positive sensitivities of these two seem to cross each other at low depths, but the negative sensitivity of FIM-4 is clearly less than that of TPIM_Square at each depth.

It can be noted that the total positive sensitivity at depths below $1\ cm$ is lower for *FIM-4* compared to *TPIM_Square* configuration. As mentioned earlier, this is because of the summation of positive and negative sensitive regions for two orthogonal measurements in FIM. The average sensitivity of FIM4 is almost double that of TPIM_Square at every depth and the peak extends greater depths compared to TPIM_Linear, FIM8 or FIM6. Again, the almost constant average positive sensitivity of both TPIM_Square and FIM4 between depths of about 1cm and 4cm may be an advantage.

The average sensitivities discussed above would be relevant when measurements are made on extended zones with the same impedivity distribution throughout. However, if the target object has impedivity that changes under two situations of measurement while the background remains the same then keeping the target object well within the focused zone of either of the FIM systems, only the positive sensitivities within the focused zone would be relevant and the results obtained above would not apply.

4.3.3 Effect of electrode separation on the sensitivity distribution

The spatial sensitivity distribution is different for different electrode configurations as shown in section 4.3.1. However, for a particular electrode configuration, the sensitivity distributions depend on both drive and receive electrode separations. Figure 4-14 shows the average sensitivity over planes parallel to the electrode plane for proportionally increasing drive and receive electrode separations (i.e. *ES_ratio* constant).

At shallow depths some of the positive sensitivities cancelled out due to the presence of negative sensitivities. Therefore, for all electrode configurations, the average sensitivity just below the electrode plane is low. The average sensitivity increases, reaches a maximum value and then decreases with increasing depth. The depth at which the average sensitivity over a plane parallel to the electrode plane reaches the maximum value was defined as *depth of maximum sensitivity, d_{max}* shown in Figure 4-14. For a constant *ES_ratio*, the depth of maximum sensitivity (d_{max}) increases with increased *drive/receive* electrode separation. The fall of average sensitivity beyond d_{max} is much steeper for lower electrode separations than that for higher electrode separations. However, overall magnitude of sensitivity decreases with increased electrode separation.

From a logical point of view the relative behaviours of all these sets of curves showed in Figure 4-14 should be the same if the volume conductor was infinite. The similarity is easily discernible in the figures.

Regarding the absolute magnitude, it can be seen that as the electrode separation increases, the magnitudes fall by almost exactly to the inverse square of separation. This is shown in Figure 4-15 in which the peak values of magnitudes for the FIM-8 value is plotted against the inverse square of the receive electrode separation (ESR).

A justification for the above may be presented from a logical analysis of the situation. When the electrode separations are doubled, the depth of the peak value also doubles as shown in Figure 4-14. Now in a semi-infinite medium, if the separation between two current-drive electrodes are doubled, the resistance faced will be doubled too, as all relevant dimensions will increase proportionately. Therefore, the current density values at the depth corresponding to the peak of average sensitivity for the larger electrode separation will be half that for the corresponding distribution at the depth corresponding to the peak of average sensitivity for the smaller electrode separation (with half *ES* value).
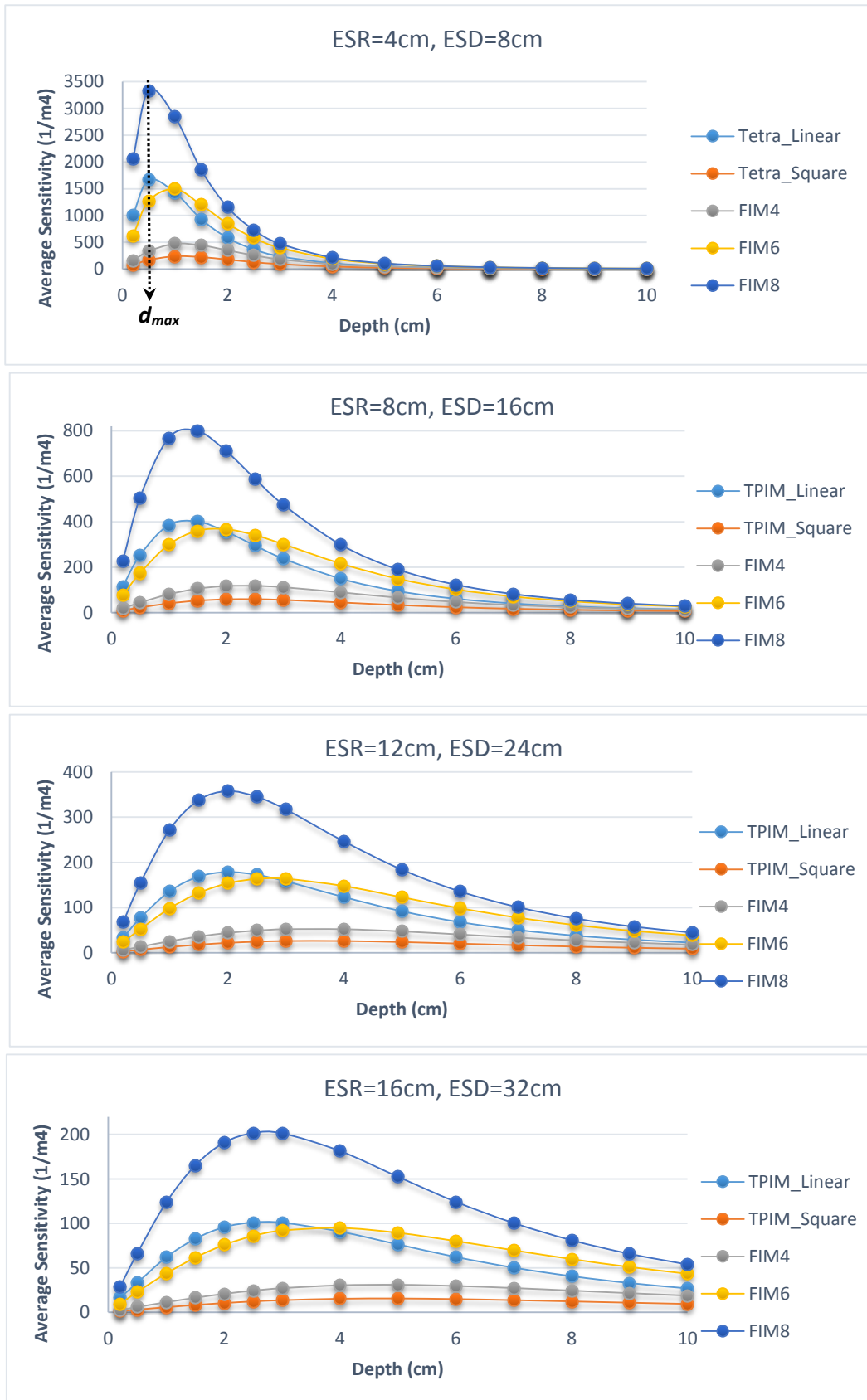
Figure 4-14 Average sensitivity over planes parallel to the electrode plane for proportional increase of drive and receive electrode separations (top to bottom) keeping ES ratio constant (2).

Since the sensitivity is given by a product of two current densities at any point due to the two sets of electrodes in TPIM (drive and receive) as in equation 4.1, therefore, the sensitivity for the larger electrode separation will be one fourth the value for the smaller electrode separation, with half the separation for both the corresponding drive and receive pairs.
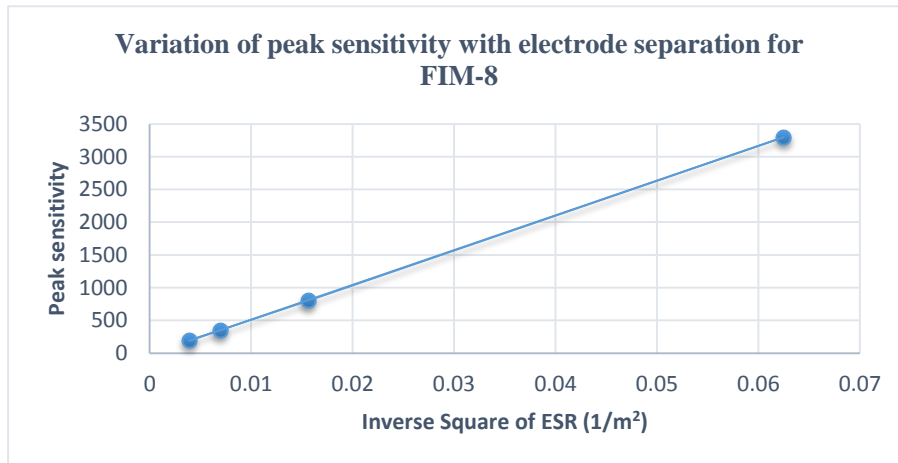
Figure 4-15 Variation of peak value of sensitivity against inverse square of receive electrode separation (ESR) for TPIM.
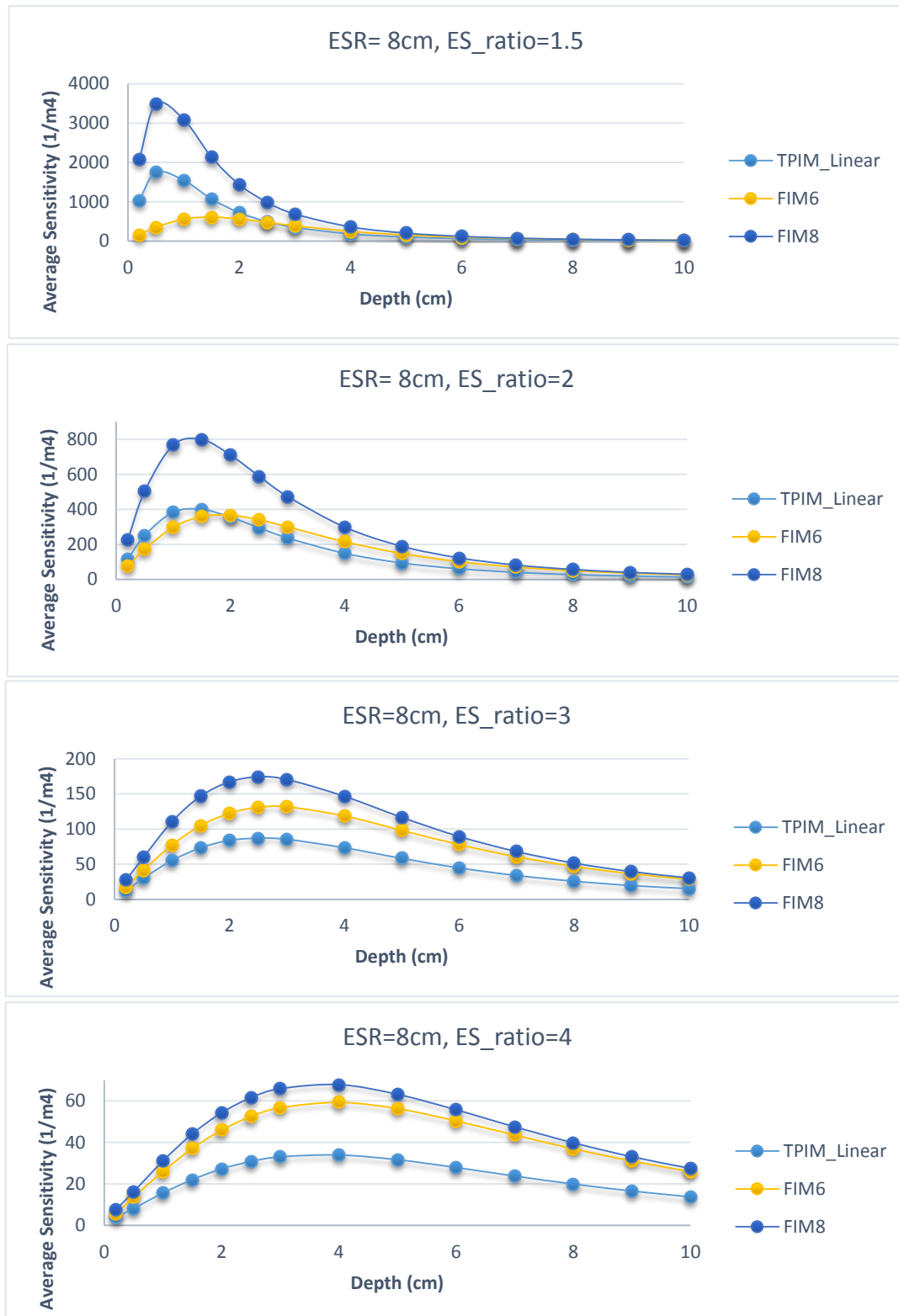
Figure 4-16 Average sensitivity over planes parallel to the electrode planes for increasing ES_ratio (top to bottom) keeping ESR=8cm.

It was also observed that spatial sensitivity distribution changes with changing drive electrode separation whilst keeping the *receive* electrode separation constant i.e for changing *ES_ratio*. Since TPIM_Square and FIM-4 configuration have only unity

112

ES_ratio, this study was performed on TPIM_Linear, FIM-6 and FIM-8 configurations only. Figure 4-16 shows the variation of average plane sensitivities against depth for various *ES_ratio* with *ESR*= 8cm.

It is clear that that depth of maximum sensitivity increases with increasing *ES_ratio* for all the three measurement techniques under investigation. Again, the overall magnitude of sensitivity decreases with increasing *ES_ratio*.

4.3.4   Percentage Depth Sensitivity (PDS)

It was observed that the depth of maximum sensitivity d_{max} changes with electrode separations for all electrode configurations (Figure 4-14 and Figure 4-16). It can be noted that the rate of fall of sensitivity beyond d_{max} is different for different electrode configurations (Figure 4-14 and Figure 4-16). For an electrode configuration, if d_{max} occurs at a shallow depth and the sensitivity falls rapidly beyond d_{max}, then the electrode configuration may not be suitable for sensing tissue/organ deep inside the body. To elaborate the idea, a new parameter *percentage depth sensitivity (PDS)* was defined as below:

$$PDS = \frac{S_{av}(d)}{S_{av}(d_{max})} \times 100 \text{ \%} \qquad \text{--- } 4\text{-}8$$

where $S_{av}(d_{max})$ is the plane average sensitivity at d_{max}, and $S_{av}(d))$ is the average plane sensitivity at any depth d. Therefore PDS is 100% at dmax. For impedance measurement of tissues/organs which are deep inside the body, one should expect an electrode configuration which has higher PDS at the desired depth.

In Figure 4-17 *PDS* was plotted against depth for proportional increase of *drive* and *receive* electrode separations keeping *ES_ratio* constant (ES_ratio = 2 for TPIM_Linear, FIM-6 and FIM-8 electrode configurations while ES_ratio = 1 for TPIM_Square and FIM-4 electrode configurations). It is evident that the depth of maximum sensitivity d_{max} (i.e. depth where PDS=100%) increases with increased drive/receive electrode separation for all measurement methods. Moreover, d_{max} is relatively higher for FIM-4 and TPIM_Square configurations compared to that for TPIM_Linear and FIM-8 configurations. Again, it may be observed that PDS values at a depth of 2.5cm for ESR=4cm are close to corresponding values for a depth of 10cm for ESR=16cm. This is also expected based on the proportional geometries of these configurations.

In Figure 4-18 *PDS* was plotted against depth for variable *ES_ratio* keeping *ESR* constant at 8cm. Since *ES_ratio* is always unity for *TPIM_Square* and *FIM-4*, this study was performed only for *TPIM_Linear*, *FIM-6* and *FIM-8* configurations. It was observed that the depth of maximum sensitivity (d_{max}) increased with increasing *ES_ratio*. For lower ES_ratio, d_{max} was relatively higher for FIM-6 configuration. However, for higher ES_ratio, PDS for all the three electrode configurations are similar.

It was observed that the depth of maximum sensitivity d_{max} increases with increased *ESR*
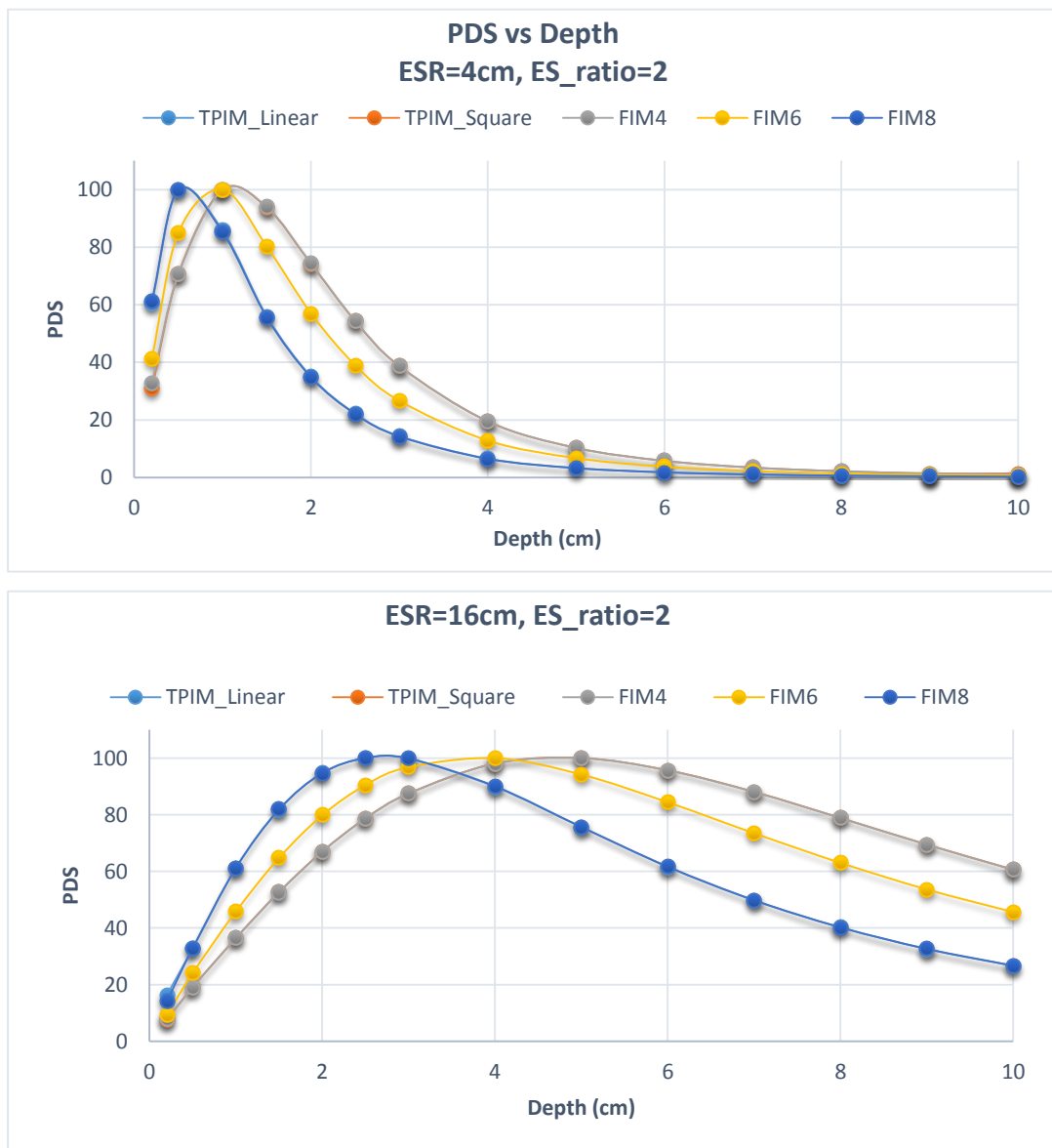
Figure 4-17 variation of percentage depth sensitivity (PDS) with depth at ESR=4cm (upper) and ESR=16 (lower) having ES_ratio=2 in both case

as well as with *ES_ratio*. In Figure 4-19and Figure 4-20, d_{max} was plotted against *ESR* and *ES_ratio* respectively to understand the dependence of d_{max} on ESR and ES_ratio. It is

evident that the depth of maximum sensitivity increases almost linearly with increased *ESR* for constant *ES_ratio*.

The variation of d_{max} with *ESR* is almost similar for *TPIM_Linear* and *FIM-8* and also for *TPIM_Square* and *FIM-6*. The variation of depth penetration with varying *ESR* is sharper for *FIM-4/TPIM_Square* methods compared to *FIM-8/TPIM_Linear* whereas the variation is in between for *FIM-6*. It can be observed that the depth of maximum sensitivity is approximately one-sixth of the *receive* electrode separation for both *TPIM_Linear* and *FIM-8* systems with ES_ratio=2. For *FIM-4* and *TPIM_Square*
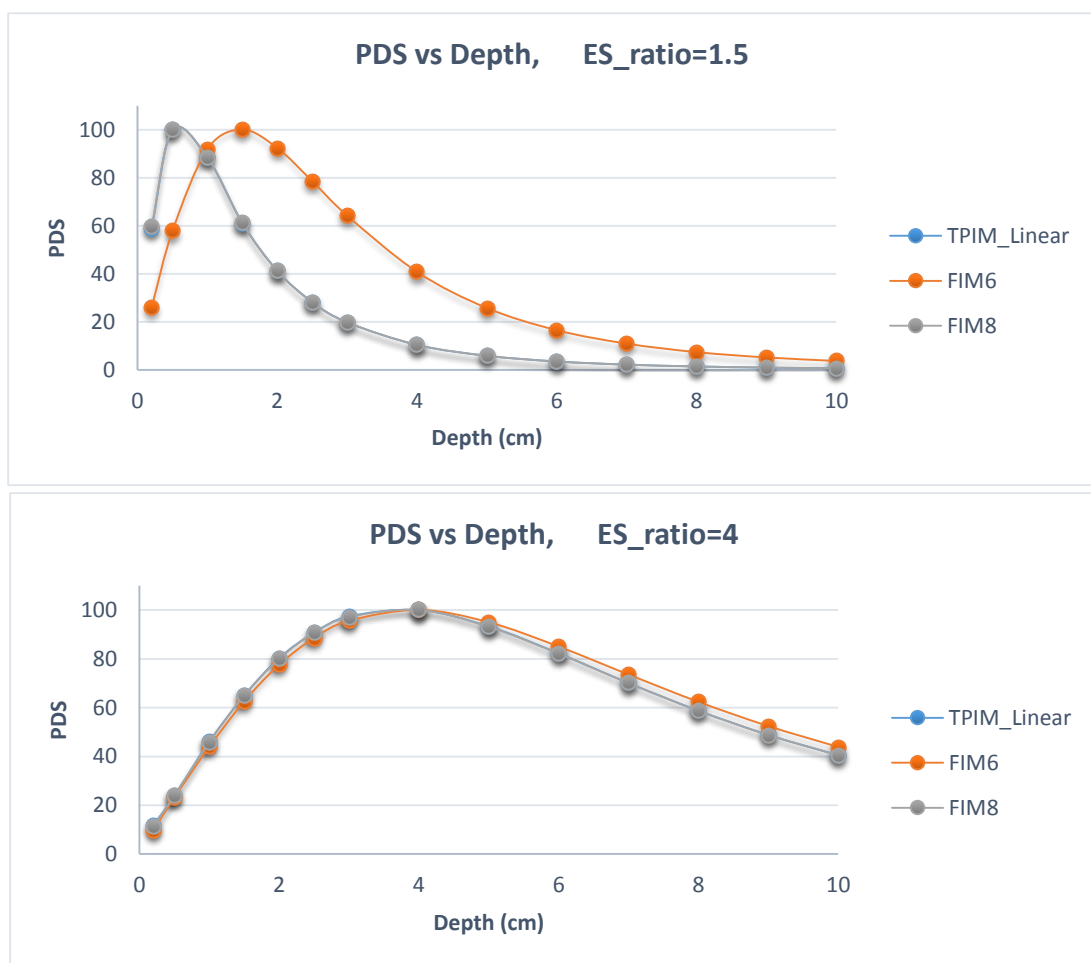
Figure 4-18 PDS plotted against depth for increasing ES_ratio keeping receive electrode separation constant (8 cm); ES_ratio = 1.5 (top) and ES_ratio = 4 (bottom). The curves for TPIM_Linear and FIM-8 overlap each other.
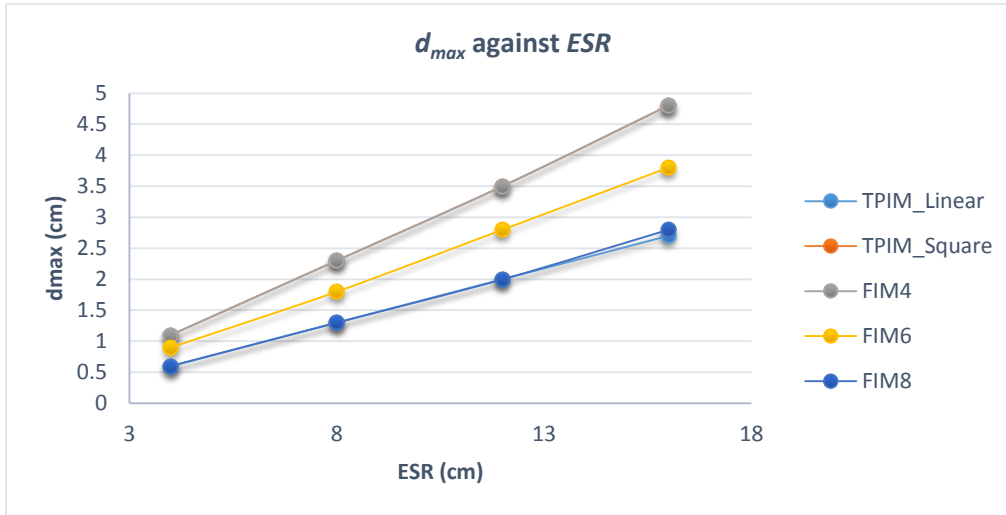
Figure 4-19 Depth of maximum sensitivity (d_max) plotted against ESR for all measurement techniques keeping ES_ratio constant.

methods, d_{max} is at about $ESR/3.47$. Again for *FIM-6*, d_{max} occurs at about $ESR/4.35$. It is evident that *FIM-4* and *TPIM_Square* have greater depth sensitivity. Again, *FIM-6* can penetrate more compared to *TPIM_Linear* and *FIM-8* but less compared to FIM-4 and TPIM_Square. Similarly, d_{max} increases with increased *ES_ratio* for constant *ESR*. For *FIM-6* with *ESR*=8cm, d_{max} is approximately equal to the numerical value of *ES_ratio*.
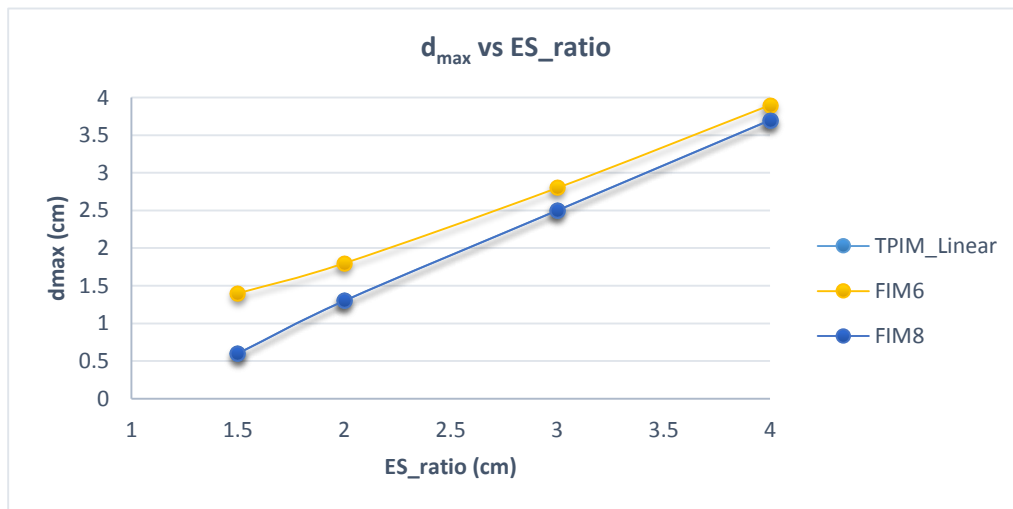
Figure 4-20 Depth of maximum sensitivity d_max plotted against ES_ratio for ESR=8cm.

4.3.5   Degree of Localization *(dol)*

Another new parameter, *'Degree of localization (dol)'* was introduced in this work as defined in *equation 4.6*. Degree of localization (*dol*) can give an idea how much of the measured transfer impedance is coming from the *focused zone* within the volume

dol against
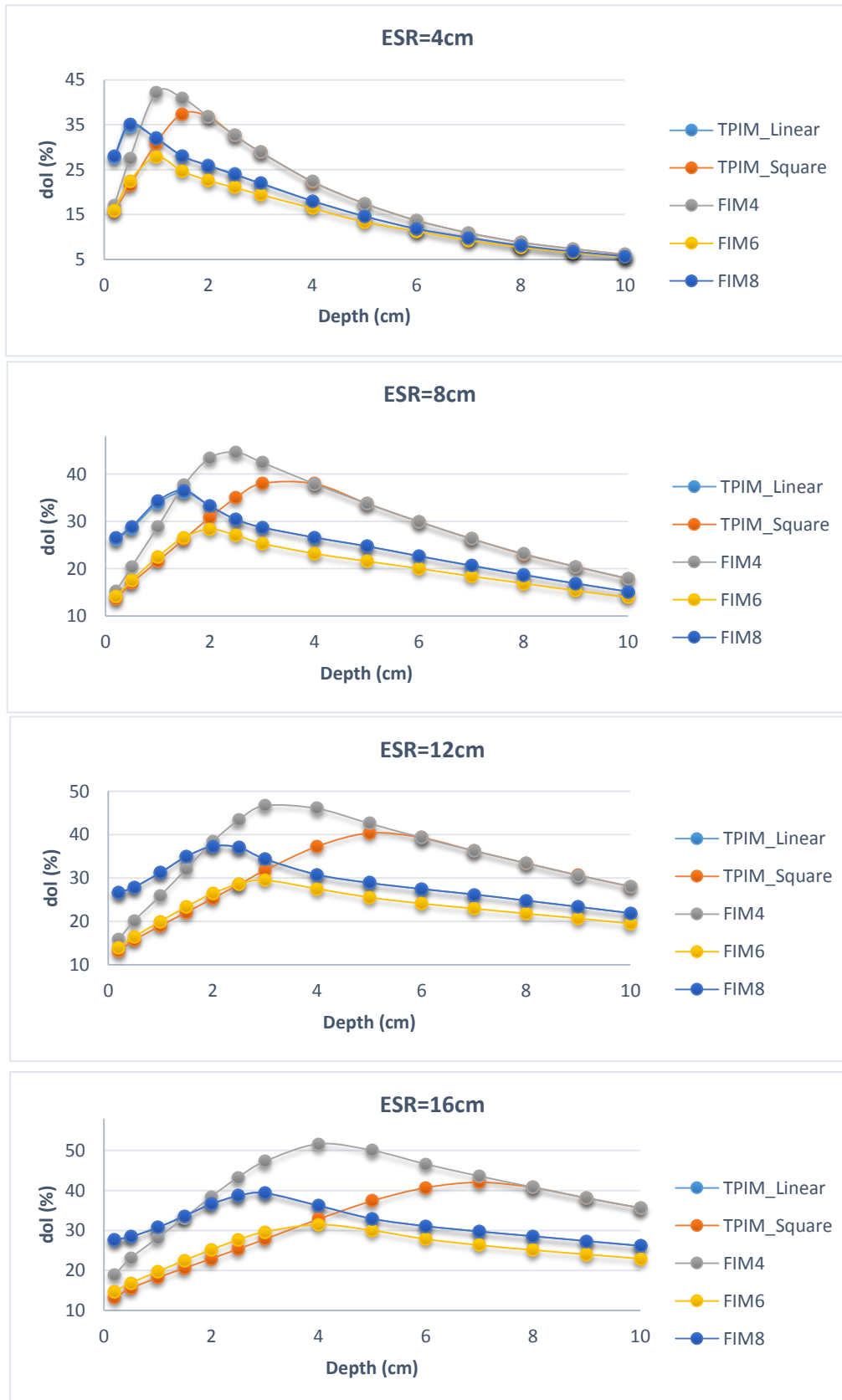
Figure 4-21 dol plotted against depth for all measurement methods with increasing electrode separations keeping ES_ratio constant.

conductor (section: 4.2.6). In Figure 4-21 *dol* for individual planes was plotted against

depth for all measurement methods keeping *ES_ratio* constant. For all measurement methods, *dol* initially increases with depth reaches a maximum and then decreases again. At shallow depths, TPIM_Linear and FIM-8 have higher localization ability compared to others. However, deep inside the volume conductor, *FIM-4* has the higher localization ability for any particular electrode separation. Overall, the localization ability increases with increased *ESR*. However, it should be noted that increased *ESR* means larger focused region. FIM-6 has relatively lower localization ability.

4.3.6   Effect of electrode diameter

To study the effect of electrode size, sensitivity distribution within the volume conductor was obtained for FIM-4 configuration using differet electrode diameters (*ELD*) as shown in Figure 4-22. The diameter of the electrodes were changed keeping the edge to edge distance constant ($8\ cm$). In Figure 4-23 and Figure 4-24, sensitivity within the volume conductor along x-axis passing through the center of the electrode array is plotted for various electrode diameters at two different depths.
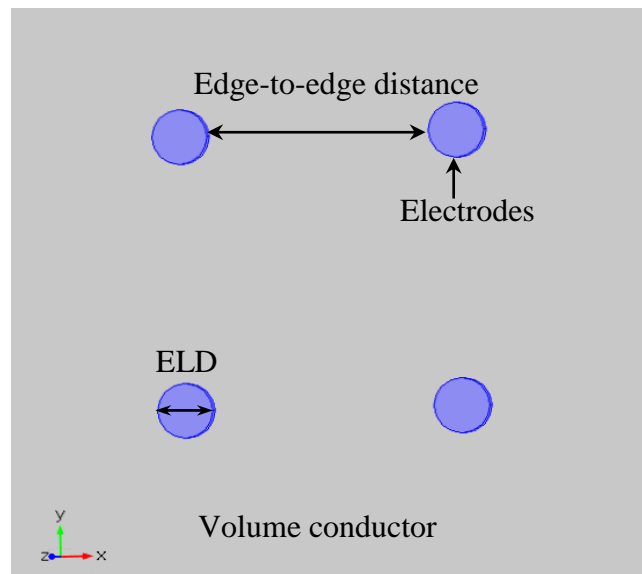
Figure 4-22 Arrangement for the study of effect of electrode dimension on the sensitivity distribution (FIM-4), only a part of the volume conductor is shown. The edge-to-edge distance between the electrodes was kept constant (8cm) while the diameter of the electrodes were changed.
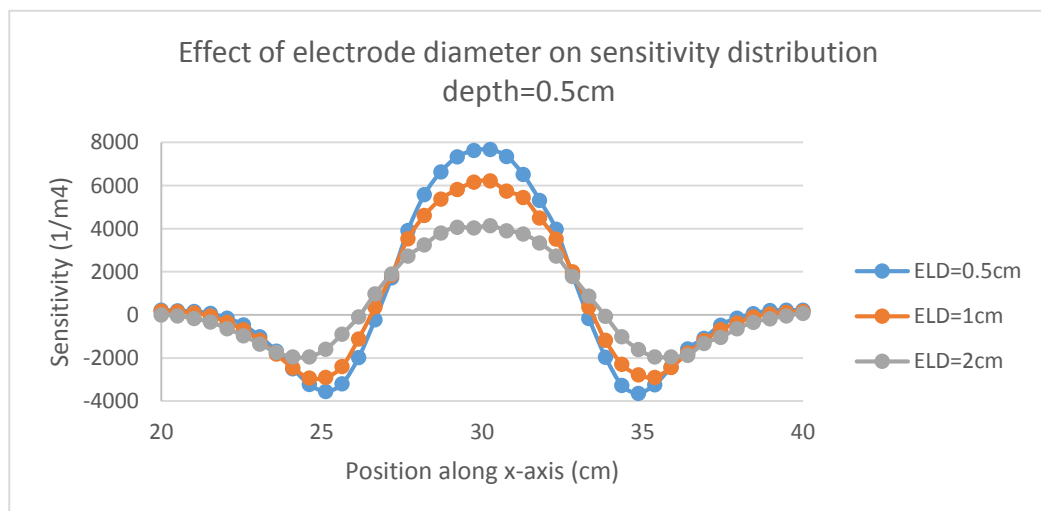
Figure 4-23 Sensitivity within the volume conductor along x axis passing through the centre of the electrode configuration at depth 0.5 cm from the electrode plane. Center of the electrode array is at 30cm, edge to edge distance between electrodes is 8cm.

118

It can be observed that the sensitivity beneath the central region of the electrode array decreases with increasing electrode diameter. Again, amplitude of negative sensitivity at shallow depths in the region between two neighbouring electrodes decreases with increasing electrode diameter.
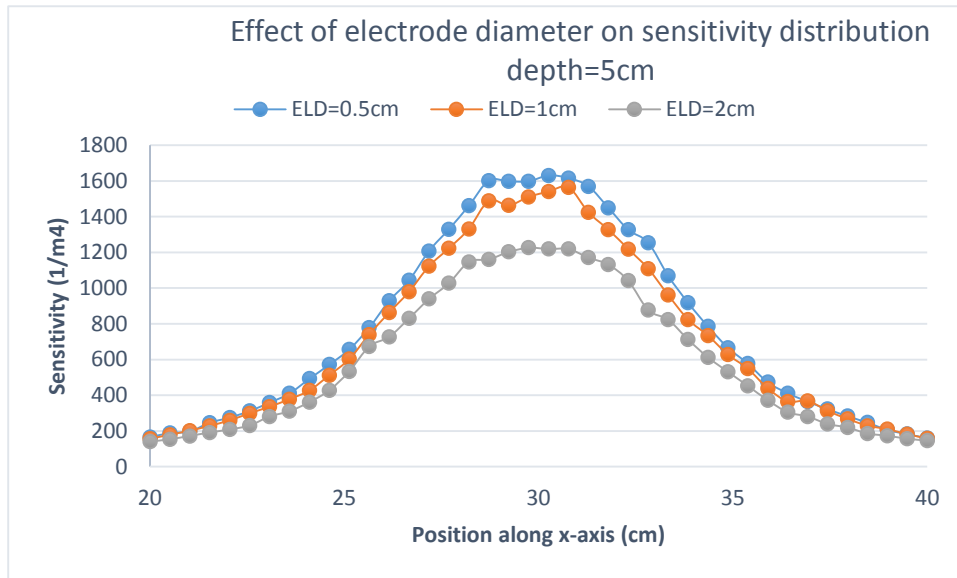
Figure 4-24 Sensitivity within the volume conductor along x axis passing through the centre of the electrode configuration at depth 5 cm from the electrode plane

The effect of electrode diameter on the center of the focused zone is illustrated in Figure 4-25 where the sensitivity along z-axis passing through the center of the electrode configuration is plotted against depth. It is evident that the sensitivity is higher for electrodes with smaller diameter. The change in sensitivity with electrode dimension is
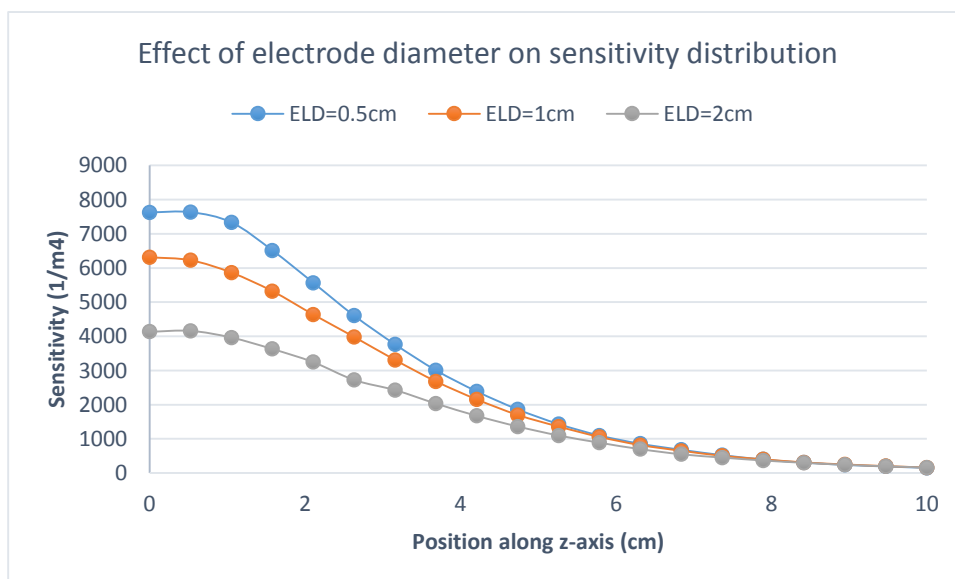
Figure 4-25 Sensitivity along z-axis passing through the center of the electrode configuration for variable electrode diameter plotted against depth. The edge-to-edge distance between electrodes is constant (8cm).

more significant at lower depths and is negligible beyond depths greater than edge-edge distance between electrodes. An increase in electrode diameter effectively spreads the injected currents in a larger volume beneath the electrode array. The spreading of current lines results decreased magnitude of current density vectors. For this reason, the sensitivity is lower with larger electrode diameter.

4.3.7   Effect of inhomogeneity

To understand how the sensitivity distribution changes with the presence of inhomogeneity (organ, fat layer etc.), 3D sensitivity distribution was obtained by introducing regions of different conductivity (both high conducting and low conducting relative to the volume conductor) at certain locations within the volume conductor. As mentioned earlier, the conductivity of the high conducting inhomogeneity was twice ($3\,S/m$) that of the background ($1.5\,S/m$) and the conductivity of the less conducting inhomogeneity was half ($0.75\,S/m$) that of the background. Sensitivity along x-axis passing through the center of the electrode configuration (FIM-4) at depth 3cm from the electrode plane was plotted in Figure 4-26. In this case the inhomogeneity was a *cylinder*
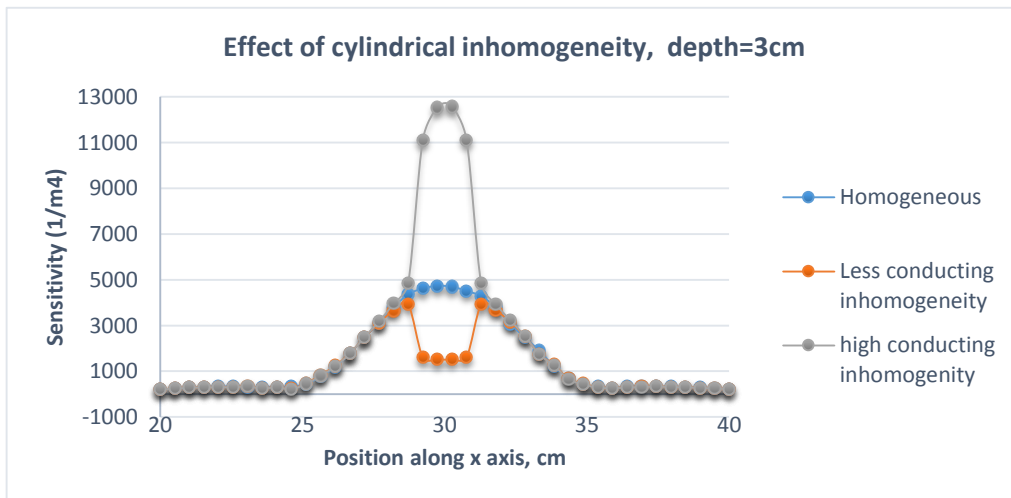
Figure 4-26 Sensitivity along x-axis passing through the center of the electrode configuration at depth 3cm from the electrode plane with the presence of a cylinder placed centrally at depth 3cm (sensitivity along the center of the cylinder).

of diameter 1cm and length 1cm placed at depth 3cm along the center of the electrode configuration. It can be observed that within the region having higher conductivity the sensitivity is more compared to that in the homogeneous volume conductor. This is expected since the current density will be higher in this region. In contrast, within the region having lower conductivity the sensitivity is lower compared to that in the homogeneous medium due to the same reason (the current density will be lower). In
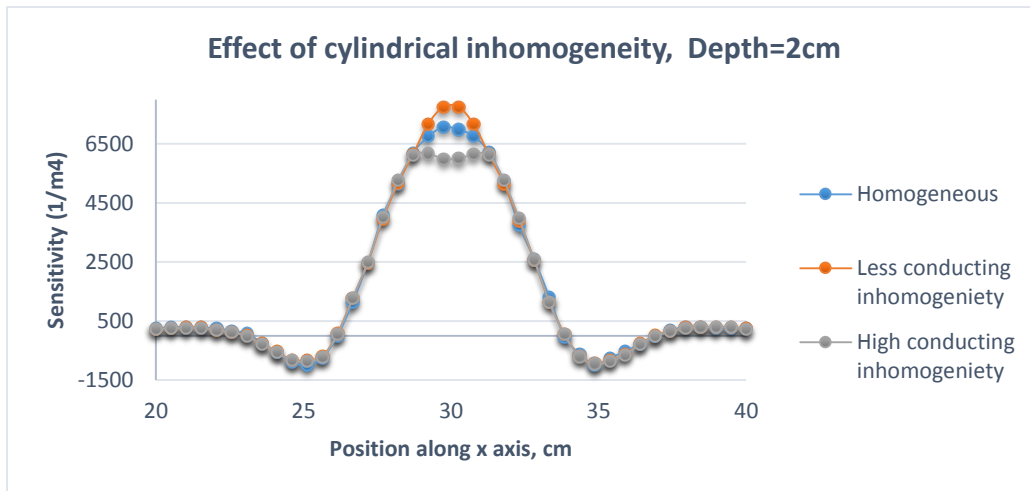
Figure 4-27 Sensitivity along x-axis passing through the center of the electrode configuration at depth 2cm (0.5 cm above the cylinder)

regions few mm away from the cylindrical object there was no significant change in sensitivity due to the presence of this inhomogeneity.

Figure 4-27 and Figure 4-28 show the sensitivity along x-axis passing through the center of the electrode configuration at slightly above and below the volume of inhomogeneity (cylinder length: 1cm, its center at depth 3cm), but within the homogeneous background. The depths chosen were 2cm (0.5 cm above the inhomogeneous disc) and 4cm (0.5 cm below the inhomogeneous disc) respectively. For a volume of inhomogeneity having higher conductivity, sensitivity in the neighbouring region both above and below the disc is lower compared to that in the homogeneous volume and the change is inverse of that within the inhomogeneity as observed in Figure 4-27. On the other hand, for a volume inhomogeneity of lower conductivity, the sensitivity in the neighbouring region is higher compared to that in the homogeneous volume, and again, the change is inverse of that
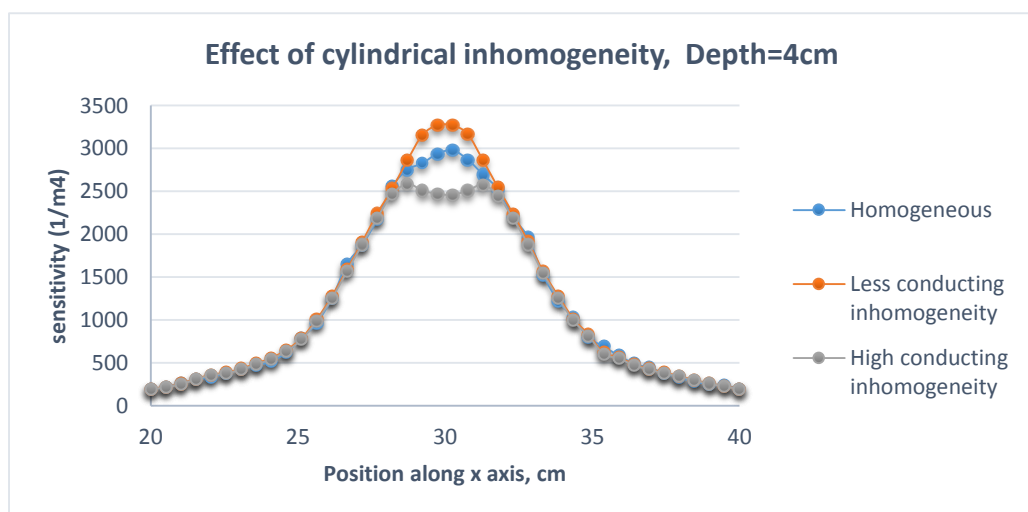
Figure 4-28 Sensitivity along x-axis passing through the center of the electrode configuration at depth 4 cm (0.5 cm below the inhomogeneous cylinder).

121

within the inhomogeneity as observed in Figure 4-28. This means the change in sensitivity immediately above and below the inhomogeneity is negative if the change in sensitivity within the inhomogeneity is considered positive.

The sensitivity along z-axis passing through the center of the electrode configuration (also through the center of the inhomogeneity) was plotted in Figure 4-29 which shows the nature of the sensitivity changes. The negative sensitivity changes (as defined above) can be clearly seen which decreases quickly behind the homogeneity, but rather less quickly in the front.

This behavior is reasonable as a more conducting volume allows more currents to flow through itself which results increased current density. Therefore the sensitivity within the more conducting inhomogeneity is high although the sensitivity is less at its neighbouring volumes. In contrast, a less conducting volume allows less current to flow, so more currents flow through the neighbouring volumes. So sensitivity within the less conducting inhomogeneity is low although the sensitivity is more at its neighbouring regions. It can be noted that the change in sensitivity is relatively higher for high conducting inhomogeneity than that for a low conducting inhomogeneity. Similar observations based on experimental results on 3D tank was also reported by (Newell et al., 1998). This is because a conductor redistributes electric fields in a greater extent than that done by an insulator.
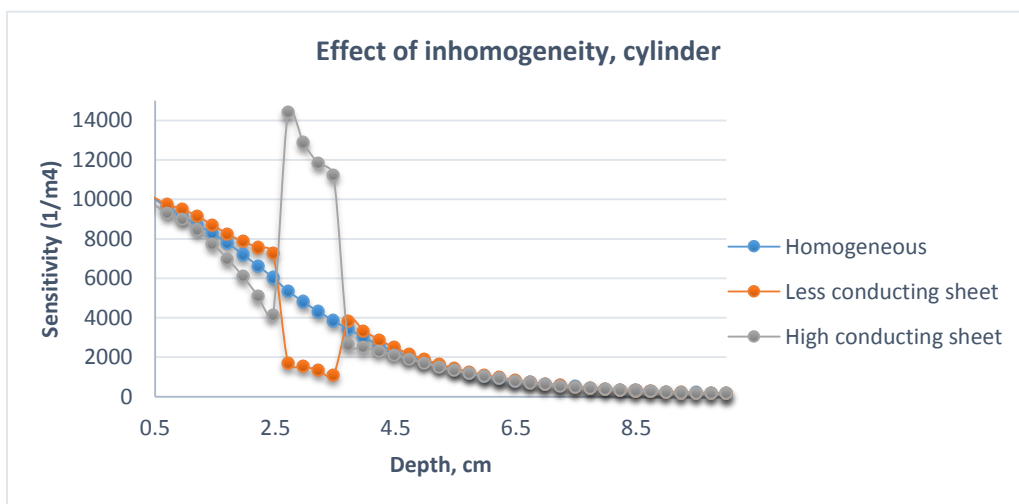
Figure 4-29 Sensitivity along z-axis passing through the center of the electrode configuration (also through the center of the inhomogeneous disc) plotted against depth.

For the inhomogeneity with the higher conductivity, more current is concentrated in the nearer region and the current density within the inhomogeneity falls sharply with depth. So the sensitivity also falls sharply with depth as seen in Figure 4-29. On the other hand, this does not happen in the inhomogeneity with the lower conductivity, so the change in sensitivity with depth is less.
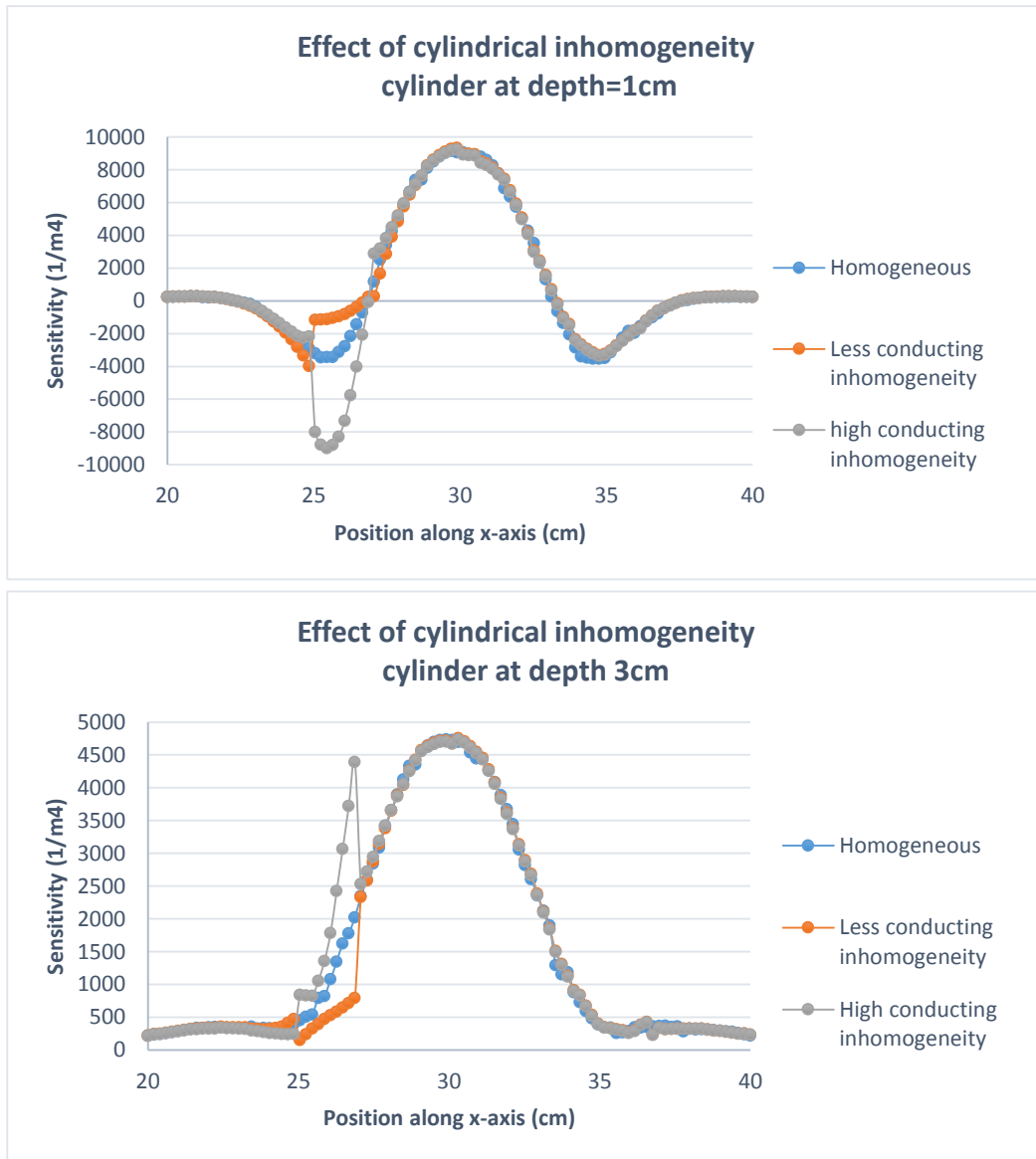
Figure 4-30 Sensitivity along x-axis passing through the center of the electrode array for cylindrical inhomogeneity placed beneath the region between drive-receive electrodes, cylinder center at x=26cm. Sensitivity at depth 1cm with cylinder center at depth 1m (top) and sensitivity at depth 3cm with cylinder center at depth 3cm (bottom).

Sensitivity profiles were obtained by placing the cylinder beneath the region between drive and receive electrodes (cylinder center at x=26cm with electrode separation 8cm) at different depths. Figure 4-30 shows the sensitivity profiles along x-axis passing through the center of the electrode array for position of the cylinder center at depths 1cm (top) and 3cm (bottom). It can be observed that the presence of the more conducting cylinder increases the sensitivity in the negative direction when the cylinder center is at 1cm. In contrast, presence of the less conducting cylinder increases the sensitivity in the positive direction. This signifies that the cylinder location is at negative sensitive zone which is evident from the curve for homogeneous medium. However, at depth 3cm, the more
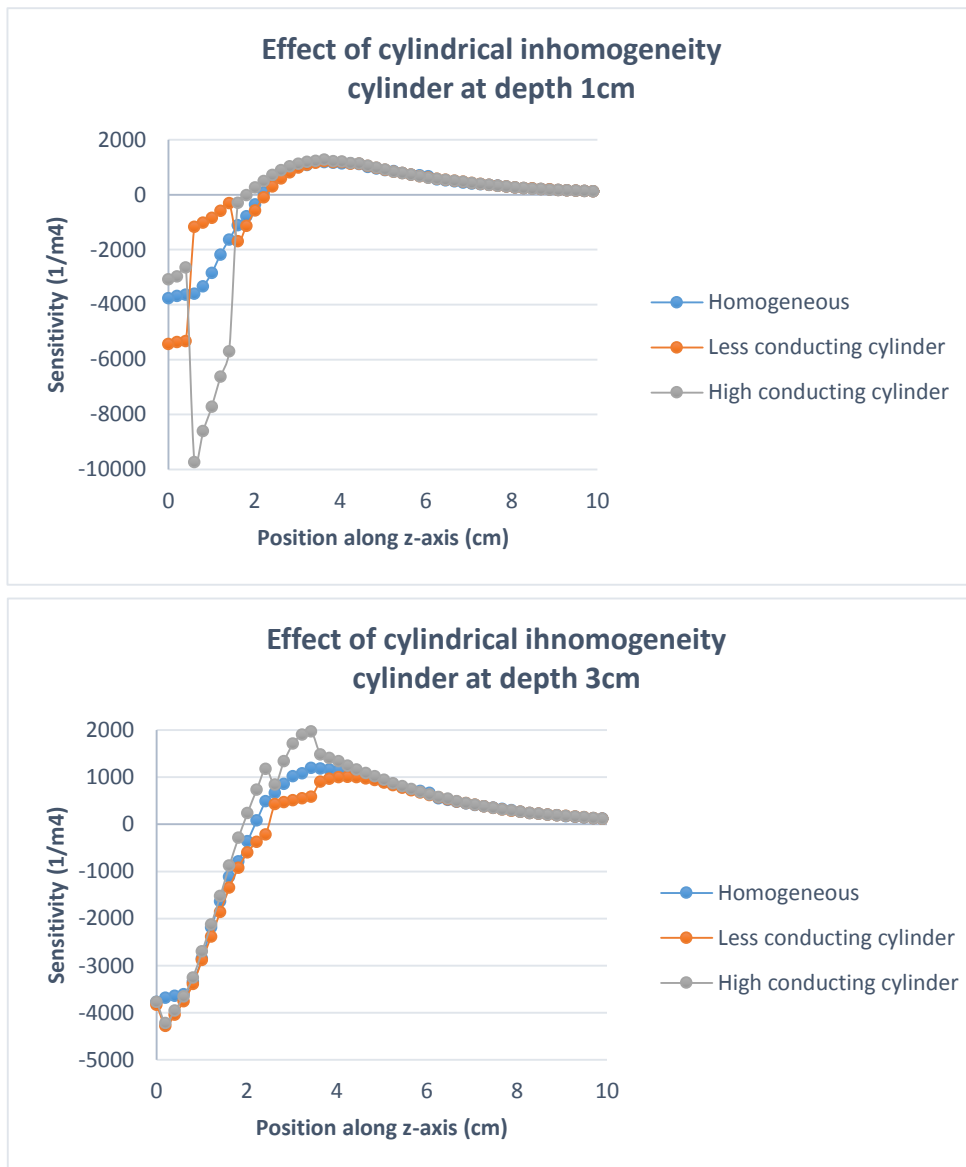
Figure 4-31 Sensitivity profiles along z-axis passing though the center of the cylinder while the cylinder was placed beneath the region between drive and receive electrodes. Electrode separation was 8cm with cylinder position x=26 cm and z=1cm (top) and cylinder position x=26 and z=3cm (bottom).

conducting inhomogeneity increases the sensitivity while the less conducting inhomogeneity decreases the sensitivity. This is expected because the inhomogeneous cylinder is in positive sensitive zone in this case.

Similar behavior can be observed from the plots of sensitivity profiles along z-axis passing through the center of the inhomogeneity as shown in Figure 4-31.

The effect of inhomogeneity was also studied by introducing a sheet of various thickness placed at depth 3 cm from the electrode plane. In width and breadth, the sheet is extended up to the boundary of the volume conductor ($60cm \times 60cm$). The sensitivity along z-axis through the center of the electrode plane ($30,30,z$) is plotted in Figure 4-32.
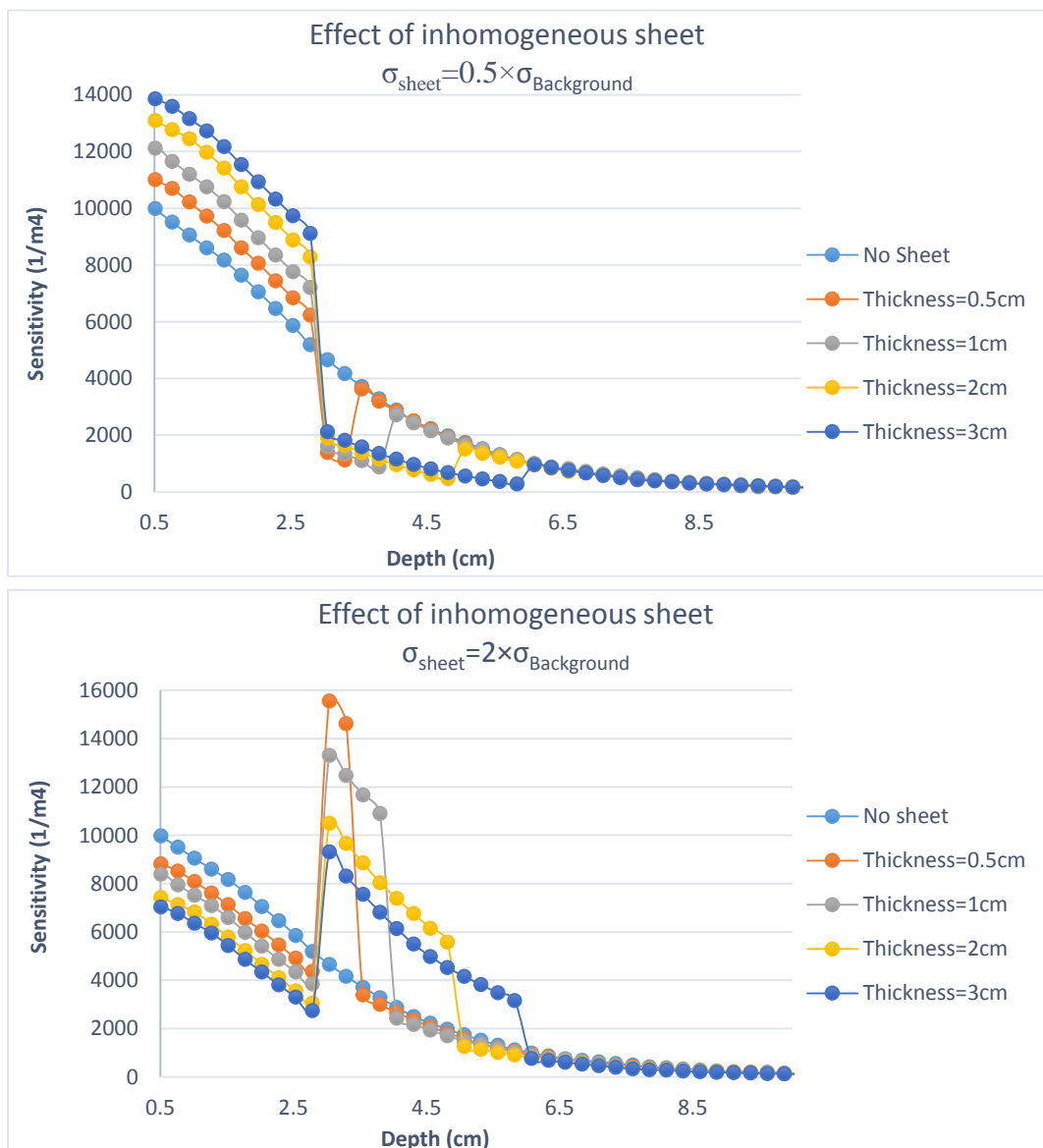
Figure 4-32 Sensitivity along z-axis through the center of the electrode configuration with sheets of different thicknesses placed at depth 3cm. Sheets with lower conductivity (up) and sheets with higher conductivity (bottom).

For a sheet of conductivity lower (half) than the volume conductor, the sensitivity in the region between electrode plane and the sheet was significantly higher than that with the volume conductor only. But within the sheet, the sensitivity was lower compared to that of the homogeneous volume conductor. Beyond the sheet, the sensitivity change from that of the homogeneous background became less significant. In contrast, for the sheet of higher conductivity compared to the volume conductor, the sensitivity in the region between the electrode plane and the sheet was significantly lower than that with the homogeneous volume conductor only. Within the sheet, the sensitivity was much higher compared to that of the homogeneous medium only. The difference in sensitivity between homogeneous and inhomogeneous medium is less significant deep inside.

It can be noted that the *change in sensitivity* in the region between the sheet and electrodes is proportional to the *thickness* of the sheet for both type of conductivities. The change in sensitivity is proportional to the sheet thickness within the sheet material as well.

4.3.8 Effect of volume conductor boundary proximity to the electrodes in sensitivity distribution

In this analysis the effect of the closeness of a volume conductor boundary to the electrodes array was investigated. 3D Sensitivity distribution was obtained for various size of the volume conductor. The electrodes were placed on a surface of the volume conductor. Electrode separations were kept constant while the volume of the conductor was reduced which effectively reduces the distance of the boundary from the electrodes
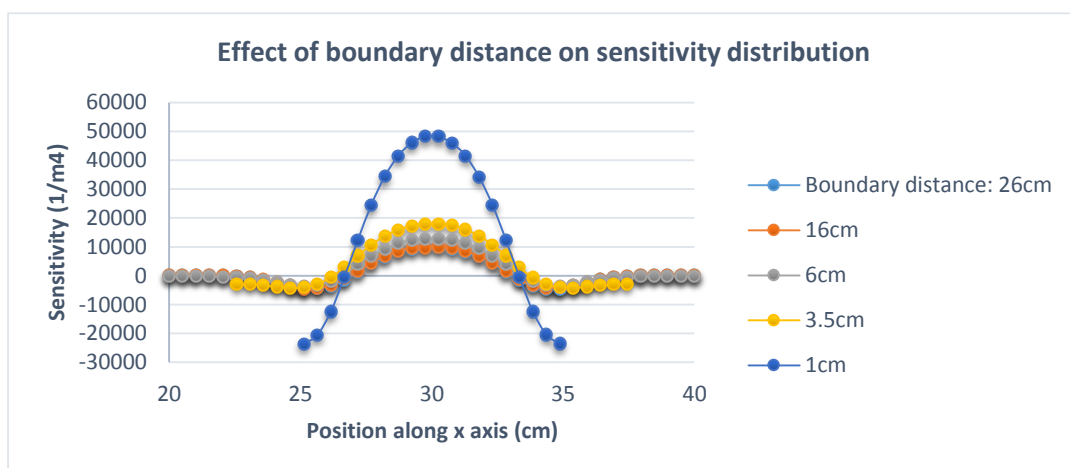
Figure 4-33 Sensitivity along x axis passing through the center of the electrode configuration at a depth 0.5 cm from the electrode plane for various distance of the boundaries from the center of the electrodes. The electrode separation was kept constant (8cm) while the edge of the cubic volume conductor was reduced.
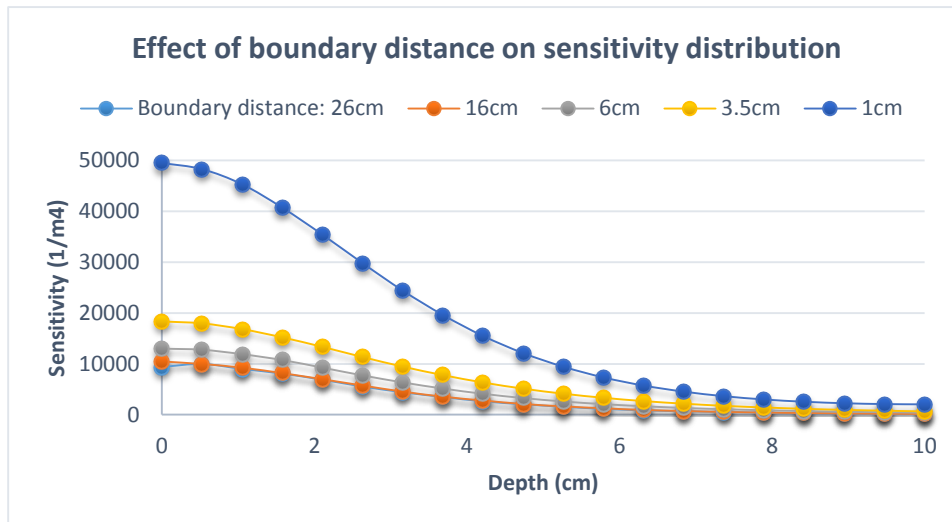
Figure 4-34 Sensitivity along z-axis passing through the center of the electrode configuration (30,30,z) against depth for various distance of the boundary from the center of the electrodes. The electrode separation was kept constant (8cm) while the edge of the cubic volume conductor was reduced.

(described in section 4.2.9). Sensitivity along x-axis passing through the center of the electrode configuration at depth $0.5\ cm$ was plotted in Figure 4-33 for various size of the volume conductor. It can be observed that the magnitude of sensitivity values (both positive and negative) increases with decreased size of the volume conductor.

In Figure 4-34 the sensitivity along z-axis (perpendicular to the electrode plane) passing through the center of the electrode configuration was plotted for various size of the volume conductor. It is evident that the change of sensitivity with the distance of the
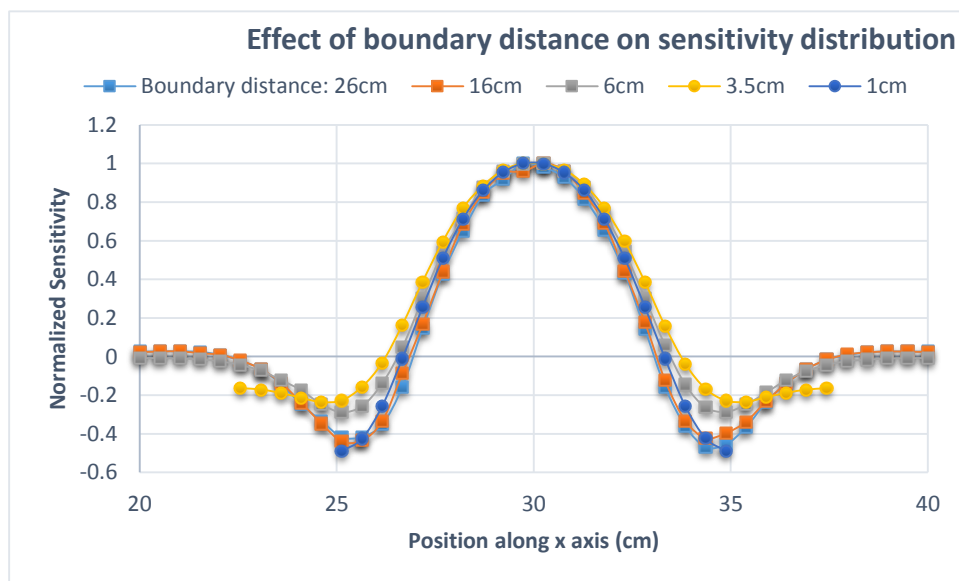
Figure 4-35 Normalized sensitivity profiles along x-axis at depth 0.5cm for different distance of the boundary from the electrodes. Electrode separation was kept constant (8cm), only the boundary distance from the electrodes were changed.

127

electrodes to the boundary is less significant when the boundary distance is more than twice of the electrode separation (in this case 16 cm). As the boundaries approach the electrodes, the magnitude of sensitivity increases throughout the volume conductor. It is expected because in a small volume conductor the current lines originating from the drive electrodes cannot spread far away. Therefore current density within the small volume is relatively higher which increases the magnitude of sensitivity.

Figure 4-35 shows the normalized sensitivity profiles (with respect to the sensitivity value at the center of the electrode array) along x-axis at depth 0.5cm for different boundary distance from the electrodes. It can be observed that the proximity to boundary from the electrodes changes the pattern of sensitivity profiles. The negative sensitivity regions are more extended outside the focused zone for more proximal boundary. A volume where the current density at the boundaries is non-zero ceases to be semi-infinite and thus the size of the volume will impact on the values of current density within it.

4.3.9   Experimental Validation

To validate the simulation results, sensitivity distributions were obtained experimentally using a cubic tank filled with saline as described in section 4.2.10. Exactly same experiment was then simulated in Comsol Multiphysics and sensitivity distribution was calculated to validate the experimental data. Figure 4-36 shows the sensitivity at depth1 mm from the electrode plane obtained experimentally for FIM-4 configuration. The
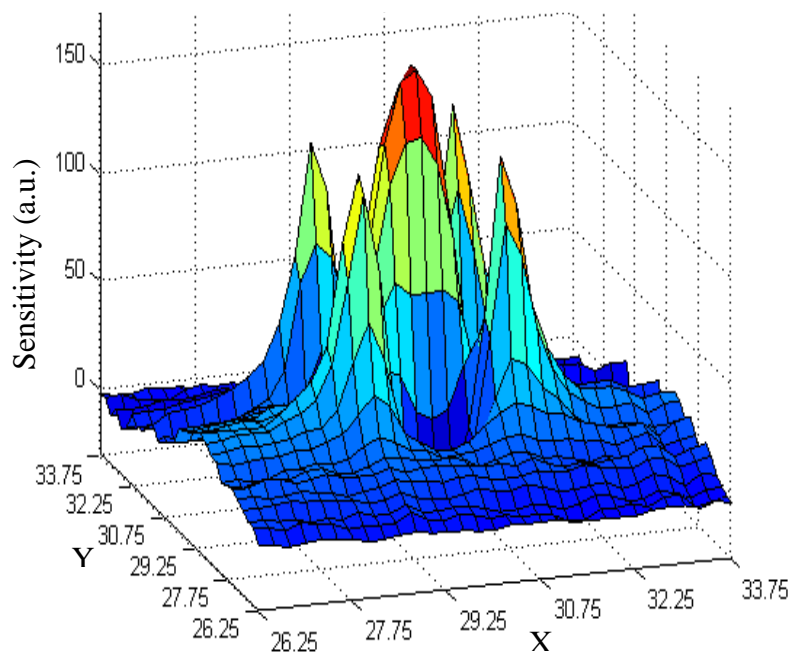
Figure 4-36 Sensitivity distribution at depth 1 mm from the electrode plane obtained experimentally using FIM-4 configuration

sensitivity at a point is the difference between voltage with and without the disc as defined in equation 4-7. Since the voltage values were measured experimentally after amplification of the voltage signal, the sensitivity values are shown in arbitrary unit (a.u.).

The sensitivity distribution obtained from experiment and that from Comsol simulation were compared in Figure 4-37. Here normalized sensitivity along x-axis passing through the center of the electrode configuration at depth $1mm$ were plotted for both experimental and simulation data. It can be observed that the overall pattern of sensitivity distribution obtained experimentally is very close to that obtained from simulation although there are slight deviations.
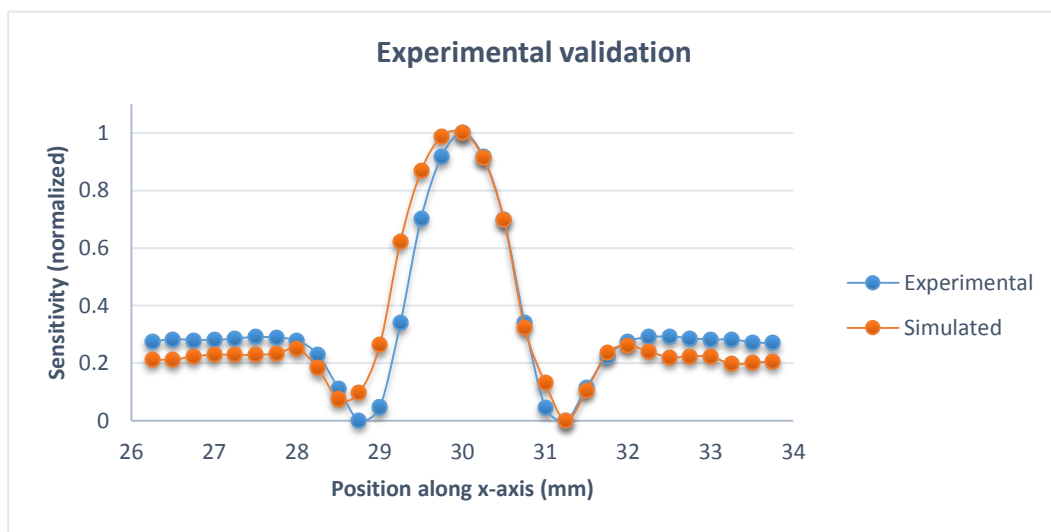
Figure 4-37 Sensitivity along x-axis passing through the center of the electrode configuration at depth 1 mm for FIM-4 with electrode separation 20mm.

4.4 Discussion

Various electrode configurations are in use for bioimpedance measurements. 3D sensitivity distributions of TPIM_Linear, TPIM_Square, FIM-4, FIM-6 and FIM-8 techniques were investigated using finite element method based simulation software Comsol Multiphysics®. The effect of electrode separation, electrode dimension, presence of inhomogeneity and boundary distance on sensitivity distributions were studied and compared among various electrode configurations. Sensitivity distributions obtained from finite element simulations were validated using experimental measurements. A cubic tank was modeled as a volume conductor for simplicity of analysis and better visualization of sensitivity distributions. A large volume conductor compared to electrode separations was used in this study to minimize boundary effect. At a distance twice the effective radius of the electrode configuration from the center of the electrode array, the peak sensitivity is 1% of its maximum value. The volume conductor used in the present work was a cube of length 60cm while the maximum electrode separation was 32 cm. Therefore the model used in this work can be considered as semi-infinite.

Different electrode configurations have different spatial sensitivity distributions and gives an idea about which portion of the volume conductor one can sense using electrodes on the surface. There are positive sensitive regions as well as negative sensitive regions for all measurement methods (section: 4.3.1). The negative sensitive regions are always below the drive-receive electrode pair and diminishes within a short distance from the electrode plane (Figure 4-12 and Figure 4-13). An increase in conductivity in the positive sensitive region or a decrease in conductivity in the negative sensitive region may result similar change in the measured transfer impedance. In bioimpedance measurements, it is not possible to interpret if a change in transfer impedance is coming due to conductivity increase in the positive sensitive region or due to conductivity decrease in the negative sensitive region and vice versa. Therefore, it is desirable not to have any negative sensitivity in the *focused zone* where change in transfer impedance is to be measured.

Due to the presence of negative sensitivity close to the electrode plane, the average sensitivity over a plane was low at shallow depths (Figure 4-12). The average sensitivity reaches a maximum and then falls again with depth because the current density decreases with depth. For *FIM-4* and *TPIM_Square* methods, d_{max} occurs at about $^1/_{3.5}$ of the electrode separation, ESR (Figure 4-20) which is close to the value $^1/_3$ obtained using

analytical calculations considering point electrodes (Brown et al., 2000a, Islam et al., 2010). The depth of maximum *average sensitivity* is about $\frac{1}{6}$ of the electrode separation for TPIM Linear and FIM-8 configurations and is $\frac{1}{4.3}$ of the electrode separation for FIM-6 configuration. The depth of maximum sensitivity, d_{max} could be increased either by increasing the *ESR* keeping *ES_ratio* constant or by increasing the *ES_ratio* keeping *ESR* constant (Figure 4-19 and Figure 4-20). However, *focused zone* increases with increased *ESR*. Therefore, to investigate a small area close to body surface one should choose small *ESR* with smaller *ES_ratio*. A large object just below the surface can be studied with large ESR but smaller ES_ratio. Small objects which are located deep inside the body can be investigated choosing small *ESR* but large *ES_ratio*. Again, to investigate an extended object deep inside the body, one should choose higher *ESR* as well as higher *ES_ratio*.

The magnitude of sensitivity values decreased with increased depth (Figure 4-12) because the current density decreases with distance from the electrodes. Among the 5 impedance measurement techniques under investigation, the magnitude of sensitivity is higher for *TPIM_Linear* and *FIM-8* whereas the magnitude of sensitivity is lower for *TPIM_Square* and *FIM-4*. But the percentage depth sensitivity *(PDS)* is higher for *TPIM_Square* and *FIM-4*. Therefore, *TPIM_Square* and *FIM-4* have superior depth penetration ability having relatively less contribution from tissues at shallow depths. In an application, where the change of transfer impedance is to be monitored due to conductivity change of an organ inside the body minimizing contribution from tissues at shallow depths (eg. Lungs), the latter two methods can be chosen.

To get information from a localized zone within the body minimizing contribution from neighbouring regions, degree of localization *(dol)* should be higher. Having relatively higher *dol* as well as higher *PDS*, *FIM-4* configuration could be a better choice, to monitor localized change in transfer impedance due to conductivity changes in lungs during breathing minimizing changes in chest muscle and ribcage. Since the magnitude of sensitivity is relatively lower for FIM-4, the measurement device should be highly sensitive to a small change of transfer impedance.

PDS and ***dol*** are two new parameters for TPIM or for FIM, introduced in the present work, which would be useful in all related work. It should be realized however that if a target object lies entirely within the positive sensitivity zone and if a change in impedance

of the object is to be measured due to certain changes in the experimental study while the background remains unchanged, then the negative sensitivity of surrounding zones, however large, will not be of concern.

It is known that the electrode-tissue contact impedance is relatively lower for electrodes of larger diameter. Larger electrodes are also useful in injecting higher ac current avoiding tissue heating. But the dimension of the electrodes could significantly change the transfer impedance. Electrodes with increased diameter effectively spread the injected currents to a larger volume which result reduced magnitude in sensitivity (Figure 4-23 - Figure 4-25).

The bioimpedance measurements obtained from human body should be interpreted carefully as human body is an inhomogeneous volume conductor. In an inhomogeneous volume conductor, a more conducting region allows more currents to enter into it which results increased sensitivity because of increased current density. In contrast, a less conducting region within an inhomogeneous volume conductor allows fewer currents which results reduced sensitivity because of reduced current density. It should also be noted that the sensitivity within a more conducting inhomogeneity is not only increased but its presence decreases sensitivity in its surrounding regions and vice versa (Figure 4-26 - Figure 4-31). The presence of resistive layer (e.g. fat layer in human body) increases the sensitivity in the region between electrode plane and the resistive layer (Figure 4-32). It can be noted that the change in sensitivity is proportional to the sheet thickness. Within the resistive layer sensitivity is lower compared to that in a homogeneous medium. The presence of resistive layer does not change the sensitivity distribution significantly beyond the layer. Therefore, one should minimize conductivity changes in the region between electrode plane and fat layer to monitor impedance changes of organs beyond the fat layer. The behavior of sensitivity changes is opposite for conducting layer.

It was observed that the sensitivity does not change significantly due to changes in conductor boundary if the distance of boundary from the electrodes is much higher compared to the electrode separations. However, as the boundary of the volume conductor approaches close to the electrodes, the magnitude of sensitivity increases greatly (Figure 4-33 and Figure 4-34). The proximity of the boundary to the electrodes also changes the pattern of sensitivity profiles Figure 4-35. Therefore the distance of boundary

of the volume conductor under study should be considered while interpreting impedance measurements.

The sensitivity distributions obtained experimentally are very similar to that obtained from finite element method simulations. The slight mismatch between the experimental and simulated results may be because of the experimental measurement system not being centred on the centre of the electrode array. However, within experimental limit, the experimental data closely match the simulation data.

3D sensitivity analysis is useful to choose an appropriate measurement method with proper electrode separations for a particular application. Experimental validation of sensitivity distribution builds up the confidence of using Comsol Multiphysics for transfer impedance measurements from FEM model of human thorax which is discussed in the next part.

Part: 2

4.5 Application of FIM in the study of localized lung ventilation

In respiratory physiology, ventilation is the exchange of air between the lungs and the environment. Lung ventilation is essential for proper gas exchange (Haldane and Priestley, 1905). In diseases like pulmonary edema, abscess, TB or pneumonia, fluids or masses are accumulated within the lungs restricting the flow of air to the alveoli (Robin et al., 1973, Nelson et al., 1995). This section describes a Finite Element Method (FEM) model of human thorax developed using Comsol Multiphysics to simulate respiratory related impedance changes in healthy and diseased conditions. The inspiration and expiration phases of breathing were modeled and the transfer impedance measurements from electrodes on the surface of thorax during inspiration and expiration phases were simulated in Comsol Multiphysics. Similar measurements were taken from a healthy human subject and compared with the simulation results. Finally, a new technique to detect localized lung ventilation disorders due to fluid accumulation in lung using multi-frequency FIM is proposed based on the results of simulation study.

4.5.1 FEM model of human thorax

4.5.1.1 Geometry

COMSOL Multiphysics is a tool to perform FEM analysis which includes tools to create 3d models. The upper part of a typical human thorax was modelled using the geometry tool of the Comsol Multiphysics software (version 5.0). The model of human thorax consists of 8 major domains:

    (i)   Left lung

    (ii)   Right lung

    (iii)   Heart containing blood

    (iv)   Ribcage

    (v)   Muscle

    (vi)   Subcutaneous fat layer

    (vii)   Skin layer
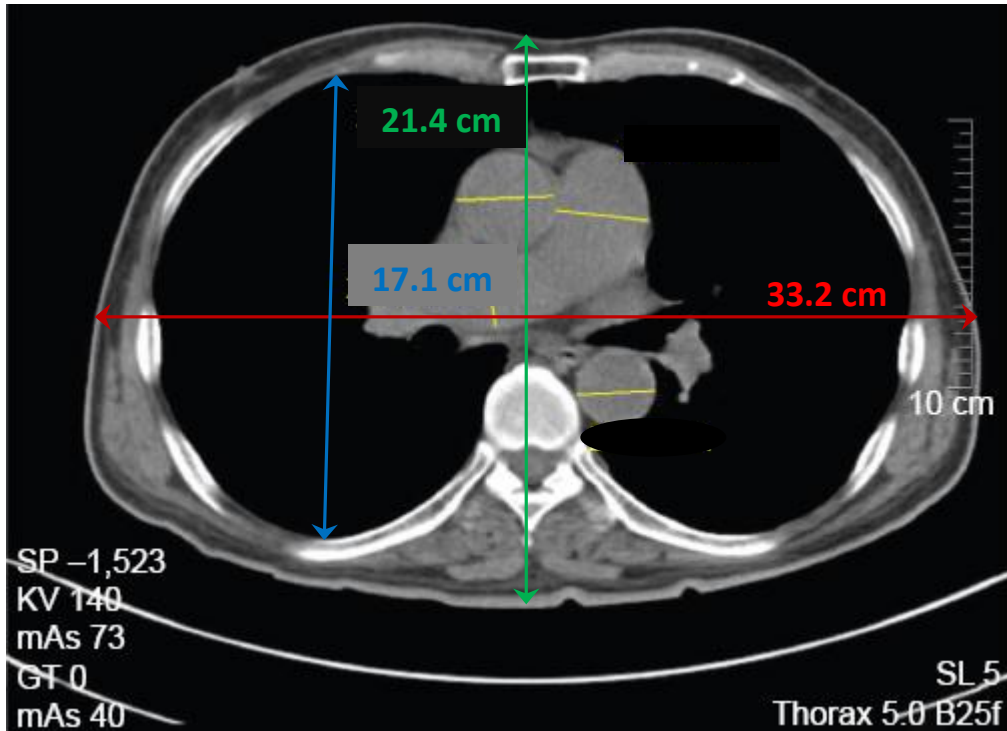
Figure 4-38 Transverse plane CT image of a human thorax at T-5 level, source (Chen et al., 2015).

The outer boundary of the thorax model was estimated from a CT images of a human subject shown in Figure 4-38 (Chen et al., 2015). The $10cm$ scale on the right hand side of the image was taken as reference from which width (left-right), depth (posterior to anterior distance) distances were calculated. Figure 4-39 shows the cross-section (transverse plane) of the FEM model of the human thorax at the same level as the CT
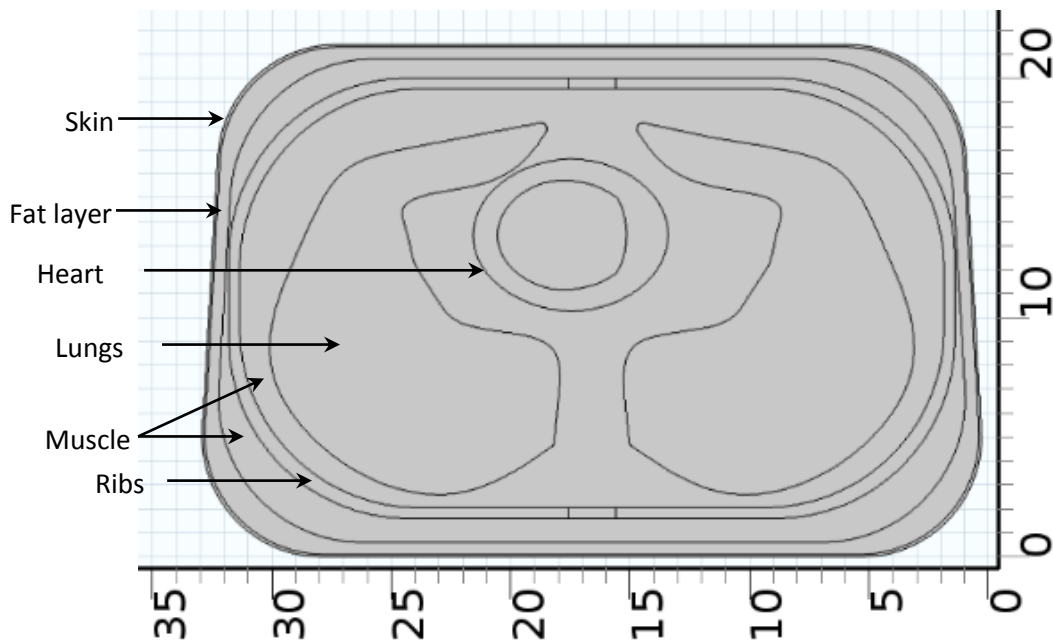
Figure 4-39 Cross-sectional view (transverse plane) of the human thorax model at level T-5. The numbers in the horizontal and vertical axis are in cm.

image (T-5). The posterior width of the modeled thorax (bottom in the figure) was 33cm whilst the anterior width was 32 cm (top in the figure). The anterior to posterior size of the modeled thorax was 21.4 cm. The outer boundary of the modeled thorax was estimated from the single CT slice shown in Figure 4-38 and kept same at all vertical levels for simplicity. Figure 4-40 shows the three-dimensional view of the thorax model. The outer most layer of the thorax was modeled as *skin* of thickness $1\ mm$. The layer inside the skin was modeled as *subcutaneous fat* of thickness $5mm$. *Muscle* tissue was modeled just inside the fat layer which also penetrated within the spaces between ribs. Different layers of the thorax were initially outlined in a 2D plane and then extruded in the 3rd dimension using the geometry tool of the Comsol Multiphysics software.
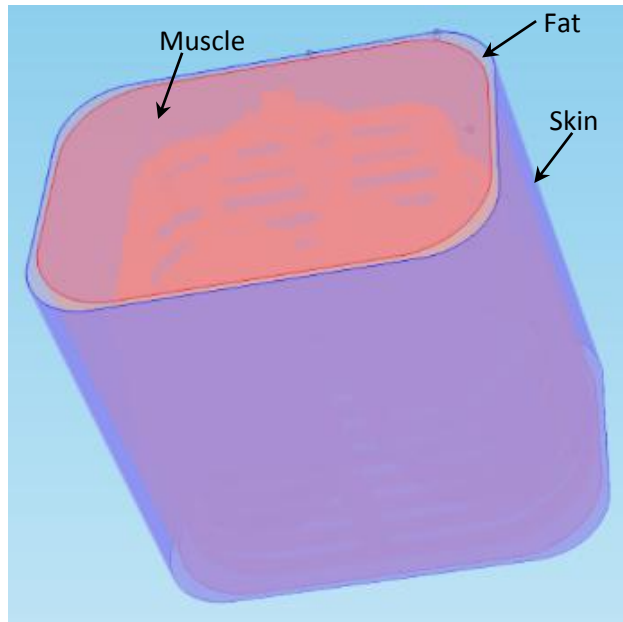
Figure 4-40 Three-dimensional view of the thorax model.

A ribcage consisting of 12 pairs of ribs and sternum was modeled as shown in Figure 4-41. Initially the shape of a rib was outlined as a 2D surface and then extruded three dimensionally. The spaces between two successive ribs were removed using the Boolean operation *difference* in the geometry tool of Comsol Multiphysics. The dimension of the ribs were estimated from the cross-sectional geometry of human ribs reported by Abrams et al (Abrams et al., 2003). However, the vertical curvatures of the ribs were ignored and all the ribs were considered as horizontal. The height of the thorax model was $31cm$ (distance from the bottom end of the 12th rib to the top edge of clavicles) as measured from a healthy male of age 35 years (height: 170cm).
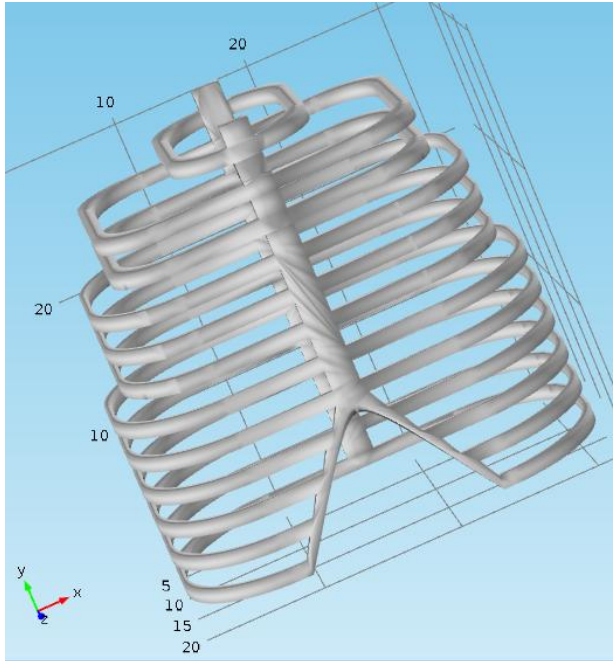
Figure 4-41 Ribcage of the modelled human thorax containing 12 pairs of ribs and sternum.

Two lungs having similar dimension and shape of human lungs were imported in to Comsol from a CAD design available online (CAD, 2016). The imported lung shapes were then scaled 3 dimensionally to resize them so that they could be placed inside the ribcage as shown in Figure 4-42. The width, depth and height of the lungs (combined) are 28cm, 17.5cm and 25.5cm respectively obtained from CT images of human thorax reported by Kramer et al (Kramer et al., 2012). Both the left and right lungs models were similar in shape and size and the volume of each lung was 2030 cm^3. Anatomically the left lung is smaller due to the position of the heart within the thorax and the position of the left lung is slightly lower compared to the right (Armstrong et al., 1982) but this was ignored in the current model.
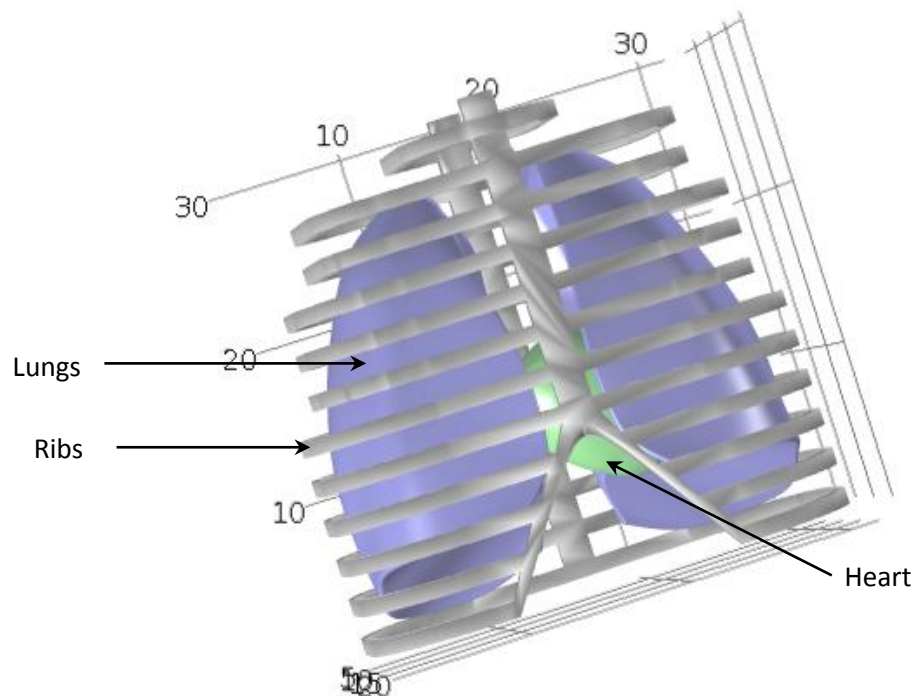
Figure 4-42 Comsol model of the human thorax showing ribcage, lungs and heart containing blood.
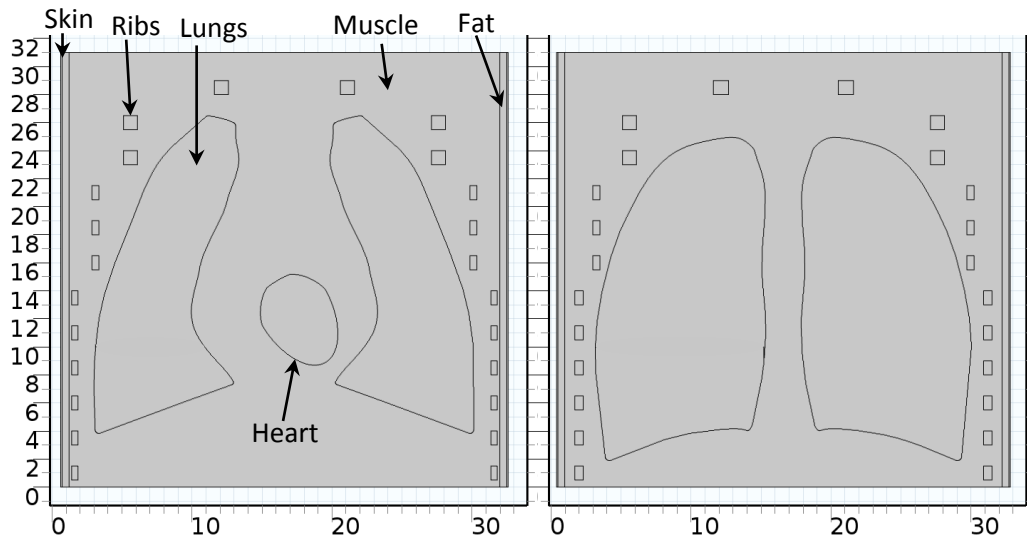
Figure 4-43 Cross-sectional (frontal plane) view of the modelled human thorax; along half-way of the thorax width from the front plane (left) and along two-third of the thorax width from the front plane. The numbers in the horizontal and vertical axes are in cm.

A heart containing blood was modeled and placed between two lungs. The length, width and depth of the modeled heart shape was 11cm, 8cm and 6cm respectively (Figure 4-42). The center of the heart was shifted towards the left and the vertical axis of the heart was tilted towards left as well. The spaces inside the *fat layer* not occupied by the ribs, lungs, or heart were simulated to be tissues having the same electrical properties as that of
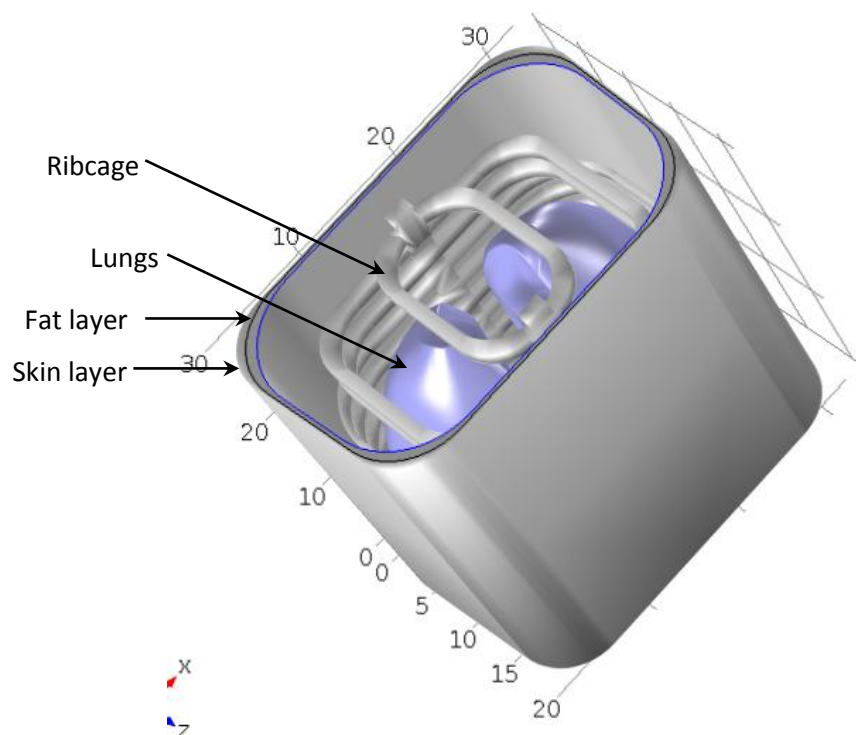
Figure 4-44 Full Comsol model of the human thorax showing various domains. For better visibility, of the inner domains, the muscle layer were kept invisible.

muscle. To build the overall model and to give it a realistic shape, the edges and corners of different geometry domains were rounded.

Figure 4-43 shows the cross-sectional (frontal plane) view of the thorax model along a plane half-way of the width from the front surface (left) and along a plane two-third of the total width away from the front surface (right). The complete 3D view model of the modelled human thorax is shown in Figure 4-44 where the muscle domain is kept invisible for better visibility of the inner domains.

The meshing tool in Comsol Multiphysics was used to generate the 3D mesh grid of the geometric model. A Physics controlled *Normal* mesh was used for computation of transfer impedance values. Figure 4-45 shows the mesh representation of the thorax model where the muscle domain was disabled for better visibility of the inner domains. The number of mesh elements was

Figure 4-45 Mesh representation of the thorax model. The muscle domain in the model was kept invisible for better visibility of the inner organs.

239469 (tetrahedral) and the number of degrees of freedom solved in computation of the transfer impedance values is around 1463412.

4.5.1.2 Electrical Properties

For simplicity, the thorax model was considered as piecewise homogeneous and isotropic. This means that any domain within the model was assumed to be homogeneous and isotropic, but electrical properties of different domains are different. In bioimpedance measurements, two dielectric parameters i.e. electrical conductivity and relative permittivity are considered. The dielectrics properties of various organs within the human thorax at different frequency was obtained from (Andreuccetti D, 1997). The values of electric conductivity and permittivity assigned to various domain of the thorax model at 10 kHz and 1 MHz is summarized in Table 4-2. The dielectric properties of lungs tissue changes as a function or air content in lungs (Nopp et al., 1993). The maximum inspiration and maximum expiration phases of respiratory cycle were therefore simulated by assigning dielectric properties of inflated and deflated lung tissues respectively.

Although the lung volume changes significantly during respiration, the volume and position of the lungs, and other organ within the current thorax model, was not changed in inspiration and expiration for simplicity; only the dielectric properties of lungs tissue were changed to simulate breathing.

Table 4-2 Dielectric properties of various domains within the human thorax model at two extreme measurement frequencies (Andreuccetti D, 1997).

Frequency Domains	10 kHz	1MHz	Unit
Lungs deflated			
Conductivity	0.2429	0.33438	S/m
Relative Permittivity	34044	1170	
Lung Inflated			
Conductivity	0.093172	0.13609	S/m
Relative Permittivity	17174	733	
Skin			
Conductivity	0.0029317	0.2214	S/m
Relative Permittivity	29010	1832	
Fat			
Conductivity	0.02383	0.025079	S/m
Relative Permittivity	1085	27	
Muscle			
Conductivity	0.34083	0.50268	S/m
Relative Permittivity	25909	1836	
Ribcage			
Conductivity	0.02043	0.024353	S/m
Relative Permittivity	521	144	
Heart			
Conductivity	0.15421	0.32753	S/m
Relative Permittivity	70054	1967	
Blood			
Conductivity	0.70004	0.82211	S/m
Relative Permittivity	5248	3026	
Body fluid			
Conductivity	1.5	1.5007	S/m
Relative Permittivity	98	84	
Electrodes			
Conductivity	4.6×10^6	4.6×10^6	S/m
Relative Permittivity	1	1	

4.5.2 Computation of transfer impedance

The simulation was performed in the frequency domain of AC/DC module at 10 kHz. Boundary conditions were set so that the current density on the outer boundary of the

thorax is zero whereas the boundaries between internal domains satisfy continuity. Physics controlled normal mesh was used for the computations. For bioimpedance measurements, cylindrical electrodes (Steel AISI-4340) of diameter 0.5 cm were placed on the skin surface of the thorax model (Figure 4-46). It was observed from the sensitivity analysis discussed in the 1st part of this chapter that FIM-4 has better depth penetration and localization ability than other FIM electrode configurations. Therefore FIM-4 configuration was used for the transfer impedance simulations. The *electric current (ec)* interface of AC/DC module of Comsol Multiphysics software was used to introduce currents (Pettersen and Høgetveit, 2011). Current was injected through electrode pair A-B while the corresponding reciprocal current was injected through the electrode pair C-D. For FIM-4 measurements, current was also injected orthogonally and sequentially through the electrode pair A-C while the corresponding reciprocal current was injected through the electrode pair B-D. If J_{AB}, J_{CD}, J_{AC} and J_{BD} are the current density vectors at a point within the thorax model for injection of current *I* through the electrode pairs (A-B), (C-D), (A-C) and (B-D) respectively (Figure 4-46), then the FIM sensitivity *FS* at that point is given by (Kadir et al., 2013)

$$FS = \frac{J_{AB} \cdot J_{CD} + J_{AC} \cdot J_{BD}}{I^2} \quad \ldots\ldots.4\text{-}9$$

Again the focused transfer impedance of an organ (say lungs) of conductivity **σ** embedded within the volume conductor can be obtained from the equation where the integration is over the lungs volume, v_l

$$FZ_{Lungs} = \int_{v_l} \frac{1}{\sigma} \left(\frac{J_{AB} \cdot J_{CD} + J_{AC} \cdot J_{BD}}{I^2} \right) dv \quad \ldots\ldots 4\text{-}10$$

Since there are several domains (organs) within the thorax model, the total focused transfer impedance of the model can be given as

$$FZ_{total} = \int_{v_t} \frac{1}{\sigma} \left(\frac{J_{AB} \cdot J_{CD} + J_{AC} \cdot J_{BD}}{I^2} \right) dv \quad \ldots.4\text{-}11$$

where the integration is over the whole volume of the thorax, v_t. In all cases the current of $1A$ was applied for ease of calculation. It can be noted that the transfer impedance value does not depend on the injected current amplitude. Throughout the thesis, *FZ* represents the absolute value (modulus) of focused transfer impedance. Two orthogonal tetra-polar impedance measurements are summed in the focused transfer impedance, *FZ*. For a homogeneous medium the sensitivity beneath the centre of the electrode array is double that of the individual measurements. However this is not the case for an inhomogeneous medium and therefore evaluation of equations *4-10* and *4.11* must be carried out in full.
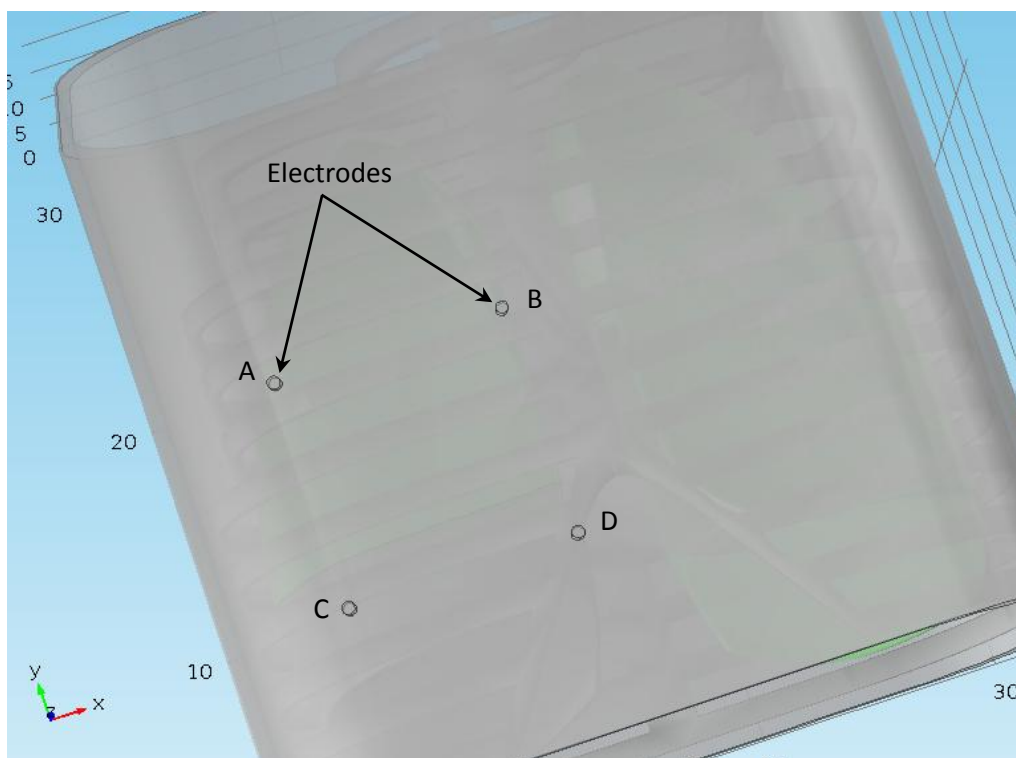
Figure 4-46 FIM-4 electrode configuration with electrode separation 9cm placed on the front plane of the thorax model for transfer impedance measurements.

4.5.3   Optimum electrode separation

As discussed earlier in section 4.3.5, the region of localisation achieved in FIM depends on the electrode configuration and the electrode separation. Having identified FIM-4 as giving the best localisation (section 4.3.5) it is now necessary to determine the optimal electrode separation for identifying regional lesions in the lung. For this purpose, the lower part of the right lung of the thorax model was partitioned and defined as a region of interest (ROI) as shown in Figure 4-47. The volume of the ROI was arbitrarily chosen as 663cm^3 so that the ROI volume remains beneath the area bounded by the electrode array. The volume of the ROI was measured using the volume integration tool in Comsol Multiphysics. Dielectric properties of various domains within the thorax model were assigned as listed in Table 4-2. The lungs were assumed to be in an inflated state and the appropriate dielectric properties were assigned. For this present study to find an optimum electrode separation the *ROI* is only partitioned geometrically from the lungs; it was assumed to be inflated with the same electrical properties as for the rest of the lungs. The electrodes were placed on the front surface of the thorax so that the center of the electrode configuration is just above the representative center of ROI as shown in Figure 4-47 where the domains between the electrodes and the lungs are not shown in this figure so that the positions of the electrode array and the *ROI* can be better visualized.
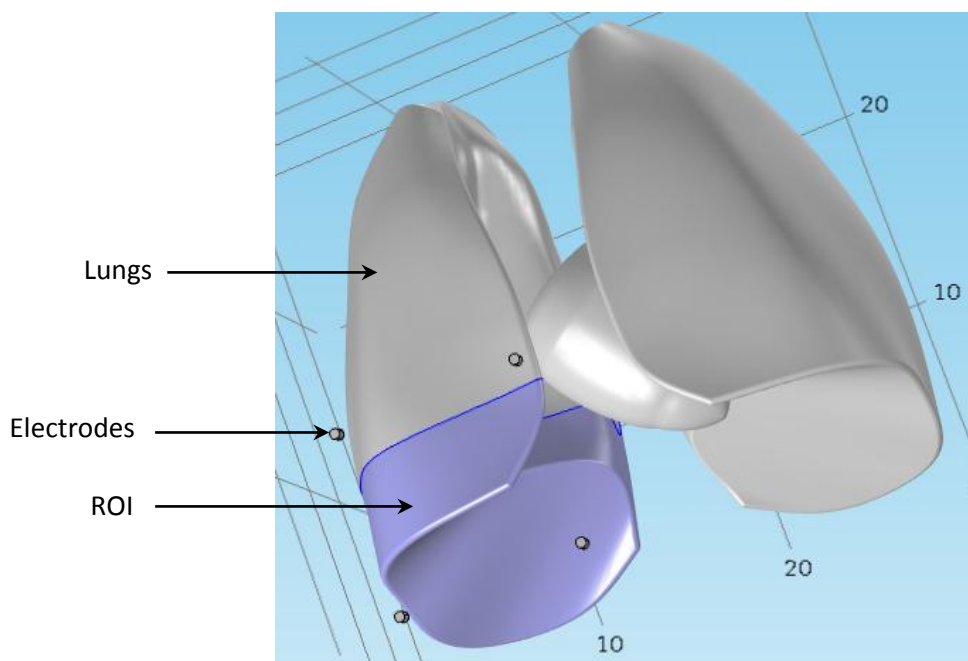
Figure 4-47 Lower part of the right lung is partitioned as region of interest (ROI). The electrodes (separation 9cm here) were placed on the thorax surface but the domains between electrodes and lungs are not shown so that the electrode array and the ROI can be better visualized.

In order to obtain an optimum separation of FIM-4 electrode configuration, the electrode separation was varied and total transfer impedance of the thorax (which includes the ROI and the rest of the thorax) as well as the transfer impedance contribution of the ROI were obtained using COMSOL simulations. The total focused transfer impedance of the whole thorax (FZ_{total}) was obtained from simulation using equation 4-3. At the same time, the focused transfer impedance of the *ROI* (FZ_{ROI}) only was also computed from simulation using equation 4-2 where the integration was performed over the volume of *ROI* only. For different electrode separations, only the positions of electrodes were changed keeping the position of *ROI* fixed beneath the electrode array. The *integration* tool under the node *component coupling* in the Comsol software was used to perform the integration where the equation and volume/domain over which integration needed to be performed can be specified.
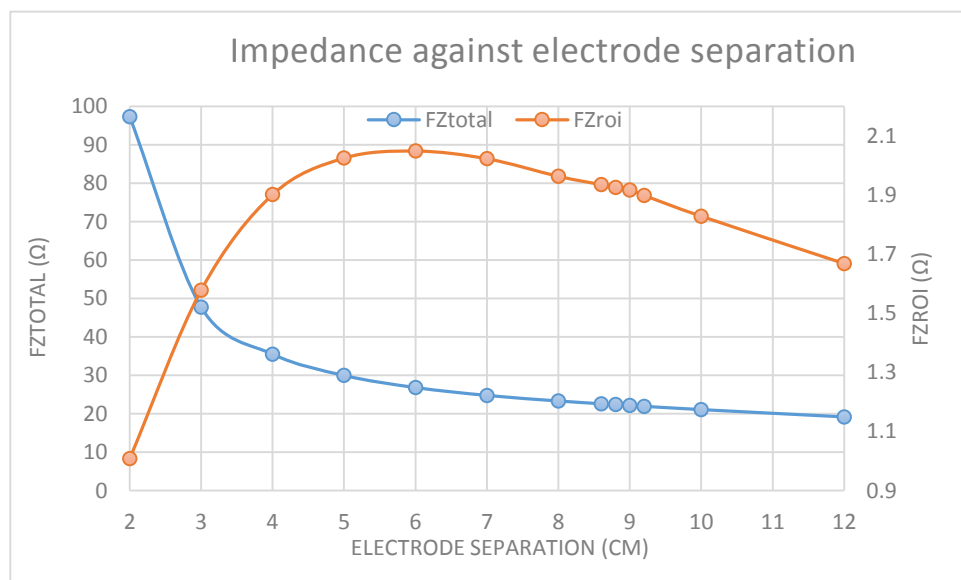
Figure 4-48 Variation of total focused impedance and contribution of ROI in the total focused impedance with electrode separation. The vertical scale on the left had side quantifies the total focused impedance and the vertical scale on right hand side quantifies the transfer impedance of ROI only in ohms

The variation of *total focused transfer impedance* (FZ_{total}) and focused *transfer impedance values of* the *ROI* only(FZ_{ROI}) (i.e., the contribution of the ROI only) are shown against electrode separation in Figure 4-48. It can be observed that total focused impedance decreases rapidly with increasing electrode separation initially, and then decreases gradually. This behaviour of transfer impedance change on thorax is in agreement with the observation that the overall sensitivity is inversely proportional to the square of electrode separation as reported in section 4.3.3 in the 1st part of this chapter. It

should be noted that this relationship will be modified by the inhomogeneity of the thorax model. As can be seen, the contribution of the region of interest (FZ_{ROI}) initially increases rapidly with electrode separation, reaches a maximum and then decreases gradually. This is because the anterior surface *ROI* is located at a depth of about 3cm from the electrode plane; for low electrode separation, more contribution comes from the tissues in front of the *ROI*, and the contribution of the ROI is small. The contribution of the *ROI* increases with increasing electrode separation initially because of higher percentage depth sensitivity (PDS) with larger electrode separation as reported in section 4.3.4. The contribution of ROI decreases beyond a certain electrode separation because at larger electrode separation the volumes outside the ROI come within the focused zone of the electrode configuration.

In practical measurements, the impedance of the ROI (FZ_{ROI}) is included within the value of total focused impedance (FZ_{total}) that cannot be measured separately. Therefore a new parameter, *fractional contribution of ROI* to the total thorax impedance as measured by a particular electrode configuration is defined as below

$$\boldsymbol{fractional\ contribution\ of\ ROI = \frac{FZ_{ROI}}{FZ_{total}} \times 100} \ \textit{...... 4-12}$$

expressed as a percentage contribution by multiplying by 100.
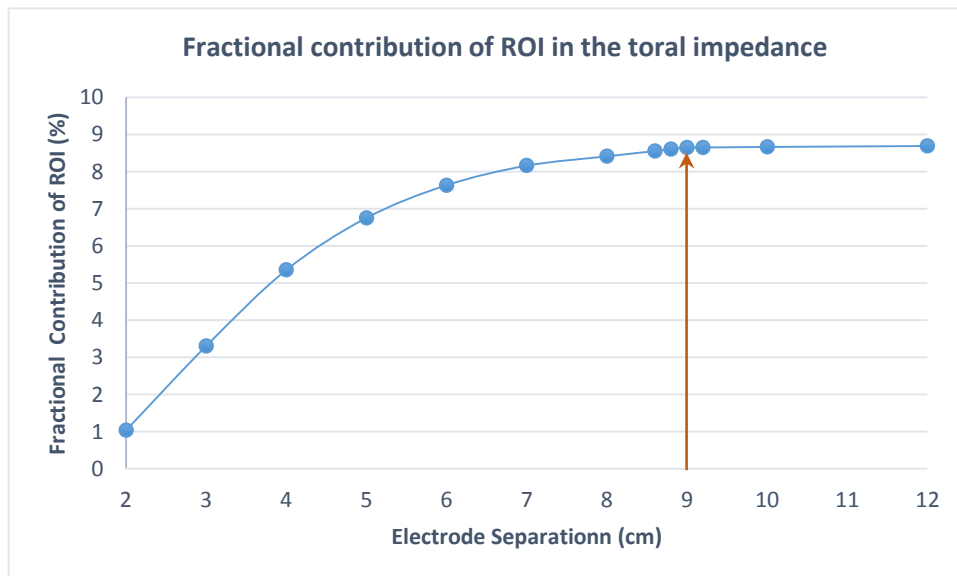
Figure 4-49 Variation of the percentage impedance of ROI in the total thorax impedance against electrode separations.

The variation of *fractional impedance of the ROI* is plotted against electrode separation in Figure 4-49. It can be observed that the *fractionall contribution of ROI* increases with

electrode separation; the increasing curve is less steep at larger electrode separations, the slope decreasing with increasing electrode separation till it levels off in a plateau. It may be observed that in this case the plateau starts at an electrode separation of $9cm$, which can be taken as an optimum electrode separation. However, an alternative approach was suggested to obtain a numerical value for the optimum electrode separation as presented below.

High values of *fractional contribution of ROI* are desirable in practical measurements, particularly in cases where the lower lung has edema or some disorder. In such a scenario, the variation of impedance between inspiration and expiration will be reduced in the ROI and to measure it with high accuracy and resolution, the contribution of the ROI should be as large as possible to the total measured focused impedance.

To optimize the electrode separation, an optimization factor is defined below as,

$Optimization\ Factor$

$$= fractional\ contribution\ of\ ROI\ \times\ impedance\ contribution\ from\ ROI$$

which essentially equals (FZ$_{ROI}$)^2/FZ$_{Total}$.
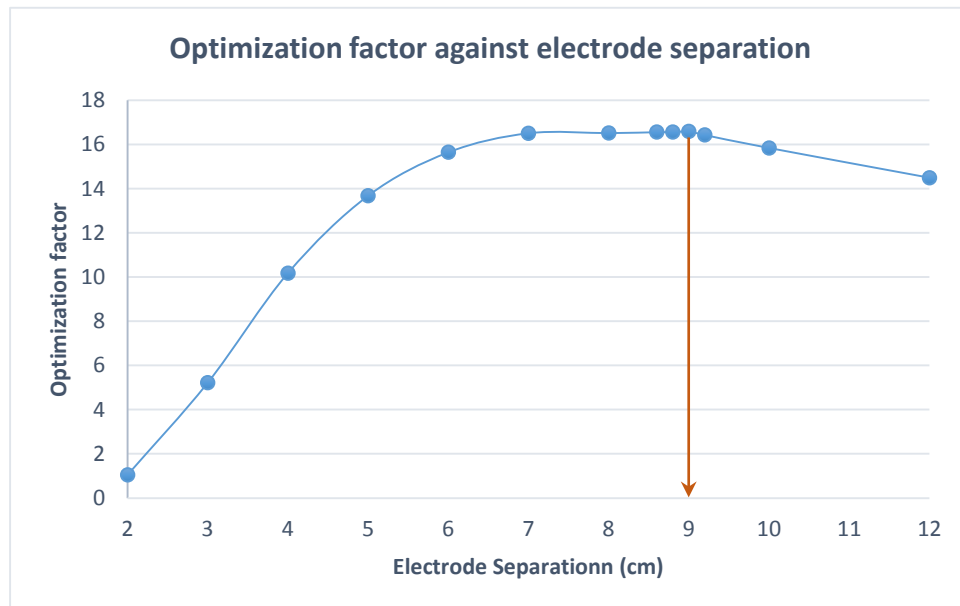
Figure 4-50 Variation of optimization factor against electrode separation. The optimization factor is maximum between electrode separation of 7cm and 9cm.

The variation of *optimization factor* with electrode separation is shown graphically in Figure 4-50. Optimization factor increases sharply with electrode separation reaches a maximum and decreases gradually. The electrode separation, at which the optimization

factor is maximum is rather broad, between 7cm and 9cm. Since the separation at the start of the levelling off of the curve in Figure 4-49 was 9cm, so the separation **9cm** was chosen as the optimum electrode separation for the lungs ventilation study. This also matches the separation chosen earlier from Figure 4-49, at the start of the levelling off of the curve.

To study the effect of subcutaneous fat layer thickness at the optimum electrode separation, similar measurements were simulated for different fat thickness of the thorax model. Although, the fat thickness was changed, the distance between the thorax surface and the lungs remained constant; only the muscle thickness were reduced to accommodate increased fat thickness. The variation of total focused transfer impedance with electrode separation for different subcutaneous fat thickness is shown in Figure 4-51. It can be observed that the total transfer impedance increases with increasing fat thickness at a particular electrode separation. This is because the impedivity of fat is higher compared to that of muscle tissue which is reduced in amount to accommodate the increased fat thickness. According to equation 4-3, the total transfer impedance of a volume conductor for a particular electrode configuration depends on various factors including: (i) sensitivity (ii) conductivity and (iii) sensitive volume over which the
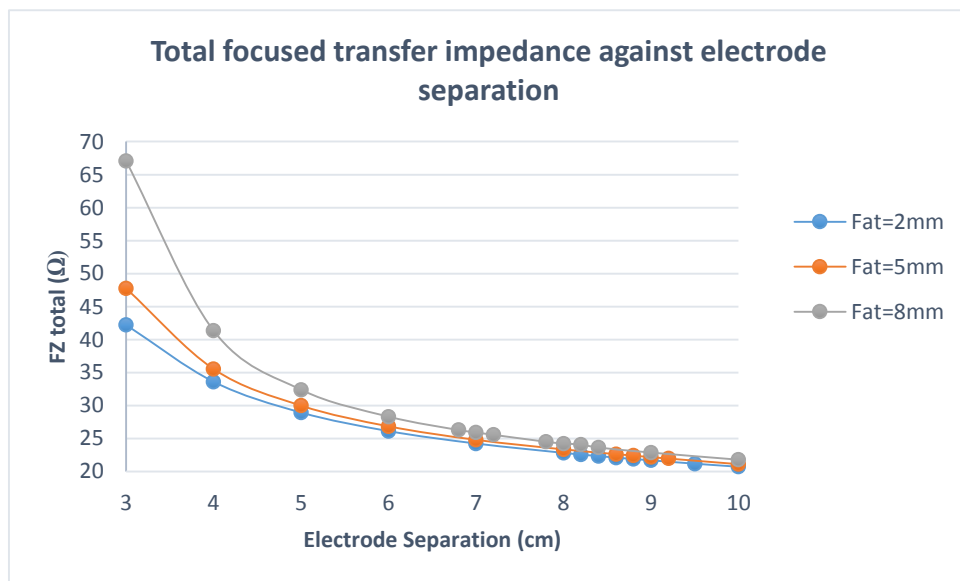
Figure 4-51 Variation total focused transfer impedance with electrode separation for various subcutaneous fat thickness.

integration is made. Therefore the increase in less conducting fat layer increases the total transfer impedance. However, the increase in total transfer impedance with fat thickness is more prominent at lower electrode separations than that at higher electrode separation. This is because at lower electrode separations, the maximum sensitivity regions are just

below the electrode array (1/3 of the electrode separation) which include substantial amount of fat tissues and therefore changes in fat thickness influence the total transfer impedance greatly. On the other hand, at higher electrode separation, maximum sensitivity regions are much extended that includes substantial amount of more conducting tissues other than fat. Therefore the influence of fat thickness to the total transfer is relatively low at higher electrode separations.

The variations of *fractional contribution of ROI* in the total focused transfer impedance against electrode separation for different fat thickness is shown in Figure 4-52. It can be observed that the general shape of the curves are similar for different fat thickness and the electrode spacing at which the plateau region starts increases with decreasing fat thickness. The fractional contribution of ROI increases with increasing electrode separation at a particular fat thickness as noted earlier and is higher for higher fat thickness. In the thorax model, the muscle and other soft tissues in between the subcutaneous fat layer and the ROI are reduced with increased thickness of the fat layer. The impedance of the bulk beyond the fat layer contributes more with increased electrode separation in which the muscle layer, being of higher conductivity, will tend to
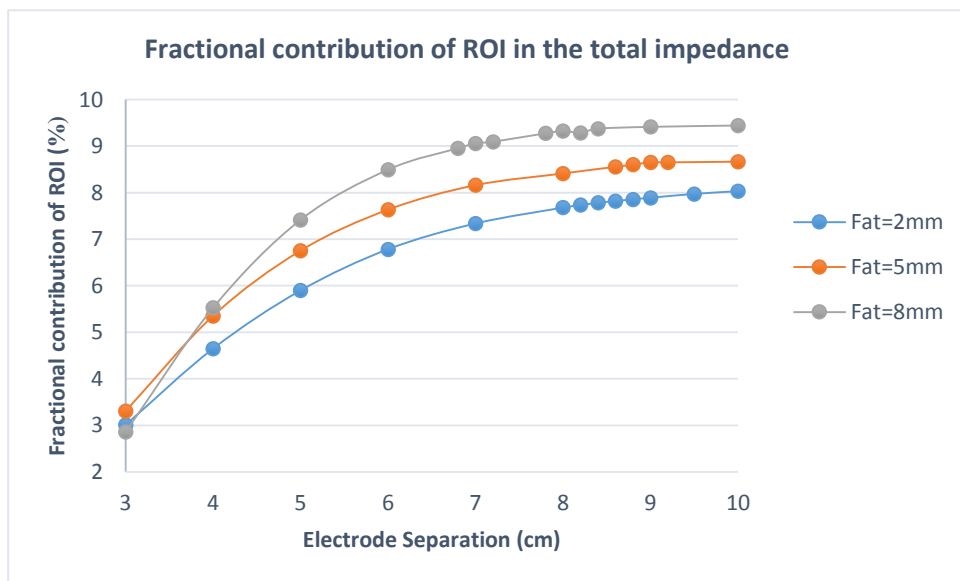
Figure 4-52 Variation of fractional contribution of ROI in the total impedance with electrode separation for various subcutaneous fat thickness.

concentrate more of the current while some will go into the inflated lungs in the ROI at the back. With increasing thickness of the fat layer, the thickness of the muscle layer will decrease, therefore, more current will go into the lung tissue of the ROI, making its contribution greater.

Figure 4-53 shows the variation of optimization factor with electrode separation for different fat thickness. The general shape of the curves are similar and the numerical values of optimization factor is higher for higher fat thickness at all electrode separations. It can be observed that the optimization factor reaches a peak value for all subcutaneous fat thickness although the electrode separation at which the peak occurs is different. The optimum electrode separation for $8mm$ thick fat layer is $7cm$ while it appears to be slightly higher for smaller fat thicknesses. However, the peaks are rather broad for $5mm$ and $2mm$ fat thicknesses and may not be clearly identified. These may be between $7cm$ and $9cm$ and between 8cm and $10cm$ respectively. It should be noted that the variation of optimization factor with electrode separation around optimum electrode separation is very small. For example, the variation of optimization factor is only 0.5% for variation of electrode separation from 7cm to 9cm in case of the subcutaneous fat layer of 5mm. Therefore, the optimum electrode separation could be changed for small changes in the shape and size of the *ROI*. The existence of the plateau also means that once the electrode separation is in the plateau region, there is only a small change in the optimization factor with separation and therefore the electrode separation is tolerant to changes in surface geometry and fat thickness.
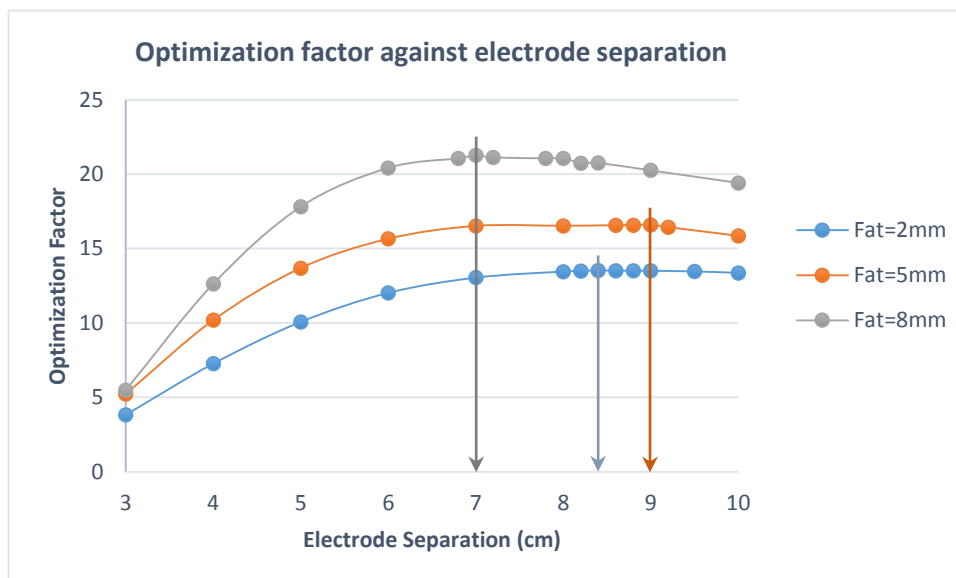
Figure 4-53 Variation of optimization factor with electrode separation for different fat thickness. The vertical arrows indicates the optimum electrode separations for the corresponding fat thickness.

4.5.4 Lung ventilation: FEM simulation study

In order to study lung ventilation using FIM it is necessary to measure the changes in the transfer impedance values of the thorax during breathing. For this purpose, two phases of respiratory cycle: full inspiration and full expiration were modelled in Comsol Multiphysics. The volume of lungs or the volume of any other domain of the thorax model was not changed between these maximum inspiration and maximum expiration phases of breathing. The inspiration and expiration phases of breathing were simulated by assigning dielectric
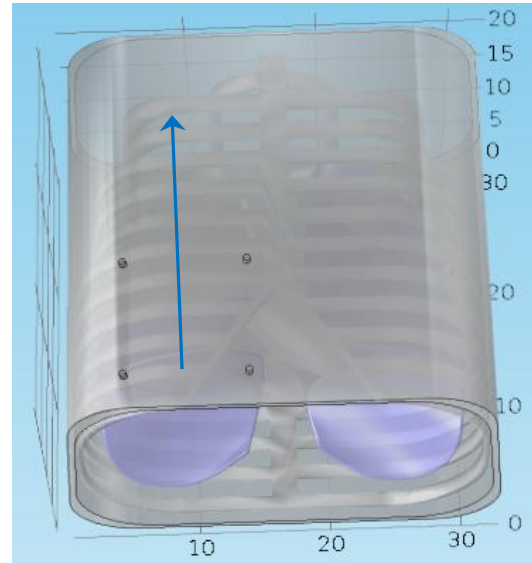
Figure 4-54 Vertical sweep of electrode configuration to compute focused impedance at different vertical level of the right lung. Optimum electrode separation 9cm were used.

properties of inflated lung tissue (σ=0.093172 S/m and μ_r=17174 at 10kHz) and deflated lung tissue (σ= 0.2429S/m and μ_r=34044 at 10kHz) to the lungs domain in the thorax model. The dielectric properties of domains except lungs were not changed in the inspiration and expiration phases of breathing. Initially, the dielectric properties of inflated lungs were assigned to the lungs domain in the model to simulate full inspiration. The total focused transfer impedance (FZ_{total}) values were computed using Comsol simulations. After that the dielectric properties of deflated lungs were assigned to the lungs domain to represent full expiration and impedance values were computed. In this study, the thorax model with a subcutaneous fat layer of $5mm$ was considered. Electrodes for the FIM-4 configuration with optimum separation ($9cm$) were place on the skin surface of the thorax model. The percentage change in focused impedance values (ΔZ) between inspiration and expiration phases were calculated using the equation below

$$\Delta Z \, (\%) = \frac{FZ_{total}(inspiration) - FZ_{total}(expiration)}{FZ_{total}(expiration)} \times 100 \quad ....4\text{-}13$$

The values of ΔZ were computed at different vertical levels of the thorax by sweeping the electrode configuration vertically as shown in Figure 4-54. The electrode configuration was moved from the lower edge of the bottom rib to the level of clavicle in steps of 3cm. Here vertical level means the vertical position of the centre of the electrode configuration

of FIM-4 on the chest surface, electrode separation being 9cm. The starting value of vertical level (6 cm) corresponds to the position where the lower electrode pair of the FIM-4 configuration is at the level of the lower edge of the lowest rib. Similarly the highest value of vertical level (26cm) corresponds to the position where the upper electrode pair of the FIM-4 configuration is at the level of clavicle. The impedance simulations were performed on both left and right side of the thorax model to cover both lungs. It was assumed that the value of ΔZ will be higher for lung regions with higher ventilation. In other words, if any localized region is not properly ventilated, then the value of ΔZ in that region will be significantly low compared to its surroundings. Also if the lungs takes up more of the total sensitive volume, the value of ΔZ will be more, and vice versa.

4.5.5   Lung ventilation: Experimental study on human subject

Focused impedance values were measured experimentally from a healthy human subject using the multi-frequency FIM system based on digital demodulation developed as part of this work and is described in Chapter 3. The purpose of this study was to investigate how closely the FEM thorax model represented the human thorax for an FIM-4 transfer impedance measurements. The subject was seated straight on a chair and a hand held electrode probe was placed on the chest surface as shown in Figure 4-55. The electrode separation was 9cm (along a side of the square geometry of the electrodes, optimum

Figure 4-55 Experimental setup for measurement of focused impedance from human subject using multi-frequency FIM system made as a part of the present work. The electrodes are mounted on a hand held portable probe.

electrode separation discussed earlier, distance measured from centre to centre of the electrodes). Cotton pads, soaked in saline, were placed at the four tips of the probe to cover metallic terminals inside. Initially the subject was instructed to breathe in fully (full inspiration) and hold it for a short time during which focused impedance values were measured. The subject was then instructed to breathe out fully (full expiration) and hold the *breathe* and FIM measurements were also performed in this phase. Similar measurements were performed by placing the electrode probe at other vertical levels on the chest surface. Each set of measurements on both left and right lung was repeated four times, twice in a day and again twice the next day. The mean values of the experimental measurements were then compared with that computed from FEM model.

4.5.6 Study of localized lung ventilation disorder

In diseases like pulmonary edema or pneumonia, fluid is accumulated in localized regions within the lungs, restricting the flow of air to the alveoli. It has long been recognized that the fluid accumulation starts at the lower part of the lungs (BASTEDO, 1917) because gravity ensures fluid is at the base of the lung when the patient is sitting or standing. The purpose of this study is to investigate if FIM measurements can detect fluid accumulation in lungs. If some portion of the lung is filled with fluid, air will not enter into that region properly. Accumulation of fluid will result in little change of lung impedance values
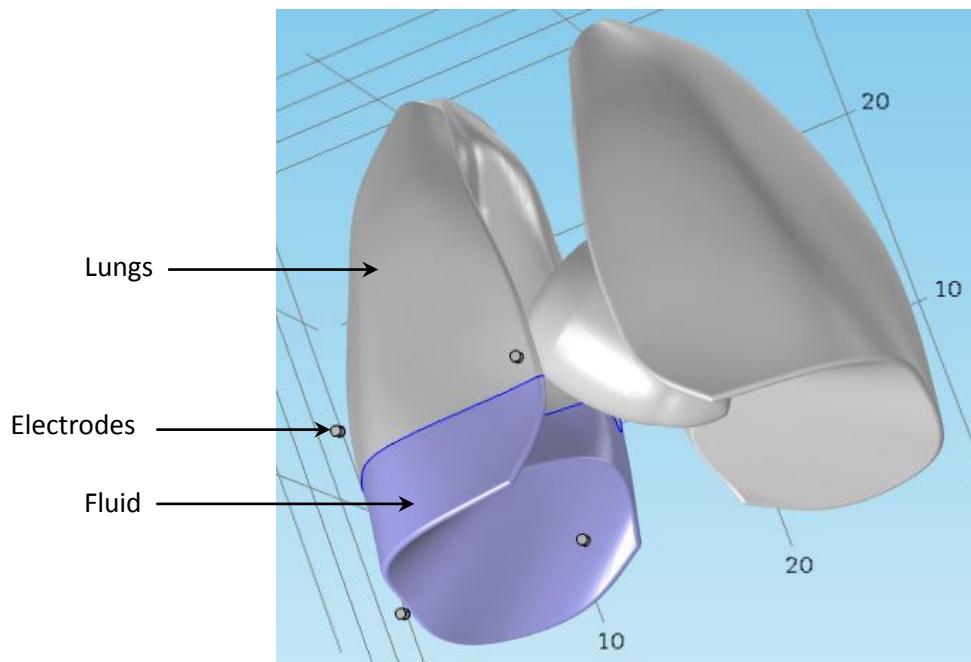
Figure 4-56 Lower part of the right lung is partitioned and defined as fluid. The electrodes (separation 9cm here) were placed on the thorax surface but the domains between electrodes and lungs are hidden for better visualization. Volume of the simulated fluid is 663cm^3 whereas the total lung volume is 4060cm^3.

between inspiration and expiration. In addition the conductivity and permittivity of the fluid filled region will be different from normal values of these parameters for the healthy lung. To study localized ventilation disorder, total focused transfer impedance values were first computed by placing electrodes at different vertical levels on the thorax during maximum inspiration and expiration. As mentioned above, maximum inspiration and maximum expiration were simulated by assigning dielectric properties of inflated lung tissue (σ=0.093172 S/m and μ_r=17174 at 10 kHz) and deflated lung tissue (σ= 0.2429S/m and μ_r=34044 at 10 kHz) to the lungs domain in the thorax model. These impedance values represented the healthy lungs. For the second set of measurements, the lower part of the right lung was partitioned to simulate fluid accumulation as shown in Figure 4-56. The dielectric properties of body fluid (σ=1.5 S/m and μ_r=98 at 10kHz) was assigned to this region only to simulate fluid accumulation in the lower part of right lung. The volume of the simulated fluid was 663cm^3 (arbitrarily chosen). The dielectric properties of lungs domains (rest of the lungs outside the ROI) were changed appropriately to represent inspiration and expiration phases of breathing by assigning inflated and deflated lung tissue properties respectively. The dielectric properties for the fluid and other domains except lungs were kept constant irrespective of whether inspiration or expiration was being modelled. Electrodes were placed on the thorax surface and then impedance measurements were simulated in Comsol Multiphysics applying unity current. Total focused transfer impedance of the whole thorax was obtained by computing equation 4-3, which represented diseased lungs. To explore the effect of fluid volume on the impedance changes, similar computations for Focused transfer impedance were performed for varying amount of simulated fluid in the right lung. Impedance measurements were also simulated at multiple frequencies for both healthy and diseased lungs to study the impedance variations with the excitation current frequency.

4.5.7 Results and observations

4.5.7.1 Sensitivity distribution

The FIM sensitivity distributions within the thorax model with subcutaneous fat thickness of $5mm$ and optimum electrode separation of $9cm$ with deflated lung property was obtained using Comsol simulations. The sensitivity distribution along the frontal planes $7cm$ (one-third of the thorax width, reference Figure 4-39) and $14cm$ (half of the thorax width) away from the electrode plane (thorax surface) is shown in Figure 4-57 where the unit of sensitivity is $1/m^4$. In this case the center of the electrode array was at a vertical level of $15cm$ (mid of the thorax height, reference being the bottom of the thorax model) on the right side of thorax. It should be noted that the minimum and maximum values of sensitivity on the colour bar of the two figures are different. It can be observed that the sensitivity is relatively higher just below the electrode array compared to the neighbouring regions. The sensitivity distributions reported earlier in Figure 4-10 of section 4.3.1 for a homogeneous medium are similar to those obtained from human thorax. Importantly, the sensitivity value on the left lung is almost negligible while the electrodes are on the right side of thorax. However, the sensitivity in the inner portion of the heart is significant because the conductivity of the blood content in the heart is higher compared to its surroundings.
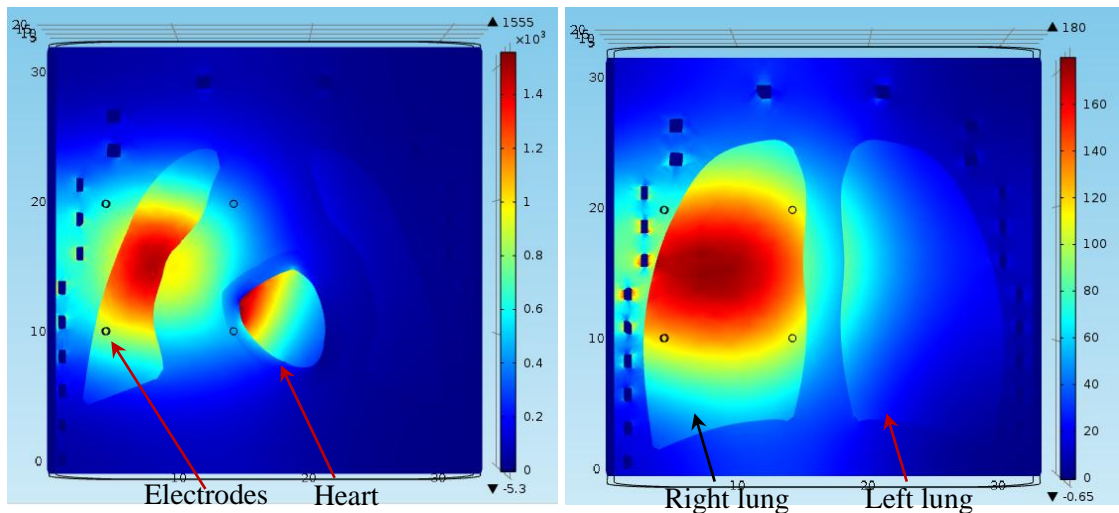
Figure 4-57 Sensitivity distributions along the frontal planes at 7cm, one-third of the thorax width (left figure); and at 14cm, half of the thorax width (right figure) away from the electrode plane (thorax surface) for electrode probe placed at a vertical level of 15cm on the right side of thorax. The minimum and maximum values of sensitivity in the colour bar are different in the two figures for better visualization. The unit of sensitivity in the colour bar is 1/m⁴.

The sensitivity distributions in the transverse (horizontal) planes along the centre of the electrode configuration for position of the centre of the electrode array at two vertical levels $6cm$ and $15cm$ are shown in Figure 4-58 (electrodes placed on the right side of thorax). There are no ribs at vertical level of 15cm (figure on the right hand side) because this transverse plane is in between two successive ribs. It is evident that the sensitivity is much higher just below the electrode array within the muscle tissue, negative sensitivities being also present. This figure shows the impact of the sensitivity profiles obtained on a homogeneous medium reported in section 4.3.1 when measurements are made on the human thorax. The sensitivity on the left lung is almost negligible while the electrodes are on the right side of thorax; only a small region of the right lung contributes to the transfer impedance. In FIM-4, negative sensitivities occur on the all four sides between the electrodes and decrease rapidly with depth, disappearing after about $1/3^{rd}$ of the electrode separation. Therefore, with an electrode separation of 9cm, negative sensitivity will be present to a depth of about 3cm, which will be the region external to the lungs in most cases, within the muscle, fat and skin tissues. Therefore, these zones with negative sensitivity will not contribute significantly to the dynamic ventilation studies of the lungs.
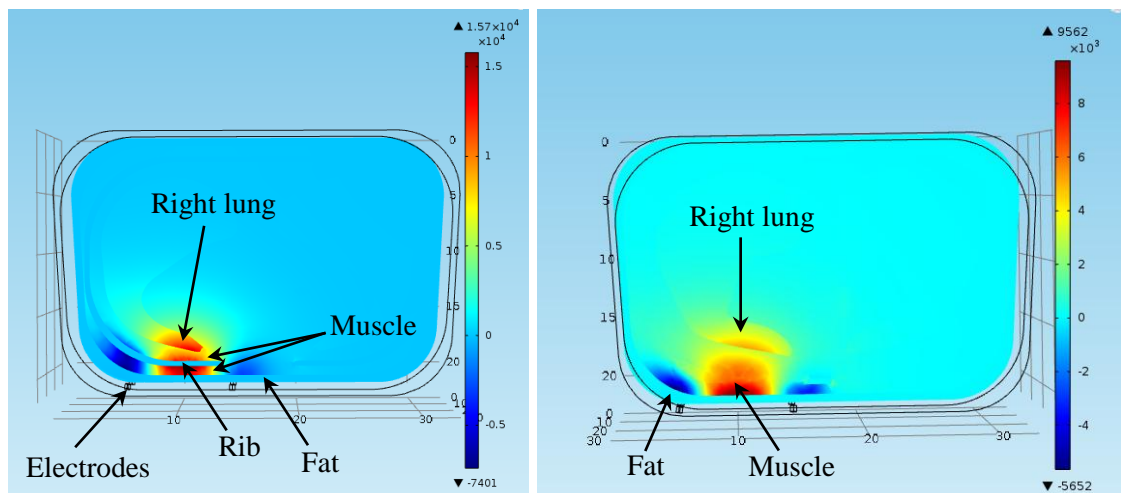
Figure 4-58 Sensitivity distributions in the transverse planes along the centre of the electrode configuration for position of the centre of the electrode array at vertical levels 6cm (left) and 15cm (right). The minimum and maximum values of sensitivity in the colour bar are different on two figures for better visualization. The unit of sensitivity in the colour bar is 1/m⁴.

In the present simulated model, since the lung volume does not change with respiration, only the change in the appropriate lung region will contribute to the total change in focused impedance. On the other hand, in a real human body, the lung volume will change with respiration so that the volumes, positions and shapes of regions external to the lungs, closer to the electrodes will also change. This will contribute substantially to the

impedance change measured, particularly for the $6cm$ height, where lower edge of the right lung is just at the edge of the focused region. Moreover, the thickness and distribution of subcutaneous fat and muscle layers and the electrode position on the chest surface may change during respiration. Tissues in negative sensitive regions near the electrode plane may change during respiration, affecting the total impedance change measured between inspiration and expiration. This may be the reason that some negative sensitivity impedance changes between inspiration and expiration were observed by (Ferdous, 2014).

4.5.7.2 Lung ventilation: FEM simulation study

The percentage change in focused impedance values between inspiration and expiration, ΔZ as defined in equation 4-5 was computed for simulated healthy lungs (no fluid) to study if FIM can detect the impedance change due to breathing. Figure 4-59 shows the variation of ΔZ against vertical levels of the thorax model for the right and left lungs respectively, at a signal frequency 10 kHz. Here vertical level means the vertical position of the centre of the electrode configuration of FIM-4 on the chest surface, the electrode separation being $9cm$. The starting value of vertical level ($6cm$) corresponds to the position where the lower electrode pair of the FIM-4 configuration is at the level of the lower edge of the lowest rib. Similarly the highest value of vertical level (26cm) correspond to the position where the upper electrode pair of the FIM-4 configuration is at the level of clavicle. It can be observed that ΔZ starts at about 16% at the lowest vertical level of measurement, increases to about 24% at a vertical level of 12cm (6cm above the lowest measured level) and gradually drops to about 5% at a vertical level of 26cm. This
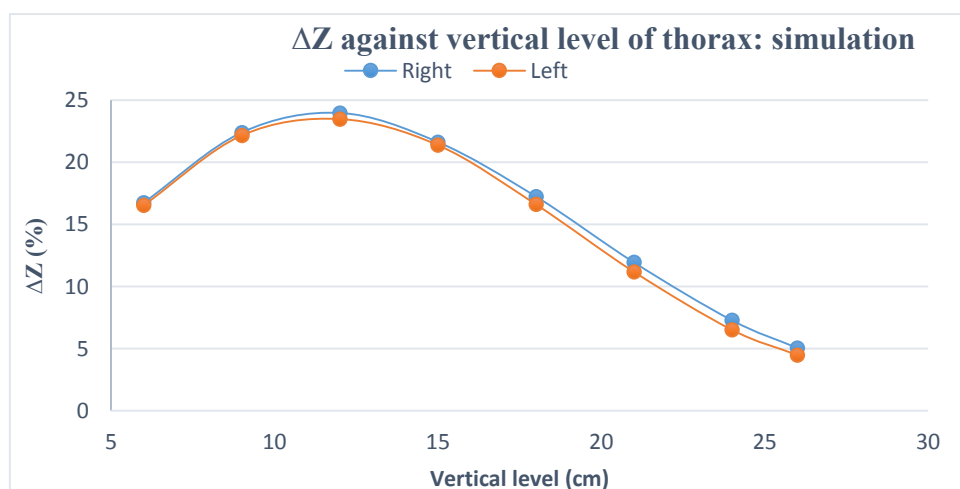
Figure 4-59 Variation of percentage change in impedance between inspiration and expiration at different vertical levels of the thorax model on both left and right sides (applied current frequency 10kHz). The reference of vertical level measurement is given

is expected as the anatomical volume of lungs tissue at different vertical levels approximately corresponds to the measured transfer impedances. In addition, non-lung tissue under the skin is thicker at the upper levels reducing the contribution of the lung to the measurement. Again, the value of ΔZ is almost the same for both the right and the left lung, only being slightly lower for the latter. This is because both the right and left lungs in the model are of same size and shape and only a small region of the lung contributes to the transfer impedance as mentioned earlier. It can be noticed that the inner region of heart, which is blood, has positive sensitivity because blood is less conducting compared to its surroundings and therefore more current flows through it. However, this has no substantial effect on the *change in total transfer impedance* because the dielectric properties of this region was not changed during respiration in the model implemented. However, in real life the geometrical position of the heart will change with respiration which may contribute to the impedance change depending on the sensitivity at its location. Again, the blood content will change with the cardiac cycle which may appear as cyclical variation in the transfer impedance at the heart rate. However, these changes may be minimised through filtering. Again, for measurements with fully expired and fully inspired lungs, the cardiac cycle related changes may be averaged out if data is acquired over a sufficient length of time.

4.5.7.3 Lung ventilation: Experimental study on human subject

The change in impedance between full inspiration and full expiration was measured experimentally on a healthy human subject using the multi-frequency FIM system in order to investigate how closely the FEM thorax model represents the real human thorax for an FIM-4 measurement. Figure 4-60 shows the variation of ΔZ with vertical levels of thorax. It can be observed from Figure 4-59 and Figure 4-60 that the values of ΔZ obtained experimentally are lower compared to that obtained by FEM simulation at corresponding vertical levels but the overall pattern of impedance change, on both sides, have remarkably similar behaviours, considering the variability that one may encounter in real life experiments on the human body. There are several factors that may contribute to the difference in the absolute value of the impedance change between the simulation and real life measurement. The model is a very simplistic one and it did not consider any tissue anisotropy which is present below the skin and fat layers. In addition, between maximum inspiration and maximum expiration the shape and volume of the thorax as well as that of lungs changes considerably which has not been considered in the current model. Importantly, the dimensions of the particular subject are definitely not the same as that of the simulated model. This shows that the FEM model of thorax developed in the study of a localized ventilation disorder is satisfactory although there is room for refining the details. It can be noted that even in human measurements, the impedance change is similar on the left and right side of the thorax although the left lung is smaller than the right lung
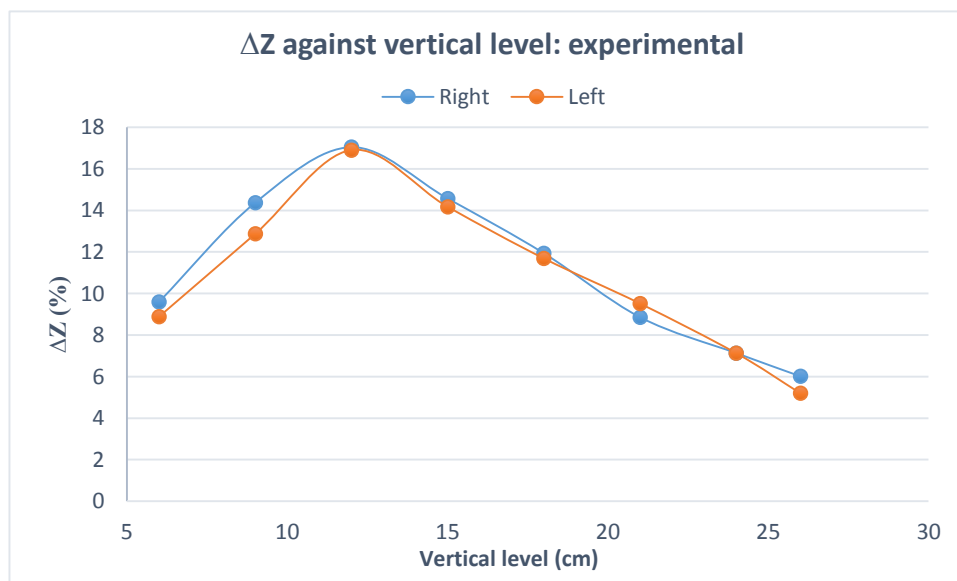
Figure 4-60 Variation of percentage change in impedance between inspiration and expiration at different vertical levels of a human thorax on both left and right sides (applied current frequency 10kHz).

in practice. This may be because of the limited area and depth sensitivity of FIM so that the volumes of each lung contributing to the two measurements are effectively the same.

4.5.7.4 Detection of localized ventilation disorder: simulation study

To study if FIM can detect a localized lung ventilation disorder (fluid accumulation in lungs) the lower portion of the right lung was partitioned and defined as fluid as described in section 4.5.6 (considered as the ROI). The volume of the simulated fluid is $663cm^3$. Focused transfer impedance values were then computed simulating the measurements at different vertical levels of the thorax model. Figure 4-61 shows the variation of ΔZ as measured at various vertical levels on the left side of the thorax model without and with fluid in the lower part of the right lung (i.e. the opposite side). The fluid has no effect on
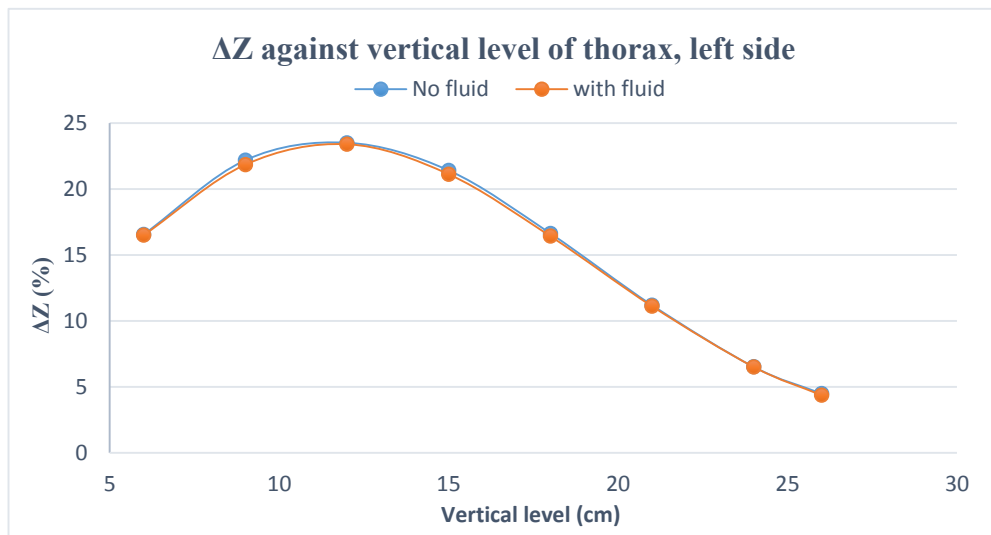
Figure 4-61 Percentage change in focused impedance between inspiration and expiration (ΔZ) on left size at different vertical levels of thorax (right lung contains fluid).

the measurement. Figure 4-62 shows the variation of ΔZ as measured at various vertical levels on the right side of the thorax model without and with fluid of various volume in the lower part of the right lung, the same side. The reduction of the variation of impedance values at the lower levels is substantial; more than one third at the level of 6cm. The difference decreases gradually with increasing vertical level, as expected, since the fluid is present in only the lower part of the lung.

Since the conductivity of the fluid region on the right lung is not changing with breathing, the change in impedance between inspiration and expiration was very low (5.1% with the presence of fluid but 16.8% for healthy lung). Although one would expect 'zero' ΔZ with fluid in the lower lung, the 9cm electrode separation will include small contributions from lung region above the fluid filled ROI, which contributed to the non-zero value. Again,
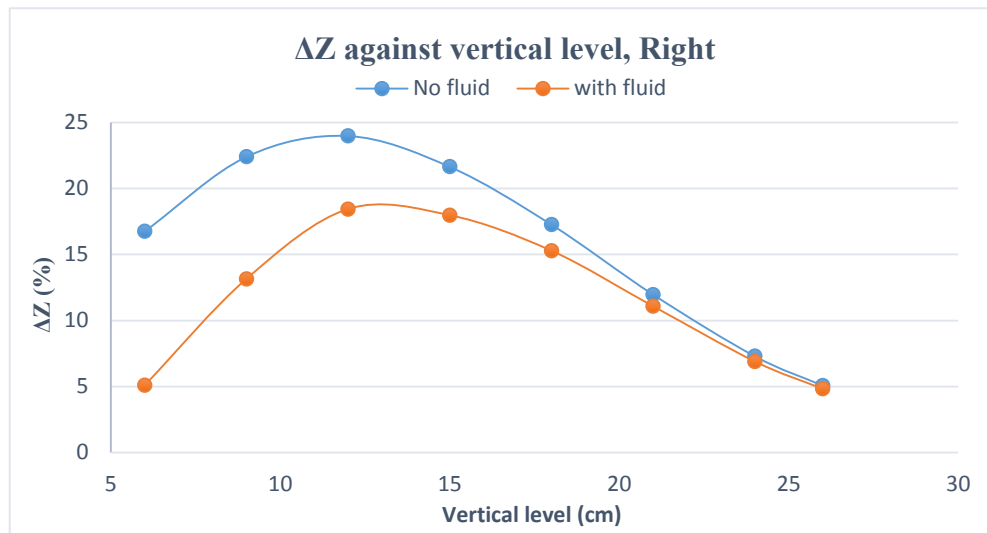
Figure 4-62 Percentage change in focused impedance between inspiration and expiration (ΔZ) on right side at different vertical levels of thorax with and without fluid (663cm³) in the lower right lung.

in human measurements, if one places the electrodes at the lower boundary of the lungs, there will be a contribution from movement of the lungs itself between exhalation and inhalation to the measured transfer impedance, so one has to be careful in interpreting such measurements. It is also interesting that the contribution of fluid on the right side to the transfer impedance measured on the left side of the thorax is negligible. This is because the chosen electrode separation for FIM-4 gives a highly localized sensitivity distribution beneath the electrode array and minimal contribution from tissues outside the focused volume to the total impedance is negligible. We hypothesize that if the values of ΔZ is significantly different between left and right side of the thorax, then there is a possibility that the lungs with the lower ΔZ have localized ventilation disorder provided that the other lung is healthy.

It was reported in Figure 4-21 of section 4.3.5 that for a homogeneous medium FIM-4 has better degree of localization than conventional tetra-polar square configuration (TPIM) up to a depth equal to one-half of the electrode separation. To explore if FIM-4 offers better localization over conventional TPIM in the thorax model, impedance measurements were performed for TPIM square configuration (current drive electrodes A,B and reciprocal current drive electrodes C,D in Figure 4-46) with same electrode separation as before (9cm) with and without fluid on the right lung. Percentage changes in transfer impedance between inspiration and expiration for tetra-polar square configuration is shown in Figure 4-63. At vertical level 6cm (fluid is beneath the electrode array) the difference in impedance change is about 11.7% and 13.6% for FIM-4 and TPIM

configurations respectively. But at vertical level 12cm where there is no fluid beneath the electrode array, the difference in impedance change is about 5.5% and 13.7% for FIM-4 and TPIM configurations respectively. Comparing Figure 4-62 and Figure 4-63 it is evident that TPIM square method includes substantial contributions from the regions that are not below its electrode array whereas the contributions are relatively much lower for FIM-4. This behaviour is the result of better localized sensitivity distribution of FIM-4 as reported in section 4.3.5.
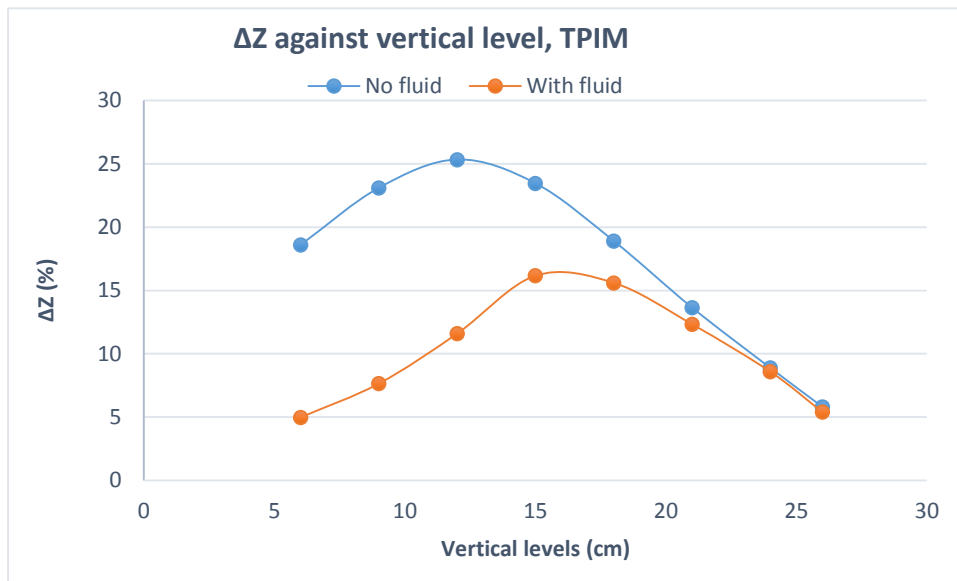
Figure 4-63 Percentage change in focused impedance between inspiration and expiration (ΔZ) on right side at different vertical levels of thorax for tetra-polar electrode configuration (right lung contains fluid of volume 663cm3).

4.5.7.5 Effect of fluid volume

The percentage changes in impedance between inspiration and expiration in the presence and absence of fluid were obtained from simulation for various volume of fluid filling the lower right lung to explore the effect of fluid volume on the impedance changes in the thorax. For this simulation, the height of the ROI was changed to contain different volumes of fluids. Three fluid volumes $349cm^3$, $476cm^3$ and $663cm^3$ (arbitrarily chosen) were considered by changing the partitioned volume on the right lung. In this measurement the subcutaneous fat thickness was fixed at 5mm. Figure 4-64 shows the percentage change in focused transfer impedance between inspiration and expiration (ΔZ) for various simulated fluid volumes as measured at various vertical levels over the right lung. It can be observed that the decrease in ΔZ is higher for greater fluid volumes and vice versa, as expected. This information may be useful in quantifying of the amount of fluid accumulated or the severity of the ventilation defect. The minimum amount of

161

fluid that can be detected will depend on the resolution and accuracy of the impedance measurement system.
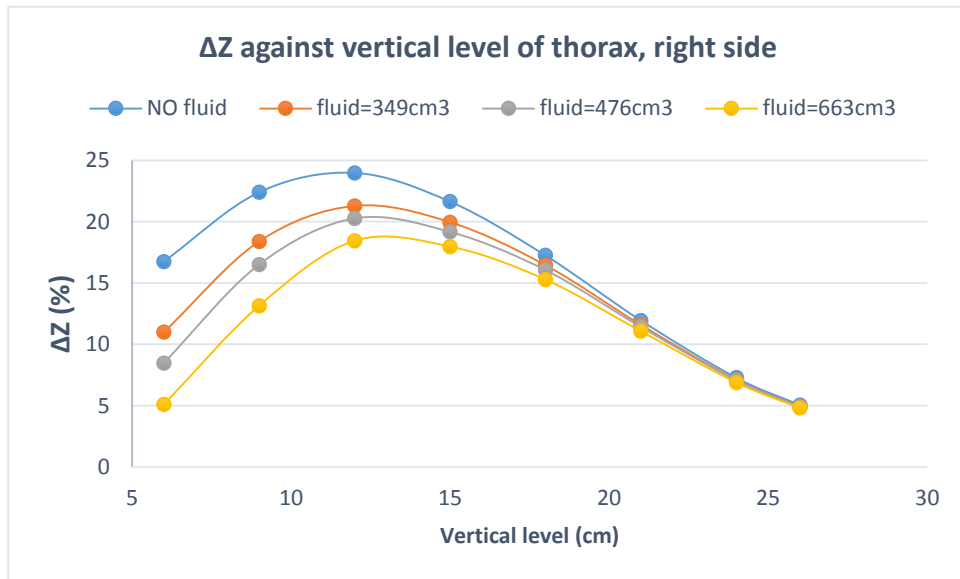
Figure 4-64 Percentage change in focused impedance between inspiration and expiration (ΔZ) on right side at different vertical levels of thorax (right lung contains fluid of various

4.5.7.6 Effect of subcutaneous fat thickness

The subcutaneous fat thickness in human thorax depends on various factors including age and weight. It was presented in section 4.5.3 that the total transfer impedance of thorax as well as the optimum electrode separation changes with subcutaneous fat layer. In order to study if the ability to detect localized ventilation disorder is valid for various fat thicknesses, impedance changes between maximum inspiration and maximum expiration
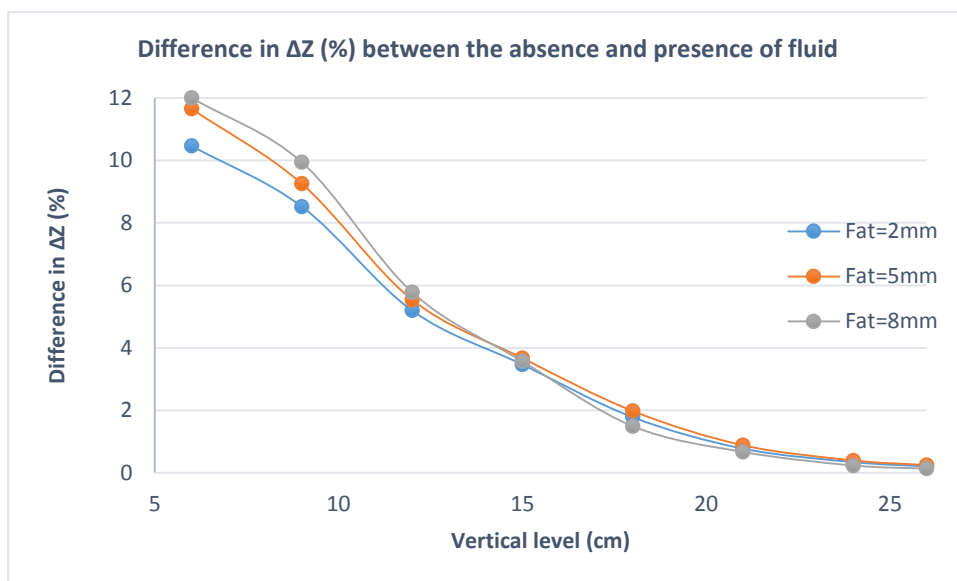
Figure 4-65 Difference in percentage change in impedance between inspiration and expiration in the absence and that in the presence of fluid in the lower right lung of the thorax model for various thickness of fat layer (the amount of fluid is 663cm³).

in the presence and absence of fluid was obtained for three different thickness of fat layers (2mm, 5mm and 8mm). The ROI and hence the fluid amount was fixed ($663cm^3$). For each thickness of fat layer, the corresponding optimum electrode separation obtained in section 4.5.3 was used. Figure 4-65 shows the *difference in ΔZ* i.e. [(the percentage change in impedance between inspiration and expiration with NO fluid on lung) − (percentage change in impedance between inspiration and expiration with fluid on lower right lung)] as measured at different vertical levels and for various fat thicknesses. Here *difference in ΔZ* represents the level of decrease in impedance between inspiration and expiration due to the presence of fluid.

It can be observed that the decrease in impedance due to the presence of fluid is higher for a higher thickness of fat layer. This is in agreement with the results reported earlier in section 4.5.3: that the fractional contribution of the ROI to the total transfer impedance is higher for higher thickness of the fat layer. Since the contribution of ROI to the total impedance is higher for higher fat thickness, the *difference in ΔZ* is also higher for higher fat thickness.

4.5.7.7 Frequency response of the impedance changes

Focused transfer impedance measurements were also simulated at multiple frequencies in order to study the variation of thorax impedance with frequency for healthy and diseased lung. Measurements were simulated at eight frequencies: 10kHz, 20kHz, 40kHz, 80kHz, 160kHz, 320kHz, 640kHz and 1024kHz. The simulations were performed in the
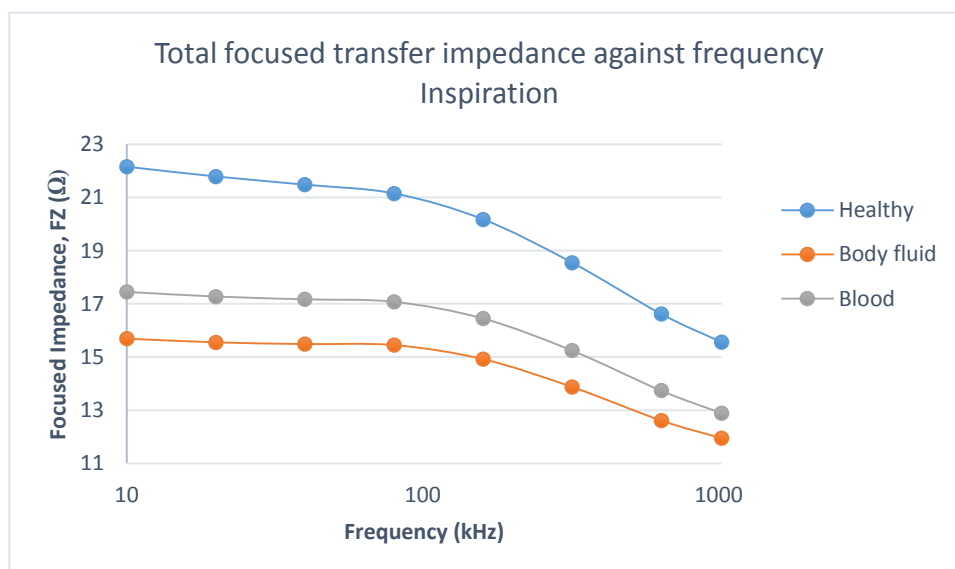
Figure 4-66 Variation of focused transfer impedance with frequency for healthy and diseased lungs during inspiration. The diseased lungs were simulated with accumulated body fluid and blood in the lower portion of right lung.

frequency domain under the AC/DC module of the Comsol Multiphysics software. For measurement at a particular frequency, all the domains within the thorax model were assigned the corresponding dielectric properties for that particular frequency (Andreuccetti D, 1997). Initially the total focused transfer impedance values were computed for healthy lungs (no fluid) during inspiration and expiration placing the electrodes on the lower portion of the right side of thorax (vertical position 6cm).Then the lower part of right lung was simulated as *body fluid* (diseased) and the focused transfer impedance values were obtained during inspiration and expiration phases of respiration. Similar measurements were also performed by simulating *blood* (diseased) on the lower right lung on the thorax model. In this study the vertical position of the electrodes were fixed (6cm) and the volume of both the body fluid and blood simulated was 663cm^3. The measurements were performed placing electrodes on the thorax surface so that the accumulated fluid/blood is at the vertical level of the FIM electrode probe, as done for the previous simulations. Two different types of fluid (body fluid and blood) were considered to investigate if multi-frequency measurements are capable of characterizing the type of accumulated fluid.
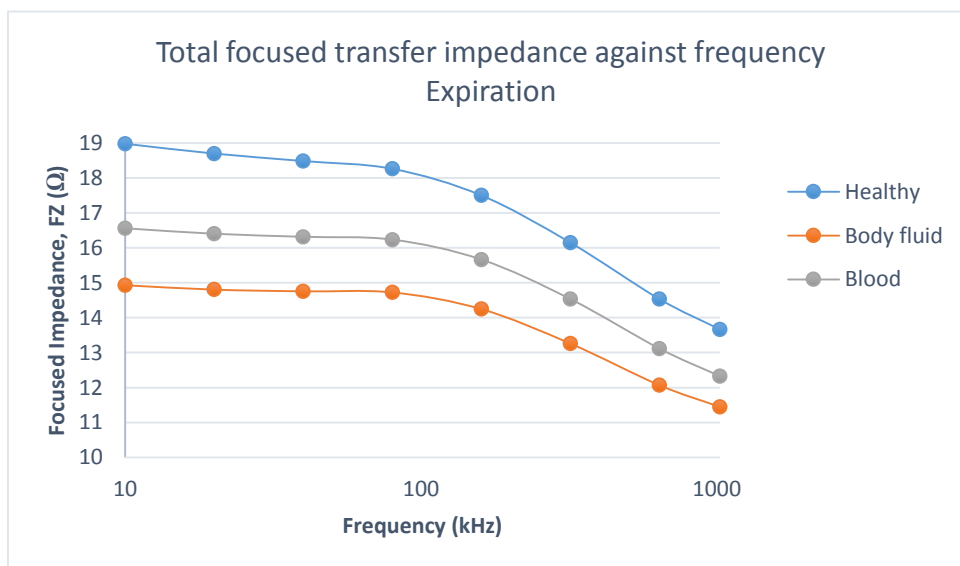
Figure 4-67 Variation of focused transfer impedance with frequency for healthy and diseased lungs during expiration. The diseased lungs were simulated with accumulated body fluid and blood in the lower portion of right lung.

Figure 4-66 and Figure 4-67 shows the variation of total focused transfer impedance of the thorax with frequency during inspiration and expiration respectively. It can be observed that for healthy lungs the focused transfer impedance of the thorax decrease with increasing frequency during both inspiration and expiration. This is because of the

combined variation of electrical parameters of fat, muscle and lung tissues all of which change with frequency substantially. The focused transfer impedance decreases with frequency with the presence of body fluid or blood as well. However, the decrease in total impedance from 10kHz to 1024kHz during inspiration is around 29.8% for healthy lungs while it is around 23.8% and 26.1% in the presence of body fluid and blood in the lower region of right lungs respectively, which is lower than that in the healthy condition. This is because that the variation of conductivity and permittivity with frequency for body fluid or blood are much less than that of the other tissues (fat, muscle) involved.
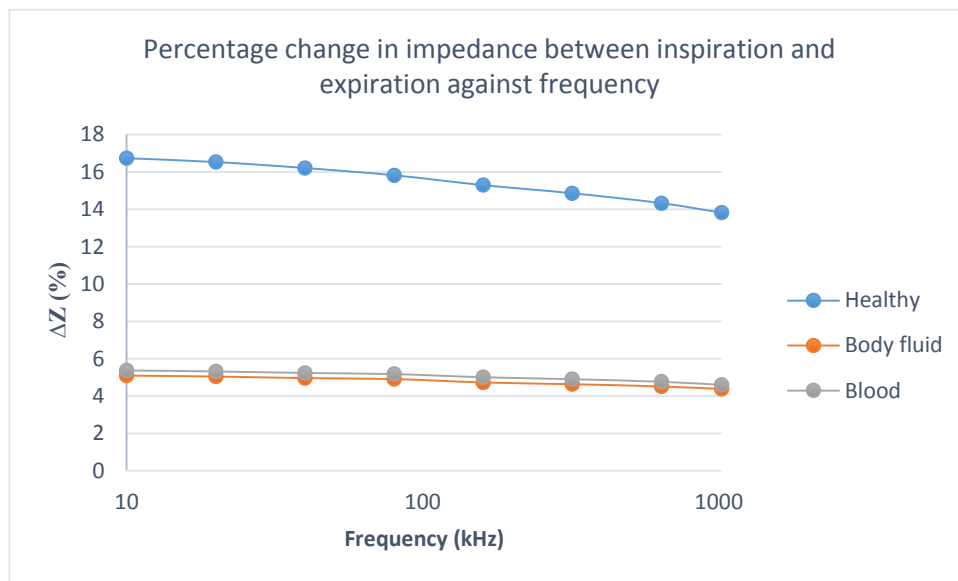
Figure 4-68 Variation of percentage change of transfer impedance between inspiration and expiration with frequency for healthy and diseased lungs. The diseased lungs were simulated with accumulated body fluid and blood in the lower portion of right lung.

The percentage change in transfer impedance (ΔZ) between inspiration expiration as defined in equation 4-5 is shown in Figure 4-68 at different frequencies. It can be noted that the percentage change in impedance between inspiration and expiration is much higher for healthy lungs compared to that for diseased lung (body fluid or blood in the lower right lung). This is expected since the conductivities of *blood* and *body fluid* do not change with respiration and as discussed before; the changes mostly occur from adjacent regions of the healthy lungs. In addition the percentage change for the healthy lungs decreases by about 3% for the maximum range of frequency considered while it is less than 1% in the presence of blood or body fluid. This is also expected since the variation of electrical parameters of lungs tissue with frequency is much greater than that of blood or body fluids. However, since the electrical parameters of blood and body fluid do not differ greatly, these materials cannot be identified from the focused impedance measurements presented above. These results suggest that single frequency FIM has the

potential to localise the lesion in the lung with the possibility that multi-frequency FIM can then determine the origin of that lesion. Further work is required to investigate this.

4.5.8 Discussions

An FEM based model of the human thorax was created in the Comsol Multiphysics software to study various aspects of impedance measurements on thorax. An FEM model calculates the sensitivity distributions in various domains within the thorax whereas one can only measure the total transfer impedance by placing electrodes on the chest surface. However, it should be noted that the model described in this chapter is simplistic with model geometry estimated from a single CT scans image. Moreover, some organs like diaphragm, liver etc. were not included in the current model. It was demonstrated that CT can be used to determine model geometry and the purpose of this part of the work was to demonstrate how such an anatomical model can be used to study multi-frequency FIM measurements on the lung.

In localized lung ventilation studies, it is desirable that the contribution of the local region of interest *(ROI)* to the total impedance is maximized with the contribution from the neighbouring regions minimized. Therefore an optimum electrode separation was calculated for the study of localized lung ventilation. It was observed that the total transfer impedance of the thorax model decreases with increased electrode separation (Figure 4-48). This is the consequence of changing sensitivity distribution with electrode separation as reported in section 4.3.3 of the 1st part of this chapter where it was noted that the overall sensitivity is inversely proportional to the square of electrode separation. For increased electrode separation the current spreads more within the volume conductor; smaller currents flowing through the same conductivity regions resulting in smaller voltage at the receive electrodes. The contribution of ROI to the total impedance increases with increased electrode separation, reaches a maximum and then decreases. The depth of the surface of the ROI is approximately 3cm from the electrode plane. It was reported in section 4.3.4 that the maximum sensitivity occurs at a depth 1/3.5 of the electrode separation (Figure 4-19). At small electrode separations, the contribution of ROI to the total impedance is low because limited depth sensitivity; the maximum sensitivities are just below the electrode plane and sensitivity at the depth where the *ROI* located is very low. With increasing electrode separation the contribution of *ROI* increases because of increased depth sensitivity. After reaching a maximum, the contribution of *ROI* again

decreases because at larger electrode separation the volumes outside the *ROI* lies within the focused zone of the electrode configuration. These results are the effect of electrode separation on sensitivity distribution reported in section 4.3.3 and section 4.3.4.

Variation of the subcutaneous fat layer thickness indicated that the optimum electrode separation depends on the fat thickness. This is because the fat thickness changes the sensitivity distribution in a volume conductor as reported in 4.3.7. For a particular thickness of subcutaneous fat layer, the variation of *optimization factor* with electrode separation is very low (Figure 4-53). For instance, the variation of optimization factor is only about 0.5% for a change of electrode separation from 7cm to 9cm as noted in section 4.5.3. So the optimum electrode separation may change for a small change in the shape and size of the ROI. It should be noted that the *electrode separation* will change during respiration because of movement of different structures in the thorax even for a fixed electrode array. However, since the variation of optimization factor with electrode separation around the optimum separation is very low, small changes in the optimization factor due changes in the shape and size of the ROI may not affect the measurement substantially.

The percentage change in focused impedance (ΔZ) between inspiration and expiration obtained from the simulation study is relatively high at lower to middle vertical levels of the thorax whereas it is low at upper vertical levels of the thorax (Figure 4-59). This is because of the shape of the lungs; at lower levels the volume of lung tissue is greater when compared to that at upper vertical levels where the lung is slightly tapered. In addition, at the upper levels, a greater thickness of non-lung tissue is interposed between the skin and the lungs. In the upper vertical levels, the optimum electrode separation may also be different because of the increased non lung tissues in between the electrode array and the lung. In the simulation study, the values of ΔZ on left and right side of the thorax are very close to each other for healthy lungs (Figure 4-59). This is because both the left and right lung in the in the thorax model are of same volume and similar shape. In the current model, the heart is located towards the left lung but there was no significant difference of transfer impedance values on left and right side of the thorax. This is because the heart is located deep inside the thorax; heart volume was beyond the sensing depth of the optimum electrode separation (9cm) and placement chosen.

To verify the predictions from the FEM model, impedance measurements were performed on a single human subject. Whilst the results from a single subject must be treated with caution, the values of change in impedance between inspiration and expiration obtained experimentally (Figure 4-60) was substantially lower when compared to that predicted by the FEM simulation but the change with vertical position of electrode array was remarkably similar. The anatomical structure and organization of human thorax is very complex and it is difficult to model accurately. The FEM model implemented is a simplified model excluding other organs and structures (e.g. the liver and diaphragm) which occupy a substantial portion of the lower thorax. The domains modeled were considered isotropic which is not the case in reality. Again, the anatomical size of thorax varies person to person. Moreover, anatomical changes of the organs within thorax during inspiration and expiration are very substantial but these were not implemented in the model. A thorax model based on segmentation from CT images may be more accurate. However, the overall pattern of transfer impedance values measured experimentally was very similar to that obtained from the simulation study (Figure 4-59 and Figure 4-60). Therefore, the introduction of a scaling factor may be useful in approximating experimental measurements by FEM simulation. However, experimental measurements on a large number of normal human subjects will be needed to make necessary changes in the FEM model so that it can be used to approximate experimental measurements more accurately. Here, factors such as body frame, subcutaneous fat and muscle thickness at the thorax, etc., may have to be considered as well. Again, the measurements on left and right sides of thorax on human subject gave similar results although the right lung is greater than the left lung. One would expect smaller changes on the left side. The optimum electrode configuration of FIM-4 only sensed a smaller portion of the lung just beneath the electrode array (Figure 4-58 and Figure 4-57) and the heart was away from the focused zone. The values of percentage changes in impedance between inspiration and expiration on different vertical levels are consistent with that obtained on ventilation mapping of chest reported by (Kadir et al., 2010).

Based on simulation study, a new technique is proposed to detect fluid accumulation in lungs using FIM measurements. It was observed that the change in the focused impedance measured above the lowest region of the lungs is low (5.1%) between inspiration and expiration on the side of thorax having accumulated fluid, compared to that of a healthy lung (16.8%) as shown in Figure 4-62. However, the degree of impedance change is

dependent on the volume of fluid. The higher the volume of fluid, the lower is the change in impedance between inspiration and expiration (Figure 4-64). In contrast, the difference of the values of change in impedance between inspiration and expiration on the side of thorax having no fluid is negligible Figure 4-61. It is because the optimum electrode configuration chosen gives a highly localized sensitivity distribution and contribution from tissues outside the focused volume will be negligible. Impedance measurements on diseased lung (fluid 663cm3) using TPIM square configuration can also detect the decreased impedance change between inspiration and expiration (Figure 4-63). However, TPIM measurements had a substantial contribution from neighbouring regions of tissues beneath the electrode array. For instance, at a vertical level of 12cm where there is no fluid beneath the electrode array, the difference in impedance change is about 5.5% and 13.7% for FIM-4 and TPIM configurations respectively. This observation is in agreement with the results reported in section 4.3.5, where it was shown that degree of localization (*dol*) is higher for FIM-4 than TPIM up to a depth one-half of the electrode separation. This supports the use of FIM in the study of localized ventilation disorders. In this study, only fluid accumulation in the lower region of the right lung was analyzed because gravity ensures fluid is at the base of the lung when the patient is sitting or standing. However, it should be noted that many people with lung disease are lying down and fluid can accumulate in other regions of any lungs. These situations needs to be studied for better understanding.

Multi-frequency measurements showed the variation of impedance with frequency for different types of fluids. In the current model, the focused transfer impedance decreases by 23% in the frequency range 10kHz to 640kHz (Figure 4-66). Brown et al reported that the impedance variation is 36% in the same frequency range based on measurements on 12 human subjects using TPIM (Brown et al., 1994), which is higher than that obtained from the current model. However, once the presence of localized disorder is detected using single frequency FIM, the type of the tissue accumulated in the lungs may be classified from the frequency spectrum of the transfer impedance which needs further investigation. Being noninvasive and using nonionizing radiation, FIM technique may be a useful screening tool to identify localized lung ventilation disorders like lung edema, pneumonia in the preliminary stage. However, the feasibility of the proposed technique needs to be evaluated by field trials on human subjects having localized ventilation disorder.

Part: 3

4.6 Classification of Breast Tumour using multi-frequency FIM

Many females come to the physicians after they feel a lump in the breast, when it is already quite large and at this stage the clinician needs to perform a biopsy to characterize whether it is benign or malignant. This is invasive and can spread malignancy to other healthy tissues. The present work aims to develop a noninvasive technique for distinguishing malignant tumours from benign ones using multi-frequency FIM measurements. The biochemical and morphological properties of malignant and benign lesions are different (Castro et al., 2008, Baba and Catoi, 2007, Liotta, 1983). It was reported by several studies that the dielectric properties of normal breast tissues and malignant tissues are significantly different (Surowiec et al., 1988, Morimoto et al., 1990, Jossinet, 1998). However, there is no significant difference in dielectric properties between normal and benign tumour tissues (Heinitz and Minet, 1995, Morimoto et al., 1990, Jossinet, 1998). This is the basis of applying multi-frequency FIM in the characterization of breast tumour whether it is benign or malignant. However, the reported differences in dielectric properties between malignant and healthy breast tissues are based on measurements performed invasively or on excised tissue with electrodes in direct contact with the tissues. The aim of the current study is to classify the tissue types from noninvasive FIM measurements placing electrodes on the breast surface.

Initial work was carried out on 19 patients who had tumours on one breast while the other breast was normal on mammogram (Al Amin et al., 2014). Impedance values were measured on both affected and healthy breast tissues using a commercially available device (Maltron Bioscan 920-II) with conventional TPIM square electrode configuration at two frequencies 5 kHz and 200 kHz. The impedance values on unaffected breast tissue was considered as control to distinguish between benign or malignant tissue on the affected breast. Using feature plots combined with machine learning algorithms it was shown that breast tumour could be classified as benign or malignant with a sensitivity of 75% and specificity 87% (Al Amin et al., 2014) although there was considerable person to person variation in the measured impedance values. The present work was taken up to investigate the feasibility of using multi-frequency FIM in the classification of breast tumours since FIM offers better localization and reduced negative sensitivity distribution compared to TPIM as described in the 1st part of this chapter. More importantly,

impedance measurements were limited in the frequency range (5kHz – 200kHz) in the previous work. Therefore, the application of the multi-frequency FIM system developed as part of this thesis described in chapter-3, will give a broader impedance spectrum in the frequency range (10kHz – 1MHz) and may provide better understanding of whether different types of breast tissue can be identified on the basis of FIM measurements.

4.6.1   Methods and Materials

The experimental study to investigate the feasibility of using FIM in the classification of breast tissues was performed on 16 female subjects of average age 35.2 years in the range 17-65 years who came to a hospital with palpable breast lumps. Since the nature of data collection was not suitable for a male, the impedance measurements on female subjects were performed in a hospital by a female MSc student.

Impedance measurements were performed using FIM-4 electrode configuration as it offers better localized sensitivity distribution beneath the electrode array compared to other FIM configurations as described in section 4.3.1 and section 4.3.5. A hand held electrode probe with electrode separation $4\ cm$ was used for impedance measurements as shown in Figure 4-69. The location, and area of the tumours were determined initially using ultrasonography. Only subjects having tumour in one breast of size greater than $1\ cm$ and no tumour in the contralateral breast on mammogram were considered for inclusion in the study.
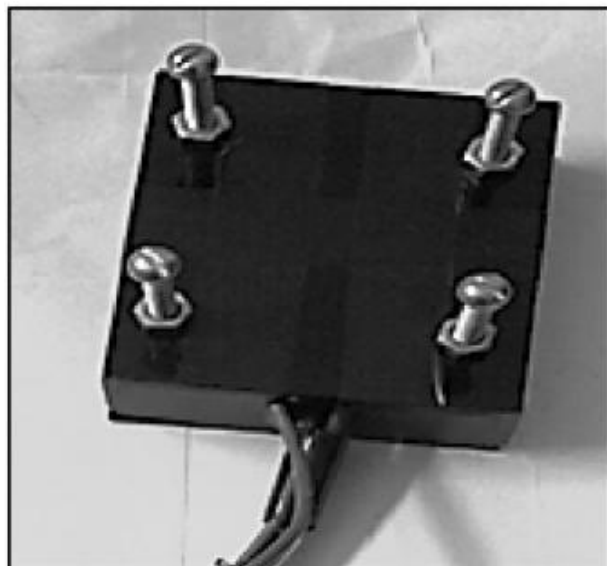
Figure 4-69 Hand held electrode probe used for FIM measurements in the breast tumour characterization study. Center to center separation between two

The sensitivity modelling described in Chapter 4 Part 1 is directly applicable to detecting and classifying breast tumours as these can be considered as a volume of altered tissue within an otherwise homogeneous volume of tissue. As described earlier, the spatial sensitivity within a volume conductor for FIM-4 is a function of electrode separation and the *percentage depth sensitivity* (PDS) is maximum at depth 1/3.5 of the electrode

separation from the electrode plane. Beyond this depth, the PDS decreases gradually and is above 20% of its maximum value up to a depth equal to the electrode separation (Figure 4-17). Assuming the size of palpable tumours to be studied is greater than $1cm$ and depth in the rage $0.5 - 4cm$, the electrode separation was chosen as *4cm* so that the maximum sensitivity regions remain within the tumour. Galvanized iron screw heads were used as electrodes having diameter $0.5cm$. Conducting electrode gel was applied on the tip of the electrodes to reduce the contact impedance. The excitation current applied by the multi-frequency FIM system was 1mA (p-p). Electrical bioimpedance techniques are noninvasive and nonionizing and there is no known health hazards. However, oral consent was taken from the subjects before data collection explaining the purpose of the study and measurement principles.

Focused impedance measurements were carried out using the multi-frequency FIM system based on digital demodulation described in *Chapter-3* of this thesis. FIM values were measured at 8 signal frequencies in the range 10 kHz to 1MHz. The magnitude of impedance values for two orthogonal measurements (*horizontal* and *vertical*) of FIM
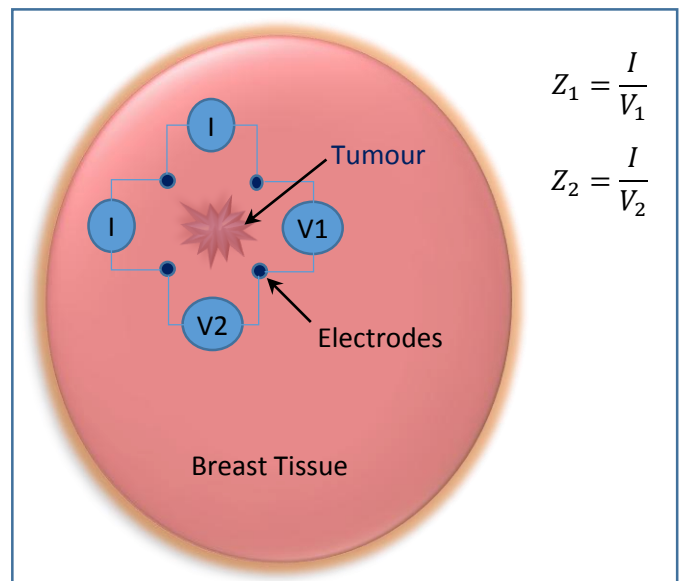
Figure 4-70 Electrode placements for two orthogonal impedance measurements from breast tissue.

were denoted as Z_1 and Z_2 as shown in Figure 4-70. The magnitude focused transfer impedance at a particular frequency is defined as

$$FZ = \frac{Z_1 + Z_2}{2} \quad \text{----- 4-14}$$

172

However, the values of two orthogonal measurements (Z_1 and Z_2) were also recorded for analysis.

In the previous study reported by Al-Amin et.al. only the healthy tissues on the unaffected contralateral breast was considered as the control and there were substantial person to person variation in the measured impedance values (Al Amin et al., 2014). The affected and unaffected breasts in malignant patients are usually asymmetric (Scutt et al., 1997) and may give different impedance values. Therefore, in the current study the neighbouring healthy areas (no tumour on ultrasonogram) away from the tumour of the affected breast of the same patient in addition to the symmetric position of the contralateral unaffected breast were considered as control measurements as this may improve the classification. This is also expected to reduce the problem of person to person variation observed previously.

The patients were instructed to lay supine; the tissue surface was cleaned and prepared for impedance measurements. For each subject, FIM measurements were performed on three locations listed below:
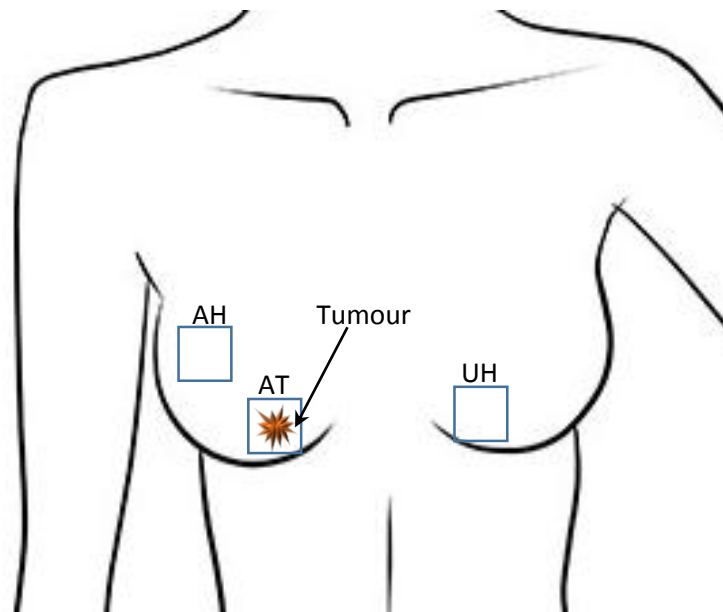
Figure 4-71 Locations of impedance measurements from patients. AT: tumour on the affected breast, AH: healthy tissue on the affected side, UH: healthy tissue on symmetric position of the unaffected breast.

(i) **AT**: electrode probe placed on the affected breast keeping the tumour beneath the probe; measured impedance denoted as FZ_{AT}

(ii) **AH**: electrode probe placed on healthy tissue of the affected breast away from the tumour, no tumour below the probe; measured impedance denoted as FZ_{AH}

(iii) **UH**: electrodes placed on the opposite unaffected breast but a symmetric position as that of the tumour; measured impedance denoted as FZ_{UH}

The three locations of impedance measurements as defined above for a particular subject is shown graphically in Figure 4-71. The corners of each square are the positions of FIM-4 electrodes for measurements on a location. In this figure the tumour is located in the lower inner quadrant of the right breast; so the impedance measurements on the symmetric position of the unaffected breast was performed on the lower inner quadrant of the left breast as shown. Only a single measurement was taken from each site as time was limited for access to patients within the clinical environment.

The diagnosis whether the breast lump is benign or malignant was confirmed by biopsy which was considered as the gold standard; the impedance measurements were made following clinical diagnosis. There were 8 subjects with malignant tumour and another 8 subjects with benign tumour. The same number of patients with benign and malignant tumours were chosen for equal representation of the both classes in the sample data set.

4.6.2 Results

Figure 4-72 shows the variation of focused transfer impedance (FZ) against measurement frequency for 8 patients with malignant breast tumour. Similarly, the variation of FZ
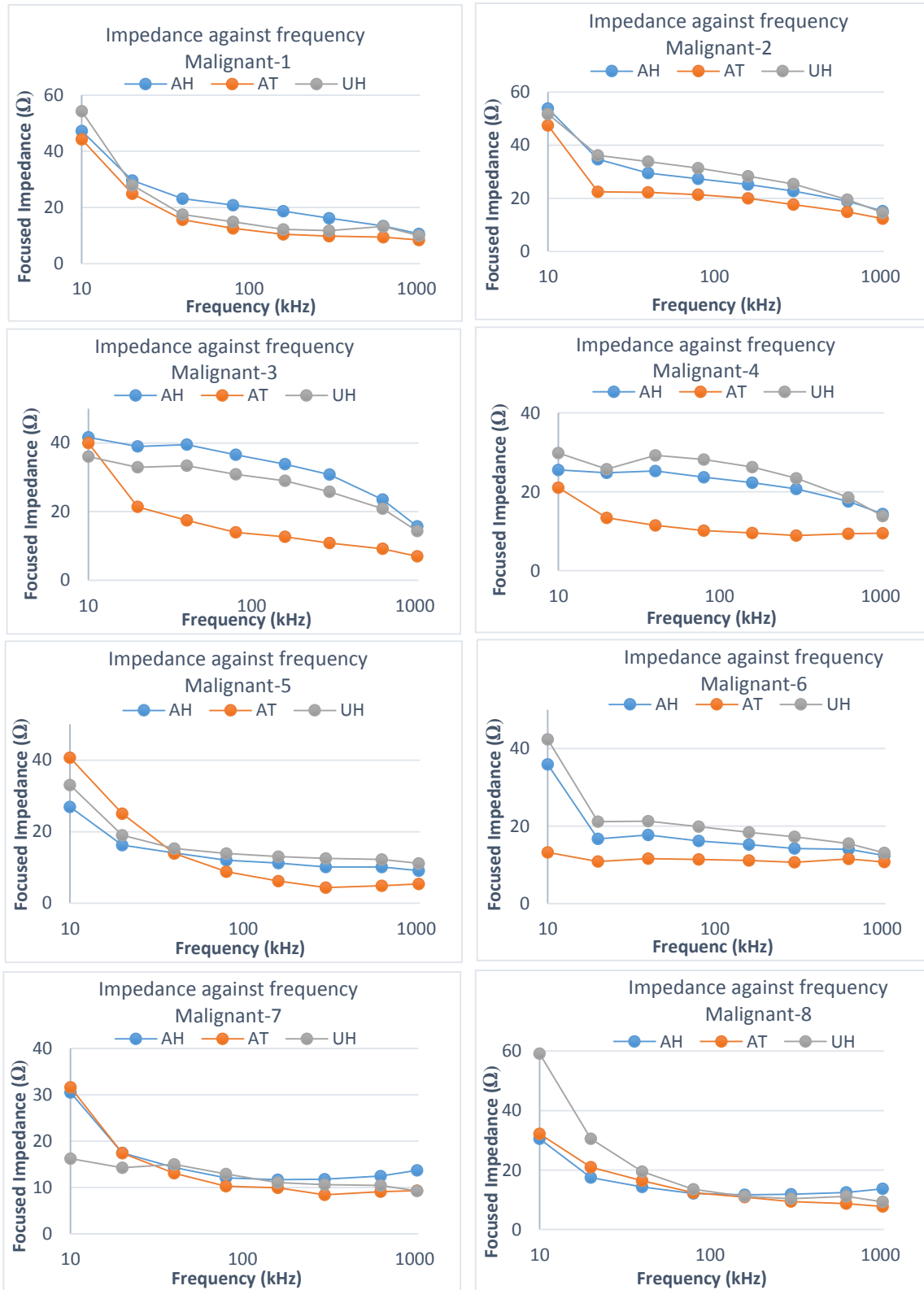
Figure 4-72 Variation of measured focused impedance against frequency for 8 patients with malignant breast tumours.

against measurement frequency for patients with benign breast tumour is shown in Figure 4-73. It can be observed that the impedance decreases with increasing frequency for all subjects and for tissue types. This is in agreement with typical in impedance with

175
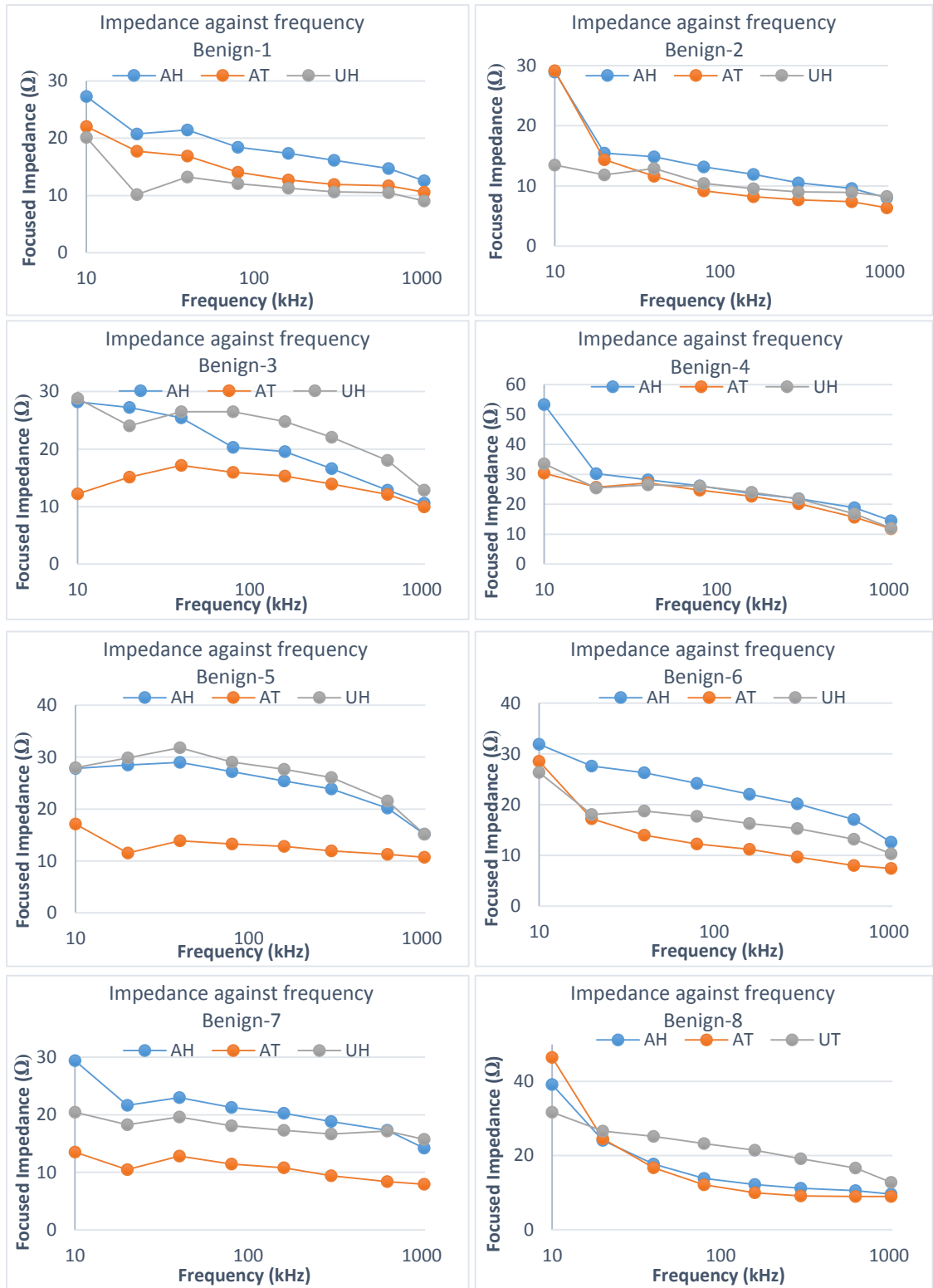
Figure 4-73 Variation of measured focused impedance against frequency for 8 patients with benign breast tumours.

frequency for biological tissues. However, there are substantial person to person variation in the measured impedance values. The mean impedance values with standard deviation at the three different positions defined above for patients with malignant and benign

Focused transfer impedance against frequency with standard deviation
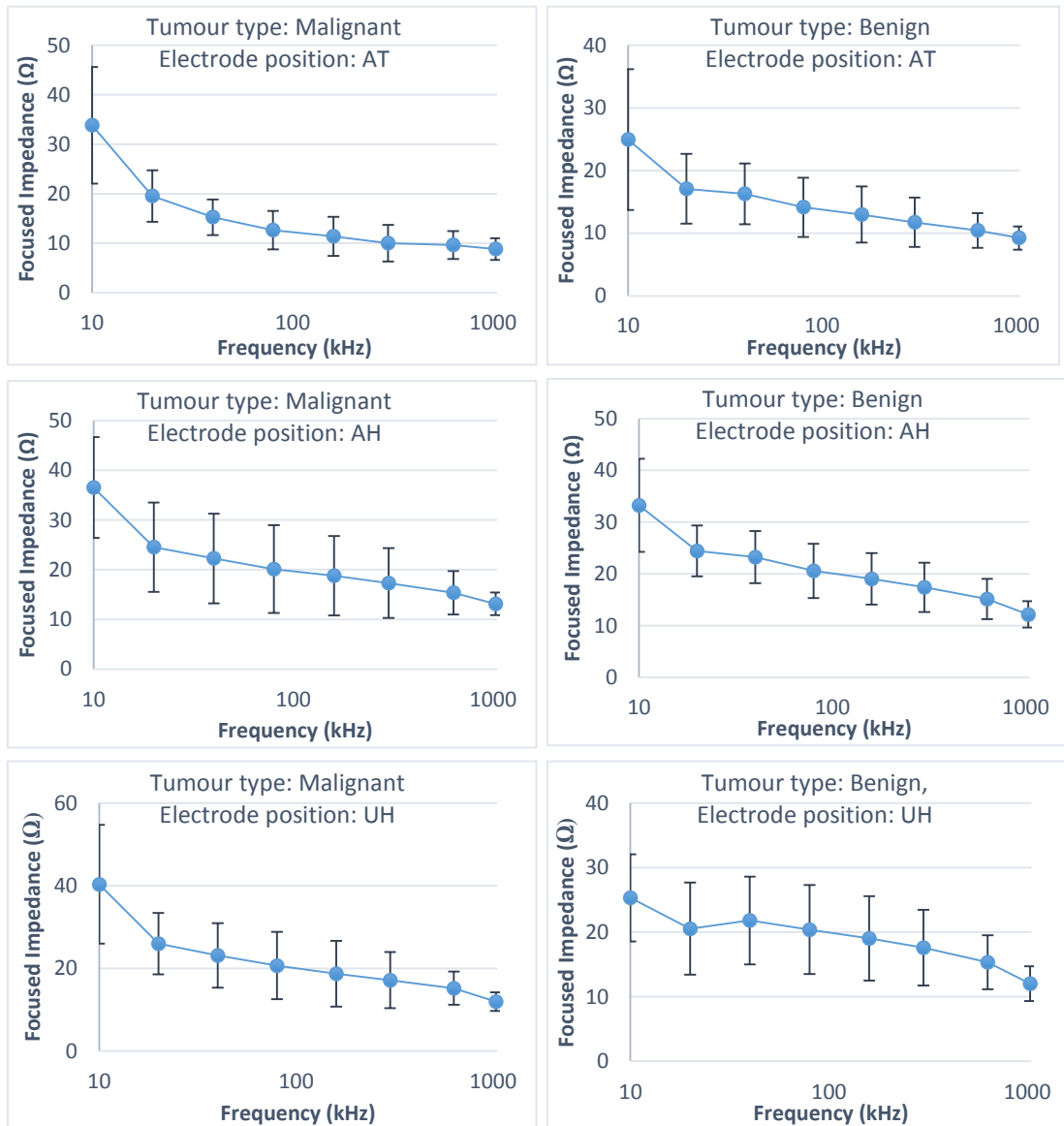
Figure 4-74 Variation of measured focused impedance against frequency on different types of breast tissues. The graphs on the lift hand side are for patients with malignant tumours and that in the right hand side are for patients with benign tumour. The standard deviation at each frequency are shown as vertical lines.

tumours is plotted in Figure 4-74. It can be observed that there is substantial person to person variation in the measured impedance values and the standard deviations are high compared to the mean values. The person to person variation of measured impedance values can be attributed to the different percentage of fatty tissues compared to glandular tissues for subjects of different ages (Vandeweyer and Hertens, 2002). The average impedance values for malignant and benign subjects at different positions are also tabulated (Table 4-3) for intergroup comparison. It can be observed that the mean focused

Table 4-3 Mean impedance values for malignant and benign patients groups at different positions.

Frequency (kHz)	Position: AT		Position: AH		Position: UH	
	Malignant (Ω)	Benign (Ω)	Malignant (Ω)	Benign (Ω)	Malignant (Ω)	Benign (Ω)
10	33.83	24.94	36.53	33.26	40.33	25.32
20	19.56	17.09	24.50	24.45	25.97	20.54
40	15.24	16.28	22.25	23.24	23.12	21.81
80	12.62	14.13	20.09	20.58	20.68	20.40
160	11.37	12.97	18.76	19.04	18.68	19.04
300	10.00	11.73	17.30	17.41	17.15	17.59
633	9.64	10.45	15.32	15.15	15.19	15.35
1033	8.81	9.22	13.11	12.17	11.94	12.03

impedance on tumour region (AT) is lower compared than that on other positions irrespective of types of the tumour. For example, the mean impedance at the position AT is 2.7Ω and 6.5Ω less than that in positions *AH* and *UH* respectively for malignant tumours at 10kHz. At the same frequency, the mean impedance at the position AT is 8.3Ω and 0.4Ω less than that in positions *AH* and *UH* respectively for benign tumours. A *Mann–Whitney U* test performed on the malignant and benign data sets at each measurement frequency to investigate if the differences of mean impedance between positions AT and AH (or between position AT and UH) are statistically significant. The p-values for differences in impedance values at different positions are listed in Table 4-4. As can be seen that the measured impedance at position AT is statistically significantly lower than that at position AH and UH for malignant tumours except 10kHz and 20kHz. On the other hand, impedance at position AT is significantly lower than that at position

Table 4-4 p-values for Mann–Whitney U test for differences in the measured impedance values at different locations at different frequencies. p-values less than 0.05 are considered as statistically significant.

Frequency (kHz)	Malignant tumour		Benign tumour	
	Between AT and AH	Between AT and UH	Between AT and AH	Between AT and UH
10	0.937	0.382	0.195	0.879
20	0.425	0.083	**0.021**	0.279
40	**0.046**	**0.028**	**0.015**	0.130
80	0.061	**0.010**	**0.028**	0.105
160	**0.009**	**0.015**	**0.038**	0.065
300	**0.006**	**0.015**	**0.038**	0.130
633	**0.004**	**0.005**	**0.021**	**0.021**
1033	**0.004**	**0.028**	**0.028**	**0.038**

AH for benign tumour except at 10kHz. However, there is no significant difference of impedance values at position AT and UH for benign tumour except 633kHz and 1033 kHz.

A visual inspection of the variation of impedance with frequency (Figure 4-74) suggests that the rate of decrease of impedance with frequency may be a characteristic feature for classification of breast tissue as to whether it is cancerous or not. For instance, the decrease in average impedance values in the frequency range 10 kHz to 1MHz are 64% and 74% in the positions AH and AT respectively for patients with malignant tumours whereas there is no difference in the decrease in impedance with frequency for patients with benign tumours. Therefore, two features for breast tumour classification was defined as below:

$$\boldsymbol{Feature(1)} = \frac{\frac{[FZ_{AH}(10kHz) - FZ_{AH}(1033kHz)]}{FZ_{AH}(10kHz)}}{\frac{[FZ_{AT}(10kHz) - FZ_{AT}(1033kHz)]}{FZ_{AT}(10kHz)}} \text{ ------ } 4\text{-}15$$

$$\boldsymbol{Feature(2)} = \frac{\frac{[FZ_{UH}(10kHz) - FZ_{UH}(1033kHz)]}{FZ_{UH}(10kHz)}}{\frac{[FZ_{AT}(10kHz) - FZ_{AT}(1033kHz)]}{FZ_{AT}(10kHz)}} \text{ ---- } 4\text{-}16$$

where

$FZ_{AH}(10kHz)$ is the focused impedance for measurements on healthy tissue of affected breast at excitation frequency 10 kHz

$FZ_{AH}(1033kHz)$ is the focused impedance for measurements on healthy tissue of affected breast at excitation frequency 1033 kHz (The instrument that we made gave 1033KHz at the target measurement at 1MHz)

$FZ_{UH}(10kHz)$ is the focused impedance for measurements on healthy tissue on symmetric position of the unaffected breast at excitation frequency 10kHz,

$FZ_{UH}(1033kHz)$ is the focused impedance for measurements on healthy tissue on symmetric position of the unaffected breast at excitation frequency 1033kHz,

$FZ_{AT}(10kHz)$ is the focused impedance for measurements on the tumour at excitation frequency 10kHz

and

$FZ_{AT}(1033kHz)$ is the focused impedance for measurements on the tumour at excitation frequency 1033kHz.

Feature(1) and *Feature(2)* represent the ratio of focused impedance values of healthy tissue on affected and unaffected breast respectively to that on tumour tissue. Both the denominator and numerator were divided by focused impedance values of the corresponding tissue at 10 kHz to minimize person to person variations.

As explained earlier focused impedance value actually contains two orthogonal TPIM transfer impedance values (Z_1 and Z_2 in Figure 4-70). The values of Z_1 and Z_2 are close to each other for isotropic tissues. However, the values of Z_1 and Z_2 are different for anisotropic tissues. Considering morphological changes in cancerous tissue, for example, the irregular boundary of malignant tumours (Kim et al., 2002), it was hypothesized that the level of anisotropy will be different for malignant tissues than that of healthy or benign tissues. So tissue anisotropy may be a factor for classification of tissue types. Therefore, two more features were defined as below:

$$Feature(3) = \frac{\frac{|Z_1(AT) - Z_2(AT)|}{Mean[Z_1(AT), Z_2(AT)]}}{\frac{|Z_1(AH) - Z_2(AH)|}{Mean[Z_1(AH), Z_2(AH)]}} \quad \text{---- } 4\text{-}17$$

$$Feature(4) = \frac{\frac{|Z_1(AT) - Z_2(AT)|}{Mean[Z_1(AT), Z_2(AT)]}}{\frac{|Z_1(UH) - Z_2(UH)|}{Mean[Z_1(UH), Z_2(UH)]}} \quad \text{----- } 4\text{-}18$$

where $Z_1(AT)$ and $Z_2(AT)$ are the TPIM transfer impedance values for *horizontal* and *vertical* measurements respectively at signal frequency 20 kHz and so on for other tissue types.

Feature(3) and *Feature(4)* represent the degree of anisotropy in the tumour tissue compared to healthy tissue. Again, both the denominator and numerator were divided by the mean value of *horizontal* and *vertical* transfer impedance values to minimize person to person variation.

The normalized feature values for all subjects is shown graphically in Figure 4-75; the *green circles* represent benign class and the *red crosses* represent malignant class. There are few outliers in the feature plot. For malignant class, the outliers in feature(1) and
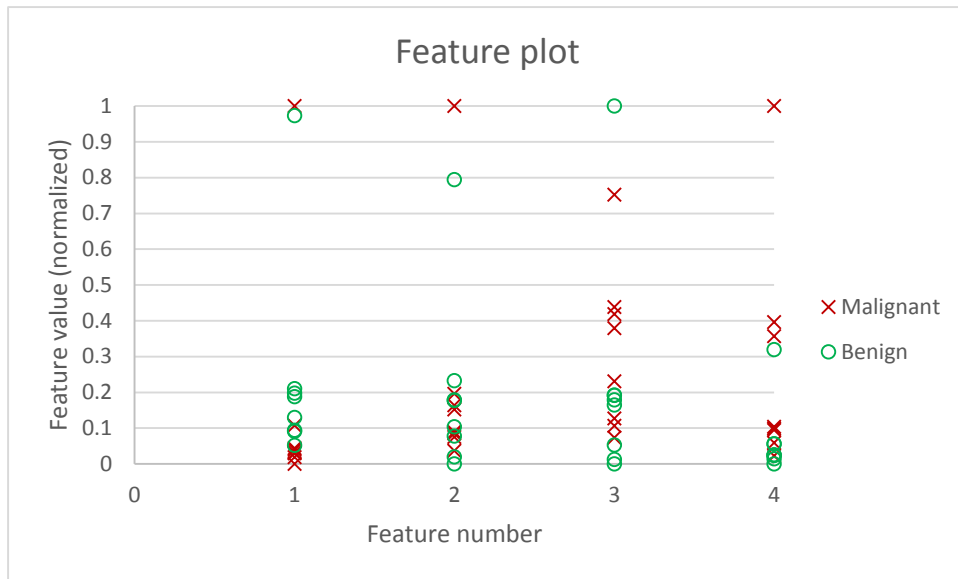
Figure 4-75 The feature plot for all 16 subjects. Green circle: Benign, Red cross: Malignant

feature(2) are the same subject. For benign class, the outliers in feature(1) and feature(2) are the same subject; and the outliers in feature(3) and feature(4) are the same subject.

Mann–Whitney U test was performed on the malignant and benign data sets for each feature to explore if the feature values are significantly different for malignant and benign tissue types. It was found that the values of *Feature(1)* and *Feature(4)* are significantly different for malignant and benign tissues with *p-values* 0.0281 and 0.0207 respectively. However, the values of *Feature(2)* and *Feature(3)* are not significantly different for the two types of tissues (*p-value*>0.05).

Therefore, for classification whether a breast tumour is cancerous (malignant) or noncancerous (benign), k-nearest neighbors (k-NN) classification (Alpaydin, 2010, Bishop, 2006) was performed for *Feature(1)* and *Feature(4)*. The k-NN algorithm is nonparametric and among the simplest of all machine learning algorithms. The k-NN classifier performs classification using a Euclidean distance metric where each of the distances of the features of the training data set from that of the corresponding test data set is evaluated. Depending on the value of *k*, the number of closest member(s) in the training data set is selected for majority voting to choose the winning class (i.e., the class to which the test set is expected to belong). The k-NN classifier was then tested using *'leave one out cross validation'* method (Refaeilzadeh et al., 2009)p-534 with *k* taking the values 1 to 5, i.e., up to five nearest neighbours. Based on biopsy results, the malignant case was considered as *Positive* and benign case was considered as *Negative*. The

predictive values of the features were assessed using standard tests for sensitivity and specificity (Altman and Bland, 1994) as shown in Table 4-5.

Table 4-5 Predictive values for breast tumour classification using k-NN algorithm based on feature(1) and   feature(4). The type of tumour was confirmed by biopsy and was considered as standard.

Parameter	K=1	K=2	K=3	K=4	K=5
Accuracy (%)	62.5	62.5	81.25	81.25	81.25
Sensitivity (%)	75	75	75	75	75
Specificity (%)	50	50	87.5	87.5	87.5
Positive Predictive Value (%)	60	60	85.71	85.71	85.71
Negative Predictive Value (%)	66.67	66.67	77.78	77.78	77.78

It can be noted that the predictive values using k-NN algorithm for k=1 and 2 are same. Again, predictive values for k=3, 4 and 5 are also same but higher. Therefore the value of k=3 was chosen as optimum for better classification.
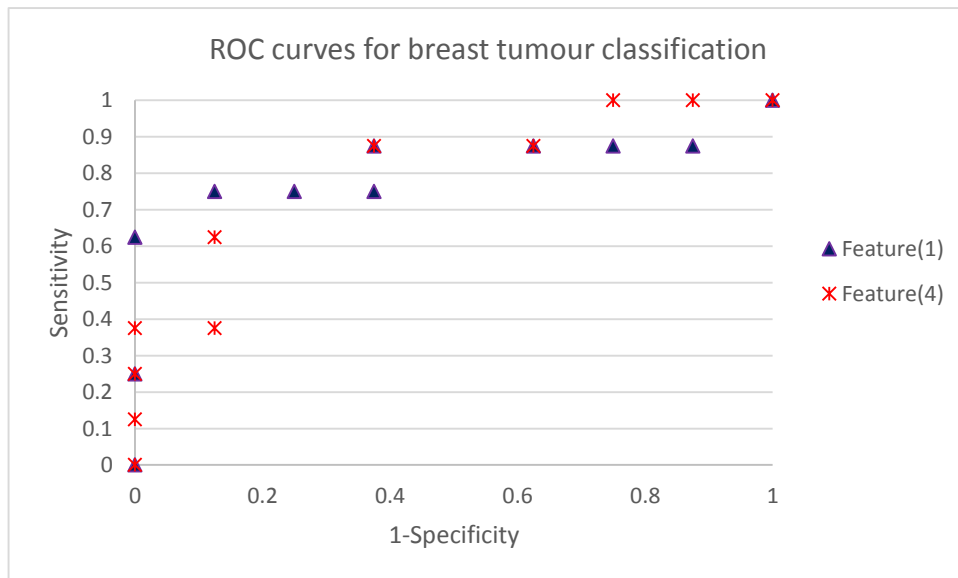
Figure 4-76 ROC curves for breast tumour classification using Feature(1) and Feature(4). The outcomes of biopsy tests were considered as gold standards.

The performance of the classification study was also examined using Receiver Operating Characteristic (*ROC*) curves. Sensitivity and specificity values for breast tumour classification were calculated considering variable *cutoff* values of *Feature(1)* and

Feature(4). *ROC* curves for the predictive values are plotted in Figure 4-76. The area under the *ROC* curve for *Feature(1)* is 0.71 and that for *Feature(4)* is 0.82. The closer is the value to '1' the more distinction ability is expected.

4.6.3 Discussion

An experimental study on 16 human subjects for classification of breast tumour (whether the tumour is benign or malignant) using multi-frequency FIM is described. The study was based on the fact that biochemical and morphological properties of healthy, benign and malignant tissues are different and therefore their electrical impedance spectra is also different. As mentioned earlier, carrying out the impedance measurements on female subjects was not suitable for a male researcher; therefore the impedance measurements on the female subjects were performed by a female MSc student and the student performed some simple analyses (Mahmud, 2017). However, the data is analysed in a completely different way in the present work involving machine learning techniques and statistical tools.

It was observed that the transfer impedance measured using FIM of the tumour region is lower than that of the healthy region. This is in agreement with the results reported by (Jossinet, 1998) where it was shown that the conductivities of malignant tissue and fibroadenoma are higher than that of adipose or connective fatty tissues. This is also in agreement with the results reported by (Brown et al., 2005) where it was shown that the low frequency resistivity in the cancerous cervical tissues is lower compared to healthy tissues. This may be because of the changed morphology of the tumour cells (Grant and Spyrou, 1985).

The variation of impedance with frequency depends on the capacitance of the cell membrane as well as on the resistance of intra and extracellular fluids. Since the cancerous cells are immature, their shape and size are different than those of healthy cells. So the membrane capacitance and the resistance of intra-celluar and extra-celluar fluids are expected to be different. Therefore the impedance variation with frequency is expected to be different for malignant tissue from that of healthy tissue.

Feature(1) represents the ratio of the decrease of focused impedance in the frequency range 10kHz to 1033kHz of the healthy region to that of the tumour region. It can be noted from Figure 4-75 that the values of *Feature(1)* for malignant tumour are clustered towards lower values whereas that for benign tumour are clustered towards higher values

giving a parameter for classification. The lower values of Feature(1) for malignant tissues is in agreement with the results reported by (Surowiec et al., 1988) where it was shown that the variation of conductivity in the frequency range 20kHz to 1MHz is higher for malignant tissues than that for normal breast tissues. The higher variation of impedance with measurement frequency for malignant tissues compared to benign tissues has been attributed to the increased blood flow in the malignant tissues (Sohn et al., 1992, Vaupel et al., 1989, Halter et al., 2015). The conductivity of blood decreases by 17.44% in the frequency range 10kHz to 1033kHz [calculated from (Andreuccetti D, 1997)]. In contrast, the conductivity of breast tissue decreases by only 4.38% in the same frequency range. Since there is more blood flow in the malignant tissue compared to healthy tissue, the impedance variation with frequency in the malignant tumour region is relatively higher. This may be the origin of the lower values of *Feature(1)* in malignant breast tumours compared to that of benign tumours in the current study.

Feature(4) represents the level of tissue anisotropy in the tumour region compared to healthy tissue. Malignant cells are immature and irregular in shape (Smith, 2010). The outer boundary of the malignant tumour is also more irregular than benign ones (Kim et al., 2002). This may be the reason of higher level of anisotropy in malignant tumour compared to benign tumour as shown in Figure 4-75.

The k-NN algorithm for breast tumour classification was tested using *'leave one out cross validation'* method with *k* taking the values 1 to 5. It was found that the value of k=3 ,4 and 5 gives same predictions and therefore the value of *k*=3 can be consider as optimum value of *k*. The prediction of sensitivity and specificity 75% and 87.5% respectively with an accuracy of 81.25%. However, caution is needed in interpreting the sensitivity and specificity values as there were only 16 subjects.

The *ROC* curves also shows good discrimination. The area under the *ROC* curve based on *Feature(1)* is 0.71 which is fair. However, the area under the *ROC* curve based on *Feature(4)* is 0.82 which is good. This indicates that *anisotropy* could be a good feature for characterization of tissue types. Breast tumour classification is another potential application of the multi-frequency FIM system described in chapter-3. The results of this study are encouraging and justify further study with a large number of subjects.

Chapter 5   Conclusion

The Focused Impedance Method (FIM) is a new modality of bioimpedance measurements that has enhanced sensitivity in the central region beneath the electrode configuration which can localize a region of interest minimizing contribution from neighboring regions. In the present work, a multi-frequency FIM (MFFIM) system capable of selecting all three FIM electrode configurations (FIM-4, FIM-6 and FIM-8) was developed. In this thesis a preliminary evaluation of the FIM technique using the developed MFFIM system was carried out into the diagnosis of lung disorders and the classification of breast tissue. The prototype MFFIM system developed allows bioimpedance measurements at multiple frequencies in the range 10kHz-1MHz from a particular FIM electrode configuration selected under software control from a PC. The design used components readily available in Bangladesh where this was possible although the availability of wideband op-amps was challenging in this regard.

A microcontroller based multi-frequency signal generator and a balanced Howland current source with a high output impedance (476 kΩ at 10 kHz and 58.3 kΩ at 1MHz) was implemented for driving currents of constant amplitude into biological tissues. Considering typical load impedance values of 2kΩ and 500Ω at 10 kHz and 1 MHz respectively (Figure 3-2), the output impedance of the implemented current source was adequate for driving constant current in biological tissues with error less than 1%. The output impedance was limited by the limited availability of high frequency opamps, high precision resistors and high precision capacitors in Bangladesh. The measured voltage signal was amplified using a bioelectric amplifier and filters which minimize noise. The measured CMRR was greater than 60dB at frequencies less than 100kHz, whilst falling to 37dB at 1024 kHz (Figure 3-27). However, the common mode noise mostly occurs from main line 50 Hz power wiring and so the value of 60dB would be relevant to the measurements. The peak values of the voltage signal were measured using two different approaches: analogue synchronous peak detection and digital demodulation. The voltage measurement circuitry based on analogue synchronous demodulation can only measure absolute values of transfer impedance. However, the circuitry based on digital demodulation can measure both the magnitude of the impedance and the phase difference.

The performance of the implemented multi-frequency FIM system was analyzed. For the designed MFFIM system based on analogue synchronous demodulation, the

measurement error is equal or less than 4% at 6 of the eight measured frequencies (10,20,40,80, 633, 1033 kHz); at 160kHz and 320kHz these were between 6% and 7% (Figure 3-36). These figures were obtained when the system was evaluated on a Cole-Cole phantom (Figure 3-34) containing impedance parameters appropriate to the human tissue. For the MFFIM based on digital demodulation, the measurement error is around 1% or less at all frequencies lower than 320 kHz while it is slightly higher, around 2% at 633kHz and around 7% at 1033 kHz (Figure 3-38). The errors in phase as measured by the system based on digital demodulation were less than 2% for the four middle frequencies (40, 80, 100, 320; all in kHz) increasing to about 4% at the lower frequencies and to about 8% at higher frequencies (Figure 3-41).

The resolution and frame rate were 0.1Ω and about 45fps respectively for the system based on analogue synchronous demodulation while these figures are, respectively, 0.2Ω and 1.35fps for the system based on digital demodulation.

A comparison was made with a commercially available system procured at a high cost (Sciospec ISX-5). For a Cole-Cole phantom with parameters typical of human tissue and for a contact impedance of 2000 Ω, the error of the developed system was less than 5% at frequencies at or below 633kHz, while it was 10% at 1033kHz (Figure 3-42). In contrast, for measurements using Sciospec system (commercial device), the maximum percentage error is 18% even at contact impedance 200Ω for signal frequency 60 kHz. At signal frequency 1MHz and contact impedance 2000Ω, the measurement error is 29.6% (Figure 3-43). For a pure resistive model, the errors of the Sciospec instrument were much higher; for 1MHz, these were 13% for a contact impedance of 1kΩ and 54% for a contact impedance of 2kΩ, while these figures were about 3% and 13% for the developed MFFIM system based on digital demodulation (Figure 3-44). Therefore, the developed system appears to be far better than the commercial system procured and the latter seems to be inappropriate for serious study of electrical impedance on human subjects at the upper frequencies.

The respiratory related impedance changes in the human thorax measured with electrodes on chest surface is around **1.5Ω** (Brown et al., 1994). A measurement frame rate of greater than 1.5fps is required to follow dynamic changes of thorax due to respiration when considering respiratory rates up to 20 per minute. On the other hand, the transfer impedance values on human breast tissue varies in the range 10-60Ω (Al Amin et al.,

2014). Therefore, the accuracy (error<2% except 1MHz), resolution (<0.2Ω) and frame rate (>1.35fps) of the designed MFFIM system is adequate for noninvasive impedance measurements on breast tissue and on thorax for respiratory related changes although the frame rate of the system based on digital demodulation is marginal for dynamic respiratory studies. The frame rate of 1.35 fps is for measurements at multiple (8) frequencies. Frame rate will be much higher for single frequency measurements. Importantly, the device satisfies the isolation and safety standards recommended by International Electrotechnical Commission (IEC) and therefore it can be used for bioimpedance measurements on human subjects.

The cardiac related impedance change in the thorax region is around **0.08Ω** (Brown et al., 1994) and a frame rate greater than 10fps is required for dynamic cardiac studies. The resolution and frame rate of the designed MFFIM system is not sufficient for impedance measurements from cardiac related changes. Again, the measurement error of the implemented MFFIM system, specially at 1MHz should also be reduced further to achieve better accuracy. Availability of a wider range of electronic components with better performance now allows systems with faster data acquisition rates and higher resolution measurement circuitry including automatic gain control mechanisms to be designed and implemented increasing the applicability of the MFFIM system. The device implemented requires a PC/laptop for data acquisition, limiting its portability. Therefore, a MFFIM system with an inbuilt processing and display will aid the implementations of trials of the applications identified in this thesis in a large number of subjects − essential if they are to have a role in routine diagnosis.

A cubic tank was modeled as volume conductor and the 3D sensitivity distributions of TPIM Linear, TPIM Square, FIM-4, FIM-6 and FIM-8 techniques were investigated using finite element method based simulation software Comsol Multiphysics®. The effect of the variations of *drive/receive electrode separation, electrode dimension,* presence of *inhomogeneity* and *boundary* distance on the sensitivity distribution were studied and compared between the 3 different FIM and 2 different TPIM electrode configurations. An experiment was also designed and performed to investigate 3D measured sensitivity distributions, which gave good agreement with the simulated results.

3D sensitivity profiles of tetrapolar bioimpedance measurement methods, including FIM, identifed the regions of the volume conductor that can be sensed using surface electrodes

(Figure 4-10 and Figure 4-11). Because of the presence of negative sensitivity close to the electrode plane, the average sensitivity was low at shallow depths (Figure 4-12c). The depth of maximum *average sensitivity* is about $1/3.5$ of the electrode separation for TPIM square and FIM-4 configurations (Figure 4-19). The depth of maximum *average sensitivity* is about $1/6$ of the electrode separation for TPIM_Linear and FIM-8 configurations and is $1/4.3$ of the electrode separation for the FIM-6 configuration. The magnitude of the sensitivity decreases with increasing electrode separation for all methods. Among the 5 impedance measurement techniques under investigation, the magnitude of sensitivity at a particular electrode separation is higher for *TPIM_Linear* and *FIM-8* whereas the magnitude of sensitivity is lower for *TPIM_Square* and *FIM-4*.

Percentage depth sensitivity **PDS** and degree of localization **dol** are two new parameters introduced in the present work. These are very useful tools for analyzing and interpreting 3D sensitivity distributions within a volume conductor.

The percentage depth sensitivity *(PDS)* is higher for *TPIM_Square* and *FIM-4* than other configurations (Figure 4-17). Therefore, *TPIM_Square* and *FIM-4* have superior depth penetration ability having relatively less contribution from tissues at shallow depths. The *degree of localization (dol)* was also found to be higher for FIM-4 configuration (Figure 4-21). The parameters *PDS* and *dol* indicated the better localization and penetration ability of FIM-4 when compared to other electrode configurations.

The sensitivity distribution was found to be affected by the electrode diameter. Electrodes with increased diameter effectively spread the injected currents to a larger volume which results in reduced sensitivity (Figure 4-23 – Figure 4-25). The change in sensitivity with electrode *diameter* is substantial at lower depths and is negligible beyond depths greater than edge-edge distance between electrodes (Figure 4-25). In a volume conductor with a localized inhomogeneity embedded within a uniform background, the sensitivity is higher within an inhomogeneity with a higher conductivity than the background, and vice versa for a lower conductivity (Figure 4-26). The presence of resistive layers increases the sensitivity in the region between electrode plane and the resistive layer (Figure 4-32).

The change in sensitivity with the distance of the electrodes from boundaries in the volume conductor is less significant when the distance of those boundaries is more than

twice the electrode separation. However, as the boundaries in the volume conductor approach the electrodes, the magnitude of sensitivity increases greatly (Figure 4-33) due to the increase in current density. The proximity of a boundary close to the electrodes also changes the pattern of sensitivity profiles (Figure 4-35). Therefore the distance of boundary of the volume conductor under study should be considered while interpreting impedance measurements.

An experiment was designed to measure 3D sensitivity profiles in a volume conductor to validate the simulation results. The sensitivity distributions obtained experimentally were in good agreement with the simulation results and well within experimental errors (Figure 4-37). This experimental validation of the sensitivity distribution gives confidence in using FEM modelling for designing transfer impedance measurements.

A human thorax was modelled in the Comsol Multiphysics FEM software to study various aspects of impedance measurements on human thorax. An FEM model provides visualization of sensitivity distributions in various domains within the thorax. Focused Impedance measurements were simulated by placing electrodes on the chest surface during the maximum inspiration and expiration phases of breathing using the FIM-4 electrode configuration. Similar measurements were also performed on a human subject using the multi-frequency FIM system develop as part of this work. The pattern of percentage changes of impedance between inspiration and expiration on different vertical locations of thorax were similar for simulation and experimental measurements (Figure 4-59 and Figure 4-60). The percentage change in impedance between maximum inspiration and expiration at different vertical levels of thorax were in the range 5-24% for the FEM model whereas the changes were in the range 5-17% for a human subject. Differences depend on several factors including organs within the thorax and body frame size that were not considered in the current model. A simulation study showed that the impedance change between maximum inspiration and expiration, measured using an FIM-4 probe with appropriate electrode separation, was substantially lower in the region of thorax where the underlying lung is filled with fluid (5.1%) compared to that without fluid (16.8%) for a fluid volume of 663cm3 (Figure 4-62). Based on this simulation study, a new technique is proposed to detect fluid accumulation in lungs using FIM measurements.

The FEM model of thorax implemented is a simplified model and included the cardio-respiratory organs but excluded the liver and diaphragm which occupy a substantial volume within the thorax. The domains modeled are considered isotropic which is not the case in reality. Again, positional and volume changes of organs within thorax during inspiration and expiration are very substantial in practice and these changes were not included in the implemented model. A thorax model based on the segmentation of CT/MRI images for the whole thorax will give a better representation of the anatomy. The tissue anisotropy and anatomical changes due to breathing can also be incorporated into a future model. The feasibility of the method proposed for the detection of localized lung ventilation disorder now needs to be tested on human subjects with lung disease confirmed by X-ray.

An experimental study was performed on 16 female subjects into the classification of breast tumours (whether the tumour is benign or malignant) based on transfer impedance measurements using the focused impedance method. It was observed that the focused impedance of the tumour region is lower than that of healthy neighbouring region in the same breast or in the opposite breast at a symmetrical location. It was also observed that focused impedance decreased with increasing frequency for all types of breast tissue. Moreover, the impedance values for the two orthogonal TPIM measurements of the FIM-4 measurement were different on all tissue types which was attributed to tissue anisotropy. The change of focused impedance with frequency and the level of anisotropy on all types of tissue mentioned above were investigated to determine if these features can classify the tumour. Applying a k-nearest neighbors (k-NN) algorithm the *sensitivity*, *specificity* and predictive *accuracy* of breast tumour classification was found to be 75%, 87.5% and 81.25% respectively for k=3 (Table 4-5). Receiver Operating Characteristic (*ROC*) curves for predictive values were also plotted and the area under *ROC* curve for the feature representing tissue anisotropy was 0.82 (Figure 4-76). However, the study to explore the feasibility of using FIM in the characterization of breast tumours was performed on 16 patients is very small. Because of this the values of sensitivity and specificity should be interpreted with caution. However, the results of this study are encouraging and justify further study. Therefore, the technique needs to be studied on a large number of subjects to assess the utility of multi-frequency FIM in the classification of breast tumour.

Overall, the present work has established the characteristics of FIM giving insights that will help in selecting suitable configurations of FIM and with suitable electrode separations required for specific physiological measurement applications. This has demonstrated in preliminary studies of lung ventilation and characterization of breast tumour – predicting whether a palpable tumour is malignant or benign. This is the first systematic study of how the FIM method can be used to make clinical measurements. The multi-frequency FIM system has been developed with the aim of assessing the utility of FIM in diagnosing lungs disorders, breast malignancy in resource constraint settings. Pneumonia, TB, edema are common lungs diseases in developing countries like Bangladesh, especially amongst children. So a small, low cost, non-invasive system that can be incorporated with the existing telemedicine infrastructure of Bangladesh, has the potential to benefit a large number of people spread over a large geographic area, particularly those living in the rural areas where modern healthcare facilities (eg. X-rays) are not available.

References

AAMI 1985. *American national standard, safe current limits for electromedical apparatus*, Association for the Advancement of Medical Instrumentation.

ABDUL, S., BROWN, B., MILNES, P. & TIDY, J. 2006. The use of electrical impedance spectroscopy in the detection of cervical intraepithelial neoplasia. *International Journal of Gynecological Cancer,* 16**,** 1823-1832.

ABRAMS, E., MOHR, M., ENGEL, C. & BOTTLANG, M. 2003. CROSS-SECTIONAL GEOMETRY OF HUMAN RIBS. *27th annual meeting of the American Society of Biomechanics.* Toledo, OH, USA.

ADLER, A., AMYOT, R., GUARDO, R., BATES, J. & BERTHIAUME, Y. 1997. Monitoring changes in lung air and liquid volumes with electrical impedance tomography. *Journal of Applied Physiology,* 83**,** 1762-1767.

AL AMIN, A., PARVIN, S., KADIR, M., TAHMID, T., ALAM, S. K. & RABBANI, K. S.-E. 2014. Classification of breast tumour using electrical impedance and machine learning techniques. *Physiological measurement,* 35**,** 965.

ALPAYDIN, E. 2010. Introduction to Machine Learning, 2nd edn. Adaptive Computation and Machine Learning. The MIT Press (February 2010).

ALTMAN, D. G. & BLAND, J. M. 1994. STATISTICS NOTES-DIAGNOSTIC-TESTS-1-SENSITIVITY AND SPECIFICITY. 3. BRITISH MED JOURNAL PUBL GROUP BRITISH MED ASSOC HOUSE, TAVISTOCK SQUARE, LONDON, ENGLAND WC1H 9JR.

ANDREUCCETTI D, F. R., PETRUCCI C. 1997. *An Internet resource for the calculation of the dielectric properties of body tissues in the frequency range 10 Hz - 100 GHz* [Online]. Available: Website at http://niremf.ifac.cnr.it/tissprop/. IFAC-CNR, Florence (Italy).

ANNUS, P., KRIVOSHEI, A., MIN, M. & PARVE, T. Excitation current source for bioimpedance measurement applications: analysis and design. Instrumentation and Measurement Technology Conference Proceedings, 2008. IMTC 2008. IEEE, 2008. IEEE, 848-853.

ARMSTRONG, J., GLUCK, E., CRAPO, R., JONES, H. A. & HUGHES, J. 1982. Lung tissue volume estimated by simultaneous radiographic and helium dilution methods. *Thorax,* 37**,** 676-679.

ASSENHEIMER, M., LAVER-MOSKOVITZ, O., MALONEK, D., MANOR, D., NAHALIEL, U., NITZAN, R. & SAAD, A. 2001. The T-SCANTM technology: electrical impedance as a diagnostic tool for breast cancer detection. *Physiological measurement,* 22**,** 1.

ATMEL, A. ATmega8 Datasheet.

BABA, A. & CATOI, C. 2007. In comparative oncology: Chapter 3, Tumor cell morphology. *The Publishing House of the Romanian Academy, Bucharest*.

BAKSHI, U. A. & GODSE, A. P. 2008. *Electronics Devices And Linear Circuits*, Technical Publications.

BARBER, D., BROWN, B. & FREESTON, I. Imaging spatial distributions of resistivity using applied potential tomography—APT. Information Processing in Medical Imaging, 1984. Springer, 446-462.

BASTEDO, W. 1917. PULMONARY EDEMA IN PNEUMONIA AND ITS TREATMENT. *Journal of the American Medical Association,* 69**,** 800-805.

BERA, T. K. & JAMPANA, N. A multifrequency constant current source suitable for electrical impedance tomography (EIT). Systems in Medicine and Biology (ICSMB), 2010 International Conference on, 2010. IEEE, 278-283.

BERTEMES-FILHO, P., FELIPE, A. & VINCENCE, V. C. 2013. High Accurate Howland Current Source: Output Constraints Analysis. *Circuits and Systems,* 4**,** 451.

BERTEMES-FILHO, P., NEGRI, L., FELIPE, A. & VINCENCE, V. Mirrored modified Howland circuit for bioimpedance applications: Analytical analysis. Journal of Physics: Conference Series, 2012. IOP Publishing, 012030.

BERTEMES FILHO, P. 2002. *Tissue characterisation using an impedance spectrosopy probe.* University of Sheffield.

BIOSCAN-II, M. *Maltron Bioscan 920-2-S,* http://www.maltronint.com/products/bioscan920-2S.php [Online].

BIRKENFELD, A. & KASE, N. G. 1994. Functional anatomy and physiology of the female breast. *Obstetrics and gynecology clinics of North America,* 21**,** 433-444.

BISHOP, C. M. 2006. Pattern recognition. *Machine Learning,* 128**,** 1-58.

BOLTON, M., WARD, L., KHAN, A., CAMPBELL, I., NIGHTINGALE, P., DEWIT, O. & ELIA, M. 1998. Sources of error in bioimpedance spectroscopy. *Physiological measurement,* 19**,** 235.

BOONE, K. & HOLDER, D. 1996. Current approaches to analogue instrumentation design in electrical impedance tomography. *Physiological measurement,* 17**,** 229.

BROWN, B., WILSON, A. & BERTEMES-FILHO, P. 2000a. Bipolar and tetrapolar transfer impedance measurements from volume conductor. *Electronics Letters,* 36**,** 2060-2062.

BROWN, B. H. 1981. Medical physics and physiological measurement.

BROWN, B. H., BARBER, D. C., MORICE, A. & LEATHARD, A. D. 1994. Cardiac and respiratory related electrical impedance changes in the human thorax. *Biomedical Engineering, IEEE Transactions on,* 41**,** 729-734.

BROWN, B. H., MILNES, P., ABDUL, S. & TIDY, J. A. 2005. Detection of cervical intraepithelial neoplasia using impedance spectroscopy: a prospective study. *BJOG: An International Journal of Obstetrics & Gynaecology,* 112**,** 802-806.

BROWN, B. H., TIDY, J. A., BOSTON, K., BLACKETT, A. D., SMALLWOOD, R. H. & SHARP, F. 2000b. Relation between tissue structure and imposed electrical current flow in cervical neoplasia. *The Lancet,* 355**,** 892-895.

CAD, D. 2016. *Lung 3D CAD Model* [Online]. Available: https://www.3dcadbrowser.com/download.aspx?3dmodel=71047 [Accessed 2016.

CAMPBELL, J., HARRIS, N., ZHANG, F., BROWN, B. & MORICE, A. 1994. Clinical applications of electrical impedance tomography in the monitoring of changes in intrathoracic fluid volumes. *Physiological measurement,* 15**,** A217.

CASTRO, N. P., OSÓRIO, C. A., TORRES, C., BASTOS, E. P., MOURÃO-NETO, M., SOARES, F. A., BRENTANI, H. P. & CARRARO, D. M. 2008. Evidence that molecular changes in cells occur before morphological alterations during the progression of breast ductal carcinoma. *Breast Cancer Research,* 10**,** R87.

CHAO, C., TOROSIAN, M. H., BORAAS, M. C., SIGURDSON, E. R., HOFFMAN, J. P., EISENBERG, B. L. & FOWBLE, B. 2001. Local recurrence of breast cancer in the stereotactic core needle biopsy site: case reports and review of the literature. *The breast journal,* 7**,** 124-127.

CHEN, D., DENG, X. & YANG, W. 2010. Comparison of three current sources for single-electrode capacitance measurement. *Review of Scientific Instruments,* 81**,** 034704.

CHEN, X., LIU, K., WANG, Z., ZHU, Y., ZHAO, Y., KONG, H., XIE, W. & WANG, H. 2015. Computed tomography measurement of pulmonary artery for diagnosis of COPD and its comorbidity pulmonary hypertension. *International journal of chronic obstructive pulmonary disease,* 10**,** 2525.

CHEREPENIN, V., KARPOV, A., KORJENEVSKY, A., KORNIENKO, V., MAZALETSKAYA, A., MAZOUROV, D. & MEISTER, D. 2001. A 3D electrical impedance tomography (EIT) system for breast cancer detection. *Physiological measurement,* 22**,** 9.

COLE, K. S. Permeability and impermeability of cell membranes for ions. Cold Spring Harbor Symposia on Quantitative Biology, 1940. Cold Spring Harbor Laboratory Press, 110-122.

COLE, K. S. & COLE, R. H. 1941. Dispersion and absorption in dielectrics I. Alternating current characteristics. *The Journal of Chemical Physics,* 9**,** 341-351.

DA SILVA, J. E., DE SÁ, J. M. & JOSSINET, J. 2000. Classification of breast tissue by electrical impedance spectroscopy. *Medical and Biological Engineering and Computing,* 38**,** 26-30.

FEIN, A., GROSSMAN, R. F., JONES, J. G., GOODMAN, P. & MURRAY, J. 1979a. Evaluation of transthoracic electrical impedance in the diagnosis of pulmonary edema. *Circulation,* 60**,** 1156-1160.

FEIN, A., GROSSMAN, R. F., JONES, J. G., GOODMAN, P. C. & MURRAY, J. F. 1979b. Evaluation of transthoracic electrical impedance in the diagnosis of pulmonary edema. *Circulation,* 60**,** 1156-1160.

FERDOUS, H. 2014. *Study of Changes in Lung Transfer Impedance due to Ventilation Using Focused Impedance Measurement (FIM) Technique.* PhD Thesis, University of Oslo, Norway.

FERDOUS, H., BAIG, T. N. & SIDDIQUE-E-RABBANI, K. 2013. Thorax mapping for localised lung impedance change using focused impedance measurement (FIM): a pilot study. *Journal of Electrical Bioimpedance,* 4**,** 57-61.

FLORENTINE, B. D., COBB, C. J., FRANKEL, K., GREAVES, T. & MARTIN, S. E. 1997. Core needle biopsy. *Cancer Cytopathology,* 81**,** 33-39.

FOSTER, K. R. & SCHWAN, H. P. 1995. Dielectric properties of tissues. *Handbook of biological effects of electromagnetic fields,* 2**,** 25-102.

FRANCO, S. 2001. *Design with operational amplifiers and analog integrated circuits*, McGraw-Hill.

FRERICHS, I. 2000. Electrical impedance tomography (EIT) in applications related to lung and ventilation: a review of experimental and clinical activities. *Physiological measurement,* 21**,** R1.

GABRIEL, C., GABRIEL, S. & COURHOUT, E. 1996a. The dielectric properties of biological tissues: I. Literature survey. *Phys Med Biol,* 41**,** l-2249.

GABRIEL, S., LAU, R. & GABRIEL, C. 1996b. The dielectric properties of biological tissues: II. Measurements in the frequency range 10 Hz to 20 GHz. *Physics in medicine and biology,* 41**,** 2251.

GABRIEL, S., LAU, R. & GABRIEL, C. 1996c. The dielectric properties of biological tissues: III. Parametric models for the dielectric spectrum of tissues. *Physics in medicine and biology,* 41**,** 2271.

GEDDES, L. & BAKER, L. 1967. The specific resistance of biological material—a compendium of data for the biomedical engineer and physiologist. *Medical and biological engineering,* 5**,** 271-293.

GESELOWITZ, D. B. 1971. An application of electrocardiographic lead theory to impedance plethysmography. *Biomedical Engineering, IEEE Transactions on***,** 38-41.

GODDI, A., BONARDI, M. & ALESSI, S. 2012. Breast elastography: a literature review. *Journal of ultrasound,* 15**,** 192-198.

GORDON, P. B. 2002. Ultrasound for breast cancer screening and staging. *Radiologic Clinics of North America,* 40**,** 431-441.

GRANT, J. & SPYROU, N. 1985. Complex permittivity differences between normal and pathological tissues: Mechanisms and medical significance. *Journal of Bioelectricity,* 4**,** 419-458.

GRIMNES, S. & MARTINSEN, O. 2008. *Bioelectricity and bioimpedance basics*, Academic Press.

GRIMNES, S. & MARTINSEN, Ø. G. 2006. Sources of error in tetrapolar impedance measurements on biomaterials and other ionic conductors. *Journal of Physics D: Applied Physics,* 40**,** 9.

GUO, D. 2013. *Choose Resistors to Minimize Errors in Grounded-Load Current Source* [Online]. Analog Devices Available: http://www.analog.com/en/analog-dialogue/articles/choose-resistors-to-minimize-errors.html.

HALDANE, J. S. & PRIESTLEY, J. G. 1905. The regulation of the lung-ventilation. *The Journal of physiology,* 32**,** 225-266.

HALL, J. E. 2015. *Guyton and Hall textbook of medical physiology*, Elsevier Health Sciences.

HALTER, R. J., HARTOV, A., POPLACK, S. P., WELLS, W. A., ROSENKRANZ, K. M., BARTH, R. J., KAUFMAN, P. A. & PAULSEN, K. D. 2015. Real-time electrical impedance variations in women with and without breast cancer. *IEEE transactions on medical imaging,* 34**,** 38-48.

HAMIDI, S., JAFARI, R., NIA, A. M. & SOLEIMANI, M. Design and implementation of a DSP-based digital phase sensitive demodulation for an EIT system. Journal of Physics: Conference Series, 2010. IOP Publishing, 012147.

HARTOV, A., SONI, N. & HALTER, R. 2005. Breast cancer screening with electrical impedance tomography. *Electrical Impedance Tomography: Methods, History and Applications***,** 167-85.

HEINITZ, J. & MINET, O. Dielectric properties of female breast tumors. Ninth International Conference on Electrical Bio-Impedance, Heidelberg, 1995.

HELMHOLTZ, H. 1853. Ueber einige Gesetze der Vertheilung elektrischer Ströme in körperlichen Leitern mit Anwendung auf die thierisch-elektrischen Versuche. *Ann. Physik und Chemie,* 89**,** 354-77.

HINTON, A., SAYERS, B. & SOLARTRON, V. R. 1998. Advanced Instrumentation for Bioimpedance Measurements. *Gen,* 1260**,** 1250-1253.

HOLDER, D. S. 2004. *Electrical impedance tomography: methods, history and applications*, CRC Press.

HOLDER, D. S. 2010. *Electrical impedance tomography: methods, history and applications*, CRC Press.

HOROWITZ, P., HILL, W. & HAYES, T. C. 1989. *The art of electronics*, Cambridge university press Cambridge.

HWANG, J.-H., KIRKPATRICK, K., MASON, T. & GARBOCZI, E. 1997. Experimental limitations in impedance spectroscopy:: Part IV. Electrode contact effects. *Solid State Ionics,* 98**,** 93-104.

IEC, I. E. C.-. 2004. International Standard IEC 60601-1-2, Medical Electrical Equipment, Part 1: General Requirements for Safety. *Medical Electrical Equipment, Part,* 1.

ISLAM, N., RABBANI, K. S.-E. & WILSON, A. 2010. The sensitivity of focused electrical impedance measurements. *Physiological measurement,* 31**,** S97.

ITOH, A., UENO, E., TOHNO, E., KAMMA, H., TAKAHASHI, H., SHIINA, T., YAMAKAWA, M. & MATSUMURA, T. 2006. Breast disease: clinical application of us elastography for diagnosis 1. *Radiology,* 239**,** 341-350.

IVORRA, A. 2003. Bioimpedance monitoring for physicians: an overview. *Centre Nacional de Microelectrònica Biomedical Applications Group***,** 1-35.

JISONG, F. Z. B. 2007. Design of A High Performance Sine Wave Current Source Based on DDS Chip AD9833 [J]. *Microcomputer Information,* 35**,** 126.

JOHANSEN, B., BJØRTUFT, O. & BOE, J. 1993. Static lung volumes in healthy subjects assessed by helium dilution during occlusion of one mainstem bronchus. *Thorax,* 48**,** 381-384.

JOSSINET, J. 1996. Variability of impedivity in normal and pathological breast tissue. *Medical and Biological Engineering and Computing,* 34**,** 346-350.

JOSSINET, J. 1998. The impedivity of freshly excised human breast tissue. *Physiological measurement,* 19**,** 61.

JOSSINET, J. & SCHMITT, M. 1999. A review of parameters for the bioelectrical characterization of breast tissue. *Annals of the New York Academy of Sciences,* 873**,** 30-41.

KADIR, M., BAIG, T. & RABBANI, K. 2009. Application of 6-electrode Focused Impedance Method (FIM) to study lungs ventilation. *Proc. EIT2009, UK*.

KADIR, M. A., AHMED, S. P., AL QUADERI, G. D., RAHMAN, R. & RABBANI, K. S.-E. Application of focused impedance method (FIM) to determine the volume of an object within a volume conductor. Proceedings of the 2013 COMSOL Conference, Bangalore, India http://www. comsol. com/paper/download/182751/kadir_paper. pdf, 2013.

KADIR, M. A., BAIG, T. N. & RABBANI, K. S.-E. 2015. FOCUSED IMPEDANCE METHOD TO DETECT LOCALIZED LUNG VENTILATION DISORDERS IN COMBINATION WITH CONVENTIONAL SPIROMETRY. *Biomedical Engineering: Applications, Basis and Communications,* 27**,** 1550029.

KADIR, M. A., FERDOUS, H., BAIG, T. N. & SIDDIQUE-E-RABBANI, K. Ventilation mapping of chest using Focused Impedance Method (FIM). Journal of Physics: Conference Series, 2010. IOP Publishing, 012031.

KERNER, T. E., PAULSEN, K. D., HARTOV, A., SOHO, S. K. & POPLACK, S. P. 2002. Electrical impedance spectroscopy of the breast: clinical imaging results in 26 subjects. *IEEE transactions on medical imaging,* 21**,** 638-645.

KIM, K., KIM, J. & MIN, B. 2002. Classification of malignant and benign tumors using boundary characteristics in breast ultrasonograms. *Journal of digital imaging,* 15**,** 224-227.

KIMURA, S., MORIMOTO, T., UYAMA, T., MONDEN, Y., KINOUCHI, Y. & IRITANI, T. 1994. Application of electrical impedance analysis for diagnosis of a pulmonary mass. *Chest Journal,* 105**,** 1679-1682.

KOLB, T. M., LICHY, J. & NEWHOUSE, J. H. 2002. Comparison of the performance of screening mammography, physical examination, and breast us and evaluation of factors that influence them: An analysis of 27,825 patient evaluations 1. *Radiology,* 225**,** 165-175.

KRAMER, G. H., CAPELLO, K., BEARRS, B., LAUZON, A. & NORMANDEAU, L. 2012. Linear dimensions and volumes of human lungs obtained from ct images. *Health physics,* 102**,** 378-383.

KUHAJDA, I., ZAROGOULIDIS, K., TSIRGOGIANNI, K., TSAVLIS, D., KIOUMIS, I., KOSMIDIS, C., TSAKIRIDIS, K., MPAKAS, A., ZAROGOULIDIS, P. & ZISSIMOPOULOS, A. 2015. Lung abscess-etiology, diagnostic and treatment options. *Annals of translational medicine,* 3.

LAVER, R. C., REED, M., HARRISON, B. J. & NEWTON, P. D. 1999. The management of women with breast symptoms referred to secondary care clinics in Sheffield: implications for improving local services. *Annals of the Royal College of Surgeons of England,* 81**,** 242.

LEEMING, M. N., RAY, C. & HOWLAND, W. S. 1970. Low-voltage, direct-current burns. *JAMA,* 214**,** 1681-1684.

LEGATT, A. D. 1995. Impairment of common mode rejection by mismatched electrode impedances: Quantitative analysis. *American Journal of EEG Technology,* 35**,** 296-302.

LIOTTA, L. A. 1983. Tumor invasion and the extracellular matrix. *Lab. Invest.,* 49**,** 636-649.

LOGAN, W. 1983. Screen-film mammography: technique. *Breast carcinoma: current diagnosis and treatment. New York: Masson***,** 141-160.

MAHMUD, S. R. 2017. *Breast Tissue Characterization Using Pigeon Hole Imaging.* M.S. , University of Dhaka.

MALMIVUO, J. & PLONSEY, R. 1995. *Bioelectromagnetism: principles and applications of bioelectric and biomagnetic fields*, Oxford University Press.

MARTINSEN, Ø. G. & GRIMNES, S. The concept of transfer impedance in bioimpedance measurements. 4th European Conference of the International Federation for Medical and Biological Engineering, 2009. Springer, 1078-1079.

MARTINSEN, O. G., GRIMNES, S. & SCHWAN, H. P. 2002. Interface phenomena and dielectric properties of biological tissue. *Encyclopedia of surface and colloid science,* 20**,** 2643-2653.

MAYER, M., BRUNNER, P., MERWA, R. & SCHARFETTER, H. 2005. Monitoring of lung edema using focused impedance spectroscopy: a feasibility study. *Physiological measurement,* 26**,** 185.

MCEWAN, A., CUSICK, G. & HOLDER, D. 2007. A review of errors in multi-frequency EIT instrumentation. *Physiological measurement,* 28**,** S197.

METHERALL, P., BARBER, D., SMALLWOOD, R. & BROWN, B. 1996. Three dimensional electrical impedance tomography. *Nature,* 380**,** 509-512.

MIKLAVČIČ, D., PAVŠELJ, N. & HART, F. X. 2006. Electric properties of tissues. *Wiley encyclopedia of biomedical engineering*.

MILNE, E., PISTOLESI, M., MINIATI, M. & GIUNTINI, C. 1985. The radiologic distinction of cardiogenic and noncardiogenic edema. *American journal of roentgenology,* 144**,** 879-894.

MIN, M., PARVE, T., RONK, A., ANNUS, P. & PAAVLE, T. 2007a. Synchronous sampling and demodulation in an instrument for multifrequency bioimpedance measurement. *Instrumentation and Measurement, IEEE Transactions on,* 56**,** 1365-1372.

MIN, M., PLIQUETT, U., NACKE, T., BARTHEL, A., ANNUS, P. & LAND, R. Signals in bioimpedance measurement: different waveforms for different tasks. 13th International Conference on Electrical Bioimpedance and the 8th Conference on Electrical Impedance Tomography, 2007b. Springer, 181-184.

MIN, M., PLIQUETT, U., NACKE, T., BARTHEL, A., ANNUS, P. & LAND, R. 2008. Broadband excitation for short-time impedance spectroscopy. *Physiological measurement,* 29**,** S185.

MORIMOTO, T., KINOUCHI, Y., IRITANI, T., KIMURA, S., KONISHI, Y., MITSUYAMA, N., KOMAKI, K. & MONDEN, Y. 1990. Measurement of the electrical bio-impedance of breast tumors. *European surgical research,* 22**,** 86-92.

MORROW, M., WATERS, J. & MORRIS, E. 2011. MRI for breast cancer screening, diagnosis, and treatment. *The Lancet,* 378**,** 1804-1811.

MOSCHETTA, M., TELEGRAFO, M., CARLUCCIO, D., JABLONSKA, J., RELLA, L., SERIO, G., CARROZZO, M., IANORA, A. S. & ANGELELLI, G. 2014. Comparison between fine needle aspiration cytology (FNAC) and core needle biopsy (CNB) in the diagnosis of breast lesions. *Il Giornale di chirurgia,* 35**,** 171.

MULTIPHYSICS, C. 2007. AC/DC Module User's Guide. COMSOL AB.

MULTIPHYSICS, C. 2012. *COMSOL multiphysics user guide (Version 4.3 a)* [Online].

NELSON, S., MASON, C. M., KOLLS, J. & SUMMER, W. R. 1995. Pathophysiology of pneumonia. *Clinics in chest medicine,* 16**,** 1-12.

NEWELL, J., PENG, Y., EDIC, P., BLUE, R., JAIA, H. & NEWELL, R. 1998. Effect of electrode size on impedance images of two-and three-dimensional objects. *IEEE transactions on biomedical engineering,* 45**,** 531-534.

NEWELL, J. C., EDIC, P., REN, X., LARSON-WISEMAN, J. & DANYLEIKO, M. 1996. Assessment of acute pulmonary edema in dogs by electrical impedance imaging. *IEEE Transactions on Biomedical Engineering,* 43**,** 133-138.

NOPP, P., RAPP, E., PFUTZNER, H., NAKESCH, H. & RUSHAM, C. 1993. Dielectric properties of lung tissue as a function of air content. *Physics in medicine and biology,* 38**,** 699.

OHMINE, Y., MORIMOTO, T., KINOUCHI, Y., IRITANI, T., TAKEUCHI, M. & MONDEN, Y. 2000. Noninvasive measurement of the electrical bioimpedance of breast tumors. *Anticancer research,* 20**,** 1941-1946.

OPHIR, J., ALAM, S., GARRA, B., KALLEL, F., KONOFAGOU, E., KROUSKOP, T. & VARGHESE, T. 1999. Elastography: ultrasonic estimation and imaging of the elastic properties of tissues. *Proceedings of the Institution of Mechanical Engineers, Part H: Journal of Engineering in Medicine,* 213**,** 203-233.

PALLAS-ARENY, R. & WEBSTER, J. G. 1993a. AC Instrumentation Amplifier for Bioimpedance Measurements. *IEEE Transactions on Biomedical Engineering,* 40**,** 831.

PALLAS-ARENY, R. & WEBSTER, J. G. 1993b. Bioelectric impedance measurements using synchronous sampling. *IEEE transactions on bio-medical engineering,* 40**,** 824-829.

PALLÁS-ARENY, R. & WEBSTER, J. G. 1991. Common mode rejection ratio in differential amplifiers. *Instrumentation and Measurement, IEEE Transactions on,* 40**,** 669-676.

PEACOCK, W. F., M ALBERT, N., D WHITE, R. & L EMERMAN, C. 2000. Bioimpedance Monitoring: Better Than Chest X-Ray for Predicting Abnormal Pulmonary Fluid? *Congestive Heart Failure,* 6**,** 86-89.

PERNKOPF, E. 1964. *Atlas of Topographical and Applied Human Anatomy: Thorax, abdomen, and extremities*, WB Saunders Co.

PETHIG, R. & KELL, D. B. 1987. The passive electrical properties of biological systems: their significance in physiology, biophysics and biotechnology. *Physics in medicine and biology,* 32**,** 933.

PETTERSEN, F.-J. & HØGETVEIT, J. O. 2011. From 3D tissue data to impedance using Simpleware ScanFE+ IP and COMSOL Multiphysics–a tutorial. *Journal of Electrical Bioimpedance,* 2**,** 13-32.

PETTERSEN, F., FERDOUS, H., KALVØY, H., MARTINSEN, Ø. G. & HØGETVEIT, J. 2014. Comparison of four different FIM configurations—a simulation study. *Physiological measurement,* 35**,** 1067.

PICOTECH. *https://www.picotech.com/download/datasheets/PicoScope2200ASeries DataSheet.pdf* [Online].

PING, Y., DANHUI, W. & LIANGYU, Y. 2008. Application of DDS Technology in Sine Wave Function Generator [J]. *Computer Measurement & Control,* 11**,** 077.

PLIQUET, U., GERSING, E. & PLIQUETT, F. 2000. Evaluation of Fast Time-domain Based Impedance Measurements on Biological Tissue-Beurteilung schneller Impedanzmessungen im Zeitbereich an biologischen Geweben. *Biomedizinische Technik/Biomedical Engineering,* 45**,** 6-13.

POMERANTZ, M., BAUMGARTNER, R., LAURIDSON, J. & EISEMAN, B. 1969. Transthoracic electrical impedance for the early detection of pulmonary edema. *Surgery,* 66**,** 260-268.

PULIGANDLA, P. S. & LABERGE, J.-M. Respiratory infections: pneumonia, lung abscess, and empyema. Seminars in pediatric surgery, 2008. Elsevier, 42-52.

RABBANI, K., HASSAN, M. & KIBER, A. 1996. 3D object localization using EIT measurements at two levels. *Physiological measurement,* 17**,** 189.

RABBANI, K. & KABIR, A. 1991. Studies on the effect of the third dimension on a two-dimensional electrical impedance tomography system. *Clinical Physics and Physiological Measurement,* 12**,** 393.

RABBANI, K. & KARAL, M. 2008. A new four-electrode Focused Impedance Measurement (FIM) system for physiological study. *Annals of biomedical engineering,* 36**,** 1072-1077.

RABBANI, K., SARKER, M., AKOND, M. & AKTER, T. 1999. Focused impedance measurement (FIM): a new technique with improved zone localization. *Annals of the New York Academy of Sciences,* 873**,** 408-420.

RAGHEB, A., GEDDES, L., BOURLAND, J. & TACKER, W. 1992. Tetrapolar electrode system for measuring physiological events by impedance. *Medical and Biological Engineering and Computing,* 30**,** 115-117.

REFAEILZADEH, P., TANG, L. & LIU, H. 2009. Cross-validation. *Encyclopedia of database systems.* Springer.

ROBIN, E. D., CROSS, C. E. & ZELIS, R. 1973. Pulmonary edema. *New England Journal of Medicine,* 288**,** 292-304.

ROGERS, K. 2011. *The Respiratory System*, Britannica Educational Publishing.

ROSS, A. S., SAULNIER, G., NEWELL, J. & ISAACSON, D. 2003. Current source design for electrical impedance tomography. *Physiological measurement,* 24**,** 509.

SARDANELLI, F., GIUSEPPETTI, G. M., PANIZZA, P., BAZZOCCHI, M., FAUSTO, A., SIMONETTI, G., LATTANZIO, V. & DEL MASCHIO, A. 2004. Sensitivity of MRI versus mammography for detecting foci of multifocal, multicentric breast cancer in fatty and dense breasts using the whole-breast pathologic examination as a gold standard. *American Journal of Roentgenology,* 183**,** 1149-1157.

SARVAZYAN, A., J HALL, T., W URBAN, M., FATEMI, M., R AGLYAMOV, S. & S GARRA, B. 2011. An overview of elastography-an emerging branch of medical imaging. *Current medical imaging reviews,* 7**,** 255-282.

SCHARFETTER, H., SCHLAGER, T., STOLLBERGER, R., FELSBERGER, R., HUTTEN, H. & HINGHOFER-SZALKAY, H. 2001. Assessing abdominal fatness with local bioimpedance analysis: basics and experimental findings. *International journal of obesity and related metabolic disorders: journal of the International Association for the Study of Obesity,* 25**,** 502-511.

SCHLEBUSCH, T., RÖTHLINGSHÖFER, L., KIM, S., KÖNY, M. & LEONHARDT, S. On the Road to a Textile Integrated Bioimpedance Early Warning System for Lung Edema. BSN, 2010. 302-307.

SCHMITT, O. H. 1957. Lead vectors and transfer impedance. *Annals of the New York Academy of Sciences,* 65**,** 1092-1109.

SCHRÖDER, J., DOERNER, S., SCHNEIDER, T. & HAUPTMANN, P. 2004. Analogue and digital sensor interfaces for impedance spectroscopy. *Measurement Science and Technology,* 15**,** 1271.

SCHWAN, H. 1968. ELECTRODE POLARIZATION IMPEDANCE AND MEASUREMENTS IN BIOLOGICAL MATERIALS*. *Annals of the New York Academy of Sciences,* 148**,** 191-209.

SCHWAN, H. P. 1957. Electrical properties of tissue and cell suspensions. *Advances in biological and medical physics,* 5**,** 147-209.

SCIOSPEC. *Sciospec ISX-5, Scientific Instruments GmbH,* http://sciospec.de/cms/products/isx-5 [Online].

SCUTT, D., MANNING, J., WHITEHOUSE, G., LEINSTER, S. & MASSEY, C. 1997. The relationship between breast asymmetry, breast size and the occurrence of breast cancer. *The British journal of radiology,* 70**,** 1017-1021.

SHAPIRO, S., COLEMAN, E. A., BROEDERS, M., CODD, M., DE KONING, H., FRACHEBOUD, J., MOSS, S., STACHENKO, S. & BALLARD-BARBASH, R. 1998. Breast cancer screening programmes in 22 countries: current policies, administration and guidelines. *International journal of epidemiology,* 27**,** 735-742.

SICKLES, E. A. 1984. Mammographic features of" early" breast cancer. *American Journal of Roentgenology,* 143**,** 461-464.

SIEBENS, A. A., ELLIOTT, D. H., HEATH, D. A., WEIBEL, E. R., CHERNIACK, N. S., BURRI, P. H. & KLOCKE, R. A. 2017. *Human Respiratory System* [Online]. Encyclopædia Britannica, inc. Available: https://www.britannica.com/science/human-respiratory-system [Accessed 30 May 2017 2017].

SMITH, R. W. 1990. Design of a real-time impedance imaging system for medical applications. *Department of Electrical and Electrical Engineering, University of Sheffield, UK., Diss.*

SMITH, S. R., FOSTER, K. R. & WOLF, G. L. 1986. Dielectric properties of VX-2 carcinoma versus normal liver tissue. *IEEE transactions on biomedical engineering*, 522-524.

SMITH, T. J. 2010. *The GcMAF Book* [Online]. Available: http://gcmaf.timsmithmd.com/book/chapter/60/

SOHN, C., GRISCHKE, E., WALLWIENER, D., KAUFMANN, M., VON FOURNIER, D. & BASTERT, G. 1992. Ultrasound diagnosis of blood flow in benign and malignant breast tumors. *Geburtshilfe und Frauenheilkunde,* 52**,** 397-403.

SONI, N. K., HARTOV, A., KOGEL, C., POPLACK, S. P. & PAULSEN, K. D. 2004. Multi-frequency electrical impedance tomography of the breast: new clinical results. *Physiological measurement,* 25**,** 301.

STAUB, N. C. 1974. Pulmonary edema. *Physiological Reviews,* 54**,** 678-811.

STEWART, B. & WILD, C. P. 2014. *World cancer report 2014* [Online]. International Agency for Research on Cancer, WHO. Available: http://www.thehealthwell.info/node/725845.

SUROVY, N. J., BILLAH, M. M., HAOWLADER, S., AL-QUADERI, G. D. & RABBANI, K. S.-E. 2012. Determination of abdominal fat thickness using dual electrode separation in the focused impedance method (FIM). *Physiological measurement,* 33**,** 707.

SUROWIEC, A. J., STUCHLY, S. S., BARR, J. R. & SWARUP, A. 1988. Dielectric properties of breast carcinoma and the surrounding tissues. *Biomedical Engineering, IEEE Transactions on,* 35**,** 257-263.

TEH, W. & WILSON, A. 1998. The role of ultrasound in breast cancer screening. A consensus statement by the European Group for Breast Cancer Screening. *European journal of cancer,* 34**,** 449-450.

TUCKER, A. S., FOX, R. M. & SADLEIR, R. J. 2013. Biocompatible, high precision, wideband, improved Howland current source with lead-lag compensation. *Biomedical Circuits and Systems, IEEE Transactions on,* 7**,** 63-70.

TUMER, R. B., LANDE, A. E., CHASE, P., HILTON, N. & WEINBERG, D. 1987. Pneumonia in pediatric outpatients: cause and clinical manifestations. *The Journal of pediatrics,* 111**,** 194-200.

VANDEWEYER, E. & HERTENS, D. 2002. Quantification of glands and fat in breast tissue: an experimental determination. *Annals of Anatomy-Anatomischer Anzeiger,* 184**,** 181-184.

VAUPEL, P., KALLINOWSKI, F. & OKUNIEFF, P. 1989. Blood flow, oxygen and nutrient supply, and metabolic microenvironment of human tumors: a review. *Cancer research,* 49**,** 6449-6465.

VIRKKI, R., JUVEN, T., RIKALAINEN, H., SVEDSTRÖM, E., MERTSOLA, J. & RUUSKANEN, O. 2002. Differentiation of bacterial and viral pneumonia in children. *Thorax,* 57**,** 438-441.

WANG, J.-R., SUN, B.-Y., WANG, H.-X., PANG, S., XU, X. & SUN, Q. 2014. Experimental Study of Dielectric Properties of Human Lung Tissue in Vitro. *Journal of Medical and Biological Engineering,* 34**,** 598-604.

WARRAICH, H. J., BHATTI, U. A., SHAHUL, S., PINTO, D., LIU, D., MATYAL, R. & MAHMOOD, F. 2011. Unilateral pulmonary edema secondary to mitral valve perforation. *Circulation,* 124**,** 1994-1995.

WILSON, A., MILNES, P., WATERWORTH, A., SMALLWOOD, R. & BROWN, B. 2001. Mk3. 5: a modular, multi-frequency successor to the Mk3a EIS/EIT system. *Physiological Measurement,* 22**,** 49.

WIPF, J. E., LIPSKY, B. A., HIRSCHMANN, J. V., BOYKO, E. J., TAKASUGI, J., PEUGEOT, R. L. & DAVIS, C. L. 1999. Diagnosing pneumonia by physical examination: relevant or relic? *Archives of Internal Medicine,* 159**,** 1082-1087.

WREN, B. G. 2007. The origin of breast cancer. *Menopause,* 14**,** 1060-1068.

WU, M. & BURSTEIN, D. E. 2004. Fine needle aspiration. *Cancer investigation,* 22**,** 620-628.

ZEXI, H., HAIFEI, Z., WENBO, W. & GUODONG, L. 2009. Design of sine wave signal generator based on DDS technology [J]. *Electronic Test,* 8**,** 021.

ZHI, H., OU, B., LUO, B.-M., FENG, X., WEN, Y.-L. & YANG, H.-Y. 2007. Comparison of ultrasound elastography, mammography, and sonography in the diagnosis of solid breast lesions. *Journal of ultrasound in medicine,* 26**,** 807-815.

ZOU, Y. & GUO, Z. 2003. A review of electrical impedance techniques for breast cancer detection. *Medical engineering & physics,* 25**,** 79-90.

ZULEY, M. L. 2010. The basics and implementation of digital mammography. *Radiologic Clinics of North America,* 48**,** 893-901.